Studying chiral magnetic wave, hadronic rescattering and $f_1(1285)$ production in high energy collisions with ALICE detector

By

PROTTAY DAS

PHYS11201705001

National Institute of Science Education and Research,
Bhubaneswar

A thesis submitted
to the Board of Studies in
School of Physical Sciences

In partial fulfillment of requirements
For the Degree of

DOCTOR OF PHILOSOPHY
of
HOMI BHABHA NATIONAL INSTITUTE

March, 2024

CERN-THESIS-2024-103
22/07/2024

Homi Bhabha National Institute

Recommendations of the Viva Voce Committee

As members of the Viva Voce Committee, we certify that we have read the dissertation prepared by **Prottay Das** entitled **"Studying chiral magnetic wave, hadronic rescattering and $f_1(1285)$ production in high energy collisions with ALICE detector"** and recommend that it may be accepted as fulfilling the thesis requirement for the award of Degree of Doctor of Philosophy.

Chairman - Prof. Sanjay Kumar Swain **Date:** 22/07/2024

Guide / Convener - Prof. Bedangadas Mohanty **Date:** 22/07/2024

External Examiner - Prof. Chitrasen Jena Chitrasen Jena **Date:** 22/07/2024

Member 1 - Dr. Victor Roy Victor Roy **Date:** 22.07.2024

Member 2 - Dr. Najmul Haque Haque **Date:** 22.07.2024

Member 3 - Dr. Aruna Kumar Nayak **Date:**
Aruna Kumar Nayak 22/07/24

Final approval and acceptance of this thesis is contingent upon the candidate's submission of the final copies of the thesis to HBNI.

I hereby certify that I have read this thesis prepared under my direction and recommend that it may be accepted as fulfilling the thesis requirement.

Date : July 22, 2024
Place : NISER, Jatni

22/07/2024
(Guide)

STATEMENT BY THE AUTHOR

This dissertation has been submitted in partial fulfillment of requirements for an advanced degree at Homi Bhabha National Institute (HBNI) and is deposited in the library to be made available to borrowers under rules of the HBNI.

Brief quotations from this dissertation are allowable without special permission, provided that accurate acknowledgement of source is made. Requests for permission for extended quotation from or reproduction of this manuscript in whole or in part may be granted by the Competent Authority of HBNI when in his or her judgment the proposed use of the material is in the interests of scholarship. In all other instances, however, permission must be obtained from the author.

Date : July 22,2024
Place : NISER, Jatni

Prottay Das
(PROTTAY DAS)

DECLARATION

I hereby declare that the investigation presented in the thesis has been carried out by me. The work is original and has not been submitted earlier as a whole or in part for a degree/diploma at this or any other Institution/University.

Date : July 22, 2024
Place : NISER, Jatni

Prottay Das
(PROTTAY DAS)

CERTIFICATION OF ACADEMIC INTEGRITY

Undertaking by the student

1. I **Prottay Das**, HBNI Enrolment No. **PHYS11201705001** hereby undertake that the thesis titled "**Studying chiral magnetic wave, hadronic rescattering and f_1(1285) production in high energy collisions with ALICE detector**" is prepared by me and is the original work undertaken by me.
2. I also hereby undertake that this document has been duly checked through a plagiarism detection tool and the document is found to be plagiarism free as per the guidelines of the Institute/UGC.
3. I am aware and undertake that if plagiarism is detected in my thesis at any stage in the future, suitable penalty will be imposed as applicable as per the guidelines of the Institute/UGC.

Prottay Das
13/07/2024
Signature of the Student with date

Endorsed by the thesis supervisor

I certify that the thesis written by the student is plagiarism free as mentioned above.

22/07/2024
Signature of the thesis supervisor with date

Name : Bedangadas Mohanty
Designation : Professor
Department / Centre : School of Physical Sciences
Name of the CI / OCC : National Institute of Science Education and Research

List of Publications arising from the thesis

Journal

Published

1. Shreyasi Acharya et al. “System-size dependence of the hadronic rescattering effect at energies available at the CERN Large Hadron Collider”. *Phys. Rev. C* 109.1 (2024). ALICE Collaboration, p. 014911. arXiv: `2308.16115 [nucl-ex]`.

2. Shreyasi Acharya et al. “Probing the chiral magnetic wave with charge-dependent flow measurements in Pb-Pb collisions at the LHC”. *JHEP* 12 (2023). ALICE Collaboration, p. 067. arXiv: `2308.16123 [nucl-ex]`.

3. Shreyasi Acharya et al. “K*(892)± resonance production in Pb-Pb collisions at $\sqrt{s_{\mathrm{NN}}}$ = 5.02 TeV”. *Phys. Rev. C* 109.4 (2024), p. 044902. arXiv: `2308.16119 [nucl-ex]`.

4. Wen-Ya Wu et al. “Global constraint on the magnitude of anomalous chiral effects in heavy-ion collisions”. *Phys. Rev. C* 107.3 (2023), p. L031902. arXiv: `2211.15446 [nucl-th]`.

Under preparation

1. “Measurement of $f_1(1285)$ production cross section in pp collisions at $\sqrt{s}$ = 13 TeV” (2024). ALICE Collaboration.

Analysis notes

1. “Search for Chiral Magnetic Wave using ALICE detector in Pb–Pb collisions at $\sqrt{s_{\mathrm{NN}}}$ = 5.02 TeV at LHC” (2020). Primary contributors: **Prottay Das**, Md. Rihan Haque, Bedangadas Mohanty. Note link: `https://alice-notes.web.cern.ch/node/1111`.

2. “K(892)^{*0} resonance production as a function of multiplicity in INEL>0 pp collisions at $\sqrt{s}$= 5.02 TeV” (2022). Primary contributors: **Prottay Das**, Ranbir Singh, Bedangadas Mohanty. Note link: `https://alice-notes.web.cern.ch/node/1316`.

3. “K*(892)$^{\pm}$ production in Pb–Pb collisions with ALICE at the LHC” (2021). Primary contributors: **Prottay Das**, Ranbir Singh, Bedangadas Mohanty. Note link: `https://alice-notes.web.cern.ch/node/1215`.

4. “$f_1(1285)$ resonance production in pp collisions at $\sqrt{s}$= 13 TeV” (2023). Primary contributors: **Prottay Das**, Bedangadas Mohanty. Note link: `https://alice-notes.web.cern.ch/node/1442`.

Conferences

1. VI International conference on Initial Stages of high energy nuclear collisions (IS 2021), *Weizmann Institute of Science, Rehovot (Israel)* [10–15 January , 2021]
Title: Search for the Chiral Magnetic Wave using the ALICE detector in Pb-Pb collisions at $\sqrt{s_{NN}}$ = 5.02 TeV.

2. LXXI International Conference Nucleus 2021, *St.Petersburg* [20–25 September, 2021]
Title: Search for the Chiral Magnetic Wave using the ALICE detector in Pb-Pb collisions

at $\sqrt{s_{NN}}$ = 5.02 TeV.

3. The 8th Asian Triangle Heavy-Ion Conference (ATHIC 2021), *Inha University, Incheon, South Korea* [5–9 November, 2021]
Title: Search for the Chiral Magnetic Wave using the ALICE detector in Pb-Pb collisions at $\sqrt{s_{NN}}$ = 5.02 TeV.

4. XLI International Conference on High Energy Physics (ICHEP2022), *Bologna, Italy* [6–13 July, 2022]
Title: Exploring the hadronic phase of relativistic heavy-ion collisions with resonances in ALICE.

5. 28th International Nuclear Physics Conference (INPC2022), *Cape Town, South Africa* [11–16 September, 2022]
Title: Search for the Chiral Magnetic Wave in Pb−Pb collisions with the ALICE detector.

6. International Conference on Physics and AstroPhysics of Quark Gluon Plasma (ICPAQGP-2023), *Puri, Odisha, India* [7–10 February, 2023]
Title: Probing heavy-ion collision evolution with resonances in ALICE at the LHC.

7. XXIV DAE-BRNS HIGH ENERGY PHYSICS SYMPOSIUM, *NISER, Jatani, Khurda-752050 , Odisha, INDIA* [14–18 December, 2020]
Title: Search for the Chiral Magnetic Wave using the ALICE detector in Pb-Pb collisions at $\sqrt{s_{NN}}$ = 5.02 TeV.

8. XXV DAE-BRNS HIGH ENERGY PHYSICS SYMPOSIUM, *IISER Mohali, India* [12–16 December, 2022]
Title: Search for local parity violation in strong interaction using the ALICE detector in Pb−Pb collisions.

9. 66th DAE Symposium on Nuclear Physics, *Cotton University, Guwahati, Assam, India* [1–5 December, 2022]
Title: Probing rescattering effect in heavy-ion collisions with ALICE at LHC.

10. XXIX International Conference Quark Matter 2022 (QM22), *Krakow, Poland* [4–10 April, 2022]
Title: $K^{*\pm}$ production in Pb−Pb collisions with ALICE at the LHC.

11. International Conference on Strangeness in Quark Matter (SQM2022), *Busan* [13–17 June, 2022]
Title: $K^{*\pm}$ production in Pb−Pb collisions with ALICE at the LHC.

12. 2nd workshop on Dynamics of QCD Matter, *NISER, Odisha, India* [7–9 October, 2023]
Title: Investigating local parity violation in strong interaction at LHC energies.

13. International Conference on Strangeness in Quark Matter (SQM2024), *Strasbourg, France* [3–7 June, 2024]
Title: Investigating the hidden strangeness content of exotic resonance with ALICE.

Date : July 22, 2024
Place : NISER, Jatni

Prottay Das
(PROTTAY DAS)

DEDICATED TO

MAA DURGA, who has been my source of wisdom, strength and perseverance throughout my life.

ACKNOWLEDGEMENTS

First and foremost, I extend my deepest gratitude to the Almighty, whose boundless wisdom and unwavering strength have illuminated my path throughout this doctoral journey. Without the Almighty's grace, nothing would have been conceivable.

I am deeply grateful to my supervisor, Prof. Bedangadas Mohanty, for entrusting me with the opportunity to delve into such captivating subject. His rigorous criticism and constructive feedback have been invaluable in shaping my understanding and growth in all aspects of my life. Without his unwavering guidance and support, I would not have been able to persevere. I extend my heartfelt thanks for his steadfast supervision and tireless assistance throughout this journey. I have been greatly benefited from his expansive knowledge and logical approach. Moreover, his ability to simplify complex physics concepts for a broader audience has been truly inspiring. Thanks to him, my dream of working on one of the largest experiments, ALICE at the Large Hadron Collider, has become a reality. I am sincerely thankful for the privilege of having him as my supervisor.

I extend my sincere appreciation to Dr. Sourav Kundu and Dr. Rihan Haque for their invaluable suggestions and enriching discussions throughout my doctoral journey. I am particularly grateful to Dr. Sourav Kundu for his unwavering support and having belief in me during a challenging period when I was about to leave the field. I owe a lot to him. Their guidance and encouragement have been instrumental in my academic growth, and I am deeply thankful for their contributions to my success.

I would also like to thank Dr. Dukhishyam Mallick, Dr. Debasish Mallick, Dr. Ashutosh Dash, Dr. Ranbir Singh, Dr. Ajay Kumar Dash and Dr. Subhasish Samanta who have been always beside me to resolve any doubt irrespective of coding or theory. Additionally, I extend my heartfelt thanks to Dr. Varchaswi Kashyap for his constant availability and

willingness to help with any matter, no matter how trivial. Regards to Dr. Shuddha Shankar Dasgupta, Dr. Ganesh Tambave, and Mr. Kirti Prasad Sharma. Thanks to Dr. Samir Banik, Dr. Vijay Iyer, Dr. Sandeep Dudi, and Mr. Rik Bhattacharya for sharing their valuable time on many occasions. I will fondly remember the late-night discussions and enjoyable moments shared with Dr. Ashish Pandav, who not only served as a senior colleague in my lab but also lived as my neighbour in the hostel. I am lucky enough to have had colleagues like Sawan, Bappaditya, Dipanwita, and Sarjeeta. I express my warm regards to Sudipta, who has been more than just a colleague; he is like a dear friend and younger brother to me. Thank you for your friendly and fun-loving nature. I am grateful to all of you for making my time at RL-202 incredibly enjoyable, which created a perfect environment for conducting research peacefully.

No words are enough to describe how grateful I am to Miss. Mouli Choudhury for being a dependable source of guidance and for always steering me away from paths that were not meant for me. Many thanks for being beside me during the tough moments of my life. I consider myself incredibly fortunate to have an elder sister like her in my workplace. I sincerely thank you for being the best support system I could ask for.

I extend my heartfelt regards to Miss. Swati Saha, with whom I have shared a significant portion of my PhD journey. The moments spent together, whether it was at NISER, CERN, national or international conferences, schools, meetings, workshops or any other place holds a special place in my heart and will forever be treasured memories during my PhD journey.

Thanks to my doctoral committee members Dr. Sanjay Kumar Swain, Dr. Victor Roy, Dr. Najmul Haque, and Dr. Aruna Kumar Nayak, for their invaluable suggestions and insightful comments on my thesis work. Special thanks to Dr. Jurgen Schukraft, Dr. Marco van Leeuwen, Dr. Alexander Philip Kalweit, Dr. Andrea Dainese, Dr. Kai Schweda, Dr.

Igor Altsybeev, and Dr. Andrea Rossi for engaging in enriching physics discussions and graciously providing academic support and recommendation letters for my postdoctoral applications. Thanks to Dr. Sergey Voloshin, Dr. Angela Badala, Dr. Anders Garritt Knospe, and Dr. Sushanta Tripathy for carefully reviewing my analysis. Additionally, I am thankful to Dr. Viktor Riabov, Dr. Neelima Agrawal, Dr. Jihye Song, Dr. Andrea Dubla, Dr. You Zhou, Dr. Alexander Dobrin, Dr. Marek Bombara, Dr. Enrico Fragiacomo, Dr. Giuseppe Mandaglio, Dr. Javier Castillo, and Dr. Francesco Prino for their thorough reviews of my papers and valuable suggestions for their improvement. Furthermore, thanks to Lund University Department of Physics-Division of Particle Physics, University of Kansas, Physics Department-Panjab University, Horia Hulubei National Institute of Physics and Nuclear Engineering, The University of Texas at Austin, HUN-REN Wigner Research Centre for Physics, Karatay University, Hiroshima University, Dipartimento di Fisica 'E.R. Caianiello' dell'Universita and Gruppo Collegato INFN, and Institute of Experimental Physics, Slovak Academy of Sciences for carefully reviewing my papers and providing their valuable comments. I would also like to thank to Dr. Bong-Hwi-Lim, and Dr. Katarina Krizkova Gajdosova for their valuable suggestions as PAG Convenors. I am grateful to Dr. Jan Fiete Grosse-Oetringhaus and Raluca Crucera for their valuable assistance during the initial phases of the hyperloop train operation. Their support played a crucial role in fulfilling my Full-Time Equivalent (FTE) requirements, a prerequisite for obtaining my doctoral degree. Many thanks to my collaborator Dr. Qiye Shou and Miss. Wenya Wu. It was a nice experience to work with both of you.

I would also like to thank the conference committee chairs of ALICE collaboration for giving me opportunities to represent ALICE collaboration on multiple occasions in international/national conferences. I would like to thank the ALICE Collaboration - Run Coordination, Physics Coordination, Software and Computing Coordination, Technical

Coordination and Trigger Coordination for their invaluable contributions for smooth running of the experiment. I gratefully acknowledge the resources and support provided by the Grid computing facilities at CERN and HPC facility at the School of Physical Sciences, NISER. I also acknowledge the support of the Department of Atomic Energy (DAE) and the Department of Science and Technology (DST), Government of India for the financial supports during my PhD.

Some who requires a special mention are my college teachers Dr. Rajen Kundu, Dr. Atisdipankar Chakraborty and school teachers especially Randhir Sir for inspiring me to persue physics as a research carrier.

Special thanks to my batchmates Sourav, Shrish, Rahul, Subhojyoti, Shuvayu, Debmalya, Amit, Sayan, Ankit, and Akash for their constant support, love, help and good wishes making the NISER life as a memorable one. Thanks to Dr. Prafulla Saha and Dr. Bimalesh Giri for all the enjoyable discussions. Thanks to my college friends Koustav, Subhadip, Rohit, Indranil, who ignited the spirit of problem solving which helped me a lot to develop my basic physics concepts. Warm words for my school friends Sayan, Subhajit, Paulami, Niladri, Pritha, Priyanjana, Ankit, Mayukh, Aparajita, Nilavra, Soumava, Samyabrata, Debopam, and Jayant who have always managed to make me feel special. Thanks for your thoughts, well-wishes, phonecalls, e-mails, visits, texts, advice and being there whenever I needed a friend.

Finally, I wish to express my heartfelt gratitude to my guardians and parents for their unwavering love and encouragement throughout my entire life. A special and sincere thanks to my eldest aunt and uncle, whose support have been instrumental in my journey. Without them, I would never have reached this point.

Contents

Contents **xxi**

Summary **xxv**

List of Figures **xxix**

List of Tables **xliii**

List of Abbreviations **xlv**

1 Introduction **1**

1.1 Standard Model 2
1.2 Quantum Chromodynamics and Quark Gluon Plasma 5
1.3 Heavy-ion collisions 8
1.4 Coordinate axis 10
1.5 Kinematic variables 10
  1.5.1 Transverse Momentum (p_{T}) 10
  1.5.2 Rapidity (y) 11
  1.5.3 Pseudorapidity (η) 11
1.6 Fundamental variables for particle production 12
  1.6.1 Multiplicity 12
  1.6.2 Invariant yield 12

1.6.3 Collision geometry of heavy-ion collision 12
1.7 Experimental signatures of QGP formation 13
1.7.1 Jet quenching 14
1.7.2 Strangeness Enhancement 16
1.7.3 Elliptic flow 18
1.8 Thesis motivation and organization 21
1.8.1 Chiral Magnetic Wave in heavy-ion collisions 22
1.8.2 System size dependence of hadronic rescattering effect at LHC energies 28
1.8.3 Measurement of an exotic resonance in ALICE 31

2 A Large Ion Collider Experiment (ALICE) 53

2.1 The Large Hadron Collider (LHC) at CERN 54
2.2 The ALICE experiment at LHC 57
2.2.1 The Inner Tracking System (ITS) 59
2.2.2 The Time Projection Chamber (TPC) 61
2.2.3 The Time Of Flight (TOF) detector 64
2.2.4 The VZERO (V0) detector 66
2.3 ALICE datasets and detector upgrades 67

3 Search for Chiral Magnetic Wave in heavy-ion collisions 73

3.1 Data sample, event and tracks selections 74
3.2 Detector acceptance correction 76
3.3 Analysis details 78
3.3.1 Q-Cumulant method for flow coefficients calculations 78
Correlation between like/unlike charges 80
3.3.2 A_{ch} estimation and correction 81
3.3.3 Event Shape Engineering technique 82
3.4 Systematic uncertainties 84
3.5 Results 86
3.5.1 A_{ch} dependence of v_n and centrality dependence of the slope r_n^{Norm} 86
3.5.2 Constraining the fraction of the CMW with the ESE 91

3.6 Summary 93

4 System size dependence of hadronic rescattering effect at LHC energies 97

4.1 Dataset, event and track selections 98
4.2 Analysis details 102
4.3 Systematic uncertainties 108
4.4 Results 110
4.5 Summary 122

5 Measurement of production cross section of an exotic $f_1(1285)$ resonance in ALICE 129

5.1 Analysis details 130
    5.1.1 Data sample, event and track selections 130
    5.1.2 Signal extraction 132
5.2 Systematic uncertainties 138
5.3 Results 140
5.4 Summary 146

Conclusions 148

A Appendix 155

A.1 CMW systematic uncertainties 155
    A.1.1 Barlow check 155
    A.1.2 Systematic variation on r_n^{Norm} due to V_z for hadrons 157
    A.1.3 Systematic variation on r_n^{Norm} due to V_z for pions 159
    A.1.4 Systematic variation on r_n^{Norm} due to V_z for kaons 161
    A.1.5 Systematic variation on r_n^{Norm} due to V_z for protons 163
    A.1.6 Systematic variation on r_n^{Norm} due to χ^2_{TPC} for hadrons 165
    A.1.7 Systematic variation on r_n^{Norm} due to χ^2_{TPC} for pions 167
    A.1.8 Systematic variation on r_n^{Norm} due to χ^2_{TPC} for kaons 169
    A.1.9 Systematic variation on r_n^{Norm} due to χ^2_{TPC} for protons 171
    A.1.10 Systematic variation on r_n^{Norm} due to TPC Cluster for hadrons . . . 173
    A.1.11 Systematic variation on r_n^{Norm} due to TPC Cluster for pions 175
    A.1.12 Systematic variation on r_n^{Norm} due to TPC Cluster for kaons 177

A.1.13 Systematic variation on r_n^{Norm}due to TPC Cluster for protons . . . 179
A.1.14 Systematic variation on r_n^{Norm}due to $|\eta| > 0.6$ for hadrons 181
A.1.15 Systematic variation on r_n^{Norm}due to $|\eta| > 0.6$ for pions 183
A.1.16 Systematic variation on r_n^{Norm}due to $|\eta| > 0.5$ for kaons 185
A.1.17 Systematic variation on r_n^{Norm}due to $|\eta| > 0.5$ for protons 187
A.1.18 Systematic variation on r_n^{Norm}due to PID for pions 189
A.1.19 Systematic variation on r_n^{Norm}due to PID for kaons 191
A.1.20 Systematic variation on r_n^{Norm}due to PID for protons 193
A.1.21 Systematic variation on r_n^{Norm}due to DCA for hadrons 195
A.1.22 Systematic variation on r_n^{Norm}due to DCA for pions 197
A.1.23 Systematic variation on r_n^{Norm}due to DCA for kaons 199
A.1.24 Systematic variation on r_n^{Norm}due to DCA for protons 201
A.2 BlastWave LCC model 202

Summary

Interactions among elementary particles in the universe are mediated by four fundamental forces: strong, electromagnetic, weak, and gravitational interactions. While the standard model of elementary particles describes three of these forces, it excludes gravity. In the standard model, the theory of strong interaction is Quantum Chromodynamics (QCD). QCD predicts that under extreme conditions, such as very high temperatures and/or density, a new phase of strongly interacting nuclear matter called quark-gluon plasma (QGP) can exist. In this phase, quarks and gluons are no longer confined within hadrons. It is believed that QGP also existed in the early universe just a few microseconds after the Big Bang, and it may persist in the dense cores of massive astrophysical objects like neutron stars, where lower temperatures but higher densities prevail. To explore the emerging properties of this strongly interacting medium, heavy-ion collisions are conducted at the Large Hadron Collider (LHC). In these collisions, the system experiences initial large transient magnetic fields (**B**) of the order of 10^{15} Tesla due to the relativistically moving spectator protons. This magnetic field, perpendicular to the reaction plane, formed by the colliding nuclei's impact parameter and the beam direction, provides a unique opportunity to investigate novel

QCD phenomena, leading to local parity violation in strong interactions. The presence of this magnetic field, along with non-zero vector and axial currents, results in a collective excitation in the QGP known as the Chiral Magnetic Wave (CMW). CMW induces a finite electric quadrupole moment measurable through charge-dependent anisotropic flow measurements. The experimental signature of CMW is charge-dependent elliptic flow, v_2. Specifically, the normalized difference of v_2 between positive and negative charges, denoted as $\Delta v_2/\langle v_2\rangle$, is expected to exhibit a positive slope (r_2^{Norm}) as a function of the asymmetry (A_{ch}) in the number of positively and negatively charged particles in an event. However, non-CMW mechanisms such as Local Charge Conservation (LCC), intertwined with collective flow, can also contribute to a similar slope. One way to probe this background is by performing similar measurements with v_3, as it is not expected to be affected by the CMW phenomenon. This study investigates charge-dependent anisotropic flow coefficients in Pb–Pb collisions at a center-of-mass energy per nucleon–nucleon collision of $\sqrt{s_{\mathrm{NN}}} = 5.02$ TeV to explore the CMW phenomenon. Specifically, the slope of the normalized difference in elliptic (v_2) and triangular (v_3) flow coefficients of positively and negatively charged particles is reported as a function of their event-wise normalized number difference for both inclusive and identified particles. Additionally, using the Event Shape Engineering technique, the fraction of the CMW signal and its upper limit at a 95% confidence level are extracted.

During the evolution of heavy-ion collisions, quarks and gluons undergo a process called hadronization, transforming into colorless hadrons. Once hadronization occurs, the system reaches a specific temperature known as the chemical freeze-out temperature. At this point, inelastic collisions among the hadrons stop, and the yields of stable particles become fixed. Subsequently, after chemical freeze-out, the hadrons continue to interact through elastic scattering, potentially altering the yields and shapes of their transverse momentum spectra. Later in the process, the system reaches a stage where the mean free path of the hadrons becomes much larger than the system size, termed as kinetic freeze-out, allowing the hadrons to move freely to the detectors. The phase between chemical and kinetic freeze-out, characterized by the proximity of the chemical freeze-out and quark-hadron transition temperatures, is referred to as the hadronic phase. The dynamics of this hadronic phase can be explored through measurements of the hadronic decays of short-lived resonances, particles that decay via strong interaction. Within the hadronic phase, the decay products of resonances engage into two simultaneous processes: regeneration and rescattering via elastic or pseudoelastic scattering (scattering through an intermediate state). These processes can lead to modifications in the measured resonance yields. The strength of these processes depends on the lifetime of the hadronic phase, the density of the hadronic medium, the hadronic interaction cross-section of the decay products of the resonances, and the lifetime of the resonances. Investigating the dominance of one effect over the other involves studying the yield ratios of resonances to longer-lived hadrons with the same quark content as a function of collision centrality. Measurements of $\mathrm{K}(892)^{*0}$ and $\mathrm{K}^{*}(892)^{\pm}$ have been conducted at midrapidity in pp and Pb–Pb collisions at $\sqrt{s_{\mathrm{NN}}}$ = 5.02 TeV, respectively. These measurements include the transverse momentum-integrated yield, mean transverse momentum, nuclear modification factor of K^{*}, and yield ratios of resonance to stable hadron. Comparisons are made across different collision systems (pp, p–Pb, Xe–Xe, and Pb–Pb) at similar collision energies to investigate the system size dependency of K^{*} resonance production and the effect of hadronic rescattering. Additionally, the yields of K^{*} are utilized to constrain the kinetic freeze-out temperature using the HRG-PCE model.

The QCD theory provides an understanding of how colored quarks and gluons interact through the strong force, leading to the formation of various types of hadronic matter. This encompasses conventional mesons (quark-antiquark pairs) and baryons (combinations of three quarks or antiquarks). In addition to these standard hadrons, there is ongoing interest in investigating exotic states, such as tetraquarks and pentaquarks, characterized by unconventional quark compositions. This study focuses on the measurement of such an exotic resonance, $f_1(1285)$ in ALICE. The measurement includes determining its mass, transverse momentum-integrated yield, and the average transverse momentum. Furthermore, the ratio of the transverse momentum-integrated yield of $f_1(1285)$ to that of pions is compared with calculations from the canonical statistical thermal model to gain insights into the strangeness quark content of $f_1(1285)$.

List of Figures

1.1 The schematic representation of standard model. This figure has been taken from [14]. 4

1.2 The QCD running coupling constant as a function of momentum transfer, compared with various experimental measurements, covering a wide range of momentum transfer. This figure has been taken from [17] 6

1.3 The normalized (scaled to the quadratic power of temperature) energy density, pressure density, and entropy density are depicted as functions of temperature, as per LQCD calculations with zero baryon chemical potential. These results pertain to (2+1) quark flavors. At lower temperatures, solid lines correspond to hadron resonance gas (HRG) model calculations, while at higher temperatures, the dashed line represents the outcome for a non-interacting quark-gluon gas [24]. 7

1.4 A schematic diagram for space-time evolution of heavy-ion collision [27]. . . 9

1.5 Two heavy-ions collision with a given impact parameter b [31]. 13

1.6 R_{AA} as a function of p_{T} for unidentified and identified charged particles and π^0 in central heavy-ion collision at the SPS, RHIC, and LHC energies [33]. . 15

1.7 Di-hadron azimuthal correlation of high-p_{T} charged hadrons in pp, d–Au and Au–Au collisions [21]. 16

1.8 The strangeness enhancement factor (ϵ) is plotted as a function of $\langle N_{\mathrm{part}} \rangle$ for K ($S = 1$), ϕ ($S = 0$), Λ ($S = 1$), and Ξ ($S = 2$) in Au–Au and Cu–Cu collisions at $\sqrt{s_{\mathrm{NN}}}$= 200 and 62.4 GeV [36]. 17

1.9 The profile of initial transverse energy density with its time dependence in coordinate space for a non-central heavy-ion collision [38]. The z-axis is taken to be along the beam direction and the x-axis is along the the impact parameter. 18

1.10 Schematic diagram of non central nucleus nucleus collision and susequent conversion of spatial anisotropy into momentum anisotropy [39]. 19

1.11 Elliptic flow of identified hadrons for 40–50% centrality class in Pb–Pb collisions at $\sqrt{s_{\rm NN}}$= 5.02 TeV [40]. 20

1.12 The slope parameter is presented across different collision energies as a function of centrality. Experimental measurements are compared with theoretical calculations considering varying lifetimes of the magnetic field within the medium. The figure is taken from [91]. 25

1.13 The normalized v_2 and v_3 slope parameter as a function of centrality. The figure is taken from [93]. 26

1.14 $p_{\rm T}$-integrated particle yield ratios of $\rm K^{*0}/K$ and ϕ/K as a function of $\mathrm{d}N_{\rm ch}/\mathrm{d}\eta$ measured at midrapidity for various collision systems at $\sqrt{s_{\rm NN}}$= 5.02 TeV. Measurements are compared with EPOS3 model predictions along with thermal model calculations for the most central Pb–Pb collisions. The figure is taken from [134] 30

2.1 The CERN accelerator complex and the positions of the four primary LHC experiments-ALICE, ATLAS, CMS, and LHCb situated along the LHC ring [1] 55

2.2 Schematic layout of the LHC [2]. 56

2.3 Schematic diagram for the ALICE detector systems [3]. 59

2.4 Layout for the ALICE ITS with Silicon Pixel, Silicon Strip and Silicon Drift detectors are shown [8]. 60

2.5 A schematic layout for the ALICE TPC [10]. 62

2.6 A schematic illustration of the working principle of the TPC [11]. 63

2.7 Average energy loss of tracks as a function of momentum using TPC in Pb–Pb collisions at $\sqrt{s_{\rm NN}}$= 5.02 TeV [13]. 64

2.8 The distribution of β, obtained through the Time-of-Flight (TOF) detector, is analyzed as a function of the momentum of particles reaching the TOF detector in Pb–Pb collisions at a center-of-mass energy of $\sqrt{s_{\rm NN}}$ = 5.02 TeV [13]. . . . 66

2.9 ALICE PID and reconstruction capabilities of various hadrons as a function of transverse momentum [14]. 67

3.1 Left panel figure shows the tracking efficiency for charged unidentified hadrons and right panel shows the same for pions in Pb–Pb collisions at $\sqrt{s_{\rm NN}}$= 5.02 TeV. Red markers are for particles and blue for their corresponding antiparticles. 76

3.2 Left panel figure shows the tracking efficiency for charged kaons and right panel shows the same for protons in Pb–Pb collisions at $\sqrt{s_{\rm NN}}$= 5.02 TeV. Red markers are for particles and blue for their corresponding antiparticles. 77

3.3 Left panel figure shows the purity for pions and right panel for protons in Pb–Pb collisions at $\sqrt{s_{\rm NN}}$= 5.02 TeV. 77

3.4 Azimuthal distribution of charged particles before and after acceptance correction in Pb–Pb collisions at $\sqrt{s_{\rm NN}}$ = 5.02 TeV. 78

3.5 (Left panel): Raw $A_{\rm ch}$ distribution in Pb–Pb collisions at $\sqrt{s_{\rm NN}}$ = 5.02 TeV for the 40–50% centrality interval. Red dotted lines depict the edges of the ten $A_{\rm ch}$ classes. (Right panel): Correlation between true and raw $A_{\rm ch}$ obtained from HIJING simulations combined with a GEANT3 detector model for Pb–Pb collisions at $\sqrt{s_{\rm NN}}$ = 5.02 TeV in the 40–50% centrality interval. The figure is taken from [17]. 83

3.6 Calibrated V0 event plane angle in Pb–Pb collisions at $\sqrt{s_{\rm NN}}$ = 5.02 TeV in 10–60% centrality interval. The red line shows the fit to the event plane angle distribution after calibration. 84

3.7 The top left panel shows the v_2 of positively (red markers) and negatively (blue markers) charged hadrons as a function of the corrected $A_{\rm ch}$, while the top right panel shows the same for v_3. Statistical uncertainties are shown by bars and uncorrelated (correlated) systematic uncertainties by open boxes (shaded bands). The bottom left panel shows $\Delta v_2/\langle v_2\rangle$ as a function of the corrected $A_{\rm ch}$ and bottom right panel shows the same for $\Delta v_3/\langle v_3\rangle$, all for the 40–50% centrality interval in Pb–Pb collisions at $\sqrt{s_{\rm NN}}$ = 5.02 TeV. The dotted blue line shows the linear fit to the data points to obtain the values of normalized slopes ($r_2^{\rm Norm}$ and $r_3^{\rm Norm}$). The figure is taken from [17]. 88

3.8 Centrality dependence of normalized slopes r_2^{Norm} and r_3^{Norm} for inclusive charged hadrons in Pb−Pb collisions at $\sqrt{s_{\mathrm{NN}}}$ = 5.02 TeV compared with CMS results [22] and a BW+LCC model calculation [23]. Statistical (systematic) uncertainties are depicted by bars (boxes). ALICE r_2^{Norm} and r_3^{Norm} and CMS r_2^{Norm} data points are slightly shifted horizontally for visibility. The figure is taken from [17]. 89

3.9 Centrality dependence of normalized slopes r_2^{Norm} (left panel) and r_3^{Norm} (right panel) for inclusive and identified charged hadrons in Pb–Pb collisions at $\sqrt{s_{\mathrm{NN}}}$ = 5.02 TeV. Statistical (systematic) uncertainties are depicted by bars (boxes). The data points for charged pions and kaons are slightly shifted horizontally for visibility. The figure is taken from [17] 90

3.10 Dependence of ΔIC on v_2 of shape-selected events from the 0–10% (top left panel) to the 50–60% (bottom right panel) centrality intervals of Pb–Pb collisions at $\sqrt{s_{\mathrm{NN}}}$ = 5.02 TeV. The solid lines are straight line fit to the data points. Only statistical uncertainties are shown. The bands represent the three standard deviation uncertainties from the linear fit. The figure is taken from [17]. . . . 91

3.11 Centrality dependence of the extracted CMW fraction. The 95% confidence level of the upper limit is also shown by the dotted magenta line. Statistical uncertainties are depicted by bars, while the correlated systematic uncertainty is represented by a shaded band on the right edge. The blue line is the constant fit line of the data points. The figure is taken from [17]. 92

4.1 Invariant mass distribution of $\mathrm{K_S^0}$ for $\mathrm{K^*(892)^\pm}$ in the p_{T} interval of 0.4 to 0.8 GeV/c. 102

4.2 (Left panel): Invariant mass distribution of $\mathrm{K_S^0}\pi^\pm$ pairs in same (black marker) and mixed events (red marker). (Right panel): Invariant mass distribution of $\mathrm{K_S^0}\pi^\pm$ pairs after the subtraction of normalized mixed-event background distribution [17]. The solid red curve is the fit function defined by Eq. 4.1, with the dotted blue line describing the residual background distribution given by Eq. 4.2. 104

4.3 The acceptance times efficiency correction for $\mathrm{K^{*\pm}}$ (left) and $\mathrm{K^{*0}}$ (right) as a function of p_{T} for different centrality/ multiplicity intervals [17]. 106

4.4 (Left panel): The reweight factor for $\mathrm{K}^{*\pm}$ in Pb–Pb collisions at $\sqrt{s_{\mathrm{NN}}}$= 5.02 TeV. (Right panel): The reweight factor for K^{*0} in pp collisions at $\sqrt{s}$= 5.02 TeV 107

4.5 The event and signal loss factors for K^{*0} in pp collisions at $\sqrt{s}$= 5.02 TeV. . . 108

4.6 The p_{T} distributions of $\mathrm{K}^{*\pm}$ meson in various centrality intervals in Pb−Pb collisions at $\sqrt{s_{\mathrm{NN}}}$ = 5.02 TeV. The statistical and systematic uncertainties are shown as bars and boxes, respectively. The figure is taken from [17]. 111

4.7 Upper panel: The p_{T} spectra of K^{*0} in various multiplicity classes of pp collisions at $\sqrt{s}$ = 5.02 TeV. Lower panel: The ratios of the multiplicity-dependent p_{T} spectra to the multiplicity-integrated INEL> 0 spectra. The statistical and systematic uncertainties are shown as bars and boxes, respectively. The figure is taken from [25]. 112

4.8 The left panel shows the p_{T} distributions of K^{*0} meson in four different centrality classes of Xe–Xe collisions at $\sqrt{s_{\mathrm{NN}}}$ = 5.44 TeV [25]. The right panel shows the comparison among the K^{*0} p_{T} spectrum in 0−30% Xe–Xe collisions at $\sqrt{s_{\mathrm{NN}}}$ = 5.44 TeV, 20−30% Pb–Pb [23] collisions and 20-40% $\mathrm{K}^{*\pm}$ in Pb–Pb collisions at $\sqrt{s_{\mathrm{NN}}}$ = 5.02 TeV [17], all having similar multiplicities. The statistical and systematic uncertainties are shown by bars and boxes, respectively.113

4.9 The p_{T}distributions of $\mathrm{K}^{*\pm}$ (blue circles) and K^{*0} (red squares) [23] in 0−10% (left) and 40−60% (right) centrality intervals in Pb–Pb collisions at $\sqrt{s_{\mathrm{NN}}}$= 5.02 TeV. Statistical and systematic uncertainties are shown by bars and shaded boxes, respectively. The bottom panels show the $\mathrm{K}^{*\pm}$ to K^{*0} ratio as a function of p_{T}. The figure is taken from [17]. 114

4.10 The $\mathrm{d}N/\mathrm{d}y$(left panel) and $\langle p_{\mathrm{T}}\rangle$(right panel) of K^{*} as a function of $\langle \mathrm{d}N_{\mathrm{ch}}/\mathrm{d}\eta\rangle^{1/3}_{|\eta|<0.5}$ in pp collision at $\sqrt{s}$ = 5.02 TeV and in Xe–Xe collisions at $\sqrt{s_{\mathrm{NN}}}$ = 5.44 TeV [25]. Measurements are compared with the results obtained in p–Pb [30] and Pb–Pb [17, 23] collisions at $\sqrt{s_{\mathrm{NN}}}$ = 5.02 TeV. Bars and shaded boxes correspond to the statistical and systematic uncertainties, respectively. 115

4.11 The left panel shows the measured $\mathrm{K}^{*}/\mathrm{K}$ yield ratio along with model calculation. The right panel shows the lower limit of hadronic phase lifetime as a function of $\langle \mathrm{d}N_{\mathrm{ch}}/\mathrm{d}\eta\rangle^{1/3}_{|\eta|<0.5}$ in different collision systems [17, 25]. Bars and shaded boxes represent the statistical and systematic uncertainties, respectively. 116

4.12 The p_{T}-differential particle yield ratios $\mathrm{K}^{*\pm}/\mathrm{K}$ (a) and $\mathrm{K}^{*\pm}/\pi$(b) in pp (black marker) and Pb−Pb collisions at $\sqrt{s_{\mathrm{NN}}}$= 5.02 TeV for 0−10% (red marker) and 60−80% (blue marker) centrality intervals. The bottom panels (c) and (d) show the ratios of Pb−Pb to pp results, compared with 0−10% K^{*0} results [23]. Statistical uncertainties are shown by bars and systematic uncertainties by boxes. The statistical and systematic uncertainties on the data points are obtained by propagating the statistical and total systematic uncertainties of the measurements. The figure is taken from [17] 119

4.13 Left panel shows the R_{AA} comparison of various light-flavored hadrons [23, 44, 45], and the right panel shows the R_{AA} of $\mathrm{K}^{*\pm}$ for different centrality intervals both as a function of p_{T} in Pb−Pb collisions at $\sqrt{s_{\mathrm{NN}}}$ = 5.02. Statistical (systematic) uncertainties are shown by bars (shaded boxes). The shaded bands around unity reprsents the normalisation uncertainty on R_{AA}. The figure is taken from [17]. 121

5.1 In the left panel, the invariant mass distribution is presented for both unlike (black markers) and like-sign (red markers) $\mathrm{K}^0_{\mathrm{S}}\mathrm{K}\pi$ pairs originating from the same events. Meanwhile, the right panel displays the invariant mass distribution of $\mathrm{K}^0_{\mathrm{S}}\mathrm{K}\pi$ pairs after subtracting the like-sign background. The solid red curve is the fit function defined by Eq. 5.1, with the dotted blue line describing the residual background distribution is given by Eq. 5.2. 134

5.2 Efficiency times acceptance of $f_1(1285)$ as a function of transverse momentum in inelastic pp collisions at $\sqrt{s}$= 13 TeV. 136

5.3 Generated, reconstructed and experimental data p_{T} spectras in both unweighted and reweighted case for the $f_1(1285)$ meson in inelastic pp collisions at $\sqrt{s}$ = 13 TeV. 137

5.4 Ratio between original $A \times \epsilon_{\mathrm{rec}}$ and weighted $A \times \epsilon_{\mathrm{rec}}$ for the $f_1(1285)$ meson in inelastic pp collisions at $\sqrt{s}$ = 13 TeV. 138

5.5 Systematic uncertainty for the $f_1(1285)$ meson in inelastic pp collisions at $\sqrt{s}$ = 13 TeV. 140

5.6 Measured $f_1(1285)$ mass at midrapidity ($|y| < 0.5$) in inelastic pp collisions at $\sqrt{s}$ = 13 TeV. The statistical and systematic uncertainties are shown as bars and boxes, respectively. The blue dotted line represents the vacuum mass of $f_1(1285)$. 141

5.7 Transverse momentum spectra of $f_1(1285)$ measured at midrapidity ($|y| < 0.5$) in inelastic pp collisions at $\sqrt{s}$ = 13 TeV. The statistical and systematic uncertainties are shown as bars and boxes, respectively. The data points are fitted using a Levy-Tsallis function shown by the red dotted line. 144

5.8 Average transverse momentum of light-flavor hadrons as a function of hadron mass at midrapidity ($|y| < 0.5$) in inelastic pp collisions at $\sqrt{s}$ = 13 TeV. The statistical and systematic uncertainties are shown as bars and boxes, respectively.145

5.9 The transverse momentum integrated yield ratio f_1/π (left) and ϕ/π (right) measured in inelastic pp collisions at $\sqrt{s}$ = 13 TeV. The statistical and systematic uncertainties on the data points are shown as bars and boxes, respectively. The dotted line represents the γ_S-CSM model predictions with different strangeness content of $f_1$and ϕ mesons. 146

A.1 Left panel shows absolute systematic uncertainty for normalised v_2 slope of hadrons and right panel shows its Barlow ratio (passed) both as function of centrality. The errors shown are Barlow only. 157

A.2 Left panel shows absolute systematic uncertainty for normalised v_3 slope of hadrons and right panel shows its Barlow ratio (passed) both as function of centrality. The errors shown are Barlow only. 157

A.3 Left panel shows absolute systematic uncertainty for normalised v_2 slope of pions and right panel shows its Barlow ratio (passed) both as function of centrality. The errors shown are Barlow only. 159

A.4 Left panel shows absolute systematic uncertainty for normalised v_3 slope of pions and right panel shows its Barlow ratio (passed) both as function of centrality. The errors shown are Barlow only. 159

A.5 Left panel shows absolute systematic uncertainty for normalised v_2 slope of kaons and right panel shows its Barlow ratio (not passed) both as function of centrality. The errors shown are Barlow only. 161

A.6 Left panel shows absolute systematic uncertainty for normalised v_3 slope of kaons and right panel shows its Barlow ratio (passed) both as function of centrality. The errors shown are Barlow only. 161

A.7 Left panel shows absolute systematic uncertainty for normalised v_2 slope of protons and right panel shows its Barlow ratio (passed) both as function of centrality. The errors shown are Barlow only. 163

A.8 Left panel shows absolute systematic uncertainty for normalised v_3 slope of protons and right panel shows its Barlow ratio (not passed) both as function of centrality. The errors shown are Barlow only. 163

A.9 Left panel shows absolute systematic uncertainty for normalised v_2 slope of hadrons and right panel shows its Barlow ratio (passed) both as function of centrality. The errors shown are Barlow only. The systematic uncertainty is taken from fitting function. 165

A.10 Left panel shows absolute systematic uncertainty for normalised v_3 slope of hadrons and right panel shows its Barlow ratio (passed) both as function of centrality. The errors shown are Barlow only. 165

A.11 Left panel shows absolute systematic uncertainty for normalised v_2 slope of pions and right panel shows its Barlow ratio (not passed) both as function of centrality. The errors shown are Barlow only. The systematic uncertainty is taken from fitting function. 167

A.12 Left panel shows absolute systematic uncertainty for normalised v_3 slope of pions and right panel shows its Barlow ratio (passed) both as function of centrality. The errors shown are Barlow only. 167

A.13 Left panel shows absolute systematic uncertainty for normalised v_2 slope of kaons and right panel shows its Barlow ratio (passed) both as function of centrality. The errors shown are Barlow only. The systematic uncertainty is taken from fitting function. 169

A.14 Left panel shows absolute systematic uncertainty for normalised v_3 slope of kaons and right panel shows its Barlow ratio (passed) both as function of centrality. The errors shown are Barlow only. The systematic uncertainty is taken from fitting function. 169

A.15 Left panel shows absolute systematic uncertainty for normalised v_2 slope of protons and right panel shows its Barlow ratio (not passed) both as function of centrality. The errors shown are Barlow only. 171

A.16 Left panel shows absolute systematic uncertainty for normalised v_3 slope of protons and right panel shows its Barlow ratio (not passed) both as function of centrality. The errors shown are Barlow only. The systematic uncertainty is taken from fitting function. 171

A.17 Left panel shows absolute systematic uncertainty for normalised v_2 slope of hadrons and right panel shows its Barlow ratio (passed) both as function of centrality. The errors shown are Barlow only. The systematic uncertainty is taken from fitting function. 173

A.18 Left panel shows absolute systematic uncertainty for normalised v_3 slope of hadrons and right panel shows its Barlow ratio (passed) both as function of centrality. The errors shown are Barlow only. The systematic uncertainty is taken from fitting function. 173

A.19 Left panel shows absolute systematic uncertainty for normalised v_2 slope of pions and right panel shows its Barlow ratio (passed) both as function of centrality. The errors shown are Barlow only. The systematic uncertainty is taken from fitting function. 175

A.20 Left panel shows absolute systematic uncertainty for normalised v_3 slope of pions and right panel shows its Barlow ratio (passed) both as function of centrality. The errors shown are Barlow only. The systematic uncertainty is taken from fitting function. 175

A.21 Left panel shows absolute systematic uncertainty for normalised v_2 slope of kaons and right panel shows its Barlow ratio (passed) both as function of centrality. The errors shown are Barlow only. The systematic uncertainty is taken from fitting function. 177

A.22 Left panel shows absolute systematic uncertainty for normalised v_3 slope of kaons and right panel shows its Barlow ratio (passed) both as function of centrality. The errors shown are Barlow only. The systematic uncertainty is taken from fitting function. 177

A.23 Left panel shows absolute systematic uncertainty for normalised v_2 slope of protons and right panel shows its Barlow ratio (passed) both as function of centrality. The errors shown are Barlow only. The systematic uncertainty is taken from fitting function. 179

A.24 Left panel shows absolute systematic uncertainty for normalised v_3 slope of protons and right panel shows its Barlow ratio (passed) both as function of centrality. The errors shown are Barlow only. The systematic uncertainty is taken from fitting function. 179

A.25 Left panel shows absolute systematic uncertainty for normalised v_2 slope of hadrons and right panel shows its Barlow ratio (passed) both as function of centrality. The errors shown are Barlow only. The systematic uncertainty is taken from fitting function. 181

A.26 Left panel shows absolute systematic uncertainty for normalised v_3 slope of hadrons and right panel shows its Barlow ratio (passed) both as function of centrality. The errors shown are Barlow only. The systematic uncertainty is taken from fitting function. 181

A.27 Left panel shows absolute systematic uncertainty for normalised v_2 slope of pions and right panel shows its Barlow ratio (passed) both as function of centrality. The errors shown are Barlow only. The systematic uncertainty is taken from fitting function. 183

A.28 Left panel shows absolute systematic uncertainty for normalised v_3 slope of pions and right panel shows its Barlow ratio (passed) both as function of centrality. The errors shown are Barlow only. The systematic uncertainty is taken from fitting function. 183

A.29 Left panel shows absolute systematic uncertainty for normalised v_2 slope of kaons and right panel shows its Barlow ratio (not passed) both as function of centrality. The errors shown are Barlow only. The systematic uncertainty is taken from fitting function. 185

A.30 Left panel shows absolute systematic uncertainty for normalised v_3 slope of kaons and right panel shows its Barlow ratio (passed) both as function of centrality. The errors shown are Barlow only. The systematic uncertainty is taken from fitting function. 185

A.31 Left panel shows absolute systematic uncertainty for normalised v_2 slope of protons and right panel shows its Barlow ratio (passed) both as function of centrality. The errors shown are Barlow only. The systematic uncertainty is taken from fitting function. 187

A.32 Left panel shows absolute systematic uncertainty for normalised v_3 slope of protons and right panel shows its Barlow ratio (not passed) both as function of centrality. The errors shown are Barlow only. The systematic uncertainty is taken from fitting function. 187

A.33 Left panel shows absolute systematic uncertainty for normalised v_2 slope of pions and right panel shows its Barlow ratio (passed) both as function of centrality. The errors shown are Barlow only. The systematic uncertainty is taken from fitting function. 189

A.34 Left panel shows absolute systematic uncertainty for normalised v_3 slope of pions and right panel shows its Barlow ratio (passed) both as function of centrality. The errors shown are Barlow only. The systematic uncertainty is taken from fitting function. 189

A.35 Left panel shows absolute systematic uncertainty for normalised v_2 slope of kaons and right panel shows its Barlow ratio (passed) both as function of centrality. The errors shown are Barlow only. The systematic uncertainty is taken from fitting function. 191

A.36 Left panel shows absolute systematic uncertainty for normalised v_3 slope of kaons and right panel shows its Barlow ratio (not passed) both as function of centrality. The errors shown are Barlow only. 191

A.37 Left panel shows absolute systematic uncertainty for normalised v_2 slope of protons and right panel shows its Barlow ratio (passed) both as function of centrality. The errors shown are Barlow only. The systematic uncertainty is taken from fitting function. 193

A.38 Left panel shows absolute systematic uncertainty for normalised v_3 slope of protons and right panel shows its Barlow ratio (not passed) both as function of centrality. The errors shown are Barlow only. The systematic uncertainty is taken from fitting function. 193

A.39 Left panel shows absolute systematic uncertainty for normalised v_2 slope of hadrons and right panel shows its Barlow ratio (passed) both as function of centrality. The errors shown are Barlow only. The systematic uncertainty is taken from fitting function. 195

A.40 Left panel shows absolute systematic uncertainty for normalised v_3 slope of hadrons and right panel shows its Barlow ratio (passed) both as function of centrality. The errors shown are Barlow only. The systematic uncertainty is taken from fitting function. 195

A.41 Left panel shows absolute systematic uncertainty for normalised v_2 slope of pions and right panel shows its Barlow ratio (passed) both as function of centrality. The errors shown are Barlow only. The systematic uncertainty is taken from fitting function. 197

A.42 Left panel shows absolute systematic uncertainty for normalised v_3 slope of pions and right panel shows its Barlow ratio (passed) both as function of centrality. The errors shown are Barlow only. The systematic uncertainty is taken from fitting function. 197

A.43 Left panel shows absolute systematic uncertainty for normalised v_2 slope of kaons and right panel shows its Barlow ratio (passed) both as function of centrality. The errors shown are Barlow only. The systematic uncertainty is taken from fitting function. 199

A.44 Left panel shows absolute systematic uncertainty for normalised v_3 slope of kaons and right panel shows its Barlow ratio (passed) both as function of centrality. The errors shown are Barlow only. The systematic uncertainty is taken from fitting function. 199

A.45 Left panel shows absolute systematic uncertainty for normalised v_2 slope of protons and right panel shows its Barlow ratio (passed) both as function of centrality. The errors shown are Barlow only. The systematic uncertainty is taken from fitting function. 201

A.46 Left panel shows absolute systematic uncertainty for normalised v_3 slope of protons and right panel shows its Barlow ratio (passed) both as function of centrality. The errors shown are Barlow only. The systematic uncertainty is taken from fitting function. 201

A.47 Comparison of A_{ch} distribution obtained in BW-LCC model with ALICE data in Pb–Pb collisions at $\sqrt{s_{\mathrm{NN}}}$ = 5.02 TeV for 30-40% centrality. 203

List of Tables

2.1 Overview of the positions, acceptances in terms of pseudorapidity (η) and azimuthal angle (ϕ), and functions of the ALICE detector subsystems [4]. . . . 58

2.2 Summary of the LHC Run1 and Run2 physics programmes with the data taking periods. 68

3.1 Nominal event and track selection criteria and the corresponding variations used for the estimation of the systematic uncertainties. 86

3.2 Maximum systematic uncertainty (absolute value) on normalized slope per particle species over all centrality intervals from individual sources (see Table 3.1 for an explanation of each source). 87

4.1 Analyzed multiplicity classes in pp collisions at $\sqrt{s}$= 5.02 TeV 100

4.2 Selection criteria for K^0_S. 102

4.3 Systematic uncertainties on measured K^{*0} and $K^{*\pm}$ yields in pp and Pb−Pb collisions at $\sqrt{s_{NN}}$ = 5.02 TeV, respectively. The systematic uncertainties are shown for different sources for a low- and a high-p_T interval. 109

4.4 HRG-PCE model fits results in Pb−Pb collisions at $\sqrt{s_{NN}}$ = 5.02 TeV. Numbers in brackets show the published kinetic freeze-out temperatures obtained using blast-wave fits to $\pi^\pm$, $K^\pm$, $p(\overline{p})$ spectra [43]. 120

5.1 Selection criteria for K^0_S. 133

5.2 Systematic uncertainties on measured $f_1(1285)$ yield in pp collisions at $\sqrt{s}$ = 13 TeV. The systematic uncertainties are shown for different sources for a low- and a high-p_{T} interval. 139
5.3 Selection criteria for primary pions. 140
5.4 The p_{T}-integrated yield and mean transverse momentum of the $f_1(1285)$ meson in proton-proton collisions at a center-of-mass energy of 13 TeV. The integrated yield obtained from experimental data is compared with the thermal model (γ_{S}-CSM) calculations. 143

A.1 BW parameters for Pb–Pb collisions at $\sqrt{s_{\mathrm{NN}}}$ = 5.02 TeV. 203

List of Abbreviations

ALICE	A Large Ion Collider Experiment
CERN	Conseil Européen pour la Recherche Nucléaire, The European Organization for Nuclear Research
CMS	Compact Muon Solenoid
LHC	Large Hadron Collider
PANDA	Plastic AntiNeutrino Detector Array

CHAPTER 1

Introduction

Contents

1.1 Standard Model 2
1.2 Quantum Chromodynamics and Quark Gluon Plasma 5
1.3 Heavy-ion collisions 8
1.4 Coordinate axis 10
1.5 Kinematic variables 10
1.6 Fundamental variables for particle production 12
1.7 Experimental signatures of QGP formation 13
1.8 Thesis motivation and organization 21

The quest to unravel the mysteries of the universe has been a driving force in human inquiry for centuries. Fundamental questions such as "How did we come into existence?" and "What is matter made of?" have intrigued philosophers, scientists, and curious minds alike throughout history. In the pursuit of answers to these profound inquiries, the field of particle and nuclear physics has emerged as a cornerstone of modern scientific exploration. Since the early 20th century, physicists have embarked on a journey to understand the fundamental structure of matter and the underlying forces that govern the cosmos. Groundbreaking discoveries and revolutionary theories have shaped our current understanding of the universe, laying the groundwork for the development of the Standard Model of particle physics [1]. This theoretical framework, established since the 1960s, encapsulates our knowledge of fundamental particles and their interactions, providing a comprehensive description of the building blocks of the universe and the fundamental forces that shape their behavior. The inception of the Standard Model can be traced back to seminal works by esteemed physicists such as Peter Higgs, Sheldon Glashow, Steven Weinberg, Abdus Salam, and Murray Gell-Mann [2–6]. Higgs' proposal of the mechanism responsible for imparting mass to elementary particles, Glashow's formulation of electroweak theory, and Weinberg and Salam's unification of electromagnetic and weak interactions laid the foundation for the modern understanding of particle physics. Gell-Mann's development of the quark model provided insight into the substructure of hadrons and paved the way for a deeper understanding of the strong nuclear force.

1.1 Standard Model

The Standard Model (SM) stands as a testament to human intellect and ingenuity, weaving together a rich tapestry of experimental insights and theoretical breakthroughs into a unified framework. At its core, it delves into the intricate workings of the universe at its most fundamental level- the realm of quantum, subatomic phenomena. From the earliest conjectures about the atomic nature of matter to the pioneering explorations of electricity and magnetism, each milestone has contributed to the evolution of our understanding encapsulated in the Standard Model. In essence, the SM represents humanity's most sophisticated endeavor to encapsulate the workings of the cosmos within a single, elegant theory. Within this framework, elementary particles are classified into two primary categories: fermions, constituting matter, and bosons, which mediate fundamental forces. Fermions, further subdivided into quarks and leptons, populate the landscape of matter, while bosons, including gauge bosons and the Higgs boson, govern the interactions between these constituents. The development of the Standard Model unfolded in stages, with contributions from numerous scientists worldwide culminating in its formulation in the mid-1970s. This pivotal moment followed the experimental validation of quarks and gluons [7–9] existence, posited as the elemental building blocks of hadrons. Subsequent confirmations, such as the discovery of the top quark [10], the tau (τ) neutrino [11], and the Higgs boson [12, 13] have bolstered the model's foundations. Furthermore, the Standard Model's predictive prowess extends to various properties of weak force carriers, W and Z bosons, with remarkable accuracy.

In accordance with the Standard Model, elementary particles are categorized into distinct generations, each comprising quarks and leptons. These generations delineate the diverse array of particles populating the cosmos, from the familiar electron to the elusive neutrinos. Interactions between these particles are mediated by three fundamental forces: strong, weak, and electromagnetic. The strong force, facilitated by gluons, binds quarks together to form the building blocks of atomic nuclei. Conversely, weak interactions, mediated by W and Z bosons, govern processes such as radioactive decay, influencing atomic nuclei's stability. Meanwhile, electromagnetic forces, transmitted via photons, foster the cohesion of atoms through the creation of electric and magnetic fields.

Despite its remarkable achievements, the Standard Model grapples with inherent limitations, notably its inability to accommodate gravity or elucidate enigmatic phenomena like dark matter, dark energy, and neutrino masses. These unresolved mysteries serve as catalysts for ongoing exploration and research at the forefront of theoretical and experimental particle physics. In essence, while the Standard Model stands as a fundamental pillar of our comprehension, it also signifies humanity's relentless pursuit to unveil the universe's profound mysteries. The schematic representation of fundamental particles in the Standard Model is shown in Fig. 1.1.

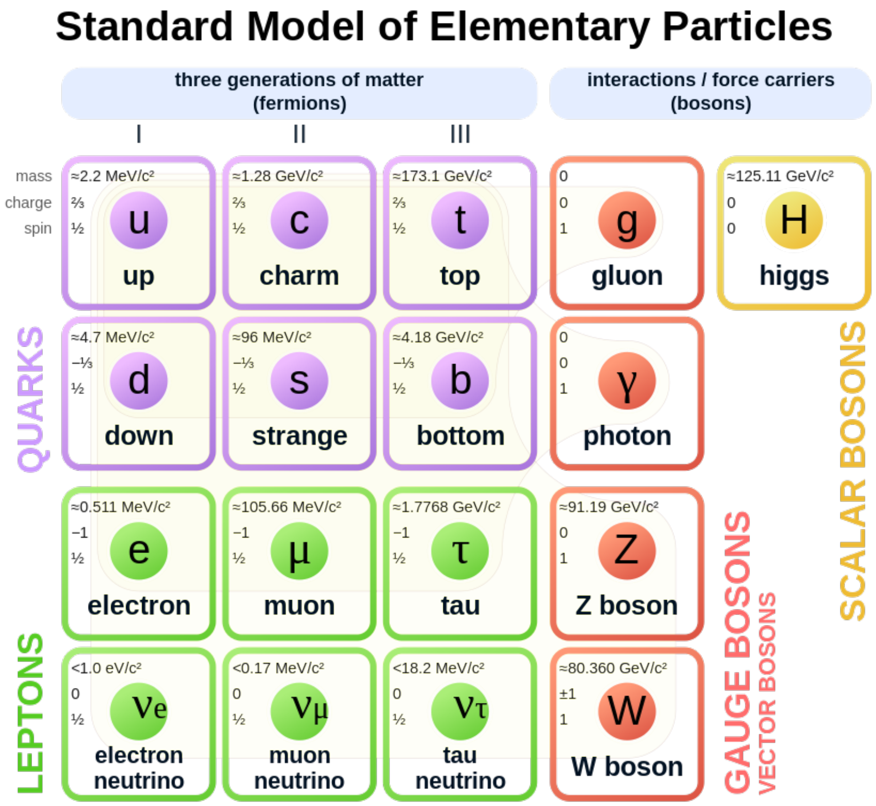
Standard Model of Elementary Particles
three generations of matter (fermions)
interactions / force carriers (bosons)
I
II
III
mass
charge
spin
≈2.2 MeV/c²
⅔
½
u
up
≈1.28 GeV/c²
⅔
½
c
charm
≈173.1 GeV/c²
⅔
½
t
top
0
0
1
g
gluon
≈125.11 GeV/c²
0
0
H
higgs
≈4.7 MeV/c²
−⅓
½
d
down
≈96 MeV/c²
−⅓
½
s
strange
≈4.18 GeV/c²
−⅓
½
b
bottom
0
0
1
γ
photon
≈0.511 MeV/c²
−1
½
e
electron
≈105.66 MeV/c²
−1
½
μ
muon
≈1.7768 GeV/c²
−1
½
τ
tau
≈91.19 GeV/c²
0
1
Z
Z boson
<1.0 eV/c²
0
½
νe
electron neutrino
<0.17 MeV/c²
0
½
νμ
muon neutrino
<18.2 MeV/c²
0
½
ντ
tau neutrino
≈80.360 GeV/c²
±1
1
W
W boson
QUARKS
LEPTONS
GAUGE BOSONS
VECTOR BOSONS
SCALAR BOSONS

FIGURE 1.1: The schematic representation of standard model. This figure has been taken from [14].

Among the trio of fundamental interactions discussed earlier, the theoretical framework governing strong interactions adheres to gauge theory principles, known as Quantum Chromodynamics (QCD) [15, 16]. This thesis embarks on an investigation into the characteristics exhibited by strongly interacting QCD matter under conditions of extreme temperature or density, as encountered in heavy-ion collisions. In this chapter, we offer an overview of relativistic heavy-ion collisions and explore discernible signatures indicative of Quark-Gluon Plasma (QGP) formation, following a brief introduction to QCD and QGP.

The chapter wraps up with a detailed discussion outlining the physics motivations that underlie the endeavors pursued within this thesis.

1.2 Quantum Chromodynamics and Quark Gluon Plasma

The Quantum Chromodynamics (QCD), a gauge field theory governing strong interactions, elucidates the interaction dynamics between quarks and gluons, both characterized by color quantum numbers. Composite colorless particles, such as mesons and baryons, are constructed from these fundamental constituents. Specifically, mesons consist of quark-antiquark pairs, while baryons comprise three valence quarks. The interaction potential in QCD can be expressed as:

$$V_{\mathrm{QCD}}(r) = -\frac{4}{3}\frac{\alpha_{\mathrm{s}}}{r} + kr, \tag{1.1}$$

Here, α_{s} denotes the running coupling constant of QCD, k represents the color string tension, and r signifies the distance between interacting partons (quarks and gluons). The QCD coupling constant varies with the momentum transfer Q^2 between partons, given by:

$$\alpha_{\mathrm{s}}(Q^2) = \frac{12\pi}{(11N_{\mathrm{c}} - 2N_{\mathrm{f}})\ln(Q^2/\lambda^2_{\mathrm{QCD}})}, \tag{1.2}$$

In this equation, N_{f} represents the number of quark flavors, N_{c} denotes the number of color charges, and λ_{QCD} signifies the non-perturbative QCD scale parameter. Perturbative QCD applies to small values of α_{s}. Eq. 1.2 ensures two notable QCD properties: quark confinement and asymptotic freedom. In accordance with Eq. 1.2, at small momentum transfers or large distance scales, the QCD coupling constant governing the interactions between quarks and gluons becomes sizable. Consequently, quarks and gluons are no longer independent entities; instead, they are bound within composite particles known

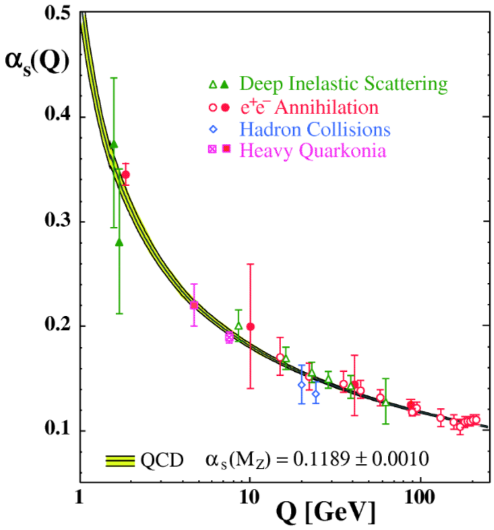

Figure 1.2: The QCD running coupling constant as a function of momentum transfer, compared with various experimental measurements, covering a wide range of momentum transfer. This figure has been taken from [17]

as hadrons, a phenomenon recognized as quark confinement [18]. Conversely, at large momentum transfers ($Q^2 >> \lambda_{\mathrm{QCD}}$) or small distance scales, the QCD coupling constant diminishes, leading to the liberated motion of quarks and gluons within the QCD vacuum- an attribute referred to as asymptotic freedom. Figure. 1.2 illustrates the compelling agreement between theoretical predictions and experimental findings regarding the QCD coupling constant across a broad range of momentum transfers. In 1973, David Gross, Frank Wilczek, and David Politzer were jointly awarded the Nobel Prize in Physics for their seminal contributions to the discovery of asymptotic freedom [15, 16, 19].

The transition from a state characterized by composite particles (hadrons) to one where quarks and gluons exist in a liberated, deconfined state is termed the deconfinement phase transition of QCD. Asymptotic freedom posits that at high momentum transfers or short distances, the force between quarks and gluons weakens, allowing them to behave as quasi-free entities. In 1974, T.D. Lee [20] envisioned the possibility of generating a dense nuclear medium comprising asymptotically free quarks and gluons by subjecting nucleons to exceedingly high densities across a relatively expansive volume. This state of dense nuclear matter, characterized by liberated partons, is referred to as the Quark-Gluon Plasma (QGP). Experimentally, QGP is described as as, **"a (locally) thermally equilibrated state of matter in which quarks and gluons are deconfined from hadrons, so that color degrees of freedom become manifest over nuclear, rather than merely nucleonic, volumes [21]."** Calculations in Lattice Quantum Chromodynamics (LQCD) [22, 23] also anticipate the presence of a QGP state at elevated temperatures. Figure. 1.3 illustrates the normalized energy density plotted against temperature, as derived from LQCD computations for various quark flavors. The normalized energy density exhibits a sharp rise at $T = T_c = 154 \pm 9$

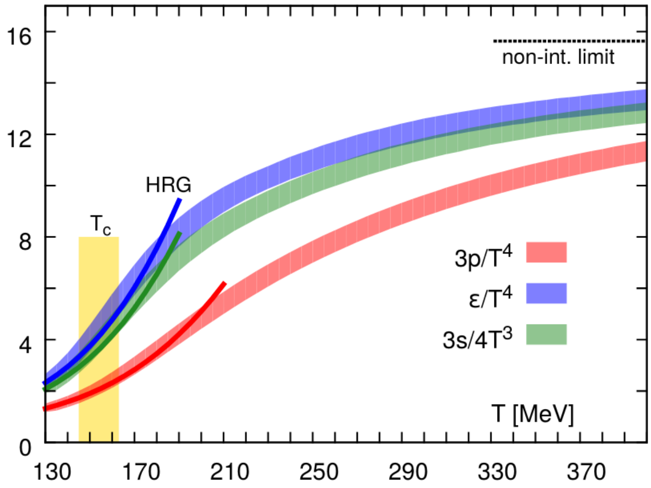

FIGURE 1.3: The normalized (scaled to the quadratic power of temperature) energy density, pressure density, and entropy density are depicted as functions of temperature, as per LQCD calculations with zero baryon chemical potential. These results pertain to (2+1) quark flavors. At lower temperatures, solid lines correspond to hadron resonance gas (HRG) model calculations, while at higher temperatures, the dashed line represents the outcome for a non-interacting quark-gluon gas [24].

MeV [24]. This phenomenon signifies an increase in the number of degrees of freedom, representing a transition from hadronic matter to a state characterized by free quarks and gluons.

1.3 Heavy-ion collisions

The QGP is hypothesized to have existed a few microseconds after the Big Bang, forming at exceptionally high temperatures and energy densities, as discussed earlier. Experimentally, the sole method known to create such a deconfined state of QCD matter in a laboratory setting is through the collision of heavy ions at relativistic energies [25]. Heavy-ion collision experiments conducted at facilities such as the Relativistic Heavy Ion Collider (RHIC), the Large Hadron Collider (LHC), and forthcoming experiments at the Facility for Antiproton and Ion Research (FAIR) are specifically designed to seek out signatures of the QGP phase and investigate its properties.

In a heavy-ion collision experiment, two massive nuclei collide at exceedingly high velocities. Due to their relativistic velocities, they undergo Lorentz contraction along the direction of motion, appearing flattened like a pancake [26]. The collision of heavy ions occurs at z, t = 0. The energy carried by the incoming hadrons is concentrated within a small region in space over a very brief period. Consequently, the energy density at the collision center becomes sufficiently high to facilitate the formation of the QGP. A schematic depiction illustrating the stages of evolution in a heavy-ion collision is presented in Fig. 1.4. Initially, the deconfined state produced may not be in thermal equilibrium. Following a brief period of approximately 1 femtosecond per speed of light (1 fm/c), known as the pre-equilibrium state, the matter attains a state of local thermal equilibrium with deconfined quarks and gluons, referred to as the Quark-Gluon Plasma (QGP). The evolution of this state is depicted by considering the plasma to behave akin to a hydrodynamic fluid. The QGP substance begins to expand due to pressure gradients, resulting in its gradual cooling

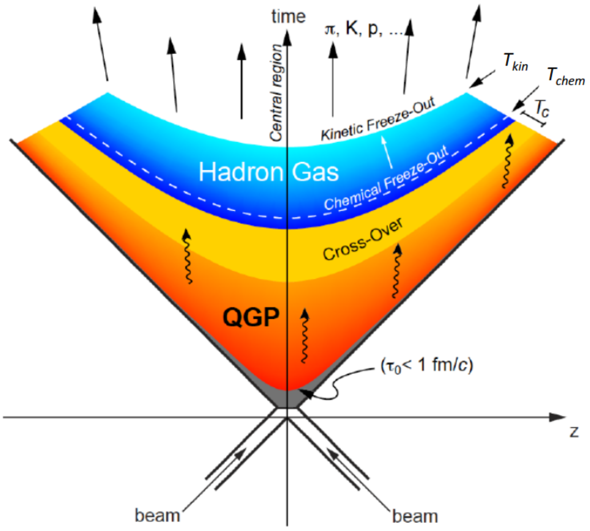
time
π, K, p, ...
Central region
T_{kin}
T_{chem}
T_C
Kinetic Freeze-Out
Hadron Gas
Chemical Freeze-Out
Cross-Over
QGP
(τ_0< 1 fm/c)
z
beam
beam

FIGURE 1.4: A schematic diagram for space-time evolution of heavy-ion collision [27].

over time. Upon reaching the critical temperature ($T = T_c$), hadronization commences from free quarks and gluons, leading to the formation of a hadron gas state. T_c, designated as the critical temperature, marks this transition. The hadron gas further expands, and at $T = T_{ch}$, the chemical freeze-out temperature, inelastic interactions between hadrons cease [28]. At this juncture, the chemical composition of the system becomes fixed, signifying that the relative abundance of various particle types remains constant as the system cools to T_{ch}. Subsequently, elastic interactions between hadrons persist until the kinetic freeze-out temperature, T_{kin}, is reached. At T_{kin}, the mean free path of hadrons becomes significantly larger than the dynamic size of the system. Post-T_{kin}, hadrons move freely toward the detector. The phase between hadronization and kinetic freeze-out is generally known as the hadronic phase of the heavy-ion collision evolution.

1.4 Coordinate axis

In the colliding beam experiment conducted at the Large Hadron Collider (LHC), the coordinate system adopted by ALICE is aligned such that the z-axis coincides with the direction of the beams. The designated interaction point, where the two beams intersect, is positioned at the center of the Time Projection Chamber (TPC) detector, denoted as (0, 0, 0) within the coordinate system. Collisions occur in a distributed manner around this interaction point, with the primary vertex of each collision discerned from the collected data.

1.5 Kinematic variables

Kinematic variables are very useful in dealing with relativistic heavy ion collision as they have simple Lorentz transformation forms. The natural units used in such high enegry collisons are $c = \hbar = 1$, where c is the speed of light in free space and $\hbar$ is the reduced Planck's constant. Here we describe few of the kinematic variables which we use in high energy collisions.

1.5.1 Transverse Momentum (p_{T})

It is defined as the momentum of a track in transverse plane (x-y plane) perpendicular to the beam direction (z axis). It is a Lorentz invariant quantity. Mathematically it is represented as:

$$p_T = \sqrt{p_x^2 + p_y^2}, \tag{1.3}$$

where p_x and p_y are the momentum of the particle in x and y directions, respectively.

1.5.2 Rapidity (y)

It is a relativistic measure for ordinary velocity. Mathematically represented by:

$$y = \frac{1}{2} ln(\frac{E + p_z}{E - p_z}), \tag{1.4}$$

where E is the energy of the particle under consideration. Its a dimensionless variable and its advantage is that it follows simple additive law under Lorentz transformation. If for example, in one frame a particle has rapidity y, and in another frame it has rapidity y' moving at a velocity β in the z-direction relative to the first. Then the rapidity under Lorentz transformation is defined as:

$y^{'} = y - y_{\beta}$, where $y_{\beta} = \frac{1}{2} ln(\frac{1+\beta}{1-\beta})$.

1.5.3 Pseudorapidity (η)

It is a spatial coordinate generally used to describe the angle of inclination of particle (θ) relative to beam axis. Mathematically represented by:

$$\eta = \frac{1}{2} ln\left(\frac{|p| + p_z}{|p| - p_z}\right). \tag{1.5}$$

or by:

$$\eta = -ln(\tan{(\theta/2)}). \tag{1.6}$$

It is independent of the mass of the particle and hence is a better observable than rapidity (y).

1.6 Fundamental variables for particle production

In heavy-ion collision experiments, charged particle multiplicity and invariant yield are basic variables commonly employed to measure the production of particles in the final state.

1.6.1 Multiplicity

Multiplicity in the context of particle and nuclear physics denotes the overall count of produced particles within a given event, corresponding to a single collision occurrence.

1.6.2 Invariant yield

The invariant yield is obtained by integrating over azimuthal angle and is defined as,

$$E\frac{\mathrm{d}^3N}{\mathrm{d}p^3} = \frac{1}{N_{\mathrm{evt}}2\pi}\frac{\mathrm{d}^2N}{p_{\mathrm{T}}\mathrm{d}p_{\mathrm{T}}\mathrm{d}y}, \tag{1.7}$$

where N_{evt} corresponds to the number of events and N is the number of produced particles. It is a Lorentz-invariant quantity.

1.6.3 Collision geometry of heavy-ion collision

Figure 1.5 provides a schematic depiction of a heavy-ion collision. During such collisions, two nuclei interact with a non-zero impact parameter, defined as the perpendicular distance between their respective centers. This impact parameter (b) spans from 0 to 2R, where R denotes the radius of the nucleus in femtometers (fm). Events in heavy-ion collisions are categorized into distinct centrality classes based on the value of the impact parameter.

Central collisions typically occur with small b values (e.g., ~3 fm for heavy nuclei like Au or Pb), while peripheral collisions involve larger b values (e.g., exceeding 10 fm for Au or Pb nuclei). As direct measurement of the impact parameter isn’t feasible in experiments, a Glauber model [29, 30] is utilized to fit the charged particle multiplicity distribution. For an event with a given impact parameter b, the Glauber Monte Carlo method is used to determine the corresponding N_{part} (number of participating nucleons) and N_{coll} (number of binary collisions). The particle multiplicity per nucleon-nucleon collision is modeled using a negative binomial distribution (NBD). To apply this model, the concept of ancestors - independently emitting sources of particles - is introduced. The number of ancestors is parameterized as $N_{\text{ancestors}} = fN_{\text{part}} + (1-f)N_{\text{coll}}$. For each Glauber Monte Carlo event, the NBD is sampled $N_{\text{ancestors}}$ times to obtain the average simulated V0 amplitude for the event. The V0 amplitude distribution is then simulated for an ensemble of events across various NBD parameter values. Finally, minimization is performed to find the NBD parameters that result in the smallest χ^2. Central collisions are marked by high charged particle multiplicities, while peripheral collisions are associated with low-multiplicity events.

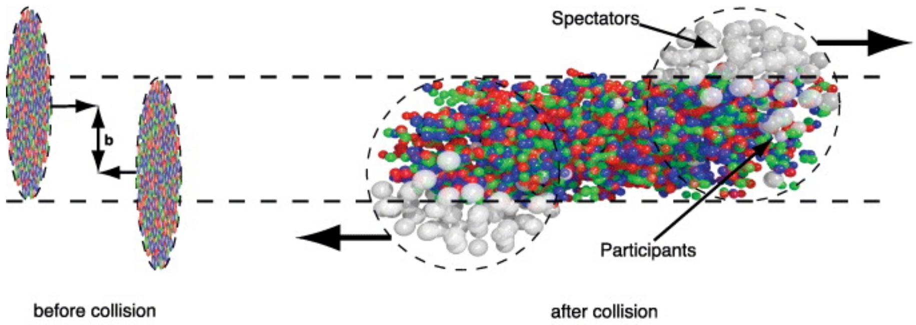

FIGURE 1.5: Two heavy-ions collision with a given impact parameter b [31].

1.7 Experimental signatures of QGP formation

Few experimental signatures have been observed for the formation of QGP in heavy-ion collisions. Here we will briefly discuss some of them.

1.7.1 Jet quenching

In high-energy hadron collisions, the initial hard scattering produces high-momentum partons. These energetic partons subsequently fragment into a concentrated cascade of particles, forming what is termed a jet. When such a jet traverses the hot and dense QGP medium, it undergoes energy loss through interactions with other partons within the medium. This loss of energy from high-p_{T} partons results in a suppression of high-p_{T} hadron yields. This phenomenon, initially proposed by Bjorken [32], is known as jet quenching. Experimentally, jet quenching can be observed by measuring the nuclear modification factor (R_{AA}), defined as:

$$R_{\mathrm{AA}} = \frac{1}{\langle T_{\mathrm{AA}} \rangle} \frac{\mathrm{d}^2 N^{\mathrm{AA}}/(\mathrm{d}y\mathrm{d}p_{\mathrm{T}})}{\mathrm{d}^2 \sigma^{\mathrm{pp}}/(\mathrm{d}y\mathrm{d}p_{\mathrm{T}})}, \tag{1.8}$$

where $\mathrm{d}^2 N^{\mathrm{AA}}/(\mathrm{d}y\mathrm{d}p_{\mathrm{T}})$ is the yield of the particle in heavy-ion collisions and σ^{pp} is its production cross section in pp collisions. The average nuclear overlap function is denoted by $\langle T_{\mathrm{AA}} \rangle$, estimated as $\langle T_{\mathrm{AA}} \rangle = \langle N_{\mathrm{coll}} \rangle / \sigma_{\mathrm{inel}}$, where $\langle N_{\mathrm{coll}} \rangle$ is the average number of binary nucleon–nucleon collisions obtained from Monte Carlo Glauber simulations and σ_{inel} is the inelastic pp cross section. If A–A collision is a simple superposition of pp collisions, then the R_{AA} becomes 1 and any deviation from 1 implies the presence of the effects caused by the medium. Figure 1.6 illustrates the nuclear modification factor of inclusive charged hadrons and π^0 particles in central A–A collisions at various center-of-mass energies ($\sqrt{s_{\mathrm{NN}}}$ = 0.017, 0.2, 2.76, and 5.02 TeV). The phenomenon of jet quenching is evident at both RHIC and LHC energies.

In di-jet events resulting from hard scattering, jets are invariably produced in opposing directions due to momentum conservation. Frequently, one jet emerges near the periphery of the medium, known as the near-side jet, while another jet forms within the medium

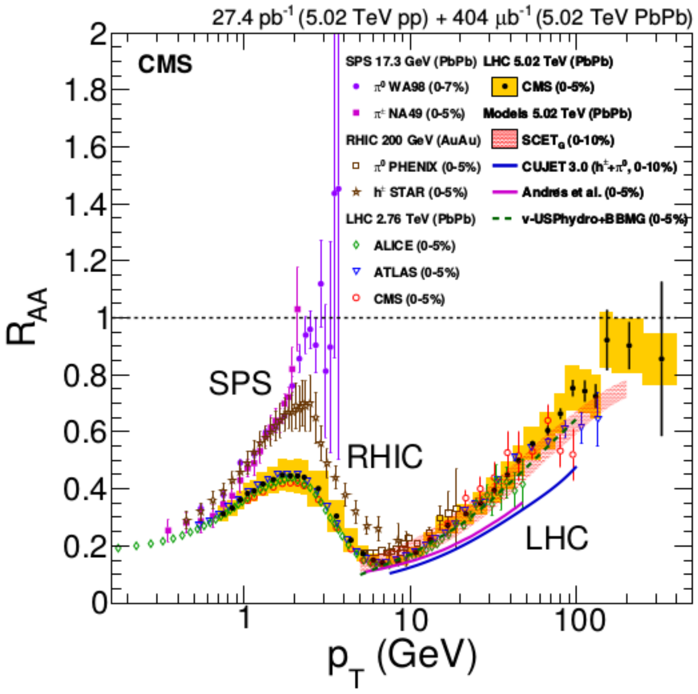

FIGURE 1.6: R_{AA} as a function of p_T for unidentified and identified charged particles and π^0 in central heavy-ion collision at the SPS, RHIC, and LHC energies [33].

itself, termed the away-side jet. The away-side jet traverses the medium more extensively compared to the near-side jet. Consequently, the away-side jet experiences more quenching relative to the near-side jet.

This disparity can be observed experimentally by examining the azimuthal correlation between a high-p_T trigger particle and associated particles. Figure 1.7 presents the di-hadron correlation of trigger hadrons ($p_T > 4$ GeV/c) with associated hadrons ($p_T > 2$ GeV/c) for pp, d–Au, and Au–Au collisions. In Au–Au collisions, the away-side peak (occurring around 3.14 radians) is suppressed compared to the near-side peak (around 0 radians), indicative of the greater quenching experienced by the away-side jet. However, no such suppression of the away-side jet is observed in pp and d–Au collisions, suggesting the absence of jet quenching effects in smaller collision systems.

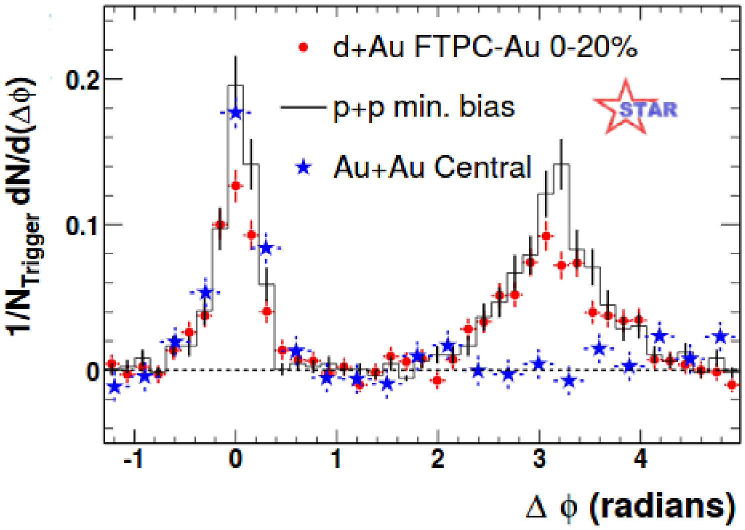

FIGURE 1.7: Di-hadron azimuthal correlation of high-p_T charged hadrons in pp, d–Au and Au–Au collisions [21].

1.7.2 Strangeness Enhancement

Enhanced production of strange particles in heavy-ion collisions stands out as a key indicator of QGP formation [34]. In both heavy-ion (A–A) and proton-proton (pp) collisions, the net strangeness remains zero before and after the collisions. Strange quarks primarily arise from two processes: gluon-gluon collisions ($gg \rightarrow s\bar{s}$) and light quark annihilation ($q\bar{q} \rightarrow s\bar{s}$).

Within the gluon-rich QGP medium, the dominance of gluon-gluon collisions results in enhanced production of $s\bar{s}$ pairs compared to pp collisions, where light quark annihilation prevails as the primary channel for strangeness production. This enhanced production of strange hadrons in the QGP is quantified by an observable, ϵ, expressed as,

$$\epsilon = \frac{2}{\langle N_{\text{part}} \rangle} \frac{\frac{dN^{\text{AA}}}{dy}}{\frac{dN^{\text{PP}}}{dy}}. \tag{1.9}$$

If ϵ exceeds unity, it indicates an enhancement in strangeness production with respect to pp collisions.

In the canonical suppression picture [35], the production of strange particles in pp collisions can be suppressed, leading to $\epsilon > 1$. While the ϕ ($s\bar{s}$) meson possesses no net strangeness, its production in pp collisions is not expected to be canonically suppressed. Conversely, the production of hadrons with open strangeness (e.g., K, Λ, Ξ, and Ω) may indeed be canonically suppressed. Therefore, measuring the ϕ meson is crucial for understanding and quantifying the extent of strangeness enhancement.

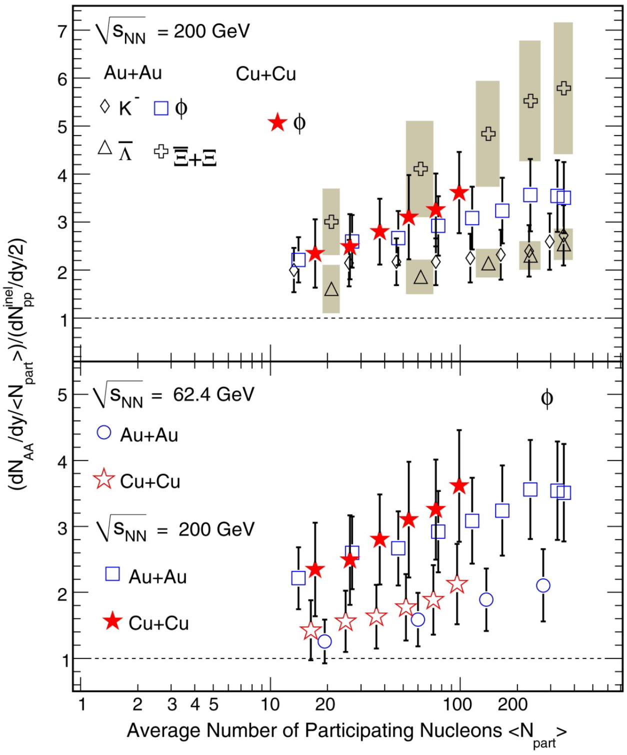

FIGURE 1.8: The strangeness enhancement factor (ϵ) is plotted as a function of $\langle N_{\text{part}}\rangle$ for K ($S = 1$), ϕ ($S = 0$), Λ ($S = 1$), and Ξ ($S = 2$) in Au–Au and Cu–Cu collisions at $\sqrt{s_{\text{NN}}}$= 200 and 62.4 GeV [36].

Figure. 1.8 illustrates the strangeness enhancement factor (ϵ) plotted against $\langle N_{\text{part}}\rangle$ for K, ϕ, Λ, and Ξ in Au–Au and Cu–Cu collisions at $\sqrt{s_{\text{NN}}}$= 200 and 62.4 GeV. The noticeable enhancement in ϕ meson production in both Au–Au and Cu–Cu collisions strongly suggests an increased production of strange quarks within the hot and dense partonic medium generated in heavy-ion collisions.

1.7.3 Elliptic flow

Collective phenomena refer to a shared behavior exhibited by a group of entities, such as water molecules moving uniformly in a specific direction, spontaneous magnetization in atoms and molecules, or the synchronized flashing of fireflies. Similarly, in heavy-ion collisions, collectivity arises from multiparticle correlations among particles due to their interactions.

In relativistic heavy-ion collisions, the initially anisotropic volume of the interacting system in coordinate space undergoes a transformation into momentum-space anisotropy through multiple interactions among the produced particles. This conversion from spatial gradient to pressure gradient results in the collective flow of matter [37]. The anisotropy in the initial overlap region of the colliding nuclei in the transverse plane is illustrated in Figure 1.9.

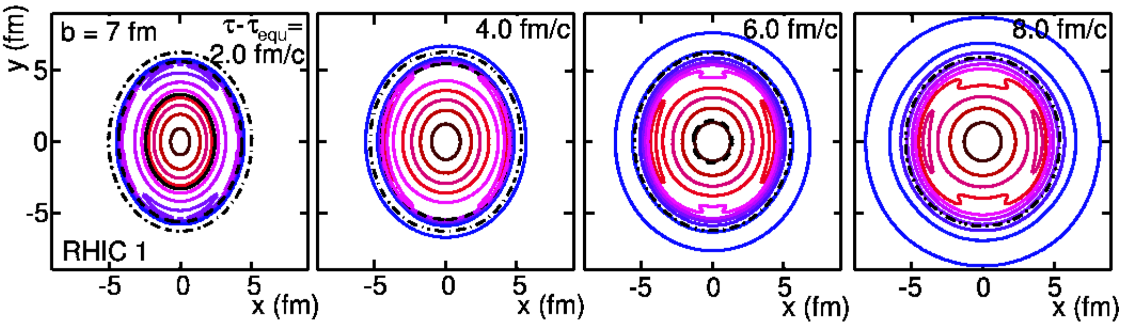

FIGURE 1.9: The profile of initial transverse energy density with its time dependence in coordinate space for a non-central heavy-ion collision [38]. The z-axis is taken to be along the beam direction and the x-axis is along the the impact parameter.

As the system expands, the initial anisotropy diminishes, indicating that azimuthal anisotropy serves as a sensitive probe of the early stages of heavy-ion collisions when the

QGP medium is formed. Therefore, studying azimuthal anisotropy provides direct insight into these initial phases. The correlation between the anisotropy in particle momentum distribution and the reaction plane (defined by the impact parameter and the beam axis, z) serves as direct experimental evidence of flow.

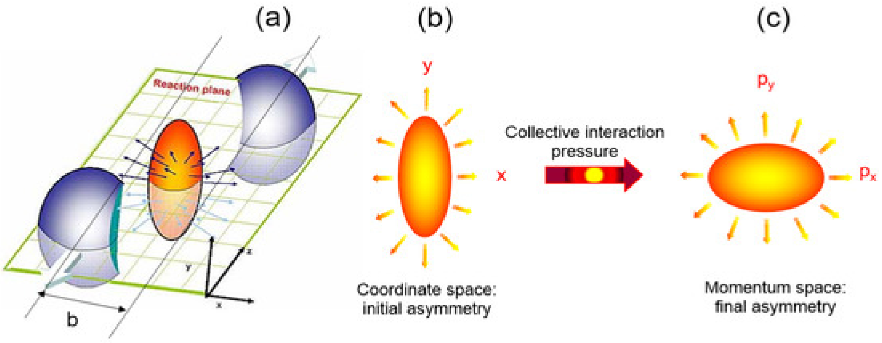

FIGURE 1.10: Schematic diagram of non central nucleus nucleus collision and susequent conversion of spatial anisotropy into momentum anisotropy [39].

The azimuthal distribution of produced particles can be expressed as,

$$E\frac{d^3N}{dp^3} = \frac{d^2N}{2\pi p_{\mathrm{T}} dp_{\mathrm{T}} dy}(1 + \sum_{n=1}^{\infty} 2v_n cos[n(\phi - \psi_R)]) \tag{1.10}$$

where ϕ is the azimuthal angle of the particle, ψ_R is the reaction plane angle(angle between the reaction plane and x axis) of an event[37], p_{T} and y are transverse momentum and rapidity of the particle respectively. Because of the reflection symmetry with the reaction plane, the sine terms in the expansion vanish. The Fourier coeffcients v_n for the nth order flow harmonic are p_{T} and y dependent and is given by

$$v_n(p_{\mathrm{T}}, y) = \langle\langle cos[n(\phi - \psi_R)]\rangle\rangle \tag{1.11}$$

Here $\langle\langle\ \rangle\rangle$ represents average over all particles in all events. The second order flow harmonic v_2 is called elliptic flow which signifies the elliptical shape of the overlap region.

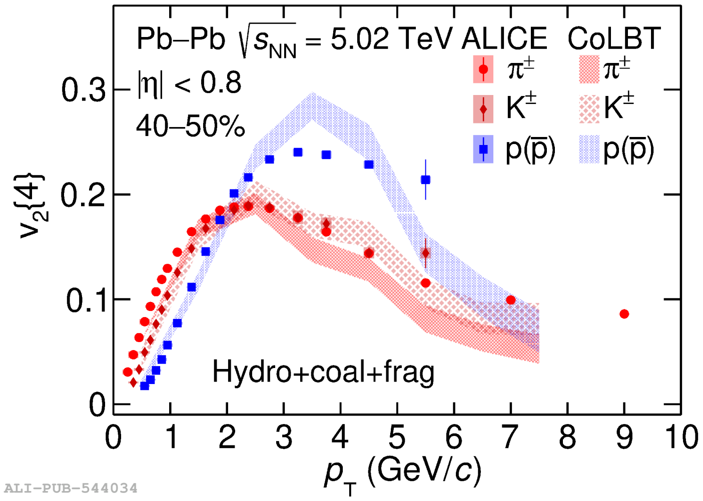

FIGURE 1.11: Elliptic flow of identified hadrons for 40–50% centrality class in Pb–Pb collisions at $\sqrt{s_{NN}}$= 5.02 TeV [40].

The elliptic flow (v_2) emerges as the dominant harmonic in heavy-ion collisions. Its magnitude serves as a sensitive indicator of fundamental transport coefficients within the QGP, such as the shear viscosity over entropy density ratio (η/s). Notably, the study of elliptic flow has played a pivotal role in substantiating the concept of a strongly-coupled QGP paradigm [41–43].

Figure 1.11 presents the v_2 values for π, K, and p in Pb–Pb collisions at $\sqrt{s_{NN}}$= 5.02 TeV [40], contrasted with predictions from the coupled linear Boltzmann transport (CoLBT) hydrodynamic model. In the low p_T region (<2 GeV/c), lighter hadrons exhibit larger v_2 compared to heavier hadrons, a phenomenon known as mass ordering of v_2, which aligns with expectations from ideal hydrodynamic calculations. In the intermediate p_T range, v_2 values for all identified hadrons segregate into two distinct groups: baryons and mesons. This separation can be interpreted within a dynamic framework where flow originates at the partonic level, followed by quark coalescence into hadrons [44]. The substantial v_2 values observed are further supported by the hydrodynamical model with QGP in the initial stage.

1.8 Thesis motivation and organization

The journey through the intricate dynamics of heavy-ion collisions traverses three distinct phases: the initial state, the formation of QGP followed by its hydrodynamic expansion, and ultimately, the transition to the final state marked by hadronization, the hadronic phase, and freeze-out. This thesis embarks on an exploration of these stages, delving into intriguing phenomena that illuminate the complexities of the collision process. The organization of the thesis is as follows:

Chapter 2: Unveiling the ALICE Experiment at CERN

This chapter offers a comprehensive guide to the ALICE experiment at CERN, unraveling the intricacies of heavy-ion collisions at the LHC. It provides detailed insights into the ALICE detectors and subsystems crucial for data analysis, with a focus on detectors responsible for tracking charged particles and their identification.

Chapter 3: Probing the Initial State with the Chiral Magnetic Wave

Diving into the collision's initial stage, this chapter investigates the captivating chiral phenomenon known as the Chiral Magnetic Wave to probe the non-trivial topological structure of the gauge fields.

Chapter 4: Exploring Final State Properties

This chapter delves into the final state properties of the medium by studying hadronic resonances in both proton-proton and heavy-ion collisions at LHC energies. It unravels the intricate characteristics of the final state medium, providing valuable insights into its behavior.

Chapter 5: Unraveling the Strangeness Content of Exotic Resonances

Dedicated to the measurement of exotic resonance production in proton-proton collisions, this chapter unveils the strangeness content of these unique particles.

Chapter 6: Concluding Reflections

The concluding chapter encapsulates the entirety of the thesis work, offering reflections on the journey undertaken. It outlines the progress made in comprehensively studying both the initial and final stages of heavy-ion collisions, summarizing key findings and contributions to the broader field of heavy-ion physics.

1.8.1 Chiral Magnetic Wave in heavy-ion collisions

The principal objective of conducting relativistic heavy-ion collisions at the LHC is to scrutinize the characteristics of the emerging and highly interacting medium known as the QGP [26, 39, 42, 45–48]. The predicted transition from conventional hadronic matter to QGP is grounded in lattice QCD calculations [49, 50]. Notably, heavy-ion collisions generate exceptionally strong and transient electromagnetic fields (B $\sim 10^{18}$ Gauss), primarily instigated by the non-colliding protons, referred to as spectators, from the incoming nuclei that evade inelastic collisions [51]. The magnetic field's direction ($\mathbf{B}$) is perpendicular to the reaction plane, defined by the impact parameter of the colliding nuclei and the beam direction. The strength and persistence of the magnetic field within the medium depend on its conductivity. This intense magnetic field presents a unique opportunity to explore novel QCD phenomena, including chiral symmetry restoration and local parity violation in strong interactions [20, 52–54].

The prospect of observing parity violation in strong interactions through ultrarelativistic heavy-ion collisions was initially explored in references [53–55], with further elucidation provided in subsequent reviews [56–59]. Theoretical investigations suggest that interactions between quarks and gluonic fields, governing transitions among distinct topological states of the QCD vacuum, induce a modification in quark chirality, thereby instigating a local chiral imbalance. This phenomenon in the presence of the strong magnetic field manifests as charge separation, or electric current, relative to the reaction plane-a phenomenon dubbed as the Chiral Magnetic Effect (CME) [54, 60–65]. Experimental endeavors aimed at identifying the CME via heavy-ion collisions have intensified over the past decade. While initial measurements exhibited some resemblance to theoretical predictions [66–68], subsequent scrutiny unveiled the significant influence of background sources, such as collective phenomena and local charge conservation (LCC) on experimental outcomes [69, 70]. LCC, in this context, refers to the principle asserting the conservation of quantum numbers, like electric charge, within a local domain of a physical system. Experimental findings suggest that the CME signal contribution to the measurement of $\gamma_{1,1}$ correlator ranges from 7% to 20% at a 95% confidence level in semicentral heavy-ion collisions [66–80].

A complementary phenomenon to the Chiral Magnetic Effect (CME) is the Chiral Separation Effect (CSE) [81, 82]. The CSE, theorized to occur in the presence of a finite electric chemical potential (μ_{e}), induces a chirality current along the magnetic field ($\mathbf{B}$). Interestingly, the CME and CSE can interact, giving rise to a long-wavelength collective excitation in the QGP, termed as the Chiral Magnetic Wave (CMW) [83–87]. Analogous to the CME-induced electric dipole moment, the CMW would manifest as a finite electric quadrupole moment in the final state [83]. This effect, if present, could be detected through charge-dependent anisotropic flow measurements [83].

Anisotropic flow, quantified by the Fourier coefficients v_{n} of the azimuthal particle distribution relative to the n^{th}-order event plane angle Ψ_n (proxy for the reaction plane) [88–90], is a key observable in heavy-ion collisions. The CMW-induced electric quadrupole moment evolves with the medium's expansion, resulting in an enhancement (reduction) of v_2 for negatively (positively) charged hadrons [83]. The difference between the v_2 values of negatively and positively charged hadrons (Δv_2) is expected to be proportional to the event-by-event charge asymmetry ($A_{\rm ch}$) [83, 84], described by:

$$\Delta v_2 = v_2^- - v_2^+ \propto r_2 A_{\rm ch}, \tag{1.12}$$

where r_2 denotes the slope parameter between Δv_2 and the event-by-event charge asymmetry, and $A_{\rm ch}$ is defined as:

$$A_{\rm ch} = \frac{(N^+ - N^-)}{(N^+ + N^-)}, \tag{1.13}$$

with N^+ (N^-) representing the counts of positively (negatively) charged hadrons measured in a given event.

The STAR Collaboration at the RHIC conducted the pioneering search for the CMW using charged pions in Au–Au collisions at $\sqrt{s_{\rm NN}}$= 200 GeV [91]. They observed a positive linear dependence on the event-by-event charge asymmetry ($A_{\rm ch}$) for the difference in elliptic flow (v_2) between π^- and π^+. The extracted positive slopes, along with their centrality dependence, were in agreement with theoretical predictions for the CMW [83–85] as shown in Fig. 1.12. Similarly, the ALICE Collaboration at the LHC reported a comparable positive correlation in semicentral Pb–Pb collisions at $\sqrt{s_{\rm NN}}$ = 2.76 TeV [92] along with the CMS collaboration at $\sqrt{s_{\rm NN}}$ = 5.02 TeV. Furthermore CMS collaboration also observed similar magnitude of slope with $A_{\rm ch}$ and Δv_3 [93] as can be seen from Fig. 1.13. Although the slopes were akin to those observed in Au–Au collisions, the faster decay of the magnetic field at LHC energies raised questions about the expected slope consistency between different collision energies [94]. This finding, coupled with observations from the STAR Collaboration [95], indicated a deviation from the expected CMW-driven signal. To facilitate comparison across experiments, a normalized slope parameter, $\Delta v_n^{\rm Norm}$, was introduced [96].

$$\Delta v_n^{\rm Norm} = \frac{v_n^- - v_n^+}{(v_n^- + v_n^+)/2} \propto r_n^{\rm Norm} A_{\rm ch}, \tag{1.14}$$

where $n = 2$ or 3.

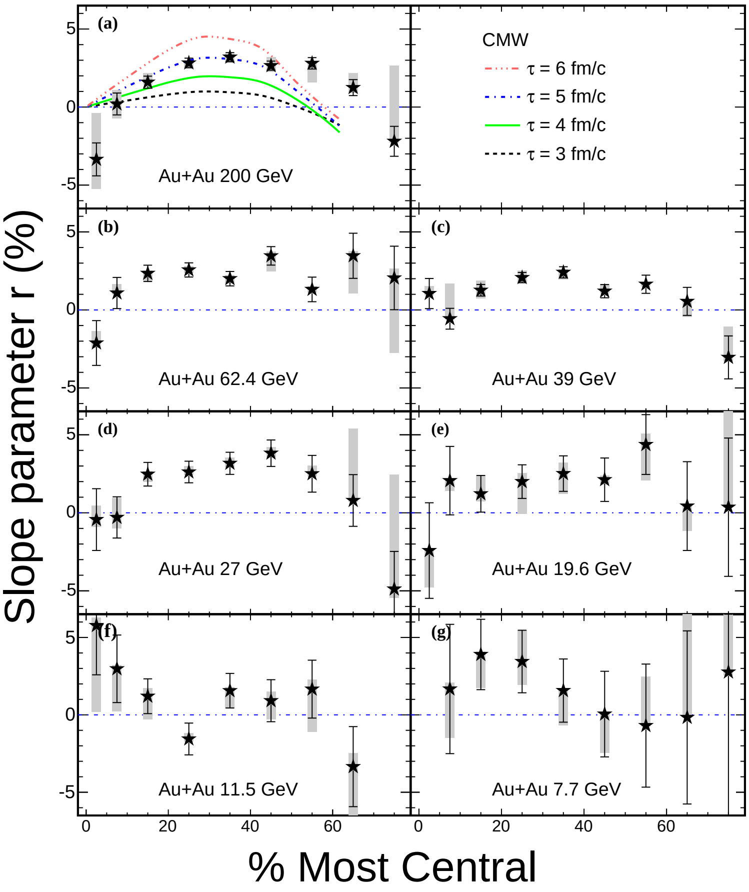

FIGURE 1.12: The slope parameter is presented across different collision energies as a function of centrality. Experimental measurements are compared with theoretical calculations considering varying lifetimes of the magnetic field within the medium. The figure is taken from [91].

Moreover, the event shape engineering (ESE) technique [97] was proposed as a means to estimate the CMW signal [96]. By selecting events with similar centrality but varying initial geometries, ESE allows for the manipulation of background contributions. Instead of the traditional $A_{\rm ch}$–v_2 slope, the integral covariance (IC) was suggested as an alternative observable [92].

$$\Delta\mathrm{IC} = \Big(\langle v_2^- A_{\rm ch}\rangle - \langle A_{\rm ch}\rangle\langle v_2^-\rangle\Big) - \Big(\langle v_2^+ A_{\rm ch}\rangle - \langle A_{\rm ch}\rangle\langle v_2^+\rangle\Big). \qquad (1.15)$$

This quantity, by design, calculates the covariance between $A_{\rm ch}$ and v_2, thus circumventing

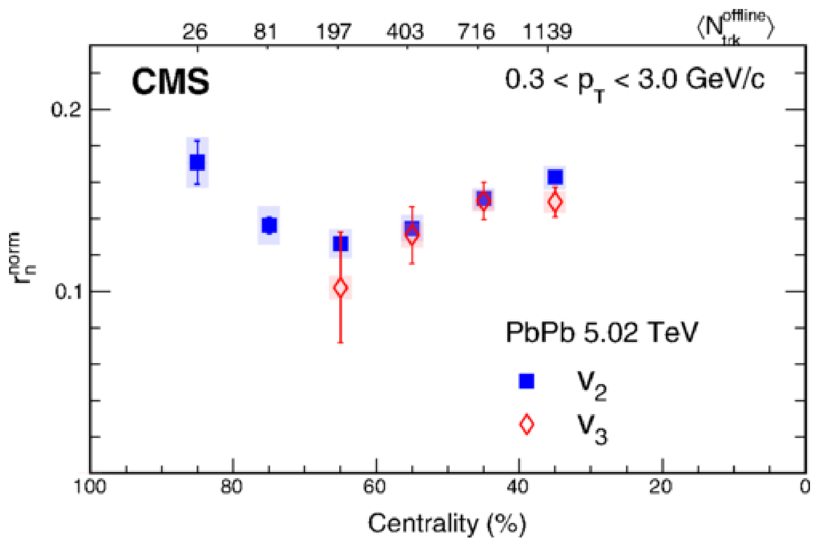

FIGURE 1.13: The normalized v_2 and v_3 slope parameter as a function of centrality. The figure is taken from [93].

issues associated with detector acceptance and reconstruction efficiency.

Understanding the various background components and their contributions to experimental measurements is paramount for isolating the CMW signal. Among these sources, the most significant is believed to be the local charge conservation (LCC), intertwined with the collective dynamics of the QGP medium. The LCC mechanism posits that pairs of particles with opposite charges, typically generated from resonance decays, contribute to this effect. This phenomenon has been studied extensively through balance function measurements in heavy-ion collisions [98, 99]. In CMW measurements, when one of the particles from such charge-conserving pairs escapes the detector's limited acceptance, a nonzero event-by-event charge asymmetry (A_{ch}) is generated. It has been demonstrated that the selection of specific A_{ch} values can bias the η–p_T phase space, potentially leading to nonzero A_{ch}–Δv_2 correlations even in the absence of CMW phenomena. Theoretical investigations into these correlations, without the presence of the CMW, have been conducted extensively [100–104]. The prevailing view is that the LCC interpretation can effectively account for both the observed A_{ch}–Δv_2 and A_{ch}–Δv_3 relations. A pure LCC mechanism is anticipated to yield an identical positive linear correlation between A_{ch}–$\Delta v_2^{\mathrm{Norm}}$ and A_{ch}–$\Delta v_3^{\mathrm{Norm}}$. Consequently, any discrepancy between the normalized slopes r_2^{Norm} and r_3^{Norm} may suggest the presence of the CMW signal.

Although measurements of the CMW have been conducted at LHC energies, there is a notable absence of measurements involving identified hadrons. Given that the primary background influence on CMW stems from the interplay between LCC and v_2, it would be advantageous to measure the CMW for identified particles, as this would afford us better control over the background related to v_2 [83]. Additionally, a hydrodynamic study [105] posits that the isospin chemical potential (μ_{I}) and the strangeness chemical potential (μ_{S}) could play pivotal roles. This investigation predicts a negative slope for kaons at RHIC energies [105]. Therefore, disentangling the CMW signal from various background contributions becomes challenging if the measurements are solely performed with inclusive charged hadrons.

This thesis presents the inaugural investigation into the normalized slopes r_2^{Norm} and r_3^{Norm}, focusing on charged hadrons as well as identified particles such as $\pi^{\pm}$, $\mathrm{K}^{\pm}$, and $\mathrm{p}+\overline{\mathrm{p}}$ in Pb–Pb collisions at $\sqrt{s_{\mathrm{NN}}}$= 5.02 TeV. These measurements offer valuable experimental insights into the evolving theoretical landscape concerning the flavor dependence of chiral anomalies. Furthermore, comparisons are drawn between the experimental findings and a recently developed blast wave model incorporating the local charge conservation (BW+LCC) background [106]. Additionally, the estimation of an upper limit on the CMW contribution is facilitated for the first time in Pb–Pb collisions at $\sqrt{s_{\mathrm{NN}}}$ = 5.02 TeV through the utilization of integral covariance measurements.

1.8.2 System size dependence of hadronic rescattering effect at LHC energies

The study of hadron production, encompassing light-flavored quarks (u, d, and s), has been extensively pursued in both heavy-ion collisions and small collision systems like pp and p–Pb at LHC energies to investigate the bulk properties of QGP [107–114]. As the system evolves and cools down, it undergoes hadronization [115–120]. Initially, at the chemical freeze-out surface [121], the hadron abundances are fixed, followed by kinetic freeze-out (T_{kin}) surface where the momenta of hadrons freeze [122, 123]. After the kinetic freeze-out surface, particles propagate freely to the detectors. In these collisions, various hadrons and resonances (hadrons which decay via strong interaction), characterized by different flavors of valence quark content, mass, and lifetime, are produced. Each of these particles offers unique insights into the properties of the medium. The experimental yields of hadrons are utilized as inputs in thermal models [124–128] to extract parameters such as the chemical freeze-out temperature, and volume of the produced matter. The transverse-momentum (p_{T}) spectra of hadrons are fitted with hydrodynamics-based models like the blast wave model [129] to determine the kinetic freeze-out temperature [123, 130] and collective radial expansion velocity [130] of the medium. As the chemical freeze-out and quark-hadron transition temperatures are close by, the phase between chemical and kinetic freeze-out is called here as the hadronic phase [119, 120, 131]. Properties of this phase can be probed by studying short-lived resonance particles. Since their lifetime is comparable to that of the hadronic phase, their decay products undergo regeneration [132, 133] and rescattering [134, 135] processes. The decay products of the resonances take part in elastic or pseudoelastic scattering (scattering through an intermediate state), which can result in modification of the measured resonance yields [136, 137]. If at least one of the decay products scatters elastically with other hadrons in the hadronic medium or pseudoelastically scatters via a different resonance state (e.g. a pion from $K^*(892)^{\pm}$ decay scatters with another pion in the hadronic medium, $\pi^-\pi^+ \rightarrow \rho^0 \rightarrow \pi^-\pi^+$), the four-momentum information about the parent resonance gets lost and the particle can no longer be reconstructed. On the other hand, pseudoelastic scatterings among the hadrons inside the medium can regenerate the resonance state (eg. $K^0_S\pi^{\pm} \rightarrow K^*(892)^{\pm} \rightarrow K^0_S\pi^{\pm}$) which can lead to an increase in resonance yield. These processes, influenced by the hadronic cross section [138–140], the density of the hadron gas, and the lifetime of the resonance, lead to modifications in the measured yields of resonance particles [136, 137].

Extensive studies have investigated the production of light-flavor resonances like K^{*0} ($\tau \approx 4$ fm/c) and $\phi(1020)$ ($\tau \approx 40$ fm/c) across various collision systems [36, 112, 135, 141–155]. In central heavy-ion collisions, a significant suppression of the p_T-integrated yield of K^{*0} relative to kaons is observed compared to other collision types and thermal model predictions, indicating predominant rescattering effects over regeneration [134]. Conversely, no such suppression is detected for the ϕ meson as can be seen from Fig. 1.14.

This suppression of K^{*0} yields at low p_T (< 3 GeV/c) is further evidenced by the p_T-differential K^{*0}/K yield ratio [134]. Additionally, high-p_T particles experience energy loss due to traversing the dense medium, affecting the production yield of K^{*0} and ϕ resonances compared to pp collisions [112, 156]. The modification in the yield of high-p_T particles is quantified using the nuclear modification factor (R_{AA}) defined in Eq. 1.8. The similar values of nuclear modification factor (R_{AA}) at high p_T (> 6 GeV/c) for K^{*0} ϕ π, K, and p imply energy loss is independent of particle species [112, 130].

Furthermore, recent investigations into light flavor hadron production in high-multiplicity pp and p–Pb collisions have revealed characteristics previously associated only with heavy-ion collisions [157–161]. These systems, categorized by the average charged-particle

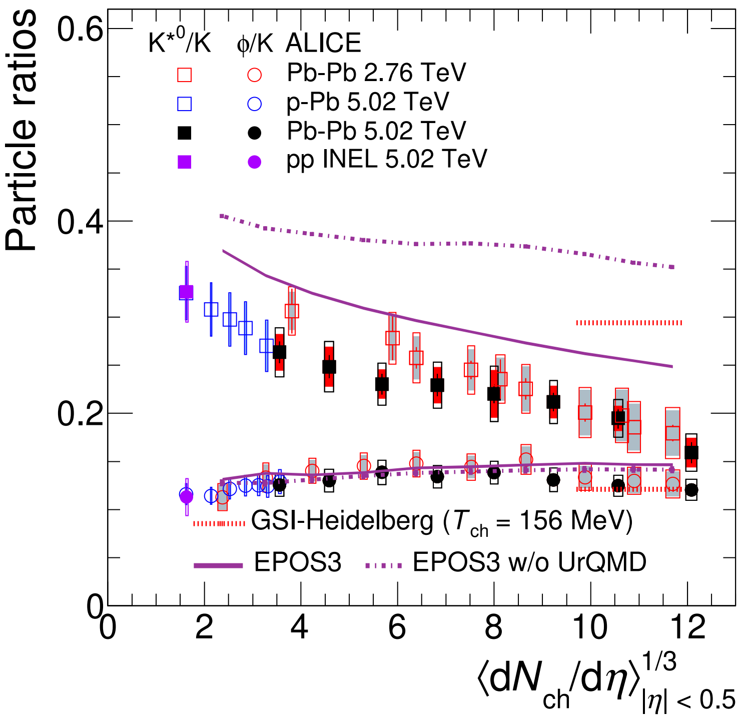

FIGURE 1.14: p_T-integrated particle yield ratios of K^{*0}/K and ϕ/K as a function of dN_{ch}/dη measured at midrapidity for various collision systems at $\sqrt{s_{NN}}$= 5.02 TeV. Measurements are compared with EPOS3 model predictions along with thermal model calculations for the most central Pb–Pb collisions. The figure is taken from [134]

pseudorapidity density (dN_{ch}/dη), exhibit a smooth evolution of hadron species yield with dN_{ch}/dη [113, 114]. However, the mean transverse momentum ($\langle p_T \rangle$), indicative of radial flow, rises more rapidly in small systems (pp, p–Pb) compared to heavy-ion (Pb–Pb) collisions [114]. Exploring resonances like K^{*0} and ϕ in these collisions aims to detect a non-zero lifetime hadronic phase in small systems. Previous findings from the ALICE Collaboration suggest a hint of K^{*0} meson suppression in high-multiplicity pp and p–Pb collisions [142]. Notably, the suppression pattern of K^{*0}/K yield ratio smoothly evolves with dN_{ch}/dη, spanning from low-multiplicity pp collisions to central Pb–Pb collisions across different collision energies.

Utilizing datasets from pp, p–Pb, Xe–Xe, and Pb–Pb collisions at $\sqrt{s_{NN}} \approx 5$ TeV, collected by the ALICE Collaboration, facilitates a systematic exploration of the system-size dependence of hadronic rescattering. This thesis presents the inaugural measurements of K^{*} (K^{*0} and $\mathrm{K}^{*}(892)^{\pm}$) mesons production at midrapidity ($|y| < 0.5$) as a function of $\mathrm{d}N_{\mathrm{ch}}/\mathrm{d}\eta$ in pp and Pb–Pb collisions, respectively at $\sqrt{s_{\mathrm{NN}}} = 5.02$ TeV. Given the similarity in quark content between $\mathrm{K}^{*}(892)^{\pm}$ ($\mathrm{u\bar{s}}$ and $\mathrm{\bar{u}s}$) and K^{*0} ($\mathrm{d\bar{s}}$ and $\mathrm{\bar{d}s}$), their momentum distributions are anticipated to be comparable, thereby complementing and completing the first excited state measurements of the kaon family. Comparisons of the measured K^{*} yield and $\mathrm{K}^{*}/\mathrm{K}$ yield ratio across different collision systems aim to elucidate the system-size dependence of K^{*} production and the influence of hadronic rescattering. The ratio $\mathrm{K}^{*}/\mathrm{K}$ is also used to constrain the hadronic phase lifetime across varying collision systems. Furthermore, the measured K^{*} yields in Pb–Pb collisions serve as experimental inputs in a partial chemical equilibrium (PCE) based thermal model HRG-PCE [162] to constrain the kinetic freeze-out temperature. The evolution of the system created in heavy-ion collisions in PCE follows the conservation of total yields and entropy of stable hadrons. Resonances decay and formation take place obeying the law of mass action. It offers a novel approach independent of assumptions about the flow velocity profile and freeze-out hypersurface. Additionally, comparisons of the mean transverse momentum ($\langle p_{\mathrm{T}} \rangle$) of K^{*} across different collision systems aid in understanding the evolution of radial flow from small to heavy-ion collisions.

1.8.3 Measurement of an exotic resonance in ALICE

The theory of QCD explains how colored quarks and gluons interact within the strong force, giving rise to various forms of hadronic matter. This includes mesons, composed of quark-antiquark pairs, and baryons, consisting of three quarks or antiquarks. Alongside conventional mesons and baryons, interest persists in exploring exotic states like tetraquarks and pentaquarks, which exhibit unconventional quark arrangements [163–171]. This pursuit of exotic states finds its roots in the early development of the constituent quark model, which offers insights into the structure of hadrons [6, 172–174].

An intriguing exotic particle under scrutiny is the $f_1(1285)$ meson. Positioned within the quark model as part of the ${}^3P_1$ axial-vector nonet, the $f_1(1285)$ was initially detected independently in $\mathrm{p\bar{p}}$ annihilation experiments at both Brookhaven National Laboratory (BNL) [175] and CERN [176] in 1965. These experiments observed a resonance decaying to $K\bar{K}\pi$ with quantum numbers $I^G(J^{PC}) = 0^+(1^{++})$. Furthermore, evidence of its existence has surfaced in various central production experiments, including WA102 [177], WA76 [178] at CERN, E690 at Fermilab [179], and in the L3 Collaboration's $\gamma\gamma$ collisions at CERN [180]. Additionally, sightings have been recorded in hadronic Z decays at LEP [181], photoproduction from a proton target with CLAS data [182], and b-hadron decays at LHCb [183]. Despite these numerous experimental observations, the exact quark composition of the $f_1(1285)$ remains ambiguous. Theoretical conjectures regarding the valence quark constitution of the $f_1(1285)$ meson can be broadly categorized into three scenarios: (i) as a bound state comprised solely of light up (u) and down (d) quarks, (ii) as a composite state formed by a mixture of light and strange (s) quarks, and (iii) as molecular configurations involving $\mathrm{K\bar{K}^*}$ [184]. The quark composition of the $f_1(1285)$ meson, exclusively involving light quarks, can be expressed as a linear combination of u and d quarks, $\frac{1}{\sqrt{2}}(\bar{u}u+\bar{d}d)$ [185]. On the other hand, the presence of strange quarks in the $f_1(1285)$ meson allows for three potential quark compositions: a tetraquark state $(\frac{1}{\sqrt{2}}(su\bar{s}\bar{u} + sd\bar{s}\bar{d}))$ [186], a bound state of light quarks with a mixture of strange quarks $(\frac{1}{\sqrt{2}}(\bar{u}u + \bar{d}d) + \delta s\bar{s})$ [187], and a bound state of light quarks with a mixture of strange quarks and gluons $(\frac{1}{\sqrt{2}}(\bar{u}u + \bar{d}d)$ $+ \delta_1 s\bar{s} + \delta_2 G)$ [188]. Such diverse quark compositions can lead to variations in hadron yields. Significantly, calculations utilizing the Gamma Canonical ensemble-based Statistical Model (γ_SCSM) [126] highlight substantial differences in hadron yields based upon their strangeness content [189].

In high-energy heavy-ion collisions, convincing evidence supports the formation of a strongly-interacting QGP [21, 39, 42, 43, 48, 190–199]. This state, characterized by strong interactions, exhibits properties akin to those of a nearly perfect liquid until the temperature nears the pseudo-critical threshold of about 155 MeV [120]. Subsequently, a transition to confined QCD matter ensues, forming a hot, dense gas of interacting hadrons. Within this environment, resonances decay, and particles interact either elastically or pseudo-elastically until they decouple. Typically, decoupling of the system produced in Pb–Pb collisions at the LHC occurs around 10 fm/c [200]. The investigation of hadronic resonances with varying lifetimes is crucial for understanding the hadronic stage of the collision [36, 112, 135, 141, 145–150, 152–155]. Rescattering and regeneration effects affect the yield of resonances, depending on their lifetime. Given $f_1(1285)$'s lifetime of approximately 8 fm/c, placing it between the lifetimes of K^{*0} and Λ^* mesons, it becomes crucial for systematically investigating rescattering effects and properties of the hadronic phase in heavy-ion collisions. Furthermore, recent theoretical work suggests that the $f_1(1285)$ meson could play a pivotal role in probing the partial restoration of chiral symmetry within the nuclear medium [201]. It has been suggested that the $f_1(1285)$ meson, acting as a chiral partner of the ω meson, may experience a significant mass shift from its vacuum expectation (1281.9 ± 0.5 MeV/c^2) in the presence of finite nucleon density. Hence, measuring $f_1(1285)$ production in pp collisions is indispensable for establishing a reference for studying the partial restoration of chiral symmetry and rescattering effects in high-energy heavy-ion collisions.

This thesis introduces the inaugural measurement of the inclusive production cross section of the $f_1(1285)$ resonance at midrapidity ($|y| < 0.5$) in inelastic pp collisions at a center-of-mass energy of 13 TeV. Its investigation delves into the strangeness content of the $f_1(1285)$ meson by comparing its transverse momentum integrated yield derived from ALICE data with that from γ_{S}CSM calculations.

Bibliography

[1] A. Pais and S. B. Treiman. "How Many Charm Quantum Numbers Are There?" *Phys. Rev. Lett.* 35 (1975), p. 1556.

[2] S. L. Glashow. "Partial Symmetries of Weak Interactions". *Nucl. Phys.* 22 (1961), pp. 579–588.

[3] Abdus Salam and John Clive Ward. "Electromagnetic and weak interactions". *Phys. Lett.* 13 (1964), pp. 168–171.

[4] Steven Weinberg. "A Model of Leptons". *Phys. Rev. Lett.* 19 (1967), pp. 1264–1266.

[5] Peter W. Higgs. "Broken symmetries, massless particles and gauge fields". *Phys. Lett.* 12 (1964), pp. 132–133.

[6] Murray Gell-Mann. "A Schematic Model of Baryons and Mesons". *Phys. Lett.* 8 (1964), pp. 214–215.

[7] Elliott D. Bloom et al. "High-Energy Inelastic e p Scattering at 6-Degrees and 10-Degrees". *Phys. Rev. Lett.* 23 (1969), pp. 930–934.

[8] Martin Breidenbach et al. "Observed behavior of highly inelastic electron-proton scattering". *Phys. Rev. Lett.* 23 (1969), pp. 935–939.

[9] R. Brandelik et al. "Evidence for Planar Events in e+ e- Annihilation at High-Energies". *Phys. Lett. B* 86 (1979), pp. 243–249.

[10] F. Abe et al. "Observation of top quark production in $\bar{p}p$ collisions". *Phys. Rev. Lett.* 74 (1995), pp. 2626–2631. arXiv: `hep-ex/9503002`.

[11] K. Kodama et al. "Observation of tau neutrino interactions". *Phys. Lett. B* 504 (2001), pp. 218–224. arXiv: `hep-ex/0012035`.

[12] Serguei Chatrchyan et al. “Observation of a New Boson at a Mass of 125 GeV with the CMS Experiment at the LHC”. *Phys. Lett. B* 716 (2012), pp. 30–61. arXiv: `1207.7235 [hep-ex]`.

[13] Georges Aad et al. “Observation of a new particle in the search for the Standard Model Higgs boson with the ATLAS detector at the LHC”. *Phys. Lett. B* 716 (2012), pp. 1–29. arXiv: `1207.7214 [hep-ex]`.

[14] Wikipedia contributors. *Standard Model — Wikipedia, The Free Encyclopedia*. [Online; accessed 22-April-2019].

[15] David J. Gross and Frank Wilczek. “Ultraviolet Behavior of Nonabelian Gauge Theories”. *Phys. Rev. Lett.* 30 (1973). Ed. by J. C. Taylor, pp. 1343–1346.

[16] H. David Politzer. “Reliable Perturbative Results for Strong Interactions?” *Phys. Rev. Lett.* 30 (1973). Ed. by J. C. Taylor, pp. 1346–1349.

[17] Siegfried Bethke. “Experimental tests of asymptotic freedom”. *Prog. Part. Nucl. Phys.* 58 (2007), pp. 351–386. arXiv: `hep-ex/0606035`.

[18] Kenneth G. Wilson. “Confinement of Quarks”. *Phys. Rev. D* 10 (1974). Ed. by J. C. Taylor, pp. 2445–2459.

[19] D. J. Gross and Frank Wilczek. “Asymptotically Free Gauge Theories - I”. *Phys. Rev. D* 8 (1973), pp. 3633–3652.

[20] T. D. Lee and G. C. Wick. “Vacuum Stability and Vacuum Excitation in a Spin 0 Field Theory”. *Phys. Rev. D* 9 (1974), pp. 2291–2316.

[21] John Adams et al. “Experimental and theoretical challenges in the search for the quark gluon plasma: The STAR Collaboration’s critical assessment of the evidence from RHIC collisions”. *Nucl. Phys. A* 757 (2005), pp. 102–183. arXiv: `nucl-ex/0501009`.

[22] Frithjof Karsch. “Lattice results on QCD thermodynamics”. *Nucl. Phys. A* 698 (2002). Ed. by T. J. Hallman et al., pp. 199–208. arXiv: `hep-ph/0103314`.

[23] R. V. Gavai and Sourendu Gupta. “The Critical end point of QCD”. *Phys. Rev. D* 71 (2005), p. 114014. arXiv: `hep-lat/0412035`.

[24] Heng-Tong Ding, Frithjof Karsch, and Swagato Mukherjee. "Thermodynamics of strong-interaction matter from Lattice QCD". *Int. J. Mod. Phys. E* 24.10 (2015), p. 1530007. arXiv: `1504.05274 [hep-lat]`.

[25] John R. Ellis. "From little bangs to the Big Bang". *J. Phys. Conf. Ser.* 50 (2006). Ed. by B. Sinha, J. Alam, and T. K. Nayak, pp. 8–21. arXiv: `astro-ph/0504501`.

[26] Wit Busza, Krishna Rajagopal, and Wilke van der Schee. "Heavy Ion Collisions: The Big Picture, and the Big Questions". *Ann. Rev. Nucl. Part. Sci.* 68 (2018), pp. 339–376. arXiv: `1802.04801 [hep-ph]`.

[27] J. D. Bjorken. "Highly Relativistic Nucleus-Nucleus Collisions: The Central Rapidity Region". *Phys. Rev. D* 27 (1983), pp. 140–151.

[28] P. Braun-Munzinger, J. Stachel, and Christof Wetterich. "Chemical freezeout and the QCD phase transition temperature". *Phys. Lett. B* 596 (2004), pp. 61–69. arXiv: `nucl-th/0311005`.

[29] Michael L. Miller et al. "Glauber modeling in high energy nuclear collisions". *Ann. Rev. Nucl. Part. Sci.* 57 (2007), pp. 205–243. arXiv: `nucl-ex/0701025`.

[30] Betty Abelev et al. "Centrality determination of Pb-Pb collisions at $\sqrt{s_{\mathrm{NN}}} = 2.76$ TeV with ALICE". *Phys. Rev. C* 88.4 (2013), p. 044909. arXiv: `1301.4361 [nucl-ex]`.

[31] Mateusz Ploskon. "Heavy-ion collisions - hot QCD in a lab". In: *14th International Workshop on Hadron Physics*. Aug. 2018. arXiv: `1808.01411 [hep-ex]`.

[32] J. D. Bjorken. "Energy Loss of Energetic Partons in Quark - Gluon Plasma: Possible Extinction of High p(t) Jets in Hadron - Hadron Collisions" (Aug. 1982).

[33] Roman Pasechnik and Michal Šumbera. "Phenomenological Review on Quark–Gluon Plasma: Concepts vs. Observations". *Universe* 3.1 (2017), p. 7. arXiv: `1611.01533 [hep-ph]`.

[34] P. Koch, Berndt Muller, and Johann Rafelski. "Strangeness in Relativistic Heavy Ion Collisions". *Phys. Rept.* 142 (1986), pp. 167–262.

[35] K. Redlich and A. Tounsi. "Strangeness enhancement and energy dependence in heavy ion collisions". *Eur. Phys. J. C* 24 (2002), pp. 589–594. arXiv: `hep-ph/0111261`.

[36] B. I. Abelev et al. “Energy and system size dependence of phi meson production in Cu+Cu and Au+Au collisions”. *Phys. Lett. B* 673 (2009), pp. 183–191. arXiv: `0810.4979 [nucl-ex]`.

[37] Jean-Yves Ollitrault. “Anisotropy as a signature of transverse collective flow”. *Phys. Rev. D* 46 (1992), pp. 229–245.

[38] Peter F. Kolb and Ulrich W. Heinz. “Hydrodynamic description of ultrarelativistic heavy ion collisions” (2003), pp. 634–714. arXiv: `nucl-th/0305084 [nucl-th]`.

[39] Ulrich W. Heinz. “The Strongly coupled quark-gluon plasma created at RHIC”. *J. Phys.* A42 (2009), p. 214003. arXiv: `0810.5529 [nucl-th]`.

[40] Shreyasi Acharya et al. “Anisotropic flow and flow fluctuations of identified hadrons in Pb–Pb collisions at $\sqrt{s_{\mathrm{NN}}}$ = 5.02 TeV”. *JHEP* 05 (2023), p. 243. arXiv: `2206.04587 [nucl-ex]`.

[41] Edward Shuryak. “Strongly coupled quark-gluon plasma in heavy ion collisions”. *Rev. Mod. Phys.* 89 (2017), p. 035001. arXiv: `1412.8393 [hep-ph]`.

[42] K Aamodt et al. “Elliptic flow of charged particles in Pb-Pb collisions at 2.76 TeV”. *Phys. Rev. Lett.* 105 (2010), p. 252302. arXiv: `1011.3914 [nucl-ex]`.

[43] K. H. Ackermann et al. “Elliptic flow in Au + Au collisions at (S(NN))**(1/2) = 130 GeV”. *Phys. Rev. Lett.* 86 (2001), pp. 402–407. arXiv: `nucl-ex/0009011`.

[44] Denes Molnar and Sergei A. Voloshin. “Elliptic flow at large transverse momenta from quark coalescence”. *Phys. Rev. Lett.* 91 (2003), p. 092301. arXiv: `nucl-th/0302014`.

[45] J. Schukraft. “Ultra-relativistic heavy-ion collisions: Searching for the quark-gluon plasma”. *Nucl. Phys. A* 553 (1993), pp. 31–44.

[46] Edward V. Shuryak. “Quantum Chromodynamics and the Theory of Superdense Matter”. *Phys. Rept.* 61 (1980), pp. 71–158.

[47] John C. Collins and M. J. Perry. “Superdense Matter: Neutrons Or Asymptotically Free Quarks?” *Phys. Rev. Lett.* 34 (1975), p. 1353.

[48] “The ALICE experiment – A journey through QCD” (Nov. 2022). arXiv: `2211.04384 [nucl-ex]`.

[49] Y. Aoki et al. “The Order of the quantum chromodynamics transition predicted by the standard model of particle physics”. *Nature* 443 (2006), pp. 675–678. arXiv: `hep-lat/0611014`.

[50] Frank R. Brown et al. “On the existence of a phase transition for QCD with three light quarks”. *Phys. Rev. Lett.* 65 (1990), pp. 2491–2494.

[51] Adam Bzdak and Vladimir Skokov. “Event-by-event fluctuations of magnetic and electric fields in heavy ion collisions”. *Phys. Lett.* B710 (2012), pp. 171–174. arXiv: `1111.1949 [hep-ph]`.

[52] T. D. Lee. “A Theory of Spontaneous T Violation”. *Phys. Rev. D* 8 (1973). Ed. by G. Feinberg, pp. 1226–1239.

[53] P. D. Morley and I. A. Schmidt. “Strong P, CP, T Violations in Heavy Ion Collisions”. *Z. Phys.* C26 (1985), p. 627.

[54] Dmitri Kharzeev, R. D. Pisarski, and Michel H. G. Tytgat. “Possibility of spontaneous parity violation in hot QCD”. *Phys. Rev. Lett.* 81 (1998), pp. 512–515. arXiv: `hep-ph/9804221 [hep-ph]`.

[55] Dmitri Kharzeev and Robert D. Pisarski. “Pionic measures of parity and CP violation in high-energy nuclear collisions”. *Phys. Rev.* D61 (2000), p. 111901. arXiv: `hep-ph/9906401 [hep-ph]`.

[56] Dmitri E. Kharzeev. “The Chiral Magnetic Effect and Anomaly-Induced Transport”. *Prog. Part. Nucl. Phys.* 75 (2014), pp. 133–151. arXiv: `1312.3348 [hep-ph]`.

[57] Dmitri E. Kharzeev. “Topology, magnetic field, and strongly interacting matter”. *Ann. Rev. Nucl. Part. Sci.* 65 (2015), pp. 193–214. arXiv: `1501.01336 [hep-ph]`.

[58] Dmitri E. Kharzeev and Jinfeng Liao. “Chiral magnetic effect reveals the topology of gauge fields in heavy-ion collisions”. en. *Nat Rev Phys* 3.1 (Jan. 2021), pp. 55–63.

[59] Sergei A. Voloshin. “Parity violation in hot QCD: How to detect it”. *Phys. Rev.* C70 (2004), p. 057901. arXiv: `hep-ph/0406311 [hep-ph]`.

[60] D. Kharzeev and A. Zhitnitsky. “Charge separation induced by P-odd bubbles in QCD matter”. *Nucl. Phys.* A797 (2007), pp. 67–79. arXiv: `0706.1026 [hep-ph]`.

[61] Kenji Fukushima, Dmitri E. Kharzeev, and Harmen J. Warringa. “The Chiral Magnetic Effect”. *Phys. Rev.* D78 (2008), p. 074033. arXiv: `0808.3382 [hep-ph]`.

[62] Dmitri E. Kharzeev, Larry D. McLerran, and Harmen J. Warringa. “The Effects of topological charge change in heavy ion collisions: ’Event by event P and CP violation’”. *Nucl. Phys.* A803 (2008), pp. 227–253. arXiv: `0711.0950 [hep-ph]`.

[63] Qiang Li et al. “Observation of the chiral magnetic effect in ZrTe5”. *Nature Phys.* 12 (2016), pp. 550–554. arXiv: `1412.6543 [cond-mat.str-el]`.

[64] Yu-Chen Liu and Xu-Guang Huang. “Anomalous chiral transports and spin polarization in heavy-ion collisions”. *Nucl. Sci. Tech.* 31.6 (2020), p. 56. arXiv: `2003.12482 [nucl-th]`.

[65] Jian-Hua Gao et al. “Recent developments in chiral and spin polarization effects in heavy-ion collisions”. *Nucl. Sci. Tech.* 31.9 (2020), p. 90. arXiv: `2005.10432 [hep-ph]`.

[66] B. I. Abelev et al. “Azimuthal Charged-Particle Correlations and Possible Local Strong Parity Violation”. *Phys. Rev. Lett.* 103 (2009), p. 251601. arXiv: `0909.1739 [nucl-ex]`.

[67] B. I. Abelev et al. “Observation of charge-dependent azimuthal correlations and possible local strong parity violation in heavy ion collisions”. *Phys. Rev. C* 81 (2010), p. 054908. arXiv: `0909.1717 [nucl-ex]`.

[68] Betty Abelev et al. “Charge separation relative to the reaction plane in Pb–Pb collisions at $\sqrt{s_{\mathrm{NN}}} = 2.76$ TeV”. *Phys. Rev. Lett.* 110.1 (2013), p. 012301. arXiv: `1207.0900 [nucl-ex]`.

[69] Soren Schlichting and Scott Pratt. “Charge conservation at energies available at the BNL Relativistic Heavy Ion Collider and contributions to local parity violation observables”. *Phys. Rev.* C83 (2011), p. 014913. arXiv: `1009.4283 [nucl-th]`.

[70] Scott Pratt, Soeren Schlichting, and Sean Gavin. “Effects of Momentum Conservation and Flow on Angular Correlations at RHIC”. *Phys. Rev.* C84 (2011), p. 024909. arXiv: `1011.6053 [nucl-th]`.

[71] L. Adamczyk et al. “Measurement of charge multiplicity asymmetry correlations in high-energy nucleus-nucleus collisions at $\sqrt{s_{NN}} = 200$ GeV”. *Phys. Rev.* C89.4 (2014), p. 044908. arXiv: `1303.0901 [nucl-ex]`.

[72] L. Adamczyk et al. "Fluctuations of charge separation perpendicular to the event plane and local parity violation in $\sqrt{s_{NN}} = 200$ GeV Au+Au collisions at the BNL Relativistic Heavy Ion Collider". *Phys. Rev.* C88.6 (2013), p. 064911. arXiv: `1302.3802 [nucl-ex]`.

[73] L. Adamczyk et al. "Beam-energy dependence of charge separation along the magnetic field in Au+Au collisions at RHIC". *Phys. Rev. Lett.* 113 (2014), p. 052302. arXiv: `1404.1433 [nucl-ex]`.

[74] Shreyasi Acharya et al. "Constraining the magnitude of the Chiral Magnetic Effect with Event Shape Engineering in Pb–Pb collisions at $\sqrt{s_{\mathrm{NN}}} = 2.76$ TeV". *Phys. Lett.* B777 (2018), pp. 151–162. arXiv: `1709.04723 [nucl-ex]`.

[75] Vardan Khachatryan et al. "Observation of charge-dependent azimuthal correlations in p-Pb collisions and its implication for the search for the chiral magnetic effect". *Phys. Rev. Lett.* 118.12 (2017), p. 122301. arXiv: `1610.00263 [nucl-ex]`.

[76] J. Adam et al. "Charge-dependent pair correlations relative to a third particle in p + Au and d+ Au collisions at RHIC". *Phys. Lett.* B798 (2019), p. 134975. arXiv: `1906.03373 [nucl-ex]`.

[77] Albert M Sirunyan et al. "Constraints on the chiral magnetic effect using charge-dependent azimuthal correlations in pPb and PbPb collisions at the CERN Large Hadron Collider". *Phys. Rev.* C97.4 (2018), p. 044912. arXiv: `1708.01602 [nucl-ex]`.

[78] Wei Li and Gang Wang. "Chiral Magnetic Effects in Nuclear Collisions". en. *Annu. Rev. Nucl. Part. Sci.* 70.1 (Oct. 2020), pp. 293–321.

[79] J. Adam et al. "Methods for a blind analysis of isobar data collected by the STAR collaboration". *Nucl. Sci. Tech.* 32.5 (2021), p. 48. arXiv: `1911.00596 [nucl-ex]`.

[80] M. S. Abdallah et al. "Search for the chiral magnetic effect with isobar collisions at $\sqrt{s_{\mathrm{NN}}} = 200$ GeV by the STAR Collaboration at the BNL Relativistic Heavy Ion Collider". *Phys. Rev. C* 105.1 (Jan. 2022), p. 014901.

[81] D. T. Son and Ariel R. Zhitnitsky. "Quantum anomalies in dense matter". *Phys. Rev. D* 70 (2004), p. 074018. arXiv: `hep-ph/0405216`.

[82] Max A. Metlitski and Ariel R. Zhitnitsky. "Anomalous axion interactions and topological currents in dense matter". *Phys. Rev. D* 72 (2005), p. 045011. arXiv: `hep-ph/0505072`.

[83] Yannis Burnier et al. "Chiral magnetic wave at finite baryon density and the electric quadrupole moment of quark-gluon plasma in heavy ion collisions". *Phys. Rev. Lett.* 107 (2011), p. 052303. arXiv: `1103.1307 [hep-ph]`.

[84] Y. Burnier et al. "From the chiral magnetic wave to the charge dependence of elliptic flow" (Aug. 2012). arXiv: `1208.2537 [hep-ph]`.

[85] Dmitri E. Kharzeev and Ho-Ung Yee. "Chiral Magnetic Wave". *Phys. Rev. D* 83 (2011), p. 085007. arXiv: `1012.6026 [hep-th]`.

[86] Ho-Ung Yee and Yi Yin. "Realistic Implementation of Chiral Magnetic Wave in Heavy Ion Collisions". *Phys. Rev. C* 89.4 (2014), p. 044909. arXiv: `1311.2574 [nucl-th]`.

[87] Seyed Farid Taghavi and Urs Achim Wiedemann. "Chiral magnetic wave in an expanding QCD fluid". *Phys. Rev. C* 91.2 (2015), p. 024902. arXiv: `1310.0193 [hep-ph]`.

[88] S. Voloshin and Y. Zhang. "Flow study in relativistic nuclear collisions by Fourier expansion of Azimuthal particle distributions". *Z. Phys.* C70 (1996), pp. 665–672. arXiv: `hep-ph/9407282 [hep-ph]`.

[89] Arthur M. Poskanzer and S. A. Voloshin. "Methods for analyzing anisotropic flow in relativistic nuclear collisions". *Phys. Rev.* C58 (1998), pp. 1671–1678. arXiv: `nucl-ex/9805001 [nucl-ex]`.

[90] Meng Wang et al. "Number-of-constituent-quark scaling of elliptic flow: a quantitative study". *Nucl. Sci. Tech.* 33.3 (Mar. 2022), p. 37.

[91] L. Adamczyk et al. "Observation of charge asymmetry dependence of pion elliptic flow and the possible chiral magnetic wave in heavy-ion collisions". *Phys. Rev. Lett.* 114.25 (2015), p. 252302. arXiv: `1504.02175 [nucl-ex]`.

[92] Jaroslav Adam et al. "Charge-dependent flow and the search for the chiral magnetic wave in Pb–Pb collisions at $\sqrt{s_{\mathrm{NN}}} = 2.76$ TeV". *Phys. Rev. C* 93.4 (2016), p. 044903. arXiv: `1512.05739 [nucl-ex]`.

[93] Albert M Sirunyan et al. “Probing the chiral magnetic wave in pPb and PbPb collisions at $\sqrt{s_{NN}}$ =5.02TeV using charge-dependent azimuthal anisotropies”. *Phys. Rev. C* 100.6 (2019), p. 064908. arXiv: `1708.08901 [nucl-ex]`.

[94] Wei-Tian Deng and Xu-Guang Huang. “Event-by-event generation of electromagnetic fields in heavy-ion collisions”. *Phys. Rev. C* 85 (2012), p. 044907. arXiv: `1201.5108 [nucl-th]`.

[95] M. I. Abdulhamid et al. “Search for the chiral magnetic wave using anisotropic flow of identified particles at energies available at the BNL Relativistic Heavy Ion Collider”. *Phys. Rev. C* 108.1 (2023), p. 014908. arXiv: `2210.14027 [nucl-ex]`.

[96] Chun-Zheng Wang et al. “Interpreting the charge-dependent flow and constraining the chiral magnetic wave with event shape engineering”. *Phys. Lett. B* 820 (2021), p. 136580. arXiv: `2104.05551 [nucl-th]`.

[97] Jurgen Schukraft, Anthony Timmins, and Sergei A. Voloshin. “Ultra-relativistic nuclear collisions: event shape engineering”. *Phys. Lett.* B719 (2013), pp. 394–398. arXiv: `1208.4563 [nucl-ex]`.

[98] Steffen A. Bass, Pawel Danielewicz, and Scott Pratt. “Clocking hadronization in relativistic heavy ion collisions with balance functions”. *Phys. Rev. Lett.* 85 (2000), pp. 2689–2692. arXiv: `nucl-th/0005044`.

[99] Betty Abelev et al. “Charge correlations using the balance function in Pb–Pb collisions at $\sqrt{s_{\mathrm{NN}}}$ = 2.76 TeV”. *Phys. Lett. B* 723 (2013), pp. 267–279. arXiv: `1301.3756 [nucl-ex]`.

[100] Guo-Liang Ma. “Final state effects on charge asymmetry of pion elliptic flow in high-energy heavy-ion collisions”. *Phys. Lett. B* 735 (2014), pp. 383–386. arXiv: `1401.6502 [nucl-th]`.

[101] Wen-Hao Zhou and Jun Xu. “Simulating the Chiral Magnetic Wave in a Box System”. *Phys. Rev. C* 98.4 (2018), p. 044904. arXiv: `1810.01030 [nucl-th]`.

[102] Zhang-Zhu Han and Jun Xu. “Charge asymmetry dependence of the elliptic flow splitting in relativistic heavy-ion collisions”. *Phys. Rev. C* 99.4 (2019), p. 044915. arXiv: `1904.03544 [nucl-th]`.

[103] Diyu Shen et al. "Charge asymmetry dependence of flow and a novel correlator to detect the chiral magnetic wave in a multiphase transport model". *Phys. Rev. C* 100.6 (2019), p. 064907. arXiv: `1911.00839 [hep-ph]`.

[104] Niseem Magdy et al. "An extended $R^{(2)}_{\Psi_m}(\Delta S_2)$ correlator for detecting and characterizing the Chiral Magnetic Wave". *Phys. Lett. B* 811 (2020), p. 135986. arXiv: `2003.02396 [nucl-ex]`.

[105] Yoshitaka Hatta, Akihiko Monnai, and Bo-Wen Xiao. "Elliptic flow difference of charged pions in heavy-ion collisions". *Nucl. Phys. A* 947 (2016), pp. 155–160. arXiv: `1507.04690 [hep-ph]`.

[106] Wen-Ya Wu et al. "Global constraint on the magnitude of anomalous chiral effects in heavy-ion collisions". *Phys. Rev. C* 107.3 (2023), p. L031902. arXiv: `2211.15446 [nucl-th]`.

[107] Betty Bezverkhny Abelev et al. "Multiplicity Dependence of Pion, Kaon, Proton and Lambda Production in p-Pb Collisions at $\sqrt{s_{NN}}$ = 5.02 TeV". *Phys. Lett. B* 728 (2014), pp. 25–38. arXiv: `1307.6796 [nucl-ex]`.

[108] Betty Abelev et al. "Centrality dependence of π, K, p production in Pb–Pb collisions at $\sqrt{s_{\mathrm{NN}}}$ = 2.76 TeV". *Phys. Rev. C* 88 (2013), p. 044910. arXiv: `1303.0737 [hep-ex]`.

[109] Jaroslav Adam et al. "Multi-strange baryon production in p-Pb collisions at $\sqrt{s_{\mathrm{NN}}}$ = 5.02 TeV". *Phys. Lett. B* 758 (2016), pp. 389–401. arXiv: `1512.07227 [nucl-ex]`.

[110] K. Aamodt et al. "Production of pions, kaons and protons in pp collisions at $\sqrt{s}$ = 900 GeV with ALICE at the LHC". *Eur. Phys. J. C* 71 (2011), p. 1655. arXiv: `1101.4110 [hep-ex]`.

[111] Jaroslav Adam et al. "Production of K^* $(892)^0$ and ϕ (1020) in p–Pb collisions at $\sqrt{s_{\mathrm{NN}}}$= 5.02 TeV". *Eur. Phys. J. C* 76.5 (2016), p. 245. arXiv: `1601.07868 [nucl-ex]`.

[112] Shreyasi Acharya et al. "Production of $\mathrm{K}^*(892)^0$ and $\phi(1020)$ in pp and Pb–Pb collisions at $\sqrt{s_{\mathrm{NN}}}$ = 5.02 TeV". *Phys. Rev. C* 106.3 (2022), p. 034907. arXiv: `2106.13113 [nucl-ex]`.

[113] Shreyasi Acharya et al. “Multiplicity dependence of light-flavor hadron production in pp collisions at $\sqrt{s} = 7$ TeV”. *Phys. Rev. C* 99.2 (2019), p. 024906. arXiv: `1807.11321 [nucl-ex]`.

[114] Shreyasi Acharya et al. “Multiplicity dependence of (multi-)strange hadron production in proton-proton collisions at $\sqrt{s} = 13$ TeV”. *Eur. Phys. J. C* 80.2 (2020), p. 167. arXiv: `1908.01861 [nucl-ex]`.

[115] V. Greco, C. M. Ko, and P. Levai. “Parton coalescence and anti-proton / pion anomaly at RHIC”. *Phys. Rev. Lett.* 90 (2003), p. 202302. arXiv: `nucl-th/0301093`.

[116] V. Greco, C. M. Ko, and P. Levai. “Parton coalescence at RHIC”. *Phys. Rev. C* 68 (2003), p. 034904. arXiv: `nucl-th/0305024`.

[117] R. J. Fries et al. “Hadronization in heavy ion collisions: Recombination and fragmentation of partons”. *Phys. Rev. Lett.* 90 (2003), p. 202303. arXiv: `nucl-th/0301087`.

[118] R. J. Fries et al. “Hadron production in heavy ion collisions: Fragmentation and recombination from a dense parton phase”. *Phys. Rev. C* 68 (2003), p. 044902. arXiv: `nucl-th/0306027`.

[119] Anton Andronic et al. “Decoding the phase structure of QCD via particle production at high energy”. *Nature* 561.7723 (2018), pp. 321–330. arXiv: `1710.09425 [nucl-th]`.

[120] A. Bazavov et al. “Chiral crossover in QCD at zero and non-zero chemical potentials”. *Phys. Lett. B* 795 (2019), pp. 15–21. arXiv: `1812.08235 [hep-lat]`.

[121] Derek Teaney. “Chemical freezeout in heavy ion collisions” (Apr. 2002). arXiv: `nucl-th/0204023`.

[122] J. Manninen and F. Becattini. “Chemical freeze-out in ultra-relativistic heavy ion collisions at $\sqrt{s_{\mathrm{NN}}} = 130$ and 200 GeV”. *Phys. Rev. C* 78 (2008), p. 054901. arXiv: `0806.4100 [nucl-th]`.

[123] Ulrich W. Heinz and Gregory Kestin. “Jozso’s Legacy: Chemical and Kinetic Freeze-out in Heavy-Ion Collisions”. *Eur. Phys. J. ST* 155 (2008), pp. 75–87. arXiv: `0709.3366 [nucl-th]`.

[124] Jamie M. Karthein et al. “Thermal-model-based characterization of heavy-ion-collision systems at chemical freeze-out”. *EPJ Web Conf.* 259 (2022), p. 11010. arXiv: `2201.03645 [hep-ph]`.

[125] A. Keranen and F. Becattini. “The Canonical effect in statistical models for relativistic heavy ion collisions”. *J. Phys. G* 28 (2002). Ed. by J. Tennant, pp. 2041–2046. arXiv: `nucl-th/0112045`.

[126] Volodymyr Vovchenko, Benjamin Dönigus, and Horst Stoecker. “Canonical statistical model analysis of pp , p–Pb, and Pb–Pb collisions at energies available at the CERN Large Hadron Collider”. *Phys. Rev. C* 100.5 (2019), p. 054906. arXiv: `1906.03145 [hep-ph]`.

[127] Jean Cleymans. “The thermal-statistical model for particle production”. *EPJ Web Conf.* 7 (2010). Ed. by David Blaschke et al., p. 01001.

[128] S. Das Gupta and A. Z. Mekjian. “The Thermodynamic Model for Relativistic Heavy Ion Collisions”. *Phys. Rept.* 72 (1981), pp. 131–183.

[129] Ekkard Schnedermann, Josef Sollfrank, and Ulrich W. Heinz. “Thermal phenomenology of hadrons from 200-A/GeV S+S collisions”. *Phys. Rev. C* 48 (1993), pp. 2462–2475. arXiv: `nucl-th/9307020`.

[130] Shreyasi Acharya et al. “Production of charged pions, kaons, and (anti-)protons in Pb–Pb and inelastic pp collisions at $\sqrt{s_{\mathrm{NN}}} = 5.02$ TeV”. *Phys. Rev. C* 101.4 (2020), p. 044907. arXiv: `1910.07678 [nucl-ex]`.

[131] J. Steinheimer et al. “Influence of the hadronic phase on observables in ultra-relativistic heavy ion collisions”. *Phys. Rev. C* 95.6 (2017), p. 064902. arXiv: `1703.06638 [nucl-th]`.

[132] Sascha Vogel and Marcus Bleicher. “Resonance absorption and regeneration in relativistic heavy ion collisions”. In: *43rd International Winter Meeting on Nuclear Physics*. May 2005. arXiv: `nucl-th/0505027`.

[133] B. I. Abelev et al. “Strange baryon resonance production in $\sqrt{s_{\mathrm{NN}}} = 200$ GeV p+p and Au+Au collisions”. *Phys. Rev. Lett.* 97 (2006), p. 132301. arXiv: `nucl-ex/0604019`.

[134] Shreyasi Acharya et al. “Evidence of rescattering effect in Pb–Pb collisions at the LHC through production of $K^*(892)^0$ and $\phi(1020)$ mesons”. *Phys. Lett. B* 802 (2020), p. 135225. arXiv: `1910.14419 [nucl-ex]`.

[135] J. Adams et al. “$K^*(892)$ resonance production in Au+Au and p+p collisions at $\sqrt{s_{\mathrm{NN}}}$ = 200 GeV at STAR”. *Phys. Rev. C* 71 (2005), p. 064902. arXiv: `nucl-ex/0412019`.

[136] Giorgio Torrieri and Johann Rafelski. “Strange hadron resonances as a signature of freezeout dynamics”. *Phys. Lett. B* 509 (2001), pp. 239–245. arXiv: `hep-ph/0103149`.

[137] Christina Markert. “What do we learn from resonance production in heavy ion collisions?” *J. Phys. G* 31 (2005). Ed. by F. Antinori et al., S169–S178. arXiv: `nucl-ex/0503013`.

[138] B. Z. Kopeliovich et al. “Pion-pion cross section from proton-proton collisions at the LHC”. *Phys. Rev. D* 91 (2015), p. 054030. arXiv: `1411.5602 [hep-ph]`.

[139] D. Aston et al. “A Study of K- pi+ Scattering in the Reaction K- p —> K- pi+ n at 11-GeV/c”. *Nucl. Phys. B* 296 (1988), pp. 493–526.

[140] S. D. Protopopescu et al. “$\pi\pi$ Partial Wave Analysis from Reactions π^+p —> π^+ π^- Δ^{++} and π^+p —> K^+ K^- Δ^{++} at 7.1 GeV/c”. *Phys. Rev. D* 7 (1973), p. 1279.

[141] B. Abelev et al. “$K^*(892)^0$ and $\phi(1020)$ production in Pb–Pb collisions at $\sqrt{s_{\mathrm{NN}}}$ = 2.76 TeV”. *Phys. Rev. C* 91 (2015), p. 024609. arXiv: `1404.0495 [nucl-ex]`.

[142] Shreyasi Acharya et al. “Multiplicity dependence of $K^*(892)^0$ and $\phi(1020)$ production in pp collisions at $\sqrt{s}$ =13 TeV”. *Phys. Lett. B* 807 (2020), p. 135501. arXiv: `1910.14397 [nucl-ex]`.

[143] Shreyasi Acharya et al. “$K*(892)^0$ and $\phi(1020)$ production in p-Pb collisions at $\sqrt{s}$ = 8.16 TeV”. *Phys. Rev. C* 107.5 (2023), p. 055201. arXiv: `2110.10042 [nucl-ex]`.

[144] S. Acharya et al. “Multiplicity and rapidity dependence of $K^*(892^0$ and $\phi(1020)$ production in p–Pb collisions at $\sqrt{s_{\mathrm{NN}}}$ = 5.02 TeV”. *Eur. Phys. J. C* 83.6 (2023), p. 540. arXiv: `2204.10263 [nucl-ex]`.

[145] C. Alt et al. “Energy dependence of ϕ meson production in central Pb+Pb collisions at $\sqrt{s_{\mathrm{NN}}}$ = 6 to 17 GeV”. *Phys. Rev. C* 78 (2008), p. 044907. arXiv: 0806.1937 [nucl-ex].

[146] S. V. Afanasiev et al. “Production of ϕ mesons in p+p, p+Pb and central Pb+Pb collisions at E(beam) = 158 A GeV”. *Phys. Lett. B* 491 (2000), pp. 59–66.

[147] T. Anticic et al. “$\mathrm{K}^*(892)^0$ and $\bar{\mathrm{K}}^*(892)^0$ production in central Pb+Pb, Si+Si, C+C and inelastic p+p collisions at 158 A GeV”. *Phys. Rev. C* 84 (2011), p. 064909. arXiv: 1105.3109 [nucl-ex].

[148] A. Adare et al. “Measurement of K_S^0 and K^{*0} in p+p, d+Au, and Cu+Cu collisions at $\sqrt{s_{\mathrm{NN}}}$ = 200 GeV”. *Phys. Rev. C* 90.5 (2014), p. 054905. arXiv: 1405.3628 [nucl-ex].

[149] N. J. Abdulameer et al. “Measurement of ϕ-meson production in Cu+Au collisions at $\sqrt{s_{\mathrm{NN}}}$ = 200 GeV and U+U collisions at $\sqrt{s_{\mathrm{NN}}}$ = 193 GeV”. *Phys. Rev. C* 107.1 (2023), p. 014907. arXiv: 2207.10745 [nucl-ex].

[150] U. Acharya et al. “Study of ϕ meson production in p+Al, p+Au, d+Au, and ^{3}He+Au collisions at $\sqrt{s_{\mathrm{NN}}}$ = 200 GeV”. *Phys. Rev. C* 106.1 (2022), p. 014908. arXiv: 2203.06087 [nucl-ex].

[151] A. Adare et al. “Nuclear modification factors of ϕ mesons in d+Au, Cu+Cu and Au+Au collisions at $\sqrt{s_{\mathrm{NN}}}$ = 200 GeV”. *Phys. Rev. C* 83 (2011), p. 024909. arXiv: 1004.3532 [nucl-ex].

[152] S. S. Adler et al. “Production of ϕ mesons at mid-rapidity in $\sqrt{s_{\mathrm{NN}}}$ = 200 GeV Au+Au collisions at RHIC”. *Phys. Rev. C* 72 (2005), p. 014903. arXiv: nucl-ex/0410012.

[153] B. I. Abelev et al. “Measurements of ϕ meson production in relativistic heavy-ion collisions at RHIC”. *Phys. Rev. C* 79 (2009), p. 064903. arXiv: 0809.4737 [nucl-ex].

[154] C. Adler et al. “$\mathrm{K}^*(892)^0$ production in relativistic heavy ion collisions at $\sqrt{s_{\mathrm{NN}}}$ = 130 GeV”. *Phys. Rev. C* 66 (2002), p. 061901. arXiv: nucl-ex/0205015.

[155] M. M. Aggarwal et al. “K^{*0} production in Cu+Cu and Au+Au collisions at $\sqrt{s_{\mathrm{NN}}}$ = 62.4 GeV and 200 GeV”. *Phys. Rev. C* 84 (2011), p. 034909. arXiv: 1006.1961 [nucl-ex].

[156] Jaroslav Adam et al. “K$^*(892)^0$ and $\phi(1020)$ meson production at high transverse momentum in pp and Pb-Pb collisions at $\sqrt{s_{\mathrm{NN}}} = 2.76$ TeV”. *Phys. Rev. C* 95.6 (2017), p. 064606. arXiv: `1702.00555 [nucl-ex]`.

[157] Jaroslav Adam et al. “Enhanced production of multi-strange hadrons in high-multiplicity proton-proton collisions”. *Nature Phys.* 13 (2017), pp. 535–539. arXiv: `1606.07424 [nucl-ex]`.

[158] Shreyasi Acharya et al. “Long- and short-range correlations and their event-scale dependence in high-multiplicity pp collisions at $\sqrt{s} = 13$ TeV”. *JHEP* 05 (2021), p. 290. arXiv: `2101.03110 [nucl-ex]`.

[159] Shreyasi Acharya et al. “Investigations of Anisotropic Flow Using Multiparticle Azimuthal Correlations in pp, p-Pb, Xe-Xe, and Pb-Pb Collisions at the LHC”. *Phys. Rev. Lett.* 123.14 (2019), p. 142301. arXiv: `1903.01790 [nucl-ex]`.

[160] C. Aidala et al. “Creation of quark–gluon plasma droplets with three distinct geometries”. *Nature Phys.* 15.3 (2019), pp. 214–220. arXiv: `1805.02973 [nucl-ex]`.

[161] Vardan Khachatryan et al. “Evidence for collectivity in pp collisions at the LHC”. *Phys. Lett. B* 765 (2017), pp. 193–220. arXiv: `1606.06198 [nucl-ex]`.

[162] Anton Motornenko et al. “Kinetic freeze-out temperature from yields of short-lived resonances”. *Phys. Rev. C* 102.2 (2020), p. 024909. arXiv: `1908.11730 [hep-ph]`.

[163] S. K. Choi et al. “Observation of a narrow charmonium-like state in exclusive $B^{\pm} \to K^{\pm}\pi^{+}\pi^{-}J/\psi$ decays”. *Phys. Rev. Lett.* 91 (2003), p. 262001. arXiv: `hep-ex/0309032`.

[164] S. K. Choi et al. “Observation of a resonance-like structure in the $pi^{\pm}\psi'$ mass distribution in exclusive $B \to K\pi^{\pm}\psi'$ decays”. *Phys. Rev. Lett.* 100 (2008). Ed. by Dongchul Son and Sun Kun Oh, p. 142001. arXiv: `0708.1790 [hep-ex]`.

[165] M. Ablikim et al. “Observation of a Charged Charmoniumlike Structure in $e^{+}e^{-} \to \pi^{+}\pi^{-}J/\psi$ at $\sqrt{s}$ =4.26 GeV”. *Phys. Rev. Lett.* 110 (2013), p. 252001. arXiv: `1303.5949 [hep-ex]`.

[166] Serguei Chatrchyan et al. “Observation of a Peaking Structure in the $J/\psi\phi$ Mass Spectrum from $B^{\pm} \to J/\psi\phi K^{\pm}$ Decays”. *Phys. Lett. B* 734 (2014), pp. 261–281. arXiv: `1309.6920 [hep-ex]`.

[167] Roel Aaij et al. "Observation of the resonant character of the $Z(4430)^-$ state". *Phys. Rev. Lett.* 112.22 (2014), p. 222002. arXiv: `1404.1903 [hep-ex]`.

[168] Roel Aaij et al. "Observation of a narrow pentaquark state, $P_c(4312)^+$, and of two-peak structure of the $P_c(4450)^+$". *Phys. Rev. Lett.* 122.22 (2019), p. 222001. arXiv: `1904.03947 [hep-ex]`.

[169] Roel Aaij et al. "Evidence for a new structure in the $J/\psi p$ and $J/\psi \bar{p}$ systems in $B_s^0 \to J/\psi p \bar{p}$ decays". *Phys. Rev. Lett.* 128.6 (2022), p. 062001. arXiv: `2108.04720 [hep-ex]`.

[170] Shreyasi Acharya et al. "KS0KS0 and KS0K± femtoscopy in pp collisions at s=5.02 and 13 TeV". *Phys. Lett. B* 833 (2022), p. 137335. arXiv: `2111.06611 [nucl-ex]`.

[171] Shreyasi Acharya et al. "Investigating the nature of the $\mathrm{K}_0^*(700)$ state with $\pi^\pm\mathrm{K}_\mathrm{S}^0$ correlations at the LHC" (Dec. 2023). arXiv: `2312.12830 [hep-ex]`.

[172] G. Zweig. "An SU(3) model for strong interaction symmetry and its breaking. Version 2". In: *DEVELOPMENTS IN THE QUARK THEORY OF HADRONS. VOL. 1. 1964 - 1978*. Ed. by D. B. Lichtenberg and Simon Peter Rosen. Feb. 1964, pp. 22–101.

[173] Robert L. Jaffe. "Multi-Quark Hadrons. 1. The Phenomenology of (2 Quark 2 anti-Quark) Mesons". *Phys. Rev. D* 15 (1977), p. 267.

[174] Harry J. Lipkin. "New Possibilities for Exotic Hadrons: Anticharmed Strange Baryons". *Phys. Lett. B* 195 (1987), pp. 484–488.

[175] D. H. Miller et al. "K Kbar pi Resonance at 1280 MeV". *Phys. Rev. Lett.* 14 (1965), p. 1074.

[176] C. d'Andlau, J. Barlow, and A. M. Adamson. "Evidence for a Nonstrange Meson of Mass 1290 MeV". *Phys. Lett.* 17 (1965), p. 347.

[177] D. Barberis et al. "A Study of the k anti-k pi channel produced centrally in p p interactions at 450-GeV/c". *Phys. Lett. B* 413 (1997), pp. 225–231. arXiv: `hep-ex/9707022`.

[178] T. A. Armstrong et al. "Study of the eta pi+ pi- system centrally produced in the reaction p p —> p(f) (eta pi+ pi-) p(s) at 300-GeV/c". *Z. Phys. C* 52 (1991), pp. 389–396.

[179] M. A. Reyes et al. “Spin parity analysis of the centrally produced K(S) K(S) system at 800-GeV”. *Nucl. Phys. B Proc. Suppl.* 56 (1997). Ed. by H. Koch, M. Kunze, and K. Peters, pp. 285–290. arXiv: hep-ex/9702010.

[180] M. Acciarri et al. “Light resonances in $K_S^0 K^\pm \pi^\mp$ and $\eta\pi^+\pi^-$ final states in $\gamma\gamma$ collisions at LEP”. *Phys. Lett. B* 501 (2001), pp. 1–11. arXiv: hep-ex/0011035.

[181] P. Gavillet. “Measurement of inclusive f(1)(1285) and f(1)(1420) production in Z decays with the DELPHI detector”. In: *31st International Symposium on Multiparticle Dynamics*. Nov. 2001, pp. 56–61. arXiv: hep-ph/0111397.

[182] R. Dickson et al. “Photoproduction of the $f_1(1285)$ Meson”. *Phys. Rev. C* 93.6 (2016), p. 065202. arXiv: 1604.07425 [nucl-ex].

[183] R Aaij et al. “Observation of $\bar{B}_{(s)} \to J/\psi f_1(1285)$ Decays and Measurement of the $f_1(1285)$ Mixing Angle”. *Phys. Rev. Lett.* 112.9 (2014), p. 091802. arXiv: 1310.2145 [hep-ex].

[184] F. Aceti, Ju-Jun Xie, and E. Oset. “The $K\bar{K}\pi$ decay of the $f_1(1285)$ and its nature as a $K^*\bar{K} - cc$ molecule”. *Phys. Lett. B* 750 (2015), pp. 609–614. arXiv: 1505.06134 [hep-ph].

[185] A. A. Osipov, A. A. Pivovarov, and M. K. Volkov. “The anomalous decay $f_1(1285) \to \rho\gamma$ and related processes”. *Phys. Rev. D* 96.5 (2017), p. 054012. arXiv: 1705.05711 [hep-ph].

[186] Y. Kanada-En’yo, O. Morimatsu, and T. Nishikawa. “Axial vector tetraquark with S = +2”. *Phys. Rev. D* 71 (2005), p. 094005. arXiv: hep-ph/0502042.

[187] Frank E. Close and Andrew Kirk. “Implications of the glueball q anti-q filter on the 1++ nonet”. *Z. Phys. C* 76 (1997), pp. 469–474. arXiv: hep-ph/9706543.

[188] P. G. Moreira and M. L. L. da Silva. “Investigating the glue content of f_1 (1285)”. *Nucl. Phys. A* 992 (2019), p. 121641. arXiv: 1712.04783 [hep-ph].

[189] Shreyasi Acharya et al. “$\mathrm{f}_0(980)$ production in inelastic pp collisions at $\sqrt{s} = 5.02$ TeV”. *Phys. Lett. B* 846 (2023), p. 137644. arXiv: 2206.06216 [nucl-ex].

[190] J. Adams et al. “Evidence from d+Au measurements for final state suppression of high p_T hadrons in Au+Au collisions at RHIC”. *Phys. Rev. Lett.* 91 (2003), p. 072304. arXiv: nucl-ex/0306024.

[191] C. Adler et al. “Disappearance of back-to-back high p_{T} hadron correlations in central Au+Au collisions at $\sqrt{s_{\mathrm{NN}}} = 200$ GeV”. *Phys. Rev. Lett.* 90 (2003), p. 082302. arXiv: nucl-ex/0210033.

[192] John Adams et al. “Particle type dependence of azimuthal anisotropy and nuclear modification of particle production in Au+Au collisions at $\sqrt{s_{\mathrm{NN}}} = 200$ GeV”. *Phys. Rev. Lett.* 92 (2004), p. 052302. arXiv: nucl-ex/0306007.

[193] K. Adcox et al. “Suppression of hadrons with large transverse momentum in central Au+Au collisions at $\sqrt{s_{\mathrm{NN}}} = 130$ GeV”. *Phys. Rev. Lett.* 88 (2002), p. 022301. arXiv: nucl-ex/0109003.

[194] K. Adcox et al. “Formation of dense partonic matter in relativistic nucleus-nucleus collisions at RHIC: Experimental evaluation by the PHENIX collaboration”. *Nucl. Phys. A* 757 (2005), pp. 184–283. arXiv: nucl-ex/0410003.

[195] I. Arsene et al. “Quark gluon plasma and color glass condensate at RHIC? The Perspective from the BRAHMS experiment”. *Nucl. Phys. A* 757 (2005), pp. 1–27. arXiv: nucl-ex/0410020.

[196] B. B. Back et al. “The PHOBOS perspective on discoveries at RHIC”. *Nucl. Phys. A* 757 (2005), pp. 28–101. arXiv: nucl-ex/0410022.

[197] K. Aamodt et al. “Suppression of Charged Particle Production at Large Transverse Momentum in Central Pb–Pb Collisions at $\sqrt{s_{\mathrm{NN}}}$= 2.76 TeV”. *Phys. Lett. B* 696 (2011), pp. 30–39. arXiv: 1012.1004 [nucl-ex].

[198] K. Aamodt et al. “Higher harmonic anisotropic flow measurements of charged particles in Pb–Pb collisions at $\sqrt{s_{\mathrm{NN}}}$=2.76 TeV”. *Phys. Rev. Lett.* 107 (2011), p. 032301. arXiv: 1105.3865 [nucl-ex].

[199] T. Niida and Y. Miake. “Signatures of QGP at RHIC and the LHC”. *AAPPS Bull.* 31.1 (2021), p. 12. arXiv: 2104.11406 [nucl-ex].

[200] K. Aamodt et al. “Two-pion Bose-Einstein correlations in central Pb-Pb collisions at $\sqrt{s_{NN}} = 2.76$ TeV”. *Phys. Lett. B* 696 (2011), pp. 328–337. arXiv: 1012.4035 [nucl-ex].

[201] Philipp Gubler, Teiji Kunihiro, and Su Houng Lee. “A novel probe of chiral restoration in nuclear medium”. *Phys. Lett. B* 767 (2017), pp. 336–340. arXiv: 1608.05141 [nucl-th].

CHAPTER 2

A Large Ion Collider Experiment (ALICE)

Contents

2.1 The Large Hadron Collider (LHC) at CERN 54
2.2 The ALICE experiment at LHC 57
2.3 ALICE datasets and detector upgrades 67

The Large Hadron Collider (LHC), an unparalleled scientific marvel of the 21st century, stands as a testament to humanity's quest for knowledge. Nestled within the sprawling campus of CERN in Geneva, Switzerland, this colossal particle accelerator was meticulously designed and built with the ambitious objective of peering into the deepest secrets of the universe. As the crown jewel of particle physics research, the LHC accelerator boasts the distinction of being the highest energy collider on the planet. Central to the LHC's array of groundbreaking experiments is the Large Ion Collider Experiment (ALICE). Since its inception, ALICE has served as a specialized detector meticulously engineered to scrutinize the outcomes of heavy-ion collisions. Delving into the intricate dance of subatomic particles, ALICE has been tirelessly gathering data from a myriad of collisions, encompassing both hadronic and nuclear interactions, since its inception in 2009.

The principal experiments conducted at the LHC illuminate the forefront of scientific exploration, ranging from unraveling the mysteries of particle interactions to probing the elusive state of Quark-Gluon Plasma (QGP). Transitioning seamlessly from this exploration, the chapter offers an insightful overview of ALICE's intricately designed sub-detectors.

2.1 The Large Hadron Collider (LHC) at CERN

The LHC accelerator is located beneath the border between Switzerland and France, housed within a 26.7 km long underground tunnel at depths ranging from approximately 50 to 150 meters. Comprising two rings of superconducting magnets along with various accelerating structures, the LHC serves to amplify the energy of particles throughout its course. Figure 2.1 depicts the CERN accelerator complex, encompassing diverse accelerator systems such as the Linear Accelerator 2 (LINAC 2), the Proton Synchrotron Booster (PSB), the Proton Synchrotron (PS), the Super Proton Synchrotron (SPS), among others.

Each of the accelerator systems involved progressively boosts the energy of particle beams prior to their introduction into the main LHC ring. Proton acceleration commences with the utilization of hydrogen gas as a source, prompting its decomposition into constituent protons and electrons through the application of an electric field. These protons are then propelled to 100 kV and directed towards a Radio Frequency Quadrupole (QRF), which accelerates and concentrates the particle stream, achieving an energy level of 750 keV. Subsequently, the proton beam is guided to the linear accelerator (LINAC 2), where further acceleration results in an energy of 50 MeV. Progressing through subsequent stages,

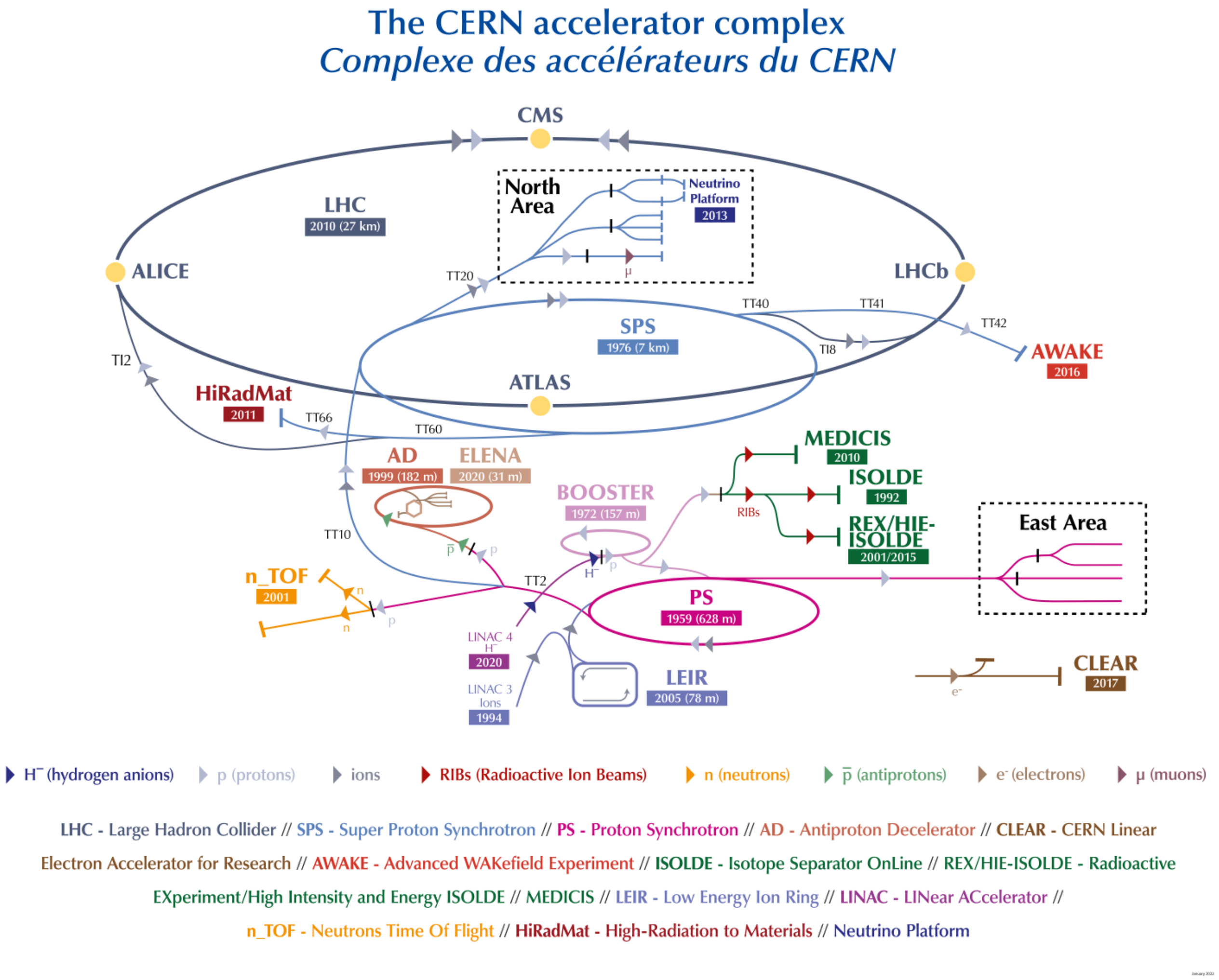
The CERN accelerator complex
Complexe des accélérateurs du CERN
CMS
LHC
2010 (27 km)
North Area
Neutrino Platform
2013
ALICE
LHCb
TT20
μ
TT40
TT41
TT42
AWAKE
2016
SPS
1976 (7 km)
TI8
TI2
ATLAS
HiRadMat
2011
TT66
TT60
MEDICIS
2010
ISOLDE
1992
REX/HIE-ISOLDE
2001/2015
RIBs
AD
1999 (182 m)
ELENA
2020 (31 m)
BOOSTER
1972 (157 m)
East Area
TT10
p̄
p
n_TOF
2001
n
TT2
H⁻
PS
1959 (628 m)
LINAC 4
H⁻
2020
LINAC 3
Ions
1994
LEIR
2005 (78 m)
CLEAR
2017
e⁻
H⁻ (hydrogen anions)
p (protons)
ions
RIBs (Radioactive Ion Beams)
n (neutrons)
p̄ (antiprotons)
e⁻ (electrons)
μ (muons)
LHC - Large Hadron Collider // SPS - Super Proton Synchrotron // PS - Proton Synchrotron // AD - Antiproton Decelerator // CLEAR - CERN Linear Electron Accelerator for Research // AWAKE - Advanced WAKefield Experiment // ISOLDE - Isotope Separator OnLine // REX/HIE-ISOLDE - Radioactive EXperiment/High Intensity and Energy ISOLDE // MEDICIS // LEIR - Low Energy Ion Ring // LINAC - LINear ACcelerator // n_TOF - Neutrons Time Of Flight // HiRadMat - High-Radiation to Materials // Neutrino Platform

FIGURE 2.1: The CERN accelerator complex and the positions of the four primary LHC experiments-ALICE, ATLAS, CMS, and LHCb situated along the LHC ring [1]

including the PSB, the PS, and the SPS, proton energy escalates to 450 GeV. Finally, protons are injected into the main LHC ring in two opposing directions, where energy levels are gradually augmented to the desired collision thresholds.

In contrast, the lead (Pb) ion beam is generated from a vapor of lead atoms produced by heating a 2 cm long, 500 mg pure lead sample to 500°C. An electric field is utilized to expel electrons from Pb atoms, yielding Pb ions. Initially accelerated by LINAC 3 to

4.2 MeV per nucleon, additional electron removal occurs within LINAC 3. Subsequent acceleration within the Low Energy Ion Ring (LIER) boosts ion energy to 72 MeV per nucleon, a process unique to heavy ions. Continuing in the PS and SPS, Pb ions' energy is elevated to 5.9 GeV per nucleon and electrons are fully stripped in the PS, while in the SPS, the Pb beam reaches 177 GeV per nucleon before injection into the LHC from two opposing directions.

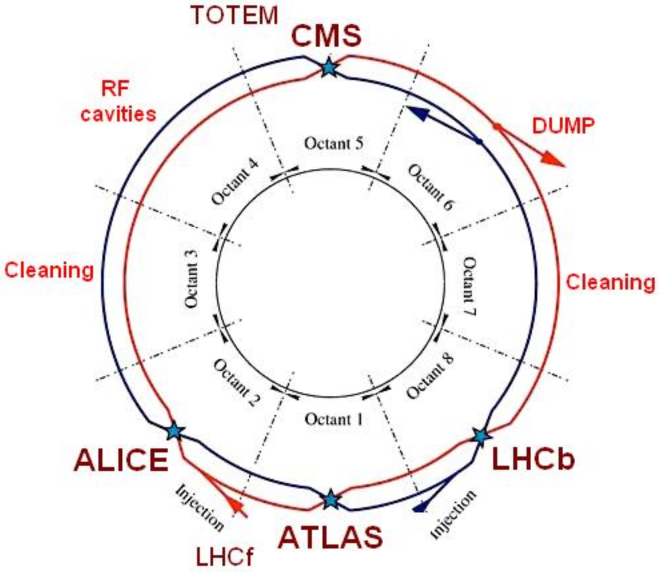
TOTEM
CMS
RF cavities
DUMP
Octant 5
Octant 4
Octant 6
Cleaning
Octant 3
Octant 7
Cleaning
Octant 2
Octant 8
Octant 1
ALICE
LHCb
Injection
injection
ATLAS
LHCf

FIGURE 2.2: Schematic layout of the LHC [2].

Particles enter the LHC ring from two opposing points, specifically points 2 and 8 (Octant 2 and Octant 8). At point 4, the Radio Frequency (RF) system propels the beam forward. Four significant intersections, namely points 1, 2, 5, and 8, mark the meeting places of the two beams, coinciding with the locations of the primary experiments: ATLAS, ALICE, CMS, and LHCb. Point 6 serves as the beam termination site, while at points 3 and 7, the collimation system operates to cleanse the beam by removing beam bunches with considerable spatial dispersion from the center of the bunch. A schematic representation of the operational points within the LHC is provided in Figure 2.2. With the current accelerator facilities at the LHC, the maximum center-of-mass energy attainable is 13.6 TeV for proton-proton collisions and 5.36 TeV per nucleon for heavy-ion collisions.

2.2 The ALICE experiment at LHC

The ALICE detector at the LHC, is specifically designed for conducting experiments involving heavy-ion collisions, with the aim of unraveling the intricacies of nuclear matter formation and evolution during such collisions. This colossal detector spans dimensions of 26 meters in length, 16 meters in width, and 16 meters in height, weighing in at an impressive 10,000 tons and is nestled approximately 56 meters below ground level in the village of St Genis-Pouilly, on the Switzerland-France border. The ALICE detector system is divided into three main categories: central-barrel detectors, forward detectors, and the muon spectrometer. Comprising a total of 19 detector subsystems, as illustrated in Figure 2.3, each subsystem serves distinct purposes within the experimental setup. Among all the detector subsystems, one noteworthy mention is the Photon Multiplicity Detector (PMD). Developed by an Indian group, this detector is specifically designed to investigate photon production in regions with high particle densities in relativistic heavy-ion collisions, particularly in the forward region. Table 2.1 summarizes the positions, η and ϕ acceptances, and functions of the various ALICE detector subsystems. The ALICE detector operates within a carefully chosen right-handed Cartesian coordinate system. Here, the z-axis aligns with the beam direction, with the origin (0, 0, 0) positioned at the center of the Time Projection Chamber (TPC) detector. The muon arm side of the ALICE detector system corresponds to the negative z-axis, while the x and y axes, perpendicular to the z-axis, point towards the LHC center and vertically upward, respectively. The ALICE tracking detectors are placed inside a magnetic field of 0.5 Tesla, parallel to z-axes.

Table 2.1: Overview of the positions, acceptances in terms of pseudorapidity (η) and azimuthal angle (ϕ), and functions of the ALICE detector subsystems [4].

Detector	Position (in cm)	η acceptance	ϕ acceptance (in °)	Purpose
Central barrel detector:				
SPD	$r = 3.9$	$\|\eta\| < 2.0$	$0° < \phi < 360°$	tracking, vertex
	$r = 7.6$	$\|\eta\| < 1.4$	$0° < \phi < 360°$	tracking, vertex
SDD	$r = 15.0$	$\|\eta\| < 0.9$	$0° < \phi < 360°$	tracking, particle identification
	$r = 23.9$	$\|\eta\| < 0.9$	$0° < \phi < 360°$	tracking, particle identification
SSD	$r = 38.0$	$\|\eta\| < 1.0$	$0° < \phi < 360°$	tracking, particle identification
	$r = 43.0$	$\|\eta\| < 1.0$	$0° < \phi < 360°$	tracking, particle identification
TPC	$85 < r < 247$	$\|\eta\| < 0.9$	$0° < \phi < 360°$	tracking, particle identification
TRD	$290 < r < 368$	$\|\eta\| < 0.8$	$0° < \phi < 360°$	tracking, $e^{\pm}$ identification
TOF	$370 < r < 399$	$\|\eta\| < 0.9$	$0° < \phi < 360°$	particle identification
PHOS	$460 < r < 478$	$\|\eta\| < 0.12$	$220° < \phi < 320°$	photons
EMCAL	$430 < r < 455$	$\|\eta\| < 0.7$	$80° < \phi < 187°$	photons
HMPID	$r = 490$	$\|\eta\| < 0.6$	$1° < \phi < 59°$	particle identification
ACORDE	$r = 850$	$\|\eta\| < 1.3$	$30° < \phi < 150°$	cosmics
Forward detector:				
PMD	$z = 367$	$2.3 < \eta < 3.9$	$0° < \phi < 360°$	photons
FMD	$z = 320$	$3.6 < \eta < 5.0$	$0° < \phi < 360°$	charged particles
	$z = 80$	$1.7 < \eta < 3.7$	$0° < \phi < 360°$	charged particles
	$z = -70$	$-3.4 < \eta < -1.7$	$0° < \phi < 360°$	charged particles
V0	$z = 329$	$2.8 < \eta < 5.1$	$0° < \phi < 360°$	charged particles
	$z = -88$	$-3.7 < \eta < -1.7$	$0° < \phi < 360°$	charged particles
T0	$z = 370$	$4.6 < \eta < 4.9$	$0° < \phi < 360°$	time, vertex
	$z = -70$	$-3.3 < \eta < -3.0$	$0° < \phi < 360°$	time, vertex
ZDC	$z = \pm 11300$	$\|\eta\| > 8.8$	$0° < \phi < 360°$	forward neutrons
ZDC	$z = \pm 11300$	$6.5 < \|\eta\| < 7.5$	$\|\phi\| < 10°$	forward protons
ZDC	$z = \pm 730$	$4.8 < \eta < 5.7$	$\|2\phi\| < 32°$	photons
Muon spectrometer:				
MCH	$-1420 < z < -540$	$-4.0 < \eta < -2.5$	$0° < \phi < 360°$	muon tracking
MTR	$-1710 < z < -1610$	$-4.0 < \eta < -2.5$	$0° < \phi < 360°$	muon trigger

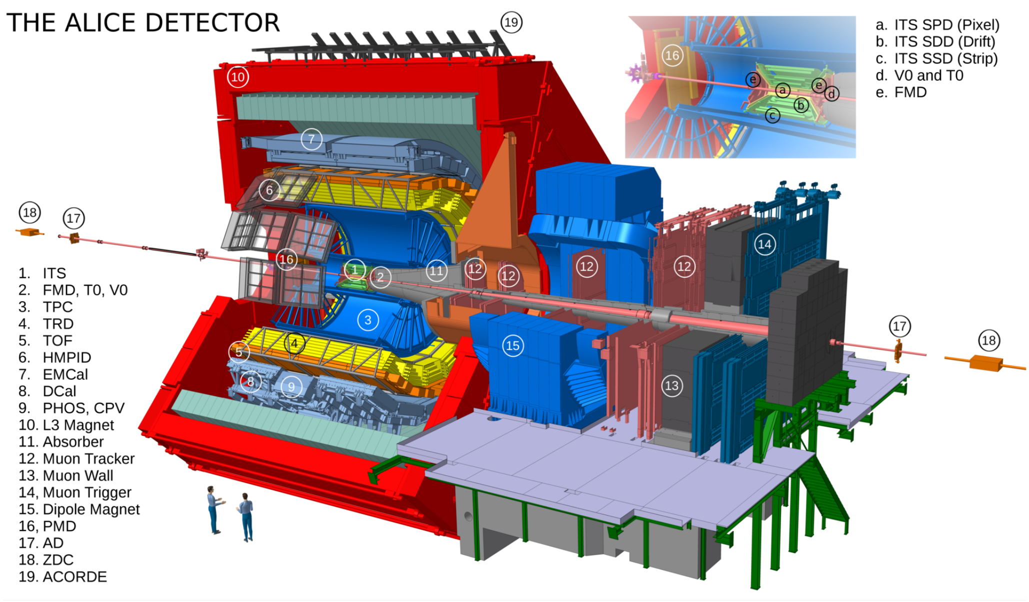
THE ALICE DETECTOR
a. ITS SPD (Pixel)
b. ITS SDD (Drift)
c. ITS SSD (Strip)
d. V0 and T0
e. FMD
1. ITS
2. FMD, T0, V0
3. TPC
4. TRD
5. TOF
6. HMPID
7. EMCal
8. DCal
9. PHOS, CPV
10. L3 Magnet
11. Absorber
12. Muon Tracker
13. Muon Wall
14, Muon Trigger
15. Dipole Magnet
16, PMD
17. AD
18. ZDC
19. ACORDE

FIGURE 2.3: Schematic diagram for the ALICE detector systems [3].

In this thesis Inner Tracking System (ITS) [5], Time Projection Chamber (TPC) [6], Time of Flight (TOF) [7] and V0 detectors are extensively used for the analysis of ALICE data. These detectors are briefly discussed in the following sub-sections.

2.2.1 The Inner Tracking System (ITS)

The Inner Tracking System (ITS) comprises six layers of cylindrical silicon detectors positioned within radii ranging from 3.9 to 43 cm, encircling the beam pipe—an 800 μm thick beryllium cylinder with a radius of 2.9 cm. A visual representation of the silicon detector's geometry is presented in Figure 2.4. Details regarding the η and ϕ acceptance for various layers of the ITS detector are provided in Table 2.1. The primary objectives of the ITS include precisely determining the primary vertex with a resolution better than 100 μm, reconstructing secondary vertices, facilitating particle identification, and tracking particles with very low momentum (less than 200 MeV/c). The ALICE ITS enables the reconstruction of tracks that traverse the inactive TPC region or very low p_{T} tracks that do not extend to the TPC. Consequently, the momentum and angular resolution of tracks reconstructed by the TPC can be enhanced by incorporating data from the ITS.

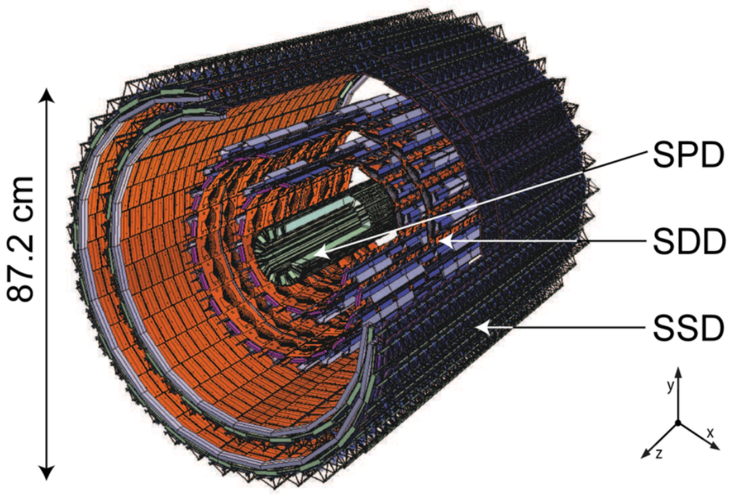

FIGURE 2.4: Layout for the ALICE ITS with Silicon Pixel, Silicon Strip and Silicon Drift detectors are shown [8].

The innermost two layers of the ITS house the Silicon Pixel Detectors (SPD), which primarily serve in determining primary and secondary vertices, capable of functioning efficiently even amidst high track densities of about 50 tracks/cm^3 and in environments with heightened radiation levels. With full azimuthal coverage and a pseudo-rapidity acceptance of $|\eta| < 2.0$, the SPD boasts nearly 9.8 million pixel cells, forming a two-dimensional matrix of reverse-biased silicon-based p-n junction diodes. Each cell within the detector matrix is linked to a corresponding cell on a front-end CMOS chip via a conductive solder ball, with the CMOS chip housing the majority of the readout electronics. Upon detecting a particle signal above the threshold, each pixel chip generates a Fast-OR digital pulse, enabling prompt triggering [9].

The third and fourth layers of the ITS host the Silicon Drift Detectors (SDD), assembled on linear structures referred to as ladders. The SDD, divided into two drift regions, guides electrons in opposing directions under a drift field of 500 V/cm. Charges are collected within each drift region using independent anodes, isolated from the drift voltage via a secondary bias supply. The z-position of a track is deduced from the charge collected along the anode, while the x and y coordinates are reconstructed from the drift time of charges. The signal measured by the SDD is proportional to the energy loss incurred by particles within the detectors, proving valuable for particle identification within the low p_{T}region.

The two outermost layers of the ITS house the Silicon Strip Detectors (SSD), each comprising double-sided strip sensors. The innermost SSD layer comprises 34 ladders, each hosting 22 modules along the beam direction, while subsequent layers consist of 38 ladders, each equipped with 25 modules. Each SSD module incorporates a 1536-strip double-sided silicon sensor, facilitating track position measurement and particle identification through energy loss measurements. Both SSD and SDD feature similar readouts boasting a broad dynamic range, enabling particle identification via energy loss for low-momentum particles down to p_{T} = 100 MeV/c.

2.2.2 The Time Projection Chamber (TPC)

The Time Projection Chamber (TPC) detector serves as the primary tracking device in the ALICE experiment, meticulously measuring the momentum of charged particles with exceptional position resolution. Its design allows for precise track measurements, with transverse plane resolutions ranging from 800 to 1100 μm and resolutions along the z-direction from 1100 to 1250 μm. Spanning a pseudo-rapidity range of $|\eta| < 0.9$ and providing full azimuthal angle coverage, the TPC encompasses an active gas volume within a cylindrical configuration. This gas detector features inner and outer radii of 80 cm and 250 cm, respectively, extending along the beam axis for 500 cm and occupying an active volume of 92 m^3.

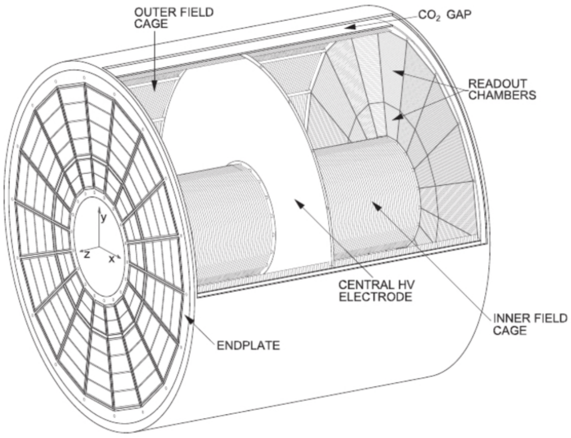

FIGURE 2.5: A schematic layout for the ALICE TPC [10].

Maintaining optimal performance, the TPC employs a gas mixture composed of 90% Ne and 10% CO_2. Within its drift volume, a cylindrical conducting electrode bisects the chamber, creating two segments and establishing a uniform axial electrostatic field of 400 V/cm. This field, parallel to the beam line and directed towards the membrane, guides charged particles through the gas volume. As charged particles traverse the active gas, they ionize and excite gas atoms along their path, resulting in energy loss per unit track length ($\mathrm{d}E/\mathrm{d}x$), contingent upon the particle's mass. The liberated free electrons migrate towards the cylinder's end plates under the influence of the electric field, while ions move towards the centrally positioned high voltage cathode. Drifted electrons undergo amplification via an avalanche process near the anode wires at the end of their path. Reconstruction of the track's x and y positions relies on hits registered on the anode pads at the end plates, while z-coordinates are derived from drift velocity information and the arrival time of drift electrons at the anode plane. The TPC incorporates Multi-Wire Proportional Chambers (MWPCs) at the end plates for signal readout, featuring two end plates, each housing 36 readout chambers arranged across 18 sectors. Each sector comprises an Outer Readout

Chamber (OROC) and an Inner Readout Chamber (IROC). Tracks are reconstructed from 3D space points, allowing determination of the track's transverse momentum (p_T) from its curvature.

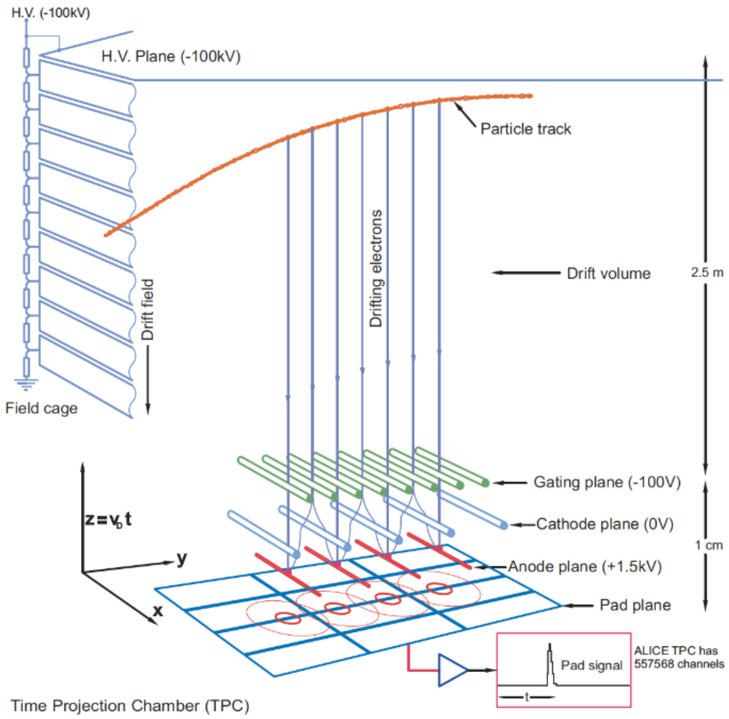
H.V. (-100kV)
H.V. Plane (-100kV)
Particle track
Drifting electrons
Drift volume
2.5 m
Drift field
Field cage
z=v$_D$t
y
x
Gating plane (-100V)
Cathode plane (0V)
Anode plane (+1.5kV)
1 cm
Pad plane
Pad signal
t
ALICE TPC has 557568 channels
Time Projection Chamber (TPC)

FIGURE 2.6: A schematic illustration of the working principle of the TPC [11].

The TPC stands as a pivotal detector within ALICE, crucial for particle identification. Identification of particles within the TPC relies on concurrent measurements of charge, momentum, and specific energy loss for every track passing through its volume. The average energy loss within the TPC is characterized by a modified Bethe-Bloch function, initially formulated by the ALEPH collaboration.

$$f(\beta\gamma) = \frac{p_1}{\beta^{p_4}}\left(p_2 - \beta^{p_4} - ln(p_3 + \frac{1}{(\beta\gamma)^{p_5}})\right). \tag{2.1}$$

Here β and γ are the velocity and lorentz factor for the track, respectively. The parameters p_1 to p_5 are extracted from the fit during each data taking period. The dE/dx distribution as a function of momentum has different bands corresponding to different masses, hence the different particles. The dE/dx resolution is around 5% for pp collisions and around 7% for Pb–Pb collisions across all the p_T ranges [12]. dE/dx of tracks as a function of momentum using the TPC detector in Pb–Pb collisions at $\sqrt{s_{NN}}$= 5.02 TeV has been shown in Fig. 2.7. The solid line corresponds to the expectations from Bethe-Bloch formula.

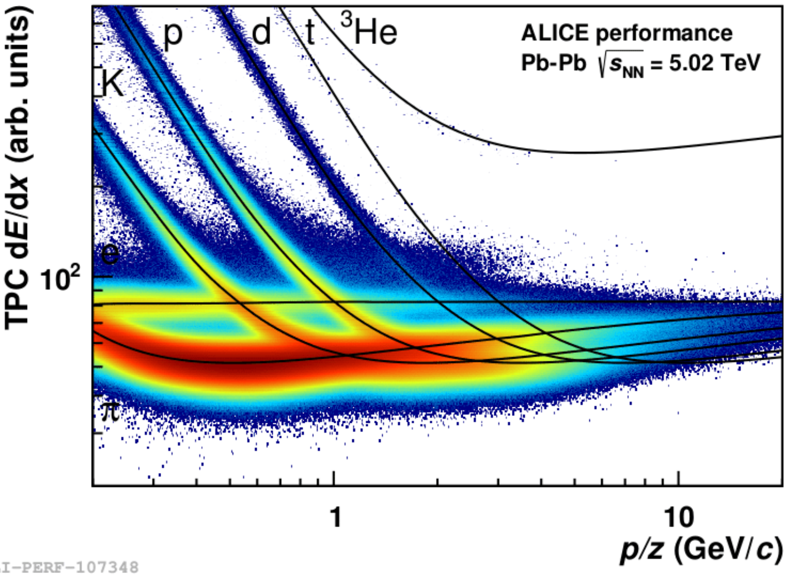

FIGURE 2.7: Average energy loss of tracks as a function of momentum using TPC in Pb–Pb collisions at $\sqrt{s_{NN}}$= 5.02 TeV [13].

2.2.3 The Time Of Flight (TOF) detector

The TOF detector, encircling the Transition Radiation Detector (TRD) within the ALICE experiment, boasts an inner radius of 3.7 m and an outer radius of 3.99 m, with acceptance criteria spanning $|\eta| < 0.9$ and 2π for ϕ. Configured as a cylindrical gas detector containing Multi-gap Resistive Plate Chambers (MRPCs), it functions by ionizing gas when charged particles traverse it, leading to the migration of avalanche electrons towards the electrode. The presence of resistive plates within each gap effectively arrests the movement of these avalanche electrons.

With a remarkably swift signal generation, characterized by a time resolution of approximately 80 ps, the TOF detector is pivotal within ALICE for particle identification in intermediate momentum ranges. It adeptly distinguishes between pions and protons with momenta up to 4 GeV/c, as well as between pions and kaons with momenta up to 2.5 GeV/c.

Particle identification within the TOF detector hinges on measuring a particle's flight time (τ_{TOF}) within the detector. This flight time is determined as the difference between the reconstructed times of hits in the TOF and T0 detectors. The T0 detector comprises two arrays of Cherenkov counters located on opposite sides of the interaction point. It provides high-precision start signal timing for the TOF detector, with a timing resolution of approximately 50 ps. The particle's velocity (β) correlates with its flight time and path length (L) via the equation $\beta = \frac{L}{c\tau_{\mathrm{TOF}}}$, with c representing the speed of light. Additionally, the particle's mass (m_0) is linked to its momentum through the equation:

$$m_0 = \frac{p}{\gamma\beta}. \tag{2.2}$$

Here p is the momentum of the particle, obtained from the TPC and γ is the lorentz factor. Figure 2.8 shows measured β for tracks using the TOF detector as a function of their momenta in Pb–Pb collisions at $\sqrt{s_{\mathrm{NN}}}$= 5.02 TeV.

Fig. 2.9 presents an overview of the ALICE capabilities for the measurement of various hadrons, where the approximate coverage, extending to very low-p_{T}, for different meson and baryon species is shown, together with the corresponding detection techniques.

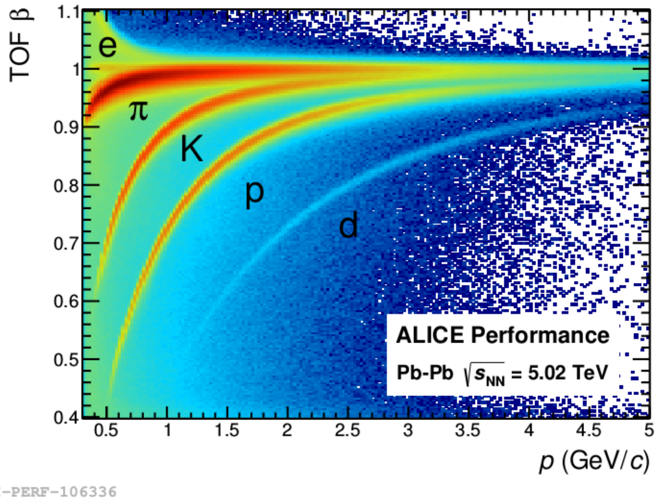

FIGURE 2.8: The distribution of β, obtained through the Time-of-Flight (TOF) detector, is analyzed as a function of the momentum of particles reaching the TOF detector in Pb–Pb collisions at a center-of-mass energy of $\sqrt{s_{\mathrm{NN}}} = 5.02$ TeV [13].

2.2.4 The VZERO (V0) detector

The V0A and V0C are plastic scintillator detectors strategically positioned in the forward directions on both sides of the ALICE collision vertex. They offer full azimuthal angle coverage and encompass specific pseudo-rapidity ranges: $2.8 < \eta < 5.1$ for the V0A detector and $-3.7 < \eta < -1.7$ for the V0C detector. Each of the V0 detectors comprises two arrays of 32 scintillator counters. Photomultipliers (PMTs) collect the scintillating light through Wave-Length Shifting (WLS) fibers.

These V0 detectors serve the purpose of providing a minimum bias trigger during the data acquisition of both proton-proton (pp) and heavy-ion collisions. Additionally, they play a role in discriminating beam-gas interactions by correlating V0A and V0C timing. Moreover, the V0 detectors contribute to determining collision centrality in heavy-ion collisions, establishing multiplicity classes in pp collisions, and measuring the event plane by analyzing the amplitudes recorded by V0A and V0C.

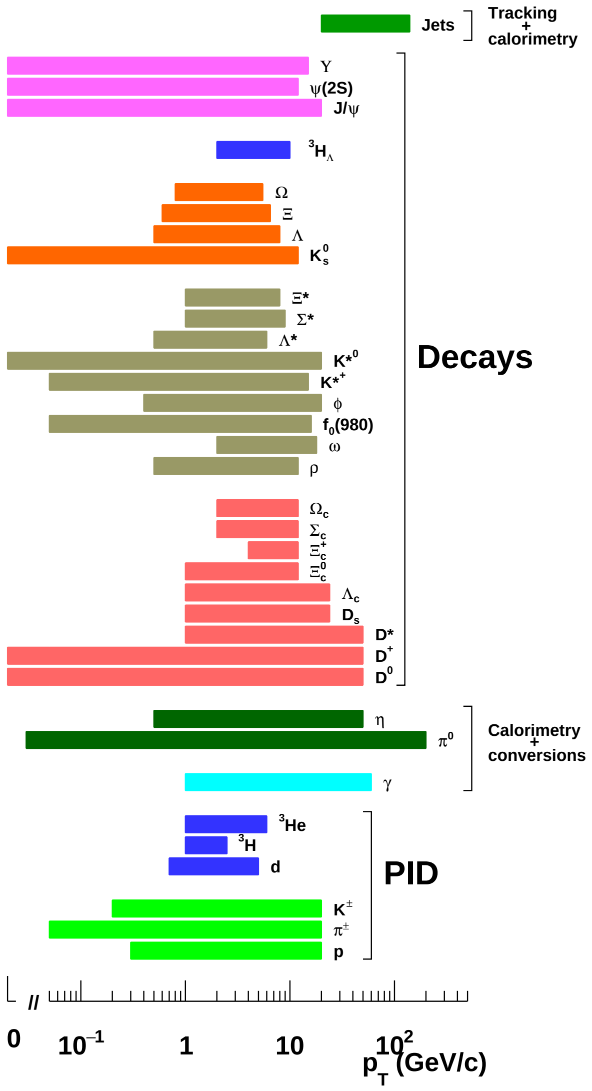

FIGURE 2.9: ALICE PID and reconstruction capabilities of various hadrons as a function of transverse momentum [14].

2.3 ALICE datasets and detector upgrades

The LHC began its collision operations in 2009, initially conducting proton-proton (pp) collisions at a center-of-mass energy ($\sqrt{s}$) of 0.9 TeV. Subsequently, the energy levels

TABLE 2.2: Summary of the LHC Run1 and Run2 physics programmes with the data taking periods.

Collision system	Year	Center of mass energy (TeV)	Integrated luminosity
Pb–Pb	2010, 2011	2.76	75mb^{-1}
	2015, 2018	5.02	800mb^{-1}
Xe–Xe	2017	5.44	0.3 mb^{-1}
p–Pb	2013	5.02	15nb^{-1}
	2016	5.02, 8.16	3nb^{-1}, 25 nb^{-1}
pp	2009-2013	0.9, 2.36, 7, 8	200mb^{-1}, 100nb^{-1}, 1.5pb^{-1}, 2.5pb^{-1}
	2015, 2017	5.02	1.3pb^{-1}
	2015-2018	13	136pb^{-1}

steadily increased, reaching 2.36 TeV and 7 TeV in 2011, followed by 8 TeV in 2012. Concurrently with the pp program, the LHC also conducted lead-lead (Pb-Pb) collisions at $\sqrt{s}$ = 2.76 TeV in November 2010 and 2011, and introduced proton-lead (p-Pb) collisions in early 2013, operating at a center-of-mass energy per nucleon of 5.02 TeV. Following this initial data collection phase, known as Run1 (2009-2013), the LHC underwent an extended shutdown (LS1) for maintenance and enhancements, preparing for a twofold increase in energy, ultimately reaching $\sqrt{s} = 13$ TeV for pp collisions. In the spring of 2015, the second data collection phase, known as Run2, commenced, beginning with pp collisions at a record-breaking center-of-mass energy of 13 TeV, maintained throughout Run2. Similarly, heavy-ion collisions, both Pb-Pb and p-Pb, were conducted at $\sqrt{s_{\mathrm{NN}}}$ = 5.02 TeV and up to 8.16 TeV, respectively. Additionally, a brief Xe-Xe run occurred at $\sqrt{s_{\mathrm{NN}}}$ = 5.44 TeV in October 2017.

This thesis focuses exclusively on the LHC Run2 dataset, encompassing pp collisions at $\sqrt{s}$ = 5.02 TeV and $\sqrt{s}$ = 13 TeV, taken from 2015 to 2018. The Pb-Pb dataset analyzed in this thesis was collected in 2018. Table.2.2 provides a summary of LHC Run1 and Run2 data taking, with the datasets analyzed in this thesis highlighted in red.

Run2 concluded in December 2018 as the LHC entered the Long Shutdown 2 (LS2), a two-year period dedicated to upgrades. The enhancements to the accelerator complex during LS2 are set to significantly surpass the specifications of the existing ALICE setup, particularly in preparation for Runs 3 and 4, focusing on heavy-ion collision parameters. Notably, the Pb-Pb instantaneous luminosity during Run 3 is expected to increase by a factor of 5 to 6, and the minimum-bias Pb-Pb interaction rate to reach approximately 50 kHz in a continuous readout mode, a substantial improvement compared to the rates recorded by ALICE during Run 2. To adapt to these challenging running conditions and achieve various physics goals, ALICE underwent various improvements and incorporated new detectors during LS2. A pivotal enhancement is the complete overhaul of the Inner Tracking System (ITS), representing a significant advancement over the silicon tracker used in Run1 and Run2. The introduction of the new ALPIDE sensor lies at the core of the upgrade. The number of sensor layers around the Interaction Point has increased from 6 to 7, with the innermost layer positioned at a radius of approximately 23 mm from the beam axis, considerably closer than the previous system's inner radius of 39 mm. The hit resolution of the detector is of about 5 μm and the material budget of each three innermost layers is reduced from the value of 1.15% (ITS) to 0.35% (new ITS) of the radiation length. These features provide an improvement by a factor of about three for the track impact parameter resolution in the transverse plane and by a factor of about six in the longitudinal direction. The pseudorapidity coverage of the tracker has expanded from $-1 < \eta < 1$ to $-1.5 < \eta < 1.5$. In addition to the ITS upgrade, the TPC undergoes a transformation by replacing the Multi-Wire Proportional Chambers with continuously operated detectors utilizing Gas Electron Multiplier (GEM) technology [15]. The readout chamber of TOF is also updated. The redesigned readout chambers are designed for continuous operation, capable of reading out all minimum-bias Pb-Pb events delivered by the LHC at the anticipated peak interaction rate of approximately 50 kHz. This substantial improvement is expected to enhance sensitivity to rare probes, considered crucial observables for characterizing the QCD matter produced in heavy-ion collisions. With these improvements, on July 5th, 2022, the LHC resumed operations and initiated its first proton-proton (pp) collisions, achieving a new record energy of 13.6 TeV. This event marked the commencement of the LHC Run3. Subsequently, the first lead-lead (Pb-Pb) run for LHC Run3 occurred on September 20th, 2023 at $\sqrt{s_{\mathrm{NN}}} = 5.36$ TeV.

Bibliography

[1] Ewa Lopienska. "The CERN accelerator complex, layout in 2022. Complexe des accélérateurs du CERN en janvier 2022" (2022). General Photo.

[2] Giuseppe Battistoni et al. "The Application of the Monte Carlo Code FLUKA in Radiation Protection Studies for the Large Hadron Collider". *Prog. Nucl. Sci. Tech.* 2 (2011). Ed. by Toshikazu Takeda, pp. 358–364.

[3] Shreyasi Acharya et al. "Real-time data processing in the ALICE High Level Trigger at the LHC". *Comput. Phys. Commun.* 242 (2019), pp. 25–48. arXiv: `1812.08036 [physics.ins-det]`.

[4] Betty Bezverkhny Abelev et al. "Performance of the ALICE Experiment at the CERN LHC". *Int. J. Mod. Phys. A* 29 (2014), p. 1430044. arXiv: `1402.4476 [nucl-ex]`.

[5] B Abelev et al. "Technical Design Report for the Upgrade of the ALICE Inner Tracking System". *J. Phys. G* 41 (2014), p. 087002.

[6] "Addendum to the Technical Design Report for the Upgrade of the ALICE Time Projection Chamber" (Feb. 2015).

[7] P. Cortese et al. "ALICE: Addendum to the technical design report of the time of flight system (TOF)". *CERN-LHCC-2002-016* ().

[8] K Aamodt et al. "Alignment of the ALICE Inner Tracking System with cosmic-ray tracks". *JINST* 5 (2010), P03003. arXiv: `1001.0502 [physics.ins-det]`.

[9] G. Dellacasa et al. “ALICE technical design report of the inner tracking system (ITS)” (June 1999).

[10] G. Dellacasa et al. “ALICE: Technical design report of the time projection chamber” (Jan. 2000).

[11] Alexander Kalweit. “Production of light flavor hadrons and anti-nuclei at the LHC”. PhD thesis. Darmstadt, Tech. Hochsch., 2012.

[12] Christian Lippmann. “Upgrade of the ALICE Time Projection Chamber” (Mar. 2014).

[13] R. Schicker. “Overview of ALICE results in pp, pA and AA collisions”. *EPJ Web Conf.* 138 (2017). Ed. by S. Bondarenko, V. Burov, and A. Malakhov, p. 01021. arXiv: `1701.04810 [nucl-ex]`.

[14] “The ALICE experiment – A journey through QCD” (Nov. 2022). arXiv: `2211.04384 [nucl-ex]`.

[15] F. Sauli. “GEM: A new concept for electron amplification in gas detectors”. *Nucl. Instrum. Meth. A* 386 (1997), pp. 531–534.

CHAPTER 3

Search for Chiral Magnetic Wave in heavy-ion collisions

Contents

3.1 Data sample, event and tracks selections 74
3.2 Detector acceptance correction 76
3.3 Analysis details 78
3.4 Systematic uncertainties 84
3.5 Results 86
3.6 Summary 93

The large initial magnetic field together with the presence of a non-zero electric and axial charge density in the matter formed in heavy-ion collisions leads to vector and axial currents called the Chiral Magnetic Effect (CME) and Chiral Separation Effect (CSE), respectively [1–6]. Their coupling gives rise to a collective excitation of the QGP called the Chiral Magnetic Wave (CMW) [7, 8]. The CMW phenomenon is essential to provide insights into the strong interaction in QCD, the properties of the quark–gluon plasma, and the topological characteristics of the early universe, offering a deeper understanding of fundamental physics in high-energy collisions. The experimental signature of the CMW is an electric charge-dependent elliptic flow of hadrons. Measurements of the charge-dependent anisotropic flow coefficients are carried out in Pb–Pb collisions at center-of-mass energy per nucleon–nucleon collision $\sqrt{s_{\mathrm{NN}}} = 5.02$ TeV to probe the CMW phenomenon. In particular, the slope of the normalized difference in elliptic (v_2) and triangular (v_3) flow coefficients of positively and negatively charged particles as a function of their event-wise normalized number difference, is reported for inclusive and identified particles.

$$\Delta v_n^{\mathrm{Norm}} = \frac{v_n^- - v_n^+}{(v_n^- + v_n^+)/2} \propto r_n^{\mathrm{Norm}} A_{\mathrm{ch}}, \tag{3.1}$$

where $n = 2$ or 3 and $A_{\mathrm{ch}}$is given by

$$A_{\mathrm{ch}} = \frac{(N^+ - N^-)}{(N^+ + N^-)}, \tag{3.2}$$

with N^+ (N^-) representing the counts of positively (negatively) charged hadrons measured in a given event. Furthermore using the Event Shape Engineering technique the fraction of CMW contribution (f_{CMW}) along with its upper limit is extracted at LHC energies.

3.1 Data sample, event and tracks selections

The analysis utilized data collected with the ALICE apparatus during the 2018 LHC Pb–Pb run at $\sqrt{s_{\mathrm{NN}}} = 5.02$ TeV. Only events featuring a reconstructed primary vertex (V_z) within ± 10 cm of the nominal interaction point along the beam direction (z axis of the ALICE reference frame) were considered. Centrality intervals were established based on percentiles of the hadronic Pb–Pb cross section, determined by the sum of the V0 signal amplitudes [9]. Central and semicentral Pb–Pb collisions were distinguished online using thresholds on the V0 signal amplitudes, resulting in two distinct trigger classes (central and semicentral triggers). The analysis encompassed various centrality intervals, ranging from 0–5% for the most central collisions to 50–60% for peripheral collisions. The total number of events analyzed after event selection amounted to approximately 240 million.

Charged particles are reconstructed using information from the TPC and the ITS within the pseudorapidity range $|\eta| < 0.8$ and transverse momentum range $0.2 < p_{\mathrm{T}} < 10$ GeV/c to determine A_{ch}. For the measurement of flow coefficients, charged particles are limited to $0.2 < p_{\mathrm{T}} < 2.0$ GeV/c. Tracks are selected with a minimum of 70 TPC space points (out of a maximum of 159), and χ^2 per TPC cluster < 2.5 for the momentum fit in the TPC. To mitigate contamination from secondary particles, such as those originating from weak decays, conversions, and secondary hadronic interactions in the detector material, only tracks with a maximum distance of closest approach (DCA) to the reconstructed primary vertex in the transverse direction ($|\mathrm{DCA_{xy}}| < 2.4$ cm) and the longitudinal direction ($|\mathrm{DCA_{z}}| < 3.2$ cm) are accepted. Furthermore, tracks are required to have at least one hit in the two SPD layers. Identification of charged pions, kaons, and (anti)protons is based on the difference between measured and expected values of dE/dx in the TPC and time of flight to the TOF detector, expressed in units of resolution ($|\mathrm{n}\sigma|_{\mathrm{TPC}}$, $|\mathrm{n}\sigma|_{\mathrm{TOF}}$), and applying a selection on the number of accepted nσ (see Table 3.1). Additionally, tracks without TOF information with p_{T} greater than 0.5 GeV/c for pions, 0.45 GeV/c for kaons, and 0.6 GeV/c for protons are rejected. All identified particle species are required to fall within the rapidity range $|y| < 0.5$. The tracking efficiency calculated as ratio of number of reconstructed charged particles to generated charged particles in Monte-Carlo simulation with exactly same selections as in real data are shown in Fig. 3.1 and Fig. 3.2. Moreover, purity for all the particles is calculated using reconstructed Monte Carlo simulations.

Exactly same selections as used in real data has been used and is defined as,

$$\text{Purity} = \frac{\text{Numberofparticles(withPDGcode)}}{\text{Numberofparticles(with}|\text{n}\sigma|_{\text{TPC}}\text{and}|\text{n}\sigma|_{\text{TOF}})} \tag{3.3}$$

These criteria guarantee a purity exceeding 90% for all particle species across the entire range of p_{T} values considered in the analysis. The purity for pions and protons are shown in Fig. 3.3.

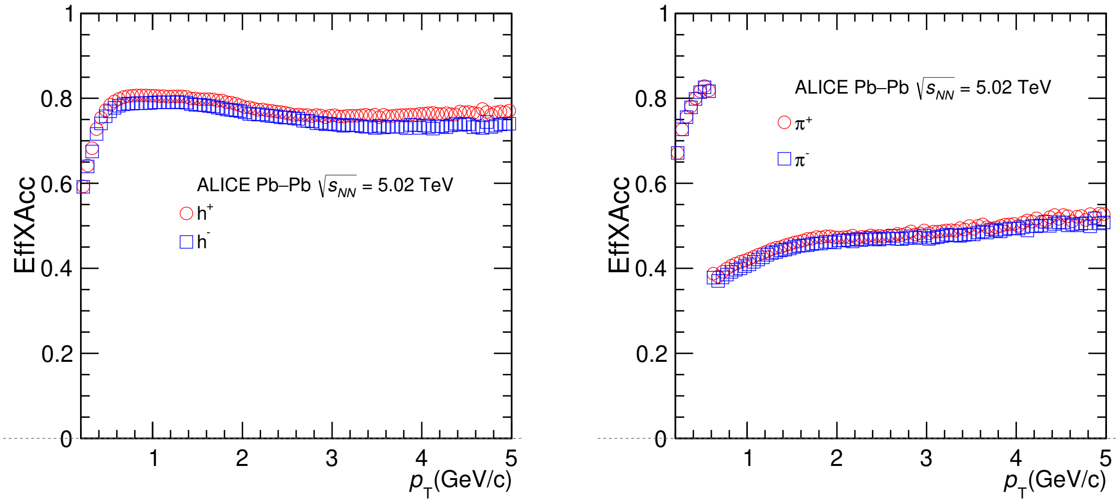

FIGURE 3.1: Left panel figure shows the tracking efficiency for charged unidentified hadrons and right panel shows the same for pions in Pb–Pb collisions at $\sqrt{s_{\mathrm{NN}}}$= 5.02 TeV. Red markers are for particles and blue for their corresponding antiparticles.

3.2 Detector acceptance correction

The observable for CMW measurement is v_2, which reflects the system's anisotropy in heavy-ion collisions. However, experimental detectors have finite acceptance in the laboratory frame, leading to anisotropic particle distributions unrelated to the true anisotropic flow originating from the initial spatial anisotropy of the collision system, which we intend to measure. Therefore, it is crucial to flatten the azimuthal distribution before conducting any measurements. The most commonly employed method for this correction involves

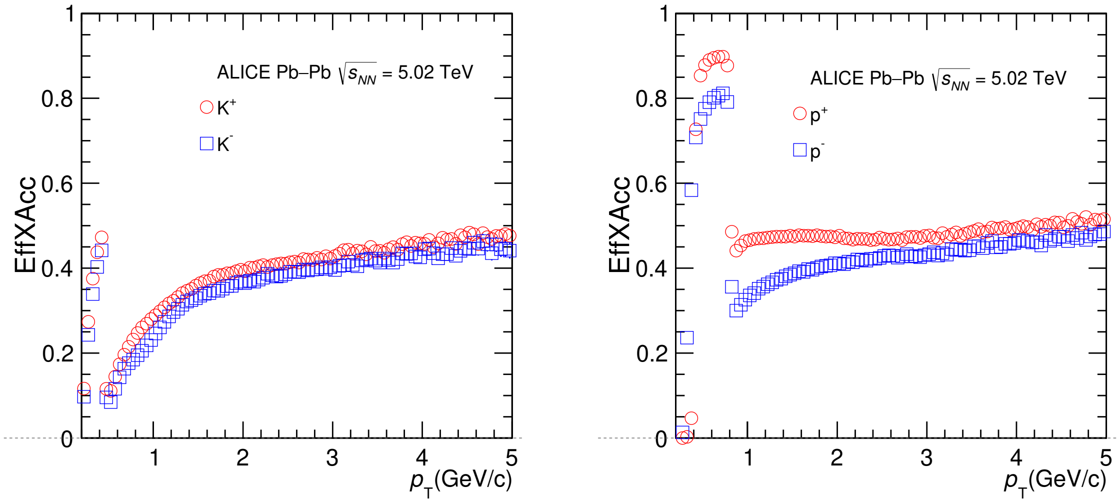

FIGURE 3.2: Left panel figure shows the tracking efficiency for charged kaons and right panel shows the same for protons in Pb–Pb collisions at $\sqrt{s_{\rm NN}}$= 5.02 TeV. Red markers are for particles and blue for their corresponding antiparticles.

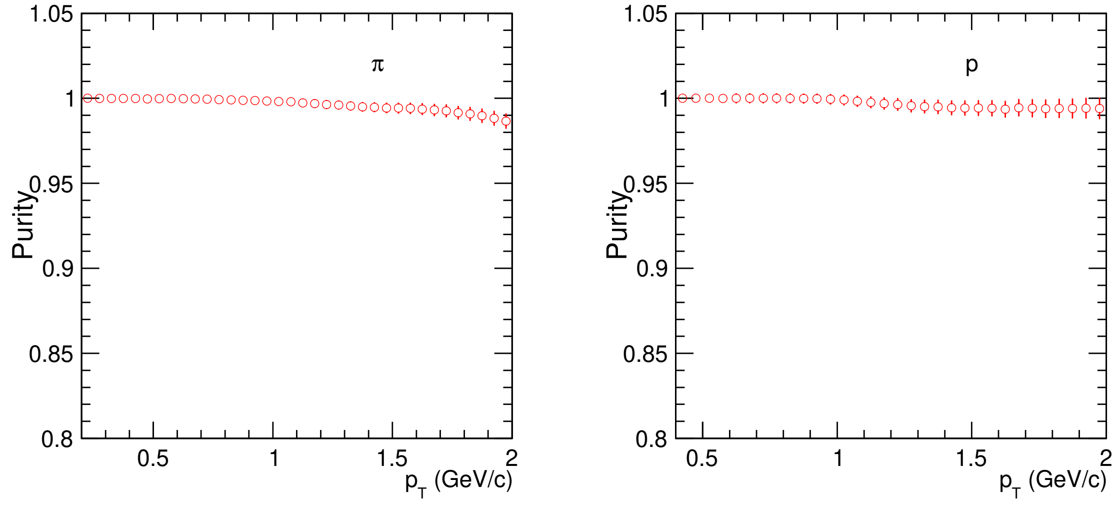

FIGURE 3.3: Left panel figure shows the purity for pions and right panel for protons in Pb–Pb collisions at $\sqrt{s_{\rm NN}}$= 5.02 TeV.

using the particle distribution itself as a means to correct for acceptance effects. In this approach, the 3D (η,ϕ,$\mathrm{V_z}$) azimuthal distribution of particles is accumulated in the laboratory frame, and then the inverse of this distribution is utilized as weights in the calculation of the flow Q-vectors (as described in section 4.2). The azimuthal distribution of charged particles before and after correction is depicted in Figure 3.4.

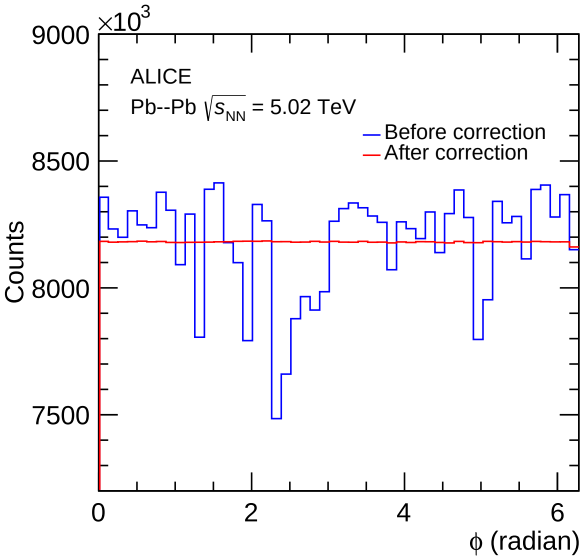

FIGURE 3.4: Azimuthal distribution of charged particles before and after acceptance correction in Pb–Pb collisions at $\sqrt{s_{\mathrm{NN}}}$ = 5.02 TeV.

3.3 Analysis details

In this investigation, we ascertain the second and third-order Fourier coefficients using the Q-cumulant method [10]. Flow characterizes the azimuthal relationship between outgoing particles and the reaction plane. However, these correlations involve additional elements such as resonance decay and quantum correlations, commonly termed non-flow effects [11]. To mitigate these influences, sub-events (labeled A and B) are constructed with designated pseudorapidity intervals between them.

3.3.1 Q-Cumulant method for flow coefficients calculations

In this analysis, the flow harmonics are measured from two particle correlations.The cumulants are expressed in terms of magnitude of correspnding flow vector Q_n [12]:

$$Q_n \equiv \sum_{i=1}^{M} w(i) e^{in\phi_i} \tag{3.4}$$

where M is the number of particles in an event and ϕ_i labels the azimuthal angle of ith particle in a fixed coordinate system in a laboratory, n is the order of the flow coefficient, $w(i)$ is the corresponding track weight which is the product of tracking efficiency and ϕ-weight for each track as described in section 3.2.

The single event average of two particle correlations can then be formulated as

$$\langle 2 \rangle = \frac{|Q_n|^2 - M}{M(M-1)} \tag{3.5}$$

In the next step we average over all events and is given as

$$\langle\langle 2 \rangle\rangle = \frac{\sum_{i=1}^{N} M_i \left(M_i - 1\right) \times \langle 2 \rangle_i}{\sum_{i=1}^{N} M_i \left(M_i - 1\right)} \tag{3.6}$$

The two particle correlator can then be written as

$$c_n\{2\} = \langle\langle 2 \rangle\rangle \tag{3.7}$$

and the reference flow $v_n$can be obtained directly as

$$v_n\{2\} = \sqrt{c_n\{2\}} \tag{3.8}$$

In order to measure differential flow of particle of interest (POI) one more vector needs to be constructed. For particles labelled as POI

$$p_n \equiv \sum_{i=1}^{m_p} w(i) e^{in\phi_i} \tag{3.9}$$

Then the reduced single and double event average two particle correlations are

$$\langle 2' \rangle = \frac{p_n Q_n^*}{m_p M} \tag{3.10}$$

$$\langle\langle 2'\rangle\rangle = \frac{\sum_{i=1}^{N}\left(w_{\langle 2'\rangle}\right)_i \langle 2'\rangle_i}{\sum_{i=1}^{N}\left(w_{\langle 2'\rangle}\right)_i} \tag{3.11}$$

where multiplicity weights are $w_{<2'>} = m_p M$ and m_p is the multiplicity of POI for a given event and Q_n^* is the complex conjugate of Q_n. The two particle differential cumulant is given by

$$d_n\{2\} = \langle\langle 2^{'}\rangle\rangle \tag{3.12}$$

The nth harmonic flow is thus calculated as

$$v'_n\{2\} = \frac{d_n\{2\}}{\sqrt{c_n\{2\}}} \tag{3.13}$$

The measurements are performed using the two-particle cumulant method [10] with a pseudorapidity gap of $|\Delta\eta| > 0.4$ to suppress non-flow, i.e. correlations not related to the reaction plane [13]. For calculating reference flow with pseudorapidity gap, we use Eq. 3.14

$$\langle 2\rangle = \frac{Q_n^A \cdot Q_n^{B^*}}{M_A M_B} \tag{3.14}$$

where Q_n^A and Q_n^B are the flow vectors calculated from reference particles for subevents A and B. M_A and M_B are multiplicities of these two subevents. Hence the reduce two particle correlation are

$$\begin{aligned}\langle 2'\rangle^A &= \frac{p_n^A \cdot Q_n^{B^*}}{m_p^A M_B}\\ \langle 2'\rangle^B &= \frac{p_n^B \cdot Q_n^{A^*}}{m_p^B M_A}\end{aligned} \tag{3.15}$$

Then v_n can be calculated by following Eq. 3.13 where $d_n\{2\} = \langle\langle 2^{'}\rangle\rangle$, and $c_n\{2\} = \langle\langle 2\rangle\rangle$.

Correlation between like/unlike charges

The reference particles can be further divided into positive(R^+) and negative(R^-) charges

$$Q_n = \sum_i e^{in\phi_i} = \sum_{i\in\{R^+\}} e^{in\phi_i} + \sum_{i\in\{R^-\}} e^{in\phi_i} \equiv Q_n^+ + Q_n^- \tag{3.16}$$

So the differential flow is given as

$$\begin{aligned} d_n\left\{2|\pi^\pm R\right\} =& \frac{p_n^\pm Q_n^*}{m_\pm M} = \frac{p_n^\pm\left(Q_n^{+*} + Q_n^{-*}\right)}{m_\pm\left(N_+ + N_-\right)} \\ =& \frac{m_\pm N_+\left(\frac{p_n^\pm Q_n^+}{m_\pm N_+}\right) + m_\pm N_-\left(\frac{p_n^\pm Q_n^{-*}}{m_\pm N_-}\right)}{m_\pm\left(N_+ + N_-\right)} \\ =& \frac{N_+ d_n\left\{2|\pi^\pm R^+\right\} + N_- d_n\left\{2|\pi^\pm R^-\right\}}{N_+ + N_-} \end{aligned} \tag{3.17}$$

where $d_n\left\{2|\pi^\pm R^+\right\} \equiv \frac{p_n^\pm Q_n^{+*}}{m_\pm N_+}$, $d_n\left\{2|\pi^\pm R^-\right\} \equiv \frac{p_n^\pm Q_n^{-*}}{m_\pm N_-}$

Finally, we have

$$\begin{aligned} d_n\left\{2|\pi^\pm R\right\} &= \frac{N_+ d_n\left\{2|\pi^\pm R^+\right\} + N_- d_n\left\{2|\pi^\pm R^-\right\}}{N_+ + N_-} \\ &= \frac{d_n\left\{2|\pi^\pm R^+\right\} + d_n\left\{2|\pi^\pm R^-\right\}}{2} + \frac{d_n\left\{2|\pi^\pm R^+\right\} - d_n\left\{2|\pi^\pm R^-\right\}}{2} A_{ch} \end{aligned} \tag{3.18}$$

The correlations between like-sign and unlike-sign particles may exhibit distinct non-flow backgrounds, potentially leading to a spurious term dependent on A_{ch} that could mimic the CMW signal. To eliminate this trivial term, a single charge sign reference is utilized instead of considering all charged hadrons as references as suggested in Ref. [14]. For instance, positive and negative particles are separately used as references to calculate v_n individually, and then the final v_n is computed as:

$$\bar{v}_n^\pi \equiv \frac{v_n^\pi\left\{2; h^+\right\} + v_n^\pi\left\{2; h^-\right\}}{2} \tag{3.19}$$

3.3.2 A_{ch} estimation and correction

The left panel of Fig. 3.5 illustrates an example of the measured raw A_{ch} distribution for the 40–50% centrality interval. This raw A_{ch} distribution is divided into ten intervals, each approximately containing an equal number of events, delineated by dashed lines in the left panel of Fig. 3.5. To compensate for the finite detector acceptance and the reconstruction and identification efficiency of charged hadrons, corrections are applied to the raw $A_{\rm ch}$ values. Utilizing simulations based on the HIJING event generator [15] combined with the GEANT3 model [16] for particle transport in the detector material, a correlation between the raw and true values of $A_{\rm ch}$ is established. A linear fit is employed to this correlation, enabling the mapping of the raw $A_{\rm ch}$ to the true $A_{\rm ch}$, as depicted in the right panel of Fig. 3.5. The slope of this linear fit increases with increase in centrality intervals. Within each $A_{\rm ch}$ interval, the flow coefficients v_2 and v_3 are separately measured for positively and negatively charged hadrons (both identified and inclusive). Subsequently, the normalized slope parameters, $r_2^{\rm Norm}$ and $r_3^{\rm Norm}$, are calculated for various centrality intervals using Eq. 3.1 with the $A_{\rm ch}$ values corrected for detector effects, as described above.

3.3.3 Event Shape Engineering technique

The ESE technique is also utilized to assess the potential contribution of the CMW signal to the ΔIC, as suggested in Ref. [18]. Specifically, the remaining magnitude of this observable as v_2 approaches zero aids in separating the potential CMW signal from background contributions [19]. The second-order reduced flow vector q_2 is employed for event shape selection, following the approach outlined in Ref. [19]. It is defined as

$$q_2 = Q_2/\sqrt{\rm M}, \tag{3.20}$$

where Q_2 is the magnitude of the flow vector as defined above and M is the multiplicity. The Q_2 is calculated from the azimuthal distribution of the energy deposited in the V0C detector. To address the non-uniform response of the detector, the V0 detector undergoes calibration through two methods: gain equalization and recentering. Gain equalization

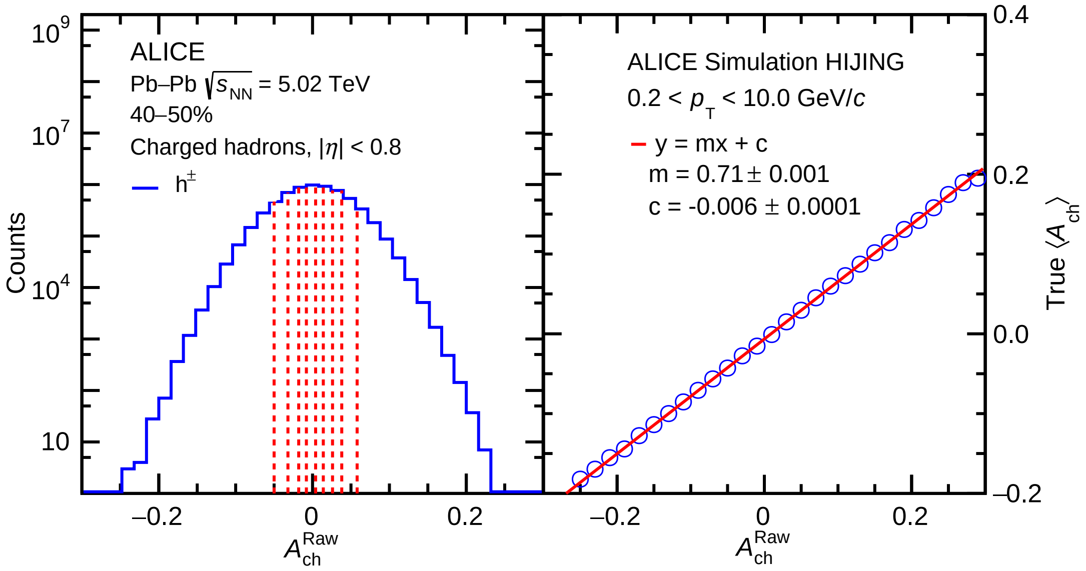

FIGURE 3.5: (Left panel): Raw A_{ch} distribution in Pb–Pb collisions at $\sqrt{s_{\text{NN}}}$ = 5.02 TeV for the 40–50% centrality interval. Red dotted lines depict the edges of the ten A_{ch} classes. (Right panel): Correlation between true and raw A_{ch} obtained from HIJING simulations combined with a GEANT3 detector model for Pb–Pb collisions at $\sqrt{s_{\text{NN}}}$ = 5.02 TeV in the 40–50% centrality interval. The figure is taken from [17].

ensures a uniform mean multiplicity distribution across the eight azimuthal sectors within each ring, while recentering corrects systematic shifts in the mean values of the Q_2 vector components [20]. The calibrated V0C event plane angle distribution is depicted in Fig. 3.6. The coefficient p_1 gives the flow contribution from the event plane itself. One can observe that after calibration the event plane is fairly flat having the coeffcient negative. Within each centrality interval, ten q_2 ranges are investigated, covering event classes ranging from the most elliptical to the most isotropic. For each centrality class, v_2, A_{ch} and their covariance is calculated in each q_2 intervals. Finally the ΔIC is computed as a function of v_2.

To distinguish between the LCC background contributions and the potential CMW signal, the ΔIC's dependence on v_2 (defined in Section 1.8.1) is modeled with a linear function. The CMW fraction in the ΔIC is then determined by comparing the observable

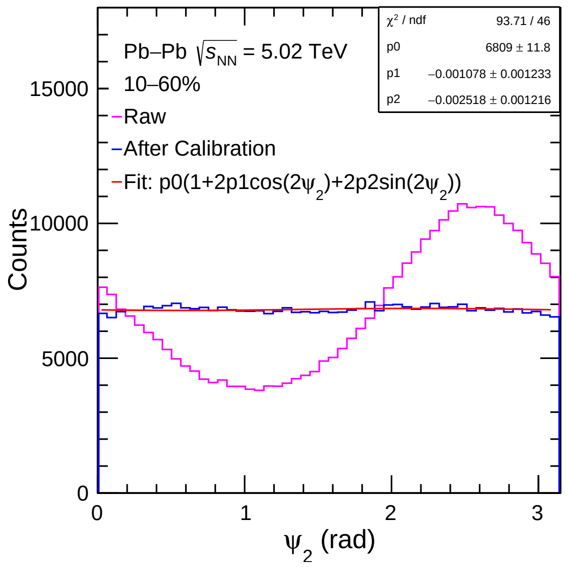

FIGURE 3.6: Calibrated V0 event plane angle in Pb–Pb collisions at $\sqrt{s_{\mathrm{NN}}}$ = 5.02 TeV in 10–60% centrality interval. The red line shows the fit to the event plane angle distribution after calibration.

at zero v_2 to that at finite v_2.

$$f_{\mathrm{CMW}} \equiv \frac{b}{a\,\langle v_2\rangle + b}, \tag{3.21}$$

where a and b are the slope and the intercept of the linear function, respectively, and $\langle v_2\rangle$ is the average value over the measured v_2 range.

3.4 Systematic uncertainties

To evaluate the systematic uncertainties on the normalized slopes and f_{CMW}, adjustments are made to the event and track selection criteria from their default settings. Table 3.1 outlines the variables used in the selections, along with their default and varied values. These adjustments involve changing the range of the z coordinate of the primary vertex from $|V_z| \leq 10$ cm to $|V_z| \leq 8$ cm to assess the detector acceptance dependence. The impact of track-quality selections is examined by adjusting the minimum number of TPC space points from 70 to 80 and varying the χ^2_{TPC} per TPC space point from 2.5 to 2.0. To assess the influence of contamination from secondary particles, stricter selection criteria than the default ones are applied to both DCA_{xy} and DCA_z. Variations in the pseudorapidity gap ($\Delta\eta$) from $|\Delta\eta| \geq 0.4$ to $|\Delta\eta| \geq 0.6$ for charged hadrons and pions, and to $|\Delta\eta| \geq 0.5$ for kaons and protons, are made to estimate the effects of non-flow contributions. Variations in the particle identification criteria, specifically $|\mathrm{n}\sigma|_{\mathrm{TPC}}$ and $|\mathrm{n}\sigma|_{\mathrm{TOF}}$, are implemented to account for potential systematic effects in the particle identification process. The reconstruction efficiency for charged hadrons is assessed using only pions, kaons, and protons, with observed differences incorporated as systematic uncertainties. For each systematic variation, corrections for non-uniform acceptance and reconstruction efficiency of inclusive and identified charged hadrons are estimated using collision data and Monte Carlo (MC) simulations. To identify statistically significant systematic sources, the ratio $B = Y/\sigma_{\mathrm{B}}$ is computed, where Y represents the difference between the results with default and modified selections, and σ_B is the error of the difference calculated as $\sqrt{|\sigma^2_{\mathrm{default}} \pm \sigma^2_{\mathrm{varied}}|}$, where "+" indicates uncorrelated and "-" denotes correlated sources. The statistical uncertainties $\sigma_{\mathrm{default}}$ and σ_{varied} are estimated separately for the results using default and varied event/particle selection criteria, employing a subsampling method with 20 equally sized independent samples. Each variation showing a significant difference from the nominal result by more than $1\sigma_{\mathrm{B}}$, following the guidelines from Ref. [21], is considered a source of systematic uncertainty. The barlow values for all the variations are given in Appendix. A.1. The total systematic uncertainties are then derived by summing the different contributions in quadrature. Table 3.2 summarizes the maximum magnitude of the systematic uncertainties on the normalized slopes over all the centrality intervals from each individual source which passes the criteria described above. The systematic sources for the f_{CMW} observable are only a few, namely Primary V_z, χ^2_{TPC}/cluster, and DCA selections. The associated uncertainties are 0.024, 0.047, and 0.068, respectively.

TABLE 3.1: Nominal event and track selection criteria and the corresponding variations used for the estimation of the systematic uncertainties.

(No.) Source	Default Value	Variations
(1) Primary $\lvert V_z \rvert$	< 10 cm	<8 cm
(2) TPC space points	>70	>80
(3) χ^2_{TPC}/cluster	<2.5	<2.0
(4) DCA$_{xy}$ (DCA$_z$)	<2.4 (3.2) cm	$<7(0.0026 + (0.005/p_{\mathrm{T}}^{1.01}))$, (2.0) cm
(5) $\lvert\Delta\eta\rvert$	>0.4	>0.6 (0.5 for K and p)
(6) PID (π)	-	-
$0.2 < p_{\mathrm{T}} < 0.5$ (GeV/c)	$\lvert n\sigma\rvert_{\mathrm{TPC}} < 3$	$\lvert n\sigma\rvert_{\mathrm{TPC}} < 2.5$
$0.5 < p_{\mathrm{T}} < 2.0$ (GeV/c)	$\sqrt{\lvert n\sigma\rvert^2_{\mathrm{TPC}} + \lvert n\sigma\rvert^2_{\mathrm{TOF}}} < 3$	$\sqrt{\lvert n\sigma\rvert^2_{\mathrm{TPC}} + \lvert n\sigma\rvert^2_{\mathrm{TOF}}} < 3$
PID (K)	-	-
$0.2 < p_{\mathrm{T}} < 0.45$ (GeV/c)	$\lvert n\sigma\rvert_{\mathrm{TPC}} < 3$	$\lvert n\sigma\rvert_{\mathrm{TPC}} < 2.5$
$0.45 < p_{\mathrm{T}} < 2.0$ (GeV/c)	$\sqrt{\lvert n\sigma\rvert^2_{\mathrm{TPC}} + \lvert n\sigma\rvert^2_{\mathrm{TOF}}} < 2.5$	$\sqrt{\lvert n\sigma\rvert^2_{\mathrm{TPC}} + \lvert n\sigma\rvert^2_{\mathrm{TOF}}} < 2$
PID (p)	-	-
$0.5 < p_{\mathrm{T}} < 0.6$ (GeV/c)	$\lvert n\sigma\rvert_{\mathrm{TPC}} < 3$	$\lvert n\sigma\rvert_{\mathrm{TPC}} < 3.5$
$0.6 < p_{\mathrm{T}} < 2.0$ (GeV/c)	$\sqrt{\lvert n\sigma\rvert^2_{\mathrm{TPC}} + \lvert n\sigma\rvert^2_{\mathrm{TOF}}} < 3.0$	$\sqrt{\lvert n\sigma\rvert^2_{\mathrm{TPC}} + \lvert n\sigma\rvert^2_{\mathrm{TOF}}} < 3.5$
(7) Efficiency calculation	All unidentified charged hadrons	Identified charged hadrons (π+K+p)

3.5 Results

3.5.1 A_{ch} dependence of v_n and centrality dependence of the slope r_n^{Norm}

The top left and top right panels of Fig. 3.7 display the v_2 and v_3 values for positively and negatively charged hadrons plotted against A_{ch} for Pb–Pb collisions at $\sqrt{s_{\mathrm{NN}}} = 5.02$ TeV within the 40–50% centrality range. A noticeable decreasing trend in v_2 is observed for positively charged hadrons as A_{ch} increases, while the trend reverses for negatively charged hadrons. Similar trends are discernible for the v_3 coefficient, albeit with larger fluctuations.

TABLE 3.2: Maximum systematic uncertainty (absolute value) on normalized slope per particle species over all centrality intervals from individual sources (see Table 3.1 for an explanation of each source).

Sources	inclusive ($h^{\pm}$)		$\pi^{\pm}$		$K^{\pm}$		p+$\overline{\text{p}}$	
	r_2^{Norm}	r_3^{Norm}	r_2^{Norm}	r_3^{Norm}	r_2^{Norm}	r_3^{Norm}	r_2^{Norm}	r_3^{Norm}
(1) Primary V_z	0.014	0.03	0.012	0.03	0.019	0.12	0.02	0.021
(2) TPC space points	0.003	0.033	0.01	0.033	0.033	0.23	0.036	0.14
(3) χ^2_{TPC}/cluster	0.009	0.047	0.0002	0.047	0.02	0.31	0.035	0.18
(4) DCA$_{xy}$ (DCA$_z$)	0.005	0.044	0.023	0.044	0.02	0.18	0.026	0.19
(5) $\|\Delta\eta\|$	0.013	0.09	0.018	0.09	0.017	0.31	0.052	0.11
(6) PID	-	-	0.05	0.05	0.013	0.11	0.004	0.13
(7) Efficiency	0.032	0.049	-	-	-	-	-	-

Shaded bands in Fig. 3.7 represent the correlated uncertainties among the hadrons and across A_{ch}intervals. The bottom left and right panels of Fig. 3.7 illustrate the normalized difference between v_2 and v_3 for positive and negative charged particles, respectively, as a function of A_{ch}. These differences, as defined in Eq. 3.1, are fitted with linear functions to determine the slopes, r_2^{Norm} and r_3^{Norm}. Notably, besides observing a positive slope for $\Delta v_2/\langle v_2\rangle$, a non-zero slope is also identified for $\Delta v_3/\langle v_3\rangle$ (i.e., $r_3^{\text{Norm}} > 0$), primarily attributable to background correlations. This non-zero r_3^{Norm} value suggests the presence of similar background contributions in r_2^{Norm}, which must be accounted for to accurately quantify the CMW effect.

Figure 3.8 shows r_2^{Norm} (red markers) and r_3^{Norm} (green markers) as a function of centrality for inclusive charged hadrons in Pb–Pb collisions at $\sqrt{s_{\text{NN}}}$ = 5.02 TeV. Despite the considerable uncertainties, r_3^{Norm} appears to be of similar magnitude to r_2^{Norm} across much of the centrality spectrum. The anticipated development of CMW aligns with the direction of the magnetic field **B**, approximately perpendicular to the second-order event plane rather than the third order. The third-order plane exhibits minimal correlation with the second-order event plane [24–26]. Consequently, the non-zero value of r_3^{Norm}

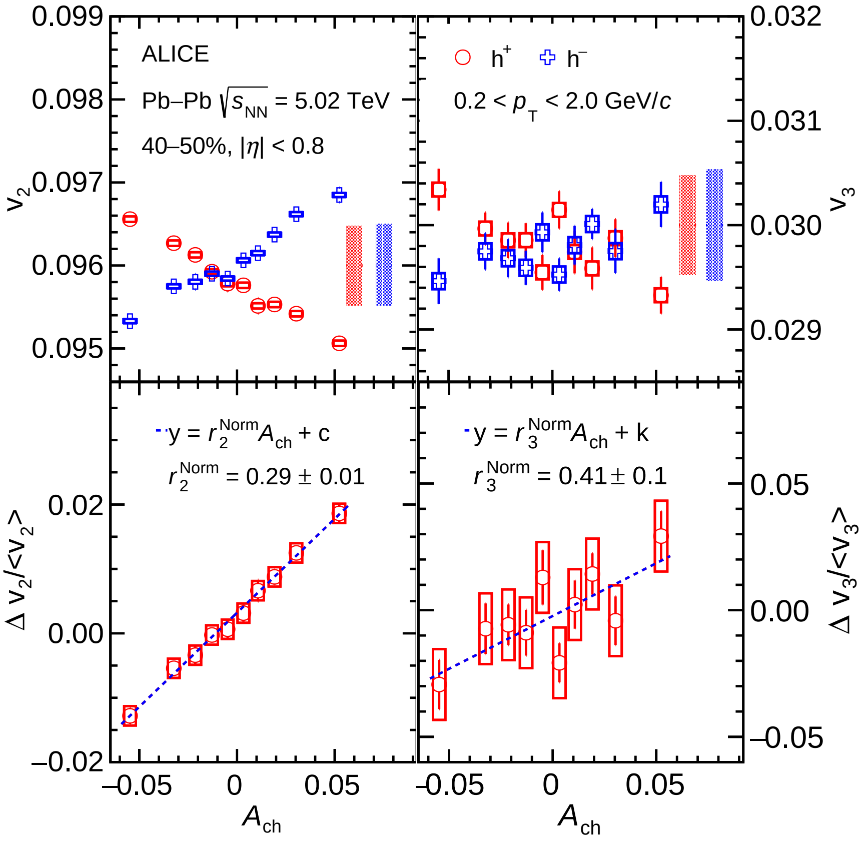

FIGURE 3.7: The top left panel shows the v_2 of positively (red markers) and negatively (blue markers) charged hadrons as a function of the corrected A_{ch} , while the top right panel shows the same for v_3. Statistical uncertainties are shown by bars and uncorrelated (correlated) systematic uncertainties by open boxes (shaded bands). The bottom left panel shows $\Delta v_2/\langle v_2\rangle$ as a function of the corrected A_{ch} and bottom right panel shows the same for $\Delta v_3/\langle v_3\rangle$, all for the 40–50% centrality interval in Pb−Pb collisions at $\sqrt{s_{\mathrm{NN}}} = 5.02$ TeV. The dotted blue line shows the linear fit to the data points to obtain the values of normalized slopes (r_2^{Norm} and r_3^{Norm}). The figure is taken from [17].

likely stems from the LCC mechanism rather than the CMW-induced electric quadrupole moment. Thus, the resemblance in the magnitudes of r_2^{Norm} and r_3^{Norm} suggests that both are predominantly influenced by the LCC background. These findings corroborate results from CMS measurements for the same collision system and energy [22]. While CMS measurements boast notable precision, this study extends the scope of measurements to encompass the most central collision scenarios. Furthermore, r_2^{Norm} is compared with

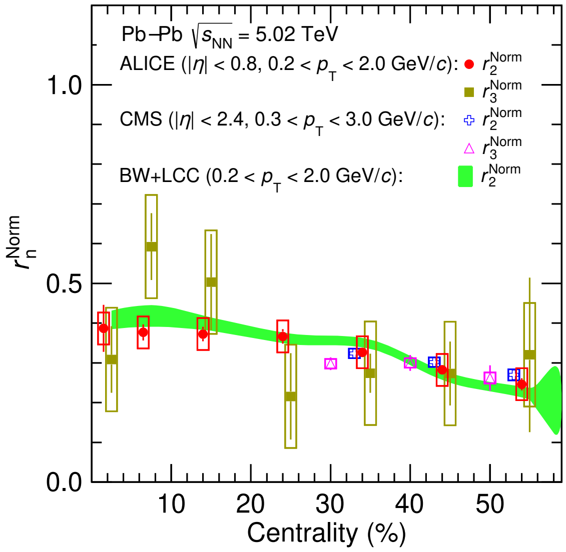

FIGURE 3.8: Centrality dependence of normalized slopes r_2^{Norm} and r_3^{Norm} for inclusive charged hadrons in Pb−Pb collisions at $\sqrt{s_{NN}}$ = 5.02 TeV compared with CMS results [22] and a BW+LCC model calculation [23]. Statistical (systematic) uncertainties are depicted by bars (boxes). ALICE r_2^{Norm} and r_3^{Norm} and CMS r_2^{Norm} data points are slightly shifted horizontally for visibility. The figure is taken from [17].

calculations from a blast wave model (green band) which accounts for the LCC effect [23]. This model employs blast wave parameters derived from simultaneous fits of p_T-differential yields and v_2 of identified particles from Pb−Pb collisions at $\sqrt{s_{NN}}$ = 5.02 TeV. The discussion about the model can be found in Appendix. A.2. The normalized slope values are calculated from the model, following the same procedure as for the data. The agreement between the model and experimental results of r_2^{Norm} suggests a substantial background contribution in the measurement. The results for r_2^{Norm} and r_3^{Norm} of identified hadrons are depicted in Fig. 3.9 as a function of centrality. For r_2^{Norm}, the slope for kaons exhibits a similar behavior to that of pions, while the slope for protons shows slight deviations with a weak A_{ch}–Δv_2 dependence on centrality. The uncertainties preclude a definitive conclusion on the PID dependence of the slopes. The LCC process, the dominant background for this

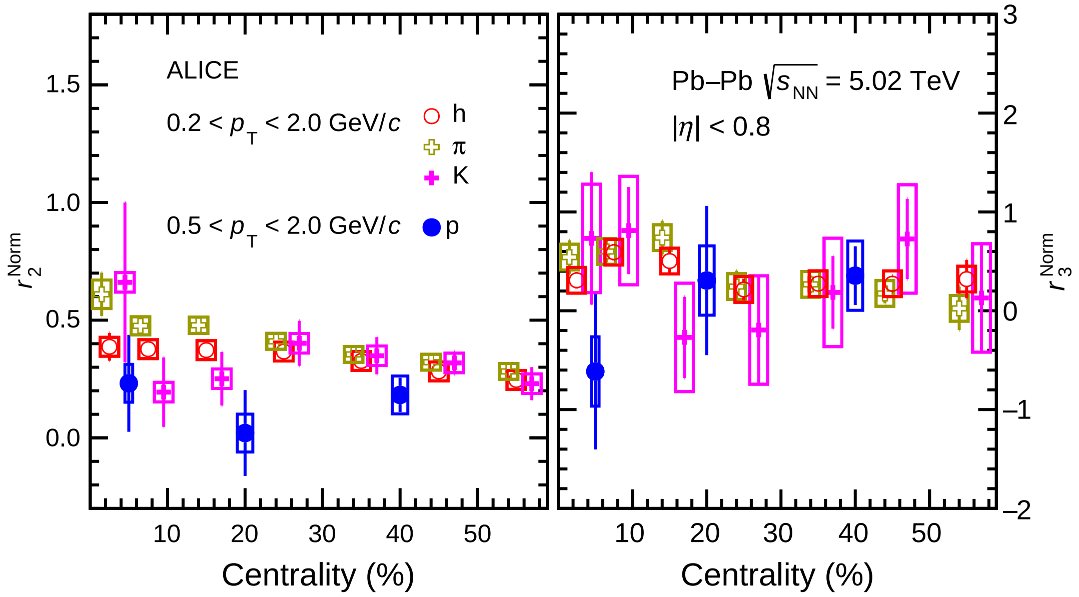

FIGURE 3.9: Centrality dependence of normalized slopes r_2^{Norm} (left panel) and r_3^{Norm} (right panel) for inclusive and identified charged hadrons in Pb–Pb collisions at $\sqrt{s_{NN}}$ = 5.02 TeV. Statistical (systematic) uncertainties are depicted by bars (boxes). The data points for charged pions and kaons are slightly shifted horizontally for visibility. The figure is taken from [17]

.

measurement, can replicate the r_2^{Norm} measurement in data. This observation contradicts hydrodynamic study predictions, which expected negative slopes for kaons and protons [27] at RHIC energies. A similar trend is evident in the STAR CMW measurement at lower collision energies, where the isospin and strangeness chemical potentials and the different absorption cross sections are anticipated to play a role [27–29]. However, at LHC energies, the values of the chemical potentials are consistent with zero, suggesting their negligible influence. Regarding r_3^{Norm}, the slopes of all measured hadron species are compatible with each other within the uncertainties. As no predictions for the CMW for different particle species exist at LHC energies, the results presented here provide experimental input for theoretical calculations.

3.5.2 Constraining the fraction of the CMW with the ESE

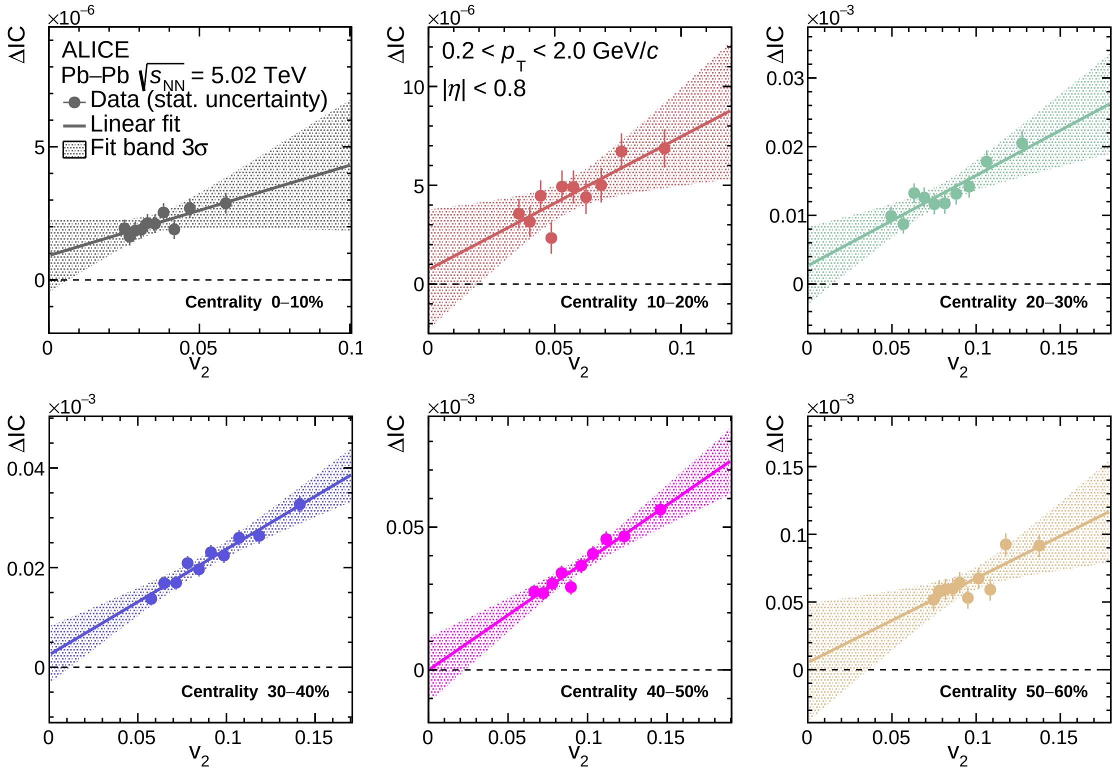

FIGURE 3.10: Dependence of ΔIC on v_2 of shape-selected events from the 0–10% (top left panel) to the 50–60% (bottom right panel) centrality intervals of Pb–Pb collisions at $\sqrt{s_{NN}}$ = 5.02 TeV. The solid lines are straight line fit to the data points. Only statistical uncertainties are shown. The bands represent the three standard deviation uncertainties from the linear fit. The figure is taken from [17].

Figure 3.10 illustrates the variation of the integrated covariance ΔIC with respect to v_2 for events selected based on q_2 in six centrality intervals. Linear fits (solid lines) along with colored bands representing three standard deviation uncertainties of the fits are also depicted. As discussed in Ref. [18], the ΔIC values demonstrate a decrease as v_2 approaches zero. The minimal intercepts observed in all centrality intervals indicate that the measurement is primarily influenced by the LCC background. Following the determination of the slope and intercept from the fit of ΔIC as a function of v_2, the fraction of the CMW signal, denoted as f_{CMW}, can be computed using Eq. 3.21. The centrality dependence of f_{CMW} is depicted in Fig. 3.11, where the error bars represent the statistical uncertainties extracted from the fits shown in Fig. 3.10. Significant measurements are challenging to obtain in the most central and peripheral collisions due to the small v_2 values and substantial statistical fluctuations. Consequently, the f_{CMW} results are solely reported within the 10–60% centrality range. Systematic uncertainties are estimated for various potential sources, as discussed in Sec. 3.4. The significant systematic sources identified across centrality intervals are combined in quadrature and depicted as a dark shaded band in Fig. 3.11, focusing on centrality around 60%. Notably, the f_{CMW} is found to be consistent with zero within the reported statistical and systematic uncertainties.

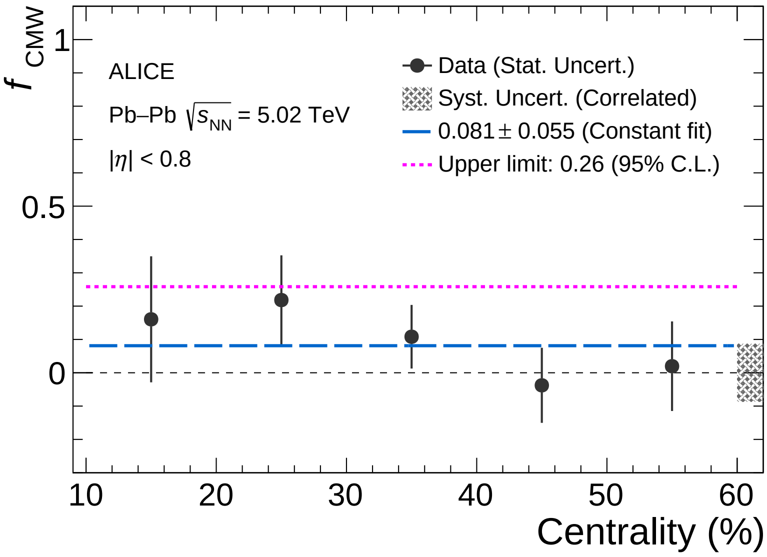

FIGURE 3.11: Centrality dependence of the extracted CMW fraction. The 95% confidence level of the upper limit is also shown by the dotted magenta line. Statistical uncertainties are depicted by bars, while the correlated systematic uncertainty is represented by a shaded band on the right edge. The blue line is the constant fit line of the data points. The figure is taken from [17].

The f_{CMW} data points depicted in Fig. 3.11 are fitted with a constant, resulting in $f_{\mathrm{CMW}} = 0.081 \pm 0.055$ (illustrated by the dashed blue line). This value is supplemented by the systematic uncertainty of 0.087 (represented by the gray box at the edge), establishing an upper limit on f_{CMW} of 26% (38%) at 95% (99.7%) confidence level, as indicated by the dotted magenta line. The upper limit is determined by the Gaussian distribution with mean parameter 0.081 and standard deviation of 0.103, which accounts for both statistical and systematic uncertainties. To obtain the upper limit, integration of the Gaussian distribution is carried out from 0 up to 95% (99.7%) of the total area. This outcome presents the first quantitative assessment of the upper limit of the fraction of the Chiral Magnetic Wave (CMW) at the highest LHC energy.

3.6 Summary

The difference between the v_2 and v_3 coefficients for positively and negatively charged particles is investigated as a function of the charge asymmetry A_{ch} in Pb–Pb collisions at $\sqrt{s_{\mathrm{NN}}}$= 5.02 TeV. The slopes r_2^{Norm} and r_3^{Norm} exhibit consistency within the reported uncertainties, indicating that the primary contribution to r_2^{Norm} is not attributed to CMW effects. By employing a blast wave parameterization that incorporates local charge conservation and is calibrated to replicate the A_{ch} distribution, the magnitude of r_2^{Norm} is effectively described, showcasing its sensitivity to CMW. Additionally, utilizing the ESE technique, both the fraction and the upper limit of the CMW signal are determined. Averaging across the 10–60% centrality range, the CMW fraction is consistent with zero within the error margins. An upper limit of 26% (38%) is estimated at 95% (99.7%) confidence level.

Bibliography

[1] Dmitri E. Kharzeev. “The Chiral Magnetic Effect and Anomaly-Induced Transport”. *Prog. Part. Nucl. Phys.* 75 (2014), pp. 133–151. arXiv: `1312.3348 [hep-ph]`.

[2] Dmitri E. Kharzeev. “Topology, magnetic field, and strongly interacting matter”. *Ann. Rev. Nucl. Part. Sci.* 65 (2015), pp. 193–214. arXiv: `1501.01336 [hep-ph]`.

[3] D. Kharzeev and A. Zhitnitsky. “Charge separation induced by P-odd bubbles in QCD matter”. *Nucl. Phys.* A797 (2007), pp. 67–79. arXiv: `0706.1026 [hep-ph]`.

[4] Dmitri E. Kharzeev, Larry D. McLerran, and Harmen J. Warringa. “The Effects of topological charge change in heavy ion collisions: ’Event by event P and CP violation’”. *Nucl. Phys.* A803 (2008), pp. 227–253. arXiv: `0711.0950 [hep-ph]`.

[5] Kenji Fukushima, Dmitri E. Kharzeev, and Harmen J. Warringa. “The Chiral Magnetic Effect”. *Phys. Rev.* D78 (2008), p. 074033. arXiv: `0808.3382 [hep-ph]`.

[6] Max A. Metlitski and Ariel R. Zhitnitsky. “Anomalous axion interactions and topological currents in dense matter”. *Phys. Rev. D* 72 (2005), p. 045011. arXiv: `hep-ph/0505072`.

[7] Yannis Burnier et al. “Chiral magnetic wave at finite baryon density and the electric quadrupole moment of quark-gluon plasma in heavy ion collisions”. *Phys. Rev. Lett.* 107 (2011), p. 052303. arXiv: `1103.1307 [hep-ph]`.

[8] Y. Burnier et al. “From the chiral magnetic wave to the charge dependence of elliptic flow” (Aug. 2012). arXiv: `1208.2537 [hep-ph]`.

[9] Betty Abelev et al. “Centrality determination of Pb-Pb collisions at $\sqrt{s_{\mathrm{NN}}} = 2.76$ TeV with ALICE”. *Phys. Rev. C* 88.4 (2013), p. 044909. arXiv: `1301.4361 [nucl-ex]`.

[10] Ante Bilandzic, Raimond Snellings, and Sergei Voloshin. “Flow analysis with cumulants: Direct calculations”. *Phys. Rev. C* 83 (2011), p. 044913. arXiv: `1010.0233 [nucl-ex]`.

[11] Nicolas Borghini, Phuong Mai Dinh, and Jean-Yves Ollitrault. “Are flow measurements at SPS reliable?” *Phys. Rev. C* 62 (2000), p. 034902. arXiv: `nucl-th/0004026`.

[12] Nicolas Borghini, Phuong Mai Dinh, and Jean-Yves Ollitrault. “A New method for measuring azimuthal distributions in nucleus-nucleus collisions”. *Phys. Rev. C* 63 (2001), p. 054906. arXiv: `nucl-th/0007063`.

[13] You Zhou et al. “Investigation of possible hadronic flow in $\sqrt{s_{NN}}$ = 5.02 TeV $p-Pb$ collisions”. *Phys. Rev. C* 91 (2015), p. 064908. arXiv: `1503.06986 [nucl-th]`.

[14] Hao-jie Xu et al. “Importance of non-flow background on the chiral magnetic wave search”. *Nucl. Phys. A* 1005 (2021). Ed. by Feng Liu et al., p. 121770. arXiv: `2002.05220 [nucl-th]`.

[15] Miklos Gyulassy and Xin-Nian Wang. “HIJING 1.0: A Monte Carlo program for parton and particle production in high-energy hadronic and nuclear collisions”. *Comput. Phys. Commun.* 83 (1994), p. 307. arXiv: `nucl-th/9502021`.

[16] R Brun et al. “GEANT Detector Description and Simulation Tool”. *CERN Program Library, CERN, Geneva* (1993).

[17] Shreyasi Acharya et al. “Probing the chiral magnetic wave with charge-dependent flow measurements in Pb-Pb collisions at the LHC”. *JHEP* 12 (2023), p. 067. arXiv: `2308.16123 [nucl-ex]`.

[18] Chun-Zheng Wang et al. “Interpreting the charge-dependent flow and constraining the chiral magnetic wave with event shape engineering”. *Phys. Lett. B* 820 (2021), p. 136580. arXiv: `2104.05551 [nucl-th]`.

[19] Shreyasi Acharya et al. “Constraining the magnitude of the Chiral Magnetic Effect with Event Shape Engineering in Pb–Pb collisions at $\sqrt{s_{\rm NN}} = 2.76$ TeV”. *Phys. Lett.* B777 (2018), pp. 151–162. arXiv: `1709.04723 [nucl-ex]`.

[20] Arthur M. Poskanzer and S. A. Voloshin. “Methods for analyzing anisotropic flow in relativistic nuclear collisions”. *Phys. Rev.* C58 (1998), pp. 1671–1678. arXiv: `nucl-ex/9805001 [nucl-ex]`.

[21] Roger Barlow. “Systematic errors: Facts and fictions”. In: *Advanced Statistical Techniques in Particle Physics. Proceedings, Conference, Durham, UK, March 18-22, 2002*. 2002, pp. 134–144. arXiv: `hep-ex/0207026 [hep-ex]`.

[22] Albert M Sirunyan et al. “Probing the chiral magnetic wave in pPb and PbPb collisions at $\sqrt{s_{NN}}$ =5.02TeV using charge-dependent azimuthal anisotropies”. *Phys. Rev. C* 100.6 (2019), p. 064908. arXiv: `1708.08901 [nucl-ex]`.

[23] Wen-Ya Wu et al. “Global constraint on the magnitude of anomalous chiral effects in heavy-ion collisions”. *Phys. Rev. C* 107.3 (2023), p. L031902. arXiv: `2211.15446 [nucl-th]`.

[24] Jaroslav Adam et al. “Correlated event-by-event fluctuations of flow harmonics in Pb–Pb collisions at $\sqrt{s_{\mathrm{NN}}} = 2.76$ TeV”. *Phys. Rev. Lett.* 117 (2016), p. 182301. arXiv: `1604.07663 [nucl-ex]`.

[25] K. Aamodt et al. “Higher harmonic anisotropic flow measurements of charged particles in Pb–Pb collisions at $\sqrt{s_{\mathrm{NN}}}$=2.76 TeV”. *Phys. Rev. Lett.* 107 (2011), p. 032301. arXiv: `1105.3865 [nucl-ex]`.

[26] Georges Aad et al. “Measurement of event-plane correlations in $\sqrt{s_{NN}} = 2.76$ TeV lead-lead collisions with the ATLAS detector”. *Phys. Rev. C* 90.2 (2014), p. 024905. arXiv: `1403.0489 [hep-ex]`.

[27] Yoshitaka Hatta, Akihiko Monnai, and Bo-Wen Xiao. “Elliptic flow difference of charged pions in heavy-ion collisions”. *Nucl. Phys. A* 947 (2016), pp. 155–160. arXiv: `1507.04690 [hep-ph]`.

[28] M. I. Abdulhamid et al. “Search for the chiral magnetic wave using anisotropic flow of identified particles at energies available at the BNL Relativistic Heavy Ion Collider”. *Phys. Rev. C* 108.1 (2023), p. 014908. arXiv: `2210.14027 [nucl-ex]`.

[29] Yoshitaka Hatta. “Analytic approaches to relativistic hydrodynamics”. *Nucl. Phys. A* 956 (2016). Ed. by Y. Akiba et al., pp. 152–159. arXiv: `1601.04128 [hep-ph]`.

CHAPTER 4

System size dependence of hadronic rescattering effect at LHC energies

Contents

4.1 Dataset, event and track selections 98
4.2 Analysis details 102
4.3 Systematic uncertainties 108
4.4 Results 110
4.5 Summary 122

Resonances are short lived particles which decay via strong interactions. They offer a unique avenue for probing the properties of the hadronic phase in heavy-ion collisions. Particularly in central A–A (Pb–Pb, Xe–Xe) collisions, where the duration of the hadronic phase is comparable to that of short-lived resonances, phenomena like regeneration and rescattering gain prominence. Investigating the production of K^{*} ($\mathrm{K}^{*}(892)^{0}$and $\mathrm{K}^{*}(892)^{\pm}$) resonance (with a lifetime of $\sim$ 4 fm/c) in A–A collisions holds significance in unraveling the characteristics of the hadronic phase.

The comprehensive datasets encompassing pp, p–Pb, Xe–Xe, and Pb–Pb collisions at $\sqrt{s_{\mathrm{NN}}} \approx 5$ TeV, amassed by the ALICE Collaboration, provide a robust platform for systematically probing the dependence of hadronic rescattering on the system size. This chapter introduces pioneering measurements of $\mathrm{K}^{*}(892)^{0}$ and $\mathrm{K}^{*}(892)^{\pm}$ meson production at midrapidity ($|y| < 0.5$) as a function of $\mathrm{d}N_{\mathrm{ch}}/\mathrm{d}\eta$ in pp and Pb–Pb collisions, respectively, at $\sqrt{s_{\mathrm{NN}}} = 5.02$ TeV. By comparing the measured K^{*} yield and $\mathrm{K}^{*}/\mathrm{K}$ yield ratio across different collision systems, we aim to unveil the system-size dependence of K^{*} production and the impact of hadronic rescattering. The $\mathrm{K}^{*}/\mathrm{K}$ ratio serves as a tool to constrain the duration of the hadronic phase across varying collision systems. Moreover, the thermal model Hadron Resonance Gas in Partial Chemical Equilibrium (HRG-PCE) [1] aids in constraining the kinetic freeze-out temperature. Additionally, comparisons of the mean transverse momentum ($\langle p_{\mathrm{T}} \rangle$) of K^{*} across different collision systems contribute to our understanding of radial flow evolution from small to heavy-ion collisions. Furthermore, scrutinizing the nuclear modification factor (R_{AA}) of K^{*} with various light flavor hadrons offers insights into the flavor dependence of energy loss of the partons in the QGP medium.

4.1 Dataset, event and track selections

The ALICE detector at the Large Hadron Collider (LHC) is utilized to measure the production yield of K^{*0} and $\mathrm{K}^{*\pm}$ mesons in pp and Pb–Pb collisions at $\sqrt{s_{\mathrm{NN}}} = 5.02$ TeV, respectively. Data from the years 2015 and 2018, collected under a magnetic field strength of B = 0.5 T, are employed for this analysis. Details regarding the ALICE detector and its performance are documented in [2, 3]. Events of interest are selected via a minimum-bias trigger requiring at least one hit in both forward scintillator detectors V0A ($2.8 < \eta < 5.1$) and V0C ($-3.7 < \eta < -1.7$) [4]. Pileup removal entails analyzing hits in the SPD detector, correlating cluster numbers in the ITS and TPC detectors, identifying multiple vertices with the SPD detector, and leveraging the correlation between the SPD and V0M detectors. Beam-induced background and pileup events are excluded through an offline event selection process, as detailed in Refs. [2, 5]. Results for pp collisions are based on the "INEL $>$ 0" event class, a subset of inelastic collisions where at least one charged particle is emitted in the pseudorapidity interval $|\eta| < 1$ [6]. Additionally, selected events must possess one primary collision vertex reconstructed using the two innermost layers of the Inner Tracking System (ITS) and located within ±10 cm along the beam axis from the nominal center of the ALICE detector. Measurements for K^{*0} and $\mathrm{K}^{*\pm}$ production yields utilize 100×10^6 and 120×10^6 minimum-bias pp and Pb–Pb collision events, respectively. The selected events are categorized into distinct classes based on their centrality in heavy-ion collisions or multiplicity in proton–proton collisions, using percentiles of the hadronic cross section. Event class categorization is achieved by analyzing the signal deposited in both V0 detectors, termed the "V0M amplitude", which is proportional to the charged-particle multiplicity. Various measured observables, such as the transverse momentum (p_{T}) spectrum, transverse-momentum-integrated yield ($\mathrm{d}N/\mathrm{d}y$), mean transverse momentum ($\langle p_{\mathrm{T}}\rangle$), yield ratios of resonances to stable particles, kinetic freeze-out temperature (T_{kin}), and nuclear modification factor (R_{AA}), are presented for different multiplicity (or centrality for heavy-ion collisions) classes as a function of pseudorapidity density ($\mathrm{d}N_{\mathrm{ch}}/\mathrm{d}\eta$) [7, 8].

In Pb–Pb collisions, the measurements of $\mathrm{K}^{*\pm}$ are conducted in five different centrality classes: 0–10%, 10–20%, 20–40%, 40–60%, and 60–80%. On the other hand, in pp collisions, the measurements of K^{*0} are performed in nine different multiplicity classes, as listed in Table 4.1, with class I having the highest multiplicity and class IX having the lowest multiplicity [9].

Charged tracks within a selected event are reconstructed using the Inner Tracking

TABLE 4.1: Analyzed multiplicity classes in pp collisions at $\sqrt{s}$= 5.02 TeV

V0M (%)	0–1	1–5	5–10	10–20	20–30	30–40	40–50	50–70	70–100
Multiplicity classes	I	II	III	IV	V	VI	VII	VIII	IX

System (ITS) [10] and the Time Projection Chamber (TPC) [11] detectors, situated within a solenoid providing a homogeneous magnetic field. Tracks originating from the primary collision vertex are chosen with a minimum transverse momentum (p_T) of 0.15 GeV/c and within a pseudorapidity ($|\eta|$) range of less than 0.8. These selected tracks must register at least one hit in the two innermost layers of the ITS and traverse a minimum of 70 out of a total of 159 rows along the transverse readout plane of the TPC. Additionally, the maximum χ^2 per space point in both the TPC and ITS from the track fit must not exceed 4 and 36, respectively. To mitigate the contribution of secondary charged particles, the distance of closest approach in the transverse plane of reconstructed tracks to the primary vertex ($\mathrm{DCA_{xy}}$) is required to be less than 7 times the standard deviation (σ) of the $\mathrm{DCA_{xy}}$ resolution. The resolution of $\mathrm{DCA_{xy}}$ is found to be dependent on p_T and is parameterized as $\sigma = 0.0105 + 0.0350/(p_T)^{1.1}$ cm. Furthermore, the longitudinal DCA is constrained to be less than 2 cm. Identification of selected charged particles is performed using information from the TPC and the Time-Of-Flight (TOF) [12] detectors, based on their specific ionization energy loss ($\mathrm{d}E/\mathrm{d}x$) in the TPC and their flight time measured in the TOF. Pions (π) and kaons (K) are identified with specific energy loss lying within 2 standard deviations (σ_{TPC}) (for $p > 0.4$), $4\sigma_{\mathrm{TPC}}$ (for $0.3 < p < 0.4$), and $6\sigma_{\mathrm{TPC}}$ (for $p < 0.3$) from their expected $\mathrm{d}E/\mathrm{d}x$, where σ_{TPC} denotes the $\mathrm{d}E/\mathrm{d}x$ resolution (typically around 5% of the measured $\mathrm{d}E/\mathrm{d}x$ value) of the TPC. Additionally, if a track has a hit in the TOF, its measured time of flight must fall within 3σ of the expected value for each particle species [13].

The secondary particle, $\mathrm{K^0_S}$, is reconstructed based on weak decay topological criteria [14]. The selection criteria for $\mathrm{K_S^0}$ reconstruction are outlined in Table 4.2. Firstly, two oppositely charged tracks within the acceptance window of $|\eta| < 0.8$ are identified as pions (daughters of $\mathrm{K_S^0}$) using a $4\sigma_{\mathrm{TPC}}$ selection criterion. The distance of closest approach (DCA) between negatively and positively charged tracks is required to be less than 0.8 cm. Additionally, the DCAs of charged tracks to the primary vertex must be greater than 0.1 cm, and the DCA of the $\mathrm{V^0}$ particle to the primary vertex in the transverse plane should be less than 0.3 cm. The cosine of the pointing angle, defined as the angle between the $\mathrm{V^0}$ momentum and the line connecting the secondary to the primary vertex, must exceed 0.98. Only $\mathrm{V^0}$ candidates with a reconstructed secondary vertex radius larger than 1.6 cm are selected. Moreover, $\mathrm{K_S^0}$ candidates exhibiting a proper lifetime, calculated as $LM_{\mathrm{K_S^0}}/p$, where L represents the linear distance between the primary and secondary vertex, $M\mathrm{K_S^0}$ is the mass of $\mathrm{K_S^0}$, and p indicates the total momentum of $\mathrm{K_S^0}$, exceeding 15 cm are removed to reduce the presence of combinatorial background originating from interactions with the detector material. To enhance the signal-to-background ratio beneath the $\mathrm{K_S^0}$ peak, a criterion is imposed on the asymmetry of pion momenta (Armenteros parameter), $(p_{\pi^-} - p_{\pi^+})/(p_{\pi^-} + p_{\pi^+})$, allowing only pairs of pions with an Armenteros parameter value exceeding 0.2 to be considered. Finally, the invariant mass of $\pi^+\pi^-$ is required to be within 2σ of the $\mathrm{K_S^0}$ nominal mass, where σ represents the detector mass resolution, found to be approximately $\sim$5 MeV/c^2 with a very weak dependence on collision centrality and particle momentum. Along with these topological criteria, only $\mathrm{K_S^0}$ candidates with $|y| < 0.5$ are included in the analysis. Figure. 4.1 shows the $\mathrm{K_S^0}$ invariant mass distribution which constitutes the $\mathrm{K^*(892)^\pm}$ signal in the 0.4-0.8 p_{T} interval for the 0-10% centrality class. With our selection criteria, we observe a very clean signal for K0s, with a mass of approximately 493 MeV/c^2 and a width of about 5 MeV/c^2.

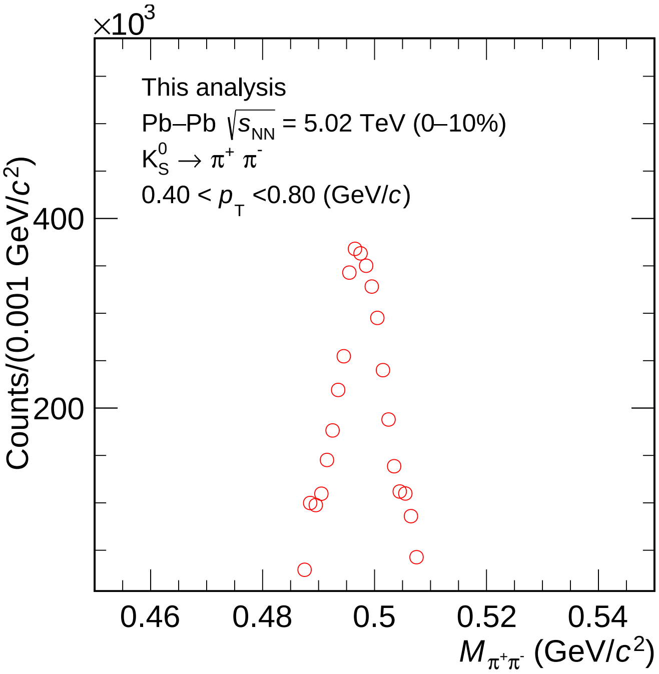

FIGURE 4.1: Invariant mass distribution of K^0_S for $K^*(892)^{\pm}$ in the p_T interval of 0.4 to 0.8 GeV/c.

TABLE 4.2: Selection criteria for K^0_S.

Selection criteria	Value	Variations
Crossed rows	>70	60, 80
Acceptance window of pions ($\|\eta\|$)	< 0.8	-
Pion dE/dx (σ)	<4	3, 5
DCA V^0 daughters	< 0.8 cm	0.4, 0.5 cm
DCA of V^0 daughters to PV	> 0.1 cm	-
DCA of V^0 particle to PV	< 0.3 cm	0.4, 0.5 cm
V^0 cosine pointing angle	> 0.98	0.985, 0.995
V^0 radius	> 1.6 cm	1 cm
Proper lifetime	< 15 cm	12, 20 cm
Armenteros parameter	> 0.2	-
K^0_Smass window (σ)	± 2	-

4.2 Analysis details

The short-lived resonance particles K^{*0} and $K^{*\pm}$ are reconstructed via their hadronic decay channels: $K^*(892)^0 \rightarrow K^{\pm}\pi^{\mp}$ and $K^{*\pm} \rightarrow K^0_S\pi^{\pm}$, respectively, with branching ratios (BR) of 66% and 33%, as reported by the Particle Data Group [15]. For K^{*0}, oppositely charged kaons and pions within the same event are paired to reconstruct the resonance signal, while for $\mathrm{K}^{*\pm}$, the reconstructed K^0_S and $\pi^\pm$ candidates are paired within the same events. The resulting invariant-mass distribution of unlike-sign charge $\mathrm{K}\pi$ pairs and $\mathrm{K}^0_\mathrm{S}\pi$ pairs contains a signal along with significant combinatorial background, which is estimated using the mixed-event method [16]. In the mixed-event invariant mass distribution, kaons (for K^{*0}) and K^0_S (for $\mathrm{K}^{*\pm}$) from one event are combined with oppositely charged pions from five other events. Only events with similar topologies, such as an absolute difference in the z-coordinate of their collision vertex less than 1 cm, and the difference in centrality (for Pb–Pb) or multiplicity percentile (for pp) less than 5%, are mixed. The mixed-event background is scaled to match the foreground distribution in the invariant mass range of 1.3–1.4 GeV/c^2. The left panel of Fig. 4.2 illustrates the invariant-mass distribution of $\mathrm{K}^0_\mathrm{S}\pi$ pairs from the same event alongside the rescaled mixed-event background in $2.5 < p_\mathrm{T} < 3.0$ GeV/c for Pb–Pb collisions at $\sqrt{s_\mathrm{NN}}$ = 5.02 TeV. The invariant mass distribution of $\mathrm{K}^0_\mathrm{S}\pi$ pairs with the mixed-event background subtracted is depicted in the right panel of Fig. 4.2. This combinatorial background-subtracted invariant mass distribution comprises the $\mathrm{K}^{*\pm}$ signal and a residual background of correlated pairs. The correlated background pairs may stem from sources like jets, decays of resonances with misidentified daughters, and decays with multiple daughters. To characterize this distribution, a fitting procedure is employed, involving a combination of a non-relativistic Breit–Wigner distribution and a product of an exponential function and a second-order polynomial (only a second-order polynomial for K^{*0}).

The fit function is defined as

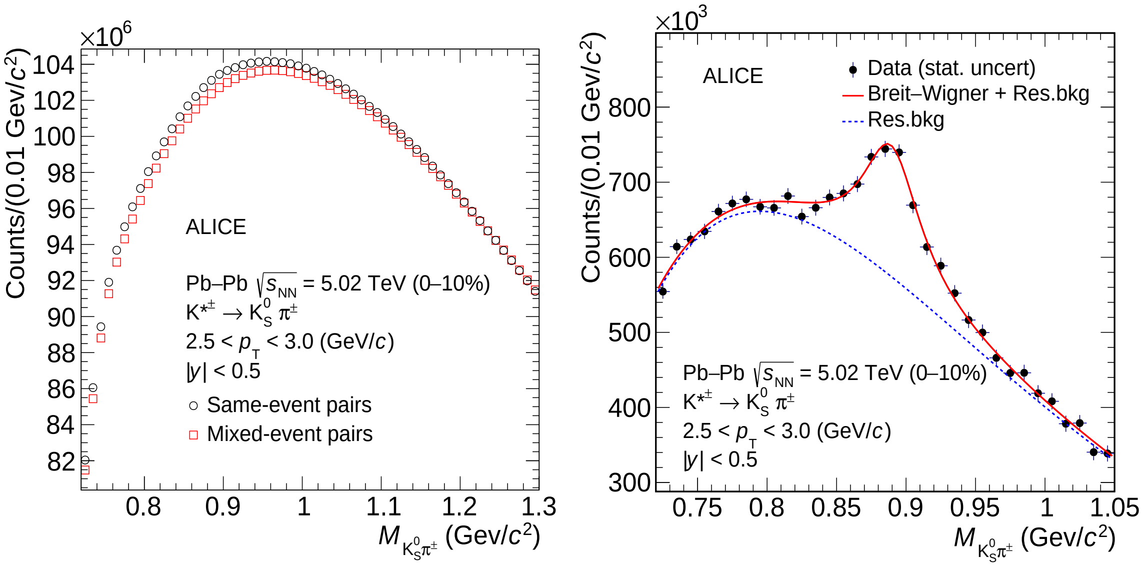

FIGURE 4.2: (Left panel): Invariant mass distribution of $K^0_S\pi^\pm$ pairs in same (black marker) and mixed events (red marker). (Right panel): Invariant mass distribution of $K^0_S\pi^\pm$ pairs after the subtraction of normalized mixed-event background distribution [17]. The solid red curve is the fit function defined by Eq. 4.1, with the dotted blue line describing the residual background distribution given by Eq. 4.2.

$$\frac{dN}{dM} = \frac{Y}{2\pi}\frac{\Gamma_0}{(M - M_0)^2 + \Gamma_0^2/4} + \text{Res.bkg}, \tag{4.1}$$

where M_0 and Γ_0 are the mass and width of $K^{*\pm}(K^{*0})$, M is invariant mass of the $K^0_S\pi^\pm(K\pi)$ pair, and the parameter Y is the normalization constant. The mass resolution of the detector for reconstruction of $K^{*\pm}$ and K^{*0} is negligible as compared to the vacuum width of the $K^{*\pm}(0.0514 \pm 0.0009)$ GeV/c^2 and $K^{*0}(0.047 \pm 0.0005)$ [15], hence it is not included. The last term in Eq. 4.1 is a residual background function (Res.bkg) and for $K^{*\pm}$ signal extraction it is taken as

$$\text{Res.bkg} = [M - (m_{\pi^\pm} + M_{K^0_S})]^{\text{n}}\exp(\text{A} + \text{B}M + \text{C}M^2), \tag{4.2}$$

where $m_{\pi^\pm}$ and $M_{K^0_S}$ are the mass of the pion, and K^0_S, respectively, and A, B, C, and n are the fit parameters. The width of $K^{*\pm}$ and K^{*0} is kept fixed to its vacuum value (0.050 and 0.047 GeV/c^2, respectively) in the fit procedure to estimate the signal, whereas it is allowed to vary freely to estimate the systematic uncertainty. The significance of the $K^{*\pm}$ signal presented in Fig. 4.2 is 23. Finally, raw yields of $K^{*\pm}$ and K^{*0} in each p_T interval and event or multiplcity class is obtained from the integral of the Breit–Wigner distribution as done in Ref. [18, 19]. Individually, the yields of particle and anti-particle are found to be consistent with each other within uncertainties.

The raw yields (N^{raw}) extracted from the data are subjected to corrections for detector acceptance and reconstruction efficiency ($A \times \epsilon_{\mathrm{rec}}$), as well as the branching ratio (BR) of the decay channel. To estimate $A \times \epsilon_{\mathrm{rec}}$, dedicated Monte Carlo (MC) event generators are utilized: PYTHIA8 [20] for pp collisions and HIJING [21] for Pb–Pb collisions. These generators simulate the passage of particles through a model of the ALICE detector constructed using GEANT3 [22]. The evaluated detector acceptance and reconstruction efficiencies for $K^{*\pm}$ (K^{*0}) in different centrality (multiplicity) intervals of Pb–Pb (pp) collisions at $\sqrt{s_{\mathrm{NN}}}$ = 5.02 TeV are shown in Fig. 4.3.

A weighting procedure is then applied to $A \times \epsilon_{\mathrm{rec}}$ to address variations over the width of a p_T interval in the measured spectrum and discrepancies in the shape between data and MC simulation [23]. An iterative procedure is performed to determine the correct weighting and therefore the correct $A \times \epsilon_{\mathrm{rec}}$.

- $A \times \epsilon_{\mathrm{rec}}$ is calculated from MC generated and reconstructed p_T spectrum in similar p_T binning as used in data.

- $A \times \epsilon_{\mathrm{rec}}$ is used to correct the measured p_T spectrum.

- $A \times \epsilon_{\mathrm{rec}}$ corrected p_T spectrum is fitted with Levy-Tsallis function [24].

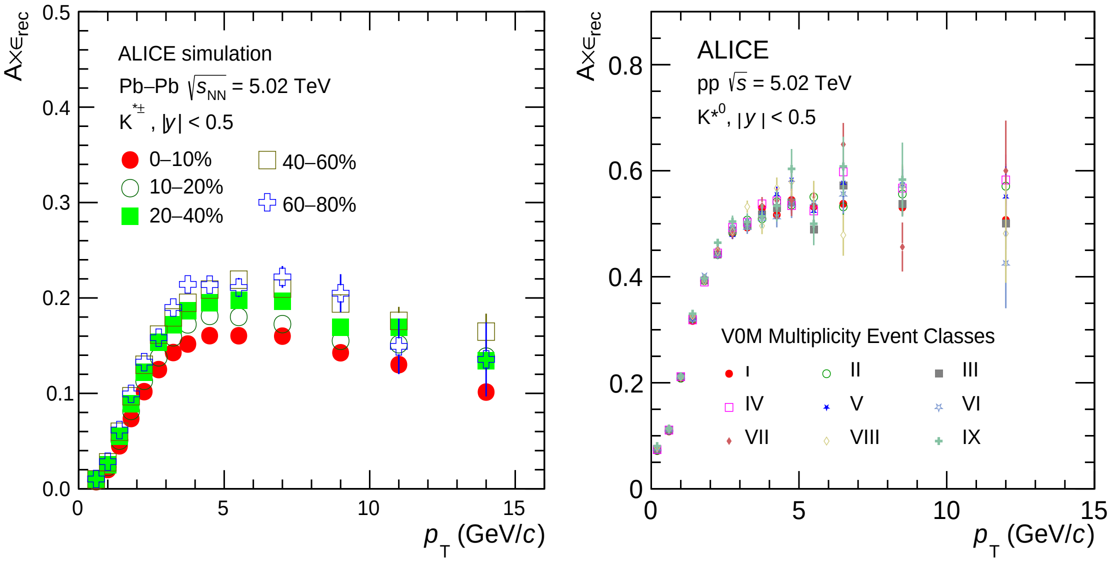

FIGURE 4.3: The acceptance times efficiency correction for K$^{*\pm}$ (left) and K^{*0} (right) as a function of p_{T} for different centrality/ multiplicity intervals [17].

- MC simulated spectra are again extracted in smaller p_{T} bins. Levy-Tsallis fit of measured spectrum is used to weight the MC generated spectrum. A p_{T} dependent weight is applied to the generated spectrum so that it follows the fit. The same weight is also applied to the reconstructed spectrum.

- Now this weighted simulated spectra are used to calculate the $A \times \epsilon_{\mathrm{rec}}$ in a similar p_{T} binning as used in data.

- Above mention procedure is repeated until the change between $A \times \epsilon_{\mathrm{rec}}$ in two successive iteration becomes < 0.1 %. It is observed that two iterations are usually sufficient for this procedure to converge.

The weight factor for K$^{*\pm}$ and K^{*0} in different centrality and multiplicity classes are shown in Fig. 4.4. This weight factor is multiplied with original $A \times \epsilon_{\mathrm{rec}}$ to obtain the resultant or corrected $A \times \epsilon_{\mathrm{rec}}$.

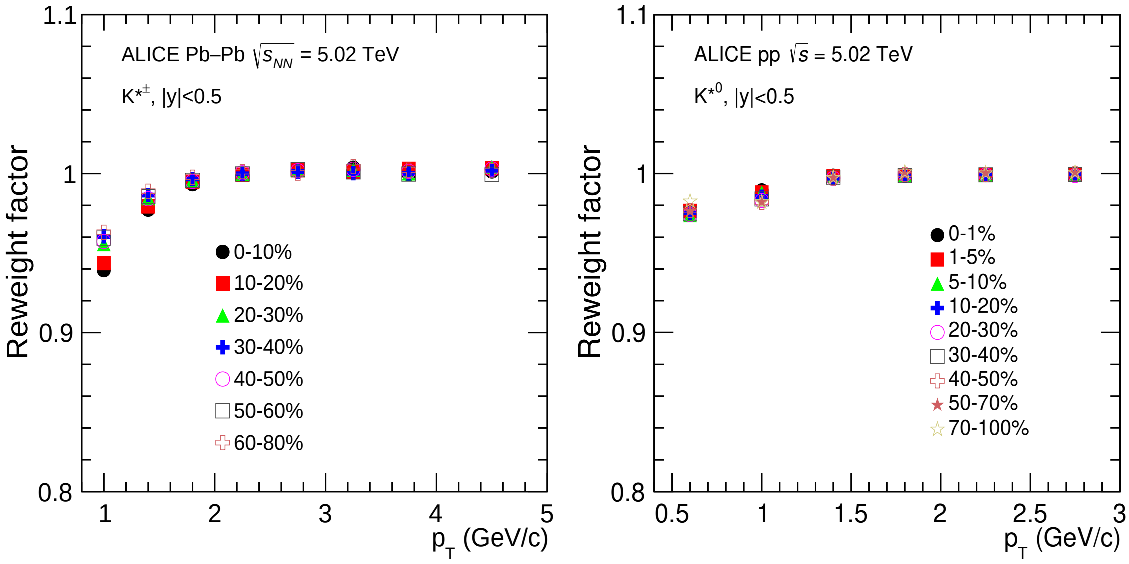

FIGURE 4.4: (Left panel): The reweight factor for $\mathrm{K}^{*\pm}$ in Pb–Pb collisions at $\sqrt{s_{\mathrm{NN}}}$= 5.02 TeV. (Right panel): The reweight factor for K^{*0} in pp collisions at $\sqrt{s}$= 5.02 TeV

Subsequently, the yields are normalized by the number of accepted events ($N^{\mathrm{acc}}_{\mathrm{event}}$) to derive the corrected p_{T} spectrum for different event classes. For measurements in pp collisions, additional corrections are made for event loss and signal loss, assessed through MC simulations. The event loss correction factor is applied in order to normalize to the true number of INEL> 0 pp collisions in a given multiplicity bin where the signal loss accounts for the losses K^{*0} mesons due to trigger and event selection criteria, which do not select the full sample of INEL> 0 collisions [5]. The signal loss correction ($\mathrm{f_{SL}}$) for K^{*0} is determined for each multiplicity class by comparing the simulated K^{*0} p_{T} spectrum before and after applying trigger and event selection criteria. Particularly in the 70–100% multiplicity class, $\mathrm{f_{SL}}$ reaches a maximum value of 22% and is most significant at low p_{T}. The event loss correction ($\mathrm{f_{ev}}$) represents the fraction of INEL > 0 events that fail to meet the event selection criteria, and its value, ranging from 0.99 in the 0–1% multiplicity class to 0.71 in the 70–100% multiplicity class, is not contingent on particle type or p_{T}. Fig. 4.5

shows the event and signal loss correction factors as a function of p_{T} in various multiplicity classes.

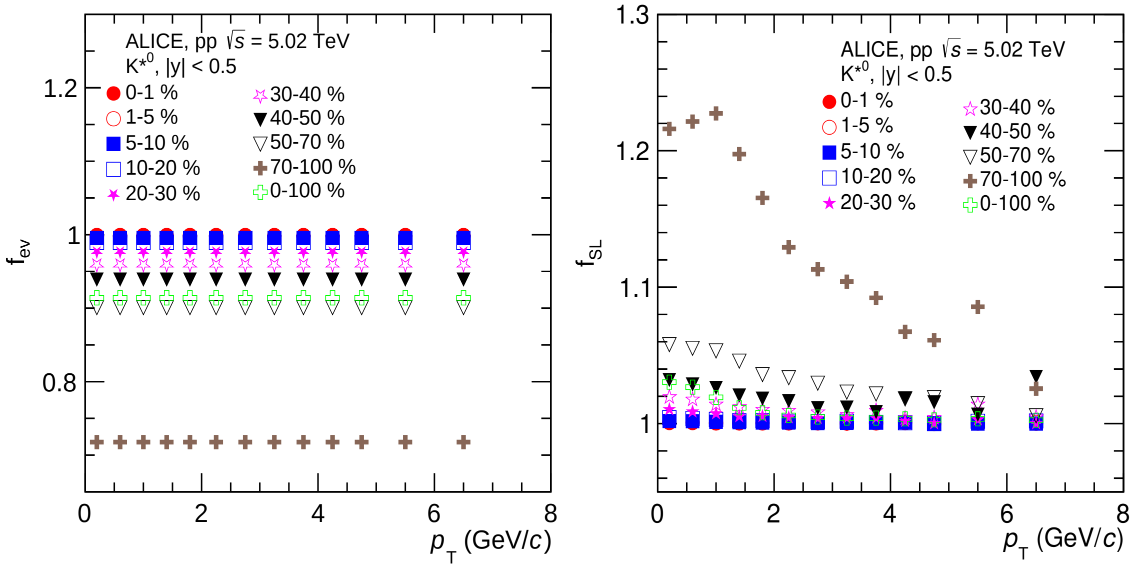

FIGURE 4.5: The event and signal loss factors for K^{*0} in pp collisions at $\sqrt{s}$= 5.02 TeV.

The corrected p_{T} spectrum can then finally be mathematically expressed as:

$$\frac{1}{N_{\mathrm{event}}}\frac{\mathrm{d}^2N}{\mathrm{d}y\mathrm{d}p_{\mathrm{T}}} = \frac{1}{N^{\mathrm{acc}}_{\mathrm{event}}}\frac{\mathrm{d}^2N^{\mathrm{raw}}}{\mathrm{d}y\mathrm{d}p_{\mathrm{T}}}\frac{\mathrm{f}_{\mathrm{ev}}\mathrm{f}_{\mathrm{SL}}}{(\mathrm{A}\times\epsilon_{\mathrm{rec}})\mathrm{BR}}, \tag{4.3}$$

where N is the number of K^{*0} or $\mathrm{K}^{*\pm}$ produced in a given transverse momentum ($\mathrm{d}p_{\mathrm{T}}$) and rapidity ($\mathrm{d}y$) interval.

4.3 Systematic uncertainties

The systematic uncertainties affecting the measured yields of $\mathrm{K}^{*\pm}$ and K^{*0} stem from several sources, encompassing the signal extraction technique, track selection, criteria for particle identification, the methodology employed for matching track segments in the Inner Tracking System (ITS) with those in the Time Projection Chamber (TPC), as well as uncertainties related to the material budget and interaction cross-section. These uncertainties are assessed by repeating the entire analysis chain while incorporating the variations outlined below. The resulting variations in the yields of resonances for each p_{T} and centrality (or multiplicity) interval are treated as systematic uncertainties. Table 4.3 provides a comprehensive overview of the systematic uncertainties associated with the measured $\mathrm{K}^{*\pm}$ yields in Pb–Pb collisions and K^{*0} yields in pp collisions. The uncertainties listed in the table are averaged across all centrality/multiplicity classes and presented separately for low- and high-p_{T} intervals.

TABLE 4.3: Systematic uncertainties on measured K^{*0} and $\mathrm{K}^{*\pm}$ yields in pp and Pb−Pb collisions at $\sqrt{s_{\mathrm{NN}}}$ = 5.02 TeV, respectively. The systematic uncertainties are shown for different sources for a low- and a high-p_{T} interval.

Systematic variation	pp [p_{T} (GeV/c)]		Pb–Pb [p_{T} (GeV/c)]	
	0–0.4	10.0–14.0	0.4–0.8	12.0–16.0
Signal extraction (%)	7.4	9.6	7.4	5.6
Primary track selection (%)	1.9	5.0	5.0	4.7
Particle identification (%)	1.4	5.5	3.7	3.2
Global tracking efficiency (%)	2	negl.	3	2.2
Material budget (%)	1.8	negl.	3.1	0.5
Hadronic interaction (%)	2.6	negl.	1.0	negl.
Total (%)	8.7	12.3	12.0	9.6

To assess the uncertainty associated with signal extraction, various parameters are adjusted, including fitting ranges, the region for rescaling the mixed-event background, the functional form used to model residual background, and the method employed for yield extraction. In the default scenario, invariant mass distributions are fitted with fixed-width fits based on the background shape. To quantify the systematic uncertainty, the boundaries of the fitting ranges are shifted by 20 MeV/c^2 on both sides. The rescaling of the mixed-event background distribution is shifted to different ranges to gauge its impact. The residual background is characterized using a third-order polynomial to analyze systematic effects.

For the primary track selection, the criteria are modified following the protocol outlined in Ref. [16]. The uncertainty in $\mathrm{K^0_S}$ reconstruction is evaluated by varying the topological selection criteria listed in Table 4.2. Uncertainties associated with the identification of primary daughter tracks are assessed by adjusting the selection criteria in the TPC and TOF. Additionally, uncertainties related to the material budget and hadronic cross-section are derived from Ref. [16]. The total uncertainty, obtained by combining the uncertainties from each source in quadrature, is averaged over all centrality/multiplicity classes. For $\mathrm{K^{*0}}$ in pp collisions, the total uncertainty ranges from 6.5% to 12.3%, while for $\mathrm{K^{*\pm}}$ in Pb–Pb collisions, it ranges from 8.8% to 12%.

4.4 Results

The corrected p_{T} distributions for $\mathrm{K^{*\pm}}$ mesons at midrapidity across various centrality intervals (0−10%, 10−20%, 20−40%, 40−60%, and 60−80%) are depicted in Fig. 4.6. Additionally, the $\mathrm{K^{*0}}$ p_{T} spectra in pp collisions at $\sqrt{s}$= 5.02 TeV for different multiplicity classes, following all corrections outlined in Section 4.2, are illustrated in the upper panel of Fig. 4.7. Meanwhile, the lower panel of Fig. 4.7 displays the ratios of the $\mathrm{K^{*0}}$ p_{T} spectra in various multiplicity classes to the spectrum obtained from multiplicity-integrated (INEL>0) pp collisions. A clear increase in the inverse slopes of the p_{T} spectra is observed from low to high multiplicity for $p_{\mathrm{T}} < 4$ GeV/c. However, at higher p_{T}, the spectra in different multiplicity classes exhibit the same shape, suggesting that low p_{T} processes primarily drive the change in the shape of the p_{T} spectra from low to high multiplicity classes.

The corrected p_{T} distributions for $\mathrm{K^{*0}}$ in four distinct centrality classes of Xe–Xe collisions at $\sqrt{s_{\mathrm{NN}}}$ = 5.44 TeV are depicted in the left panel of Fig. 4.8. In the right panel of Fig. 4.8, a comparison of the $\mathrm{K^{*0}}$ p_{T} spectrum between Xe–Xe and Pb–Pb collisions

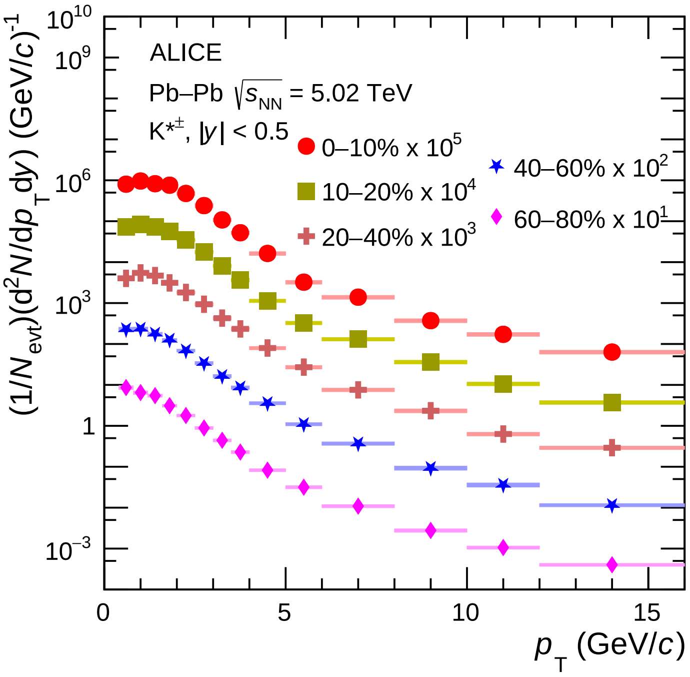

FIGURE 4.6: The p_T distributions of $K^{*\pm}$ meson in various centrality intervals in Pb−Pb collisions at $\sqrt{s_{NN}} = 5.02$ TeV. The statistical and systematic uncertainties are shown as bars and boxes, respectively. The figure is taken from [17].

is presented, alongside the $K^{*\pm}$ p_T spectrum in Pb–Pb collisions with a similar final-state charged-particle multiplicity. Notably, at comparable multiplicity values, the K^{*0} and $K^{*\pm}$ p_T distributions in Xe–Xe and Pb–Pb collisions exhibit consistency within uncertainties. This suggests that the physics processes, such as hadronic rescattering and radial flow, which influence the shape of the p_T distribution in heavy-ion collisions, exert a similar effect on the K^{*0} and $K^{*\pm}$ p_T spectra regardless of the size of the colliding nuclei.

Figure 4.9 presents a comparison of the transverse momentum distributions of $K^{*\pm}$ and K^{*0} mesons in Pb−Pb collisions at $\sqrt{s_{NN}} = 5.02$ TeV for the 0−10% and 40−60% centrality intervals. The lower panels of Fig. 4.9 depict the ratio of $K^{*\pm}$ to K^{*0}. Statistical and systematic uncertainties on the ratio are derived by propagating the corresponding statistical and total systematic uncertainties on the K^{*0} and $K^{*\pm}$ p_T spectra. Within uncertainties, the

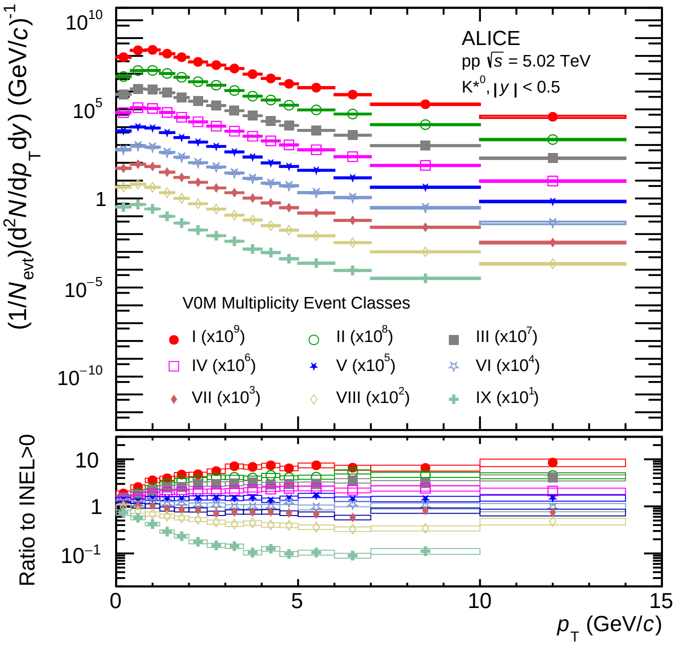

FIGURE 4.7: Upper panel: The p_{T} spectra of K^{*0} in various multiplicity classes of pp collisions at $\sqrt{s} = 5.02$ TeV. Lower panel: The ratios of the multiplicity-dependent p_{T} spectra to the multiplicity-integrated INEL> 0 spectra. The statistical and systematic uncertainties are shown as bars and boxes, respectively. The figure is taken from [25].

ratio is consistent with unity. This alignment of the spectra for $\mathrm{K}^{*\pm}$ and K^{*0} is consistent with previous observations made in pp collisions [14].

The transverse momentum integrated yields of K^{*0} and $\mathrm{K}^{*\pm}$, denoted as $\mathrm{d}N/\mathrm{d}y$, and their average transverse momentum ($\langle p_{\mathrm{T}} \rangle$) are determined from the measured p_{T} spectrum, with extrapolation to unmeasured regions facilitated by a blast wave function [23]. In pp collisions, where K^{*0} is measured down to $p_{\mathrm{T}} = 0$ GeV/c, no low-p_{T} extrapolation is necessary for extracting $\mathrm{d}N/\mathrm{d}y$ and $\langle p_{\mathrm{T}} \rangle$. The impact of extrapolation on the extracted $\mathrm{d}N/\mathrm{d}y$ for $\mathrm{K}^{*\pm}$ is approximately 8% (12%) in central (peripheral) Pb–Pb collisions. Systematic uncertainties on $\mathrm{d}N/\mathrm{d}y$ and $\langle p_{\mathrm{T}} \rangle$ are assessed by randomly varying the data points within their systematic uncertainties to obtain spectra with the softest and hardest behav-

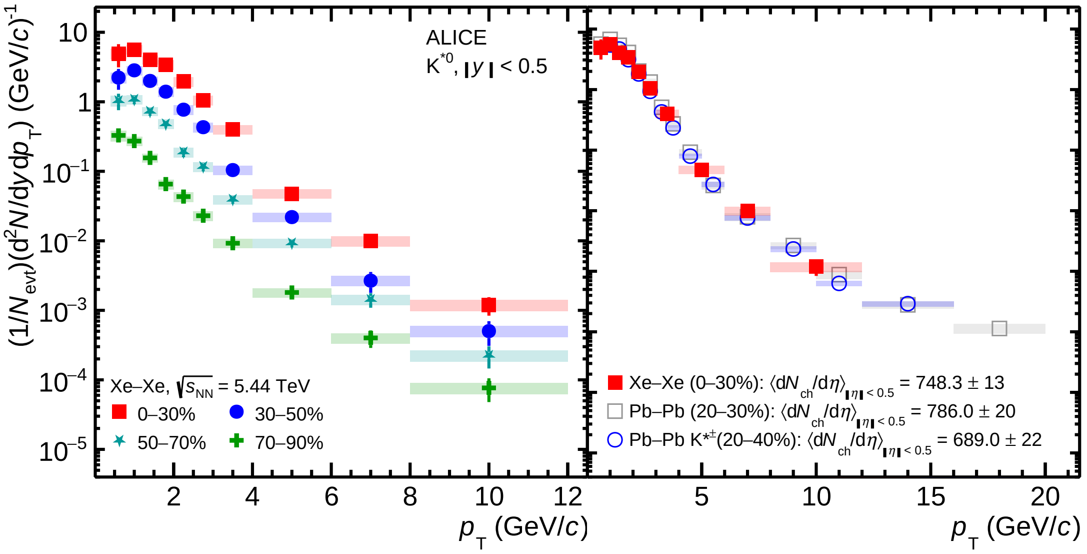

FIGURE 4.8: The left panel shows the p_{T} distributions of K^{*0} meson in four different centrality classes of Xe–Xe collisions at $\sqrt{s_{\mathrm{NN}}}$ = 5.44 TeV [25]. The right panel shows the comparison among the K^{*0} p_{T} spectrum in 0–30% Xe–Xe collisions at $\sqrt{s_{\mathrm{NN}}}$ = 5.44 TeV, 20–30% Pb–Pb [23] collisions and 20-40% K$^{*\pm}$ in Pb–Pb collisions at $\sqrt{s_{\mathrm{NN}}} = 5.02$ TeV [17], all having similar multiplicities. The statistical and systematic uncertainties are shown by bars and boxes, respectively.

iors. In Pb–Pb collisions, an additional systematic uncertainty on K$^{*\pm}$, attributed to the p_{T} spectrum extrapolation to $p_{\mathrm{T}} = 0$ GeV/c, is evaluated by employing different fit functions (Levy–Tsallis, Boltzmann, and Bose-Einstein) for the extrapolation [24, 26].

Figure 4.10 illustrates the behavior of dN/dy(left panel) and $\langle p_{\mathrm{T}} \rangle$(right panel) for K^{*0} and K$^{*\pm}$ across various collision systems, where $\langle \mathrm{d}N_{\mathrm{ch}}/\mathrm{d}\eta \rangle^{1/3}_{|\eta|<0.5}$ serves as a measure proportional to the linear (radial) path traversed through the produced matter. A consistent trend of dN/dy with $\langle \mathrm{d}N_{\mathrm{ch}}/\mathrm{d}\eta \rangle^{1/3}_{|\eta|<0.5}$ is observed across all collision systems, implying that the production of K^{*0} and K$^{*\pm}$ is primarily influenced by the final-state charged-particle multiplicity, utilized as an indicator of the system size [27]. The $\langle p_{\mathrm{T}} \rangle$ of both K^{*0} and K$^{*\pm}$ exhibits a rise with increasing $\langle \mathrm{d}N_{\mathrm{ch}}/\mathrm{d}\eta \rangle^{1/3}_{|\eta|<0.5}$ across all collision systems, indicating a heightened radial flow velocity from low- to high-multiplicity event classes. However,

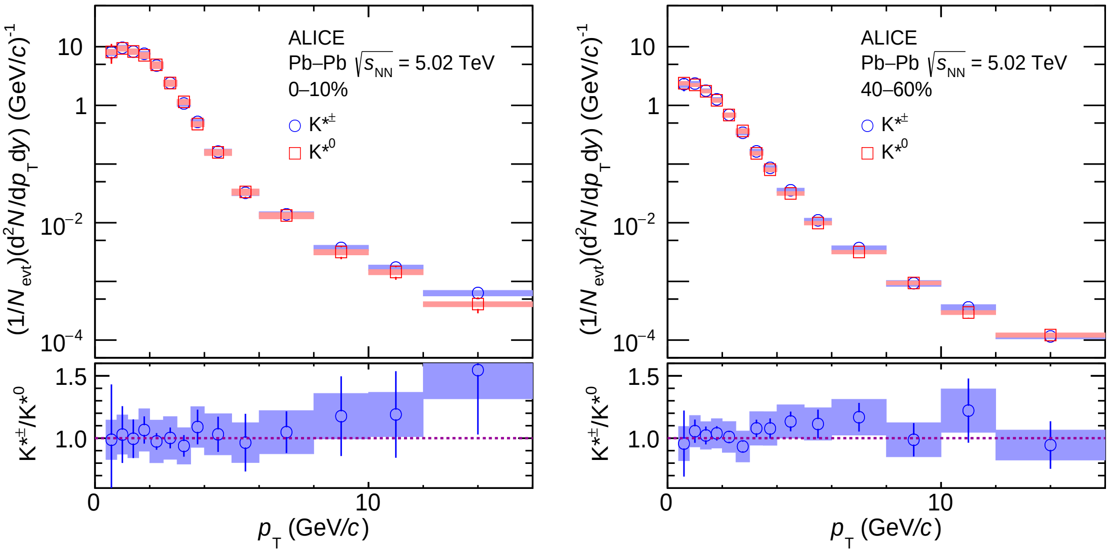

FIGURE 4.9: The $p_{\rm T}$distributions of $K^{*\pm}$ (blue circles) and K^{*0} (red squares) [23] in 0−10% (left) and 40−60% (right) centrality intervals in Pb–Pb collisions at $\sqrt{s_{\rm NN}}$= 5.02 TeV. Statistical and systematic uncertainties are shown by bars and shaded boxes, respectively. The bottom panels show the $K^{*\pm}$ to K^{*0} ratio as a function of $p_{\rm T}$. The figure is taken from [17].

in contrast to dN/dy, the intensive variable $\langle p_{\rm T}\rangle$ demonstrates a pronounced dependence on the colliding system and does not scale uniformly with charged-particle multiplicity across all systems. Specifically, the increase in $\langle p_{\rm T}\rangle$ is steeper in small collision systems compared to heavy-ion collisions. For $\langle {\rm d}N_{\rm ch}/{\rm d}\eta\rangle^{1/3}_{|\eta|<0.5} > 2$, the ordering of $\langle p_{\rm T}\rangle$ for a fixed multiplicity is observed as follows: $\langle p_{\rm T}\rangle$ (pp) > $\langle p_{\rm T}\rangle$ (p–Pb) > $\langle p_{\rm T}\rangle$ (Xe–Xe) ∼ $\langle p_{\rm T}\rangle$ (Pb–Pb). In the context of the blast wave fit, where the fit parameters are interpreted in terms of collective expansion, it is noted that small collision systems exhibit a greater pressure gradient and faster expansion of produced matter compared to heavy-ion collisions with similar charged-particle multiplicity [28, 29]. Moreover, the comparable $\langle p_{\rm T}\rangle$ of K^{*0} in Xe−Xe and Pb−Pb collisions at similar $\langle {\rm d}N_{\rm ch}/{\rm d}\eta\rangle^{1/3}_{|\eta|<0.5}$, along with $K^{*\pm}$, suggests a similar dynamical evolution of the system resulting from collisions involving large and medium-sized nuclei at LHC energies.

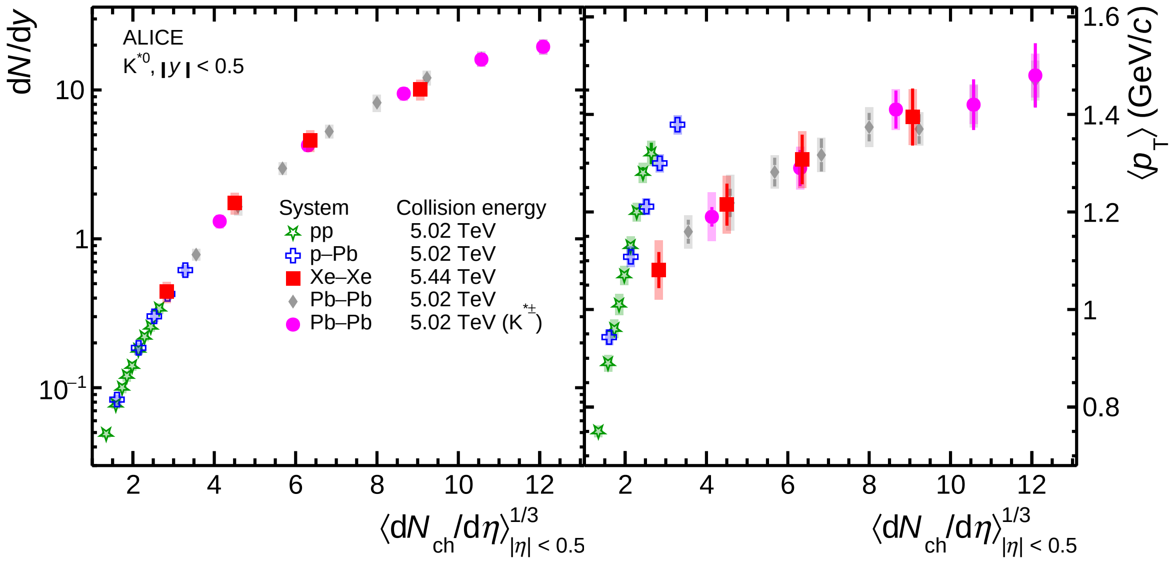

FIGURE 4.10: The dN/dy(left panel) and $\langle p_{\mathrm{T}}\rangle$(right panel) of K* as a function of $\langle \mathrm{d}N_{\mathrm{ch}}/\mathrm{d}\eta\rangle^{1/3}_{|\eta|<0.5}$ in pp collision at $\sqrt{s}$ = 5.02 TeV and in Xe–Xe collisions at $\sqrt{s_{\mathrm{NN}}}$ = 5.44 TeV [25]. Measurements are compared with the results obtained in p–Pb [30] and Pb–Pb [17, 23] collisions at $\sqrt{s_{\mathrm{NN}}}$ = 5.02 TeV. Bars and shaded boxes correspond to the statistical and systematic uncertainties, respectively.

The left panel of Fig. 4.11 presents the comparison of p_{T}-integrated K*/K yield ratio in Pb–Pb [17, 23], Xe–Xe [25], p–Pb [30] and pp collisions [25] as a function of $\langle \mathrm{d}N_{\mathrm{ch}}/\mathrm{d}\eta\rangle^{1/3}_{|\eta|<0.5}$ at akin center-of-mass energies. In the case of pp collisions at $\sqrt{s}$ = 5.02 TeV, the kaon yields are extrapolated from measurements at $\sqrt{s}$ = 13 TeV [28] and $\sqrt{s}$ = 7 TeV [31] utilizing a first-order polynomial fit to the yields as a function of $\langle \mathrm{d}N_{\mathrm{ch}}/\mathrm{d}\eta\rangle^{1/3}_{|\eta|<0.5}$. The uncertainty in the yield estimation is evaluated by constructing Gaussian distributions for each data point, where the mean corresponds to the data point value and the standard deviation (σ) represents the associated statistical or systematic uncertainty. For each data point, random values are sampled from the respective Gaussian distribution under the assumption of uncorrelated data points with multiplicity. Subsequently, linear fits are applied to these randomly sampled values, iterated thousands of times to generate multiple linear fits. The standard deviation of the fitting values obtained from these repetitions is then

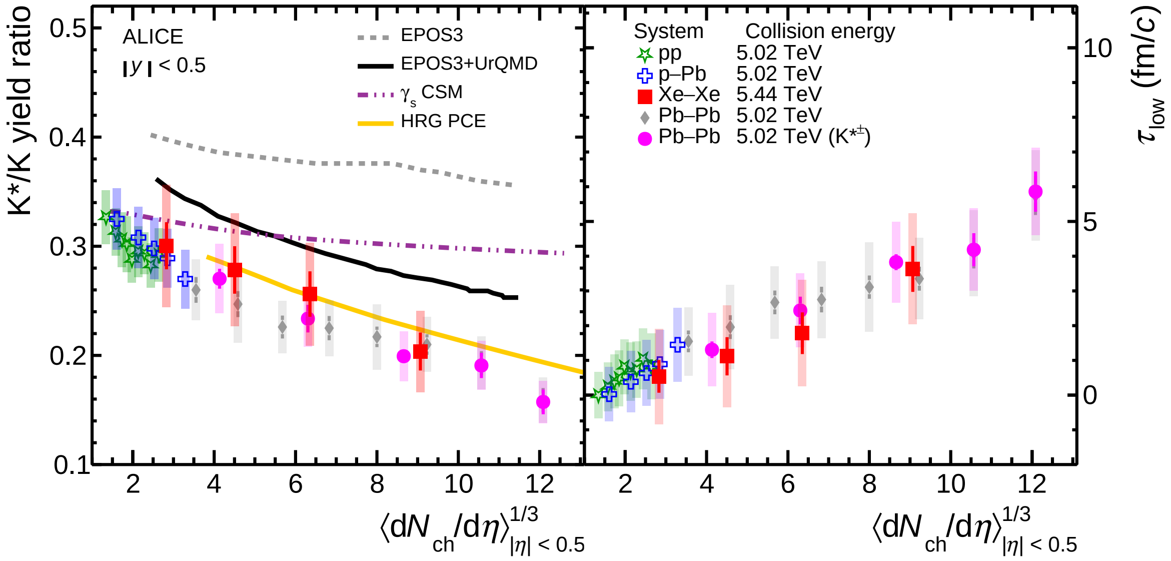

FIGURE 4.11: The left panel shows the measured K*/K yield ratio along with model calculation. The right panel shows the lower limit of hadronic phase lifetime as a function of $\langle dN_{ch}/d\eta\rangle^{1/3}_{|\eta|<0.5}$ in different collision systems [17, 25]. Bars and shaded boxes represent the statistical and systematic uncertainties, respectively.

considered as the yield uncertainty for a given multiplicity. Across various collision systems, the K*/K yield ratio exhibits a smooth evolution with $\langle dN_{ch}/d\eta\rangle^{1/3}_{|\eta|<0.5}$ and remains consistent regardless of the collision system at comparable final-state charged-particle multiplicity. This consistency underscores the smooth evolution of hadron chemistry, as observed for other light-flavor hadrons [32]. Notably, the K*/K yield ratio diminishes with increasing event multiplicity, attributed to rescattering of K* meson decay daughters within the hadronic phase [19]. The significance of suppression of $K^{*\pm}$/K reaches a level of 9.3σ [17], comparable to that observed for K^{*0}/K (6.02σ) [19]. Comparisons with EPOS3 model calculations, with and without the hadronic phase [33], are conducted, alongside examination against the canonical ensemble-based thermal model γ_s CSM [34] and the Hadron Resonance Gas (HRG) model incorporating partial chemical equilibrium (PCE) [1]. EPOS3 stands as an event generator utilizing a 3+1D viscous hydrodynamic evolution, commencing from flux tube initial conditions generated within the Gribov-Regge multiple scattering framework [35]. Each individual scattering event is identified as a Pomeron, represented by a parton ladder that ultimately manifests as flux tubes or strings. The reaction volume is segmented into a core and a corona part [36]. The core serves as the initial condition for the Quark-Gluon Plasma (QGP) evolution, where viscous hydrodynamics is applied, while the corona is comprised of hadrons resulting from string decays. Post-hadronization of the fluid (core part), these hadrons, along with the corona hadrons, are incorporated into UrQMD [37], a model describing hadronic interactions on a microscopic level. The chemical and kinetic freeze-outs take place within this phase. While the EPOS3 generator, particularly with the inclusion of the hadronic phase, qualitatively reproduces the multiplicity dependence of the K^*/K yield ratio, the γ_{s} CSM does not capture this dependency satisfactorily. Conversely, the HRG-PCE calculation accurately describes the measured data points, highlighting the influence of the hadronic phase on the K^*/K yield ratio. Additionally, the K^*/K yield ratio serves as an estimator for the lower bound of the hadronic phase lifetime (τ), representing the duration between chemical and kinetic freeze-out [19]. This relationship is expressed by the formula $[\mathrm{K}^*/\mathrm{K}]_{\mathrm{kinetic}} = [\mathrm{K}^*/\mathrm{K}]_{\mathrm{chemical}} \times e^{-\tau/\tau_{K^*}}$, where τ_{K^*} denotes the vacuum lifetime of K^* [15]. The ratio of $[\mathrm{K}^{*0}/\mathrm{K}]$ in the 70–100% multiplicity class of pp collisions at $\sqrt{s}$ = 13 TeV is utilized as a substitute for $[\mathrm{K}^*/\mathrm{K}]_{\mathrm{chemical}}$. Simultaneously, the measured K^*/K yield ratios across various multiplicity or centrality classes of pp, p–Pb, Xe–Xe, and Pb–Pb collisions serve as representative of $[\mathrm{K}^*/\mathrm{K}]_{\mathrm{kinetic}}$. This methodology aims to estimate the lower limit of τ under the assumption of no K^* regeneration in the hadronic medium. The resulting hadronic phase lifetimes, obtained through this simplified model, undergo further scaling by a Lorentz factor $\sqrt{1 + (\frac{\langle p_{\mathrm{T}} \rangle}{\text{mass of } \mathrm{K}^*})^2}$. The extracted τ values are depicted in the right panel of Fig. 4.11 as a function of $\langle \mathrm{d}N_{\mathrm{ch}}/\mathrm{d}\eta \rangle^{1/3}_{|\eta|<0.5}$. The evolution of the hadronic phase lifetime exhibits a smooth trend with multiplicity. The lifetimes in Xe–Xe and Pb–Pb collisions align consistently at comparable charged-particle multiplicities. To investigate the p_{T} dependence of the rescattering effect, the p_{T}-differential yield ratios are examined. The upper panels of Fig. 4.12 illustrate the p_{T}-differential yield ratios of $\mathrm{K}^{*\pm}/\mathrm{K}$ (a) and $\mathrm{K}^{*\pm}$/pion (b) in Pb−Pb collisions at $\sqrt{s_{\mathrm{NN}}}$ = 5.02 TeV for centrality intervals 0−10% and 60−80%, compared with pp collisions at the same energy [14]. The bottom panels (c and d) present the double ratios. At low p_{T} (< 2 GeV/c), the double ratios $(\mathrm{K}^{*\pm}/\mathrm{K})_{\mathrm{PbPb}}/(\mathrm{K}^{*\pm}/\mathrm{K})_{\mathrm{pp}}$ and $(\mathrm{K}^{*\pm}/\pi)_{\mathrm{PbPb}}/(\mathrm{K}^{*\pm}/\pi)_{\mathrm{pp}}$ exhibit suppression by up to a factor of five. This suppression is more pronounced in central collisions compared to peripheral ones due to a stronger rescattering effect in the larger system formed in central collisions. For p_{T} (> 5 GeV/c), the double ratios are consistent with unity for both central and peripheral collisions, indicating that the rescattering effect primarily manifests at low p_{T}. The lower panels of Figure 4.12 (c and d) depict the comparison of results for $\mathrm{K}^{*\pm}$ and K^{*0} [23] in the 0–10% centrality interval, demonstrating their consistency. In the intermediate p_{T} range (3–5 GeV/c), both double ratios (c and d) display an enhancement in central Pb−Pb collisions compared to peripheral and pp collisions. This enhancement, particularly pronounced for the K^{*}/π yield ratio, aligns with the notion of larger radial flow in the most central Pb–Pb collisions relative to peripheral Pb–Pb and pp collisions [28].

The duration of the hadronic phase is inferred from the temperature discrepancy between chemical and kinetic freeze-out. The kinetic freeze-out temperature is derived using the HRG-PCE model [1], fitting it to the experimentally measured yields of π, K, p, ϕ, K^{*0}, and $\mathrm{K}^{*\pm}$ in Pb−Pb collisions at $\sqrt{s_{\mathrm{NN}}}$ = 5.02 TeV. The parameters in the fit include the baryon chemical potential, chemical freeze-out temperature, kinetic freeze-out temperature, and freeze-out volume of the system. At LHC energies, the baryon chemical potential and chemical freeze-out temperature are held fixed at 0 and 155 MeV, respectively [38–41]. The

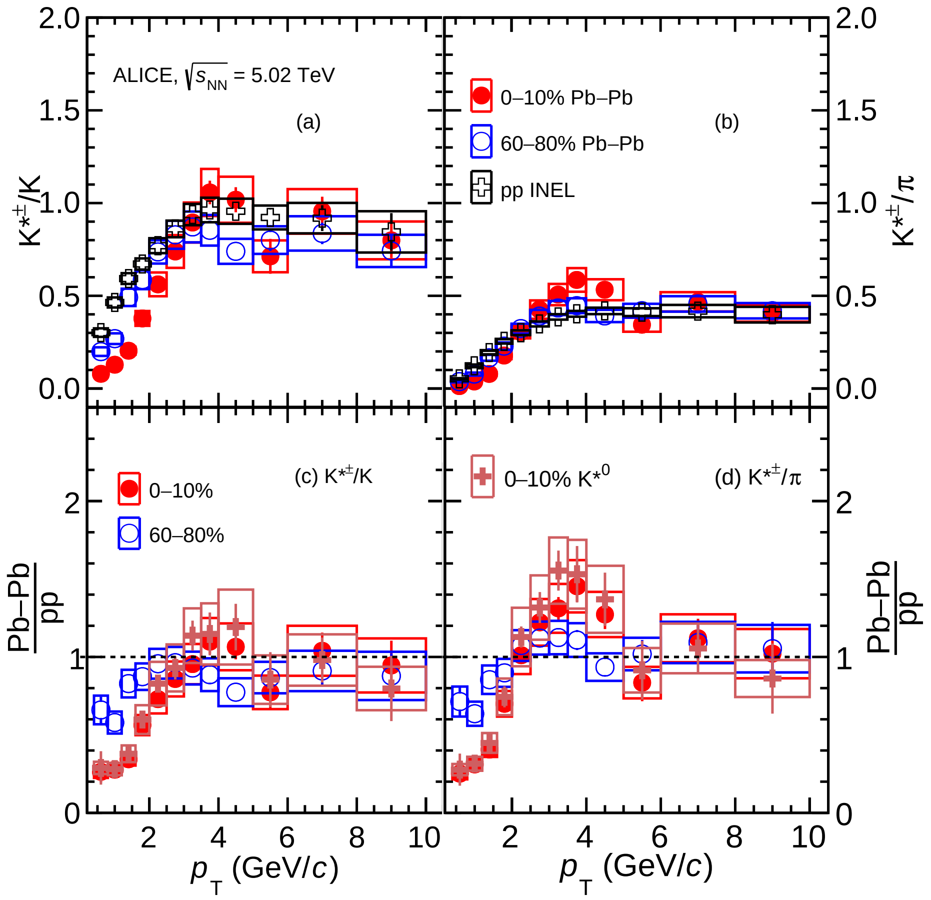

FIGURE 4.12: The $p_{\rm T}$-differential particle yield ratios $K^{*\pm}/K$ (a) and $K^{*\pm}/\pi$(b) in pp (black marker) and Pb−Pb collisions at $\sqrt{s_{\rm NN}}$= 5.02 TeV for 0−10% (red marker) and 60−80% (blue marker) centrality intervals. The bottom panels (c) and (d) show the ratios of Pb−Pb to pp results, compared with 0−10% K^{*0} results [23]. Statistical uncertainties are shown by bars and systematic uncertainties by boxes. The statistical and systematic uncertainties on the data points are obtained by propagating the statistical and total systematic uncertainties of the measurements. The figure is taken from [17]

fitting procedure employing the HRG-PCE model to the data is incorporated in THERMAL-FIST [42], which is a C++ package designed to compute HRG observables for a specified configuration. The configuration encompasses particle lists, particle interaction types, thermal parameters, conservation laws constraints etc. The calculations presented in this chapter are conducted in the Grand-Canonical ensemble. The kinetic freze-out temperature is estimated for five distinct centrality intervals: 0−10%, 10−20%, 20−40%, 40−60%, and 60−80%, as presented in Table 4.4, and is compared with blast-wave fit results of $\pi^{\pm}$, $K^{\pm}$, and $p(\overline{p})$ [43]. The fitting of p_{T} spectra within the blast-wave model relies on assumptions regarding the flow velocity profile and the freeze-out hypersurface. Conversely, the HRG-PCE model operates without such assumptions. Table 4.4 demonstrates that outcomes from the HRG-PCE model align within uncertainties with the blast-wave model results [43].

TABLE 4.4: HRG-PCE model fits results in Pb−Pb collisions at $\sqrt{s_{\rm NN}}$ = 5.02 TeV. Numbers in brackets show the published kinetic freeze-out temperatures obtained using blast-wave fits to $\pi^{\pm}$, $K^{\pm}$, $p(\overline{p})$ spectra [43].

Centrality (%)	$T_{\rm kin}$ **(MeV)**	χ^2**/Ndf**
0−10	95 ± 3 (91 ± 3)	2.25
10−20	104 ± 4 (94 ± 3)	2.17
20−40	109 ± 5 (99 ± 3)	1.48
40−60	116 ± 6 (112 ± 3)	0.77
60−80	124 ± 8 (138 ± 6)	1.63

The extracted kinetic freeze-out temperature increases from 95 MeV in 0−10% Pb−Pb collisions to 124 MeV in 60−80% Pb−Pb collisions. The results indicate the presence of the hadronic phase of a finite lifetime in heavy-ion collisions, longer lived in central collision and shorter in peripheral collision.

The left panel of Fig. 4.13 illustrates the species-specific behavior of $R_{\rm AA}$ for 0−10% Pb−Pb collisions at $\sqrt{s_{\rm NN}}$ = 5.02 TeV, encompassing species ranging in mass from 0.139 GeV/c^2 for pions to 1.020 GeV/c^2 for the ϕ meson, considering both baryons and mesons. At low $p_{\rm T}$(< 2 GeV/c), $K^{*\pm}$ and K^{*0} exhibit the smallest $R_{\rm AA}$ values among the listed hadrons, aligning with expectations based on the rescattering effect. In the intermediate momentum range of 2-7 GeV/c, $R_{\rm AA}$ shows species dependence with an evidence of baryon-meson splitting. Influences such as radial flow, parton recombination, enhanced strangeness production, steepness of particle $p_{\rm T}$ spectra in reference pp collisions, etc.,

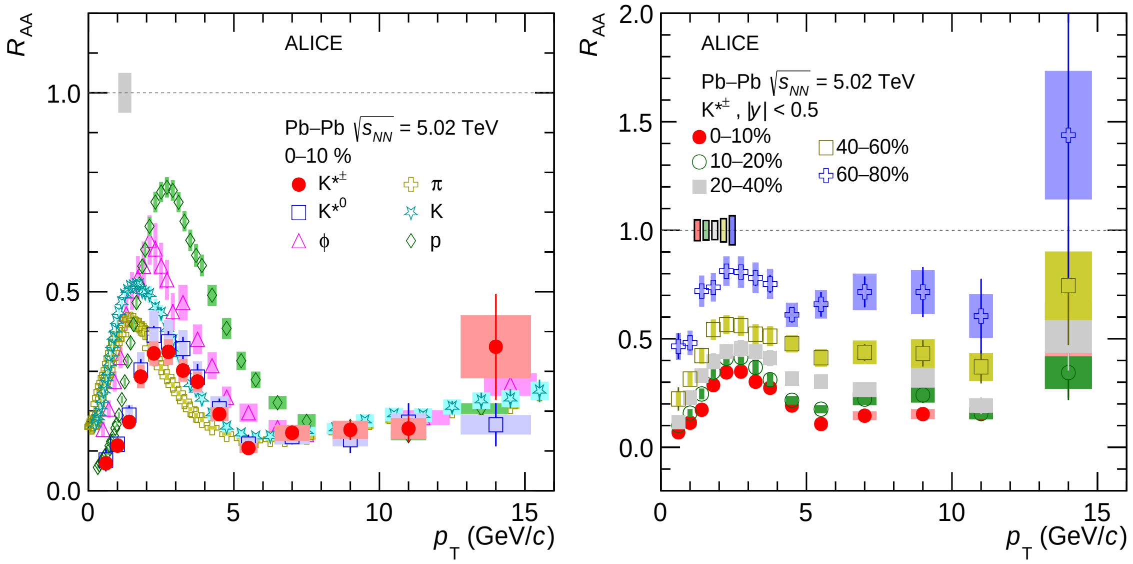

FIGURE 4.13: Left panel shows the R_{AA} comparison of various light-flavored hadrons [23, 44, 45], and the right panel shows the R_{AA} of $\mathrm{K}^{*\pm}$ for different centrality intervals both as a function of p_{T} in Pb−Pb collisions at $\sqrt{s_{\mathrm{NN}}}$ = 5.02. Statistical (systematic) uncertainties are shown by bars (shaded boxes). The shaded bands around unity reprsents the normalisation uncertainty on R_{AA}. The figure is taken from [17].

contribute to R_{AA} measurements in this p_{T} range, presenting challenges in disentangling their individual effects from R_{AA} measurements alone. For $p_{\mathrm{T}} > 8$ GeV/c, all particle species exhibit similar R_{AA} values within the uncertainties. Both light quark suppression and gluon suppression contribute to the charged hadrons R_{AA} [46]. This observation also suggests that the suppression of various light-flavored hadrons is independent of their quark content and mass. This finding constraints models that address fragmentation and energy loss mechanisms. The right panel of Fig. 4.13 portrays the evolution of R_{AA} values with centrality for $\mathrm{K}^{*\pm}$. The smallest R_{AA} is observed in the most central collisions, gradually increasing towards more peripheral collisions, similar to other light hadrons. These findings are consistent with centrality-dependent energy loss of partons in the medium.

4.5 Summary

The inaugural measurement of the $\mathrm{K}^{*\pm}$ (K^{*0}) resonance in Pb−Pb (pp) collisions has been conducted at $\sqrt{s_{\mathrm{NN}}}$ = 5.02 TeV using the ALICE detector. The transverse-momentum spectra are presented at midrapidity up to p_{T} = 16 GeV/c (14 GeV/c) in different centrality (multiplicity) intervals. A notable consistency is observed between the presented $\mathrm{K}^{*\pm}$ results and the previously published K^{*0} measurements in Pb–Pb collisions. The p_{T}-integrated K^{*} yield and $\mathrm{K}^{*}/\mathrm{K}$ yield ratio exhibit a smooth evolution with $\langle \mathrm{d}N_{\mathrm{ch}}/\mathrm{d}\eta \rangle^{1/3}_{|\eta|<0.5}$, irrespective of the colliding nuclei's size. This confirms a universal scaling of hadron chemistry or relative abundance of hadron species with final-state charged-particle multiplicity at LHC energies. However, the $\langle p_{\mathrm{T}} \rangle$, dependent on the radial expansion velocity of the produced matter, rises more sharply in smaller collision systems compared to heavy-ion collisions. This implies a more rapid expansion of matter in small collision systems. The $\mathrm{K}^{*}/\mathrm{K}$ ratio decreases with increasing final-state charged-particle multiplicity, pointing towards the rescattering of K^{*} decay daughters in the hadronic phase. Additionally, the p_{T}-differential yield ratio $\mathrm{K}^{*}/\mathrm{K}$ supports the dominance of rescattering effects at low p_{T}. The kinetic freeze-out temperature, determined in different centrality intervals using the HRG-PCE model fit to the experimental data at a fixed chemical freeze-out temperature, suggests a longer-lived hadronic phase in central collisions compared to peripheral collisions. These results align with predictions from blast-wave fits to pion, kaon, and proton p_{T} spectra. Examining the nuclear modification factor (R_{AA}) for K^{*} reveals values below unity across all centralities, consistent with parton energy loss in the hot and dense medium. R_{AA} values are smaller in more central collisions, gradually increasing towards peripheral collisions, with no observed species dependence at high p_{T}.

Bibliography

[1] Anton Motornenko et al. “Kinetic freeze-out temperature from yields of short-lived resonances”. *Phys. Rev. C* 102.2 (2020), p. 024909. arXiv: `1908.11730 [hep-ph]`.

[2] Betty Bezverkhny Abelev et al. “Performance of the ALICE Experiment at the CERN LHC”. *Int. J. Mod. Phys. A* 29 (2014), p. 1430044. arXiv: `1402.4476 [nucl-ex]`.

[3] K. Aamodt et al. “The ALICE experiment at the CERN LHC”. *JINST* 3 (2008), S08002.

[4] E. Abbas et al. “Performance of the ALICE VZERO system”. *JINST* 8 (2013), P10016. arXiv: `1306.3130 [nucl-ex]`.

[5] Shreyasi Acharya et al. “Multiplicity dependence of (multi-)strange hadron production in proton-proton collisions at $\sqrt{s}$ = 13 TeV”. *Eur. Phys. J. C* 80.2 (2020), p. 167. arXiv: `1908.01861 [nucl-ex]`.

[6] Jaroslav Adam et al. “Pseudorapidity and transverse-momentum distributions of charged particles in proton–proton collisions at $\sqrt{s}$ = 13 TeV”. *Phys. Lett. B* 753 (2016), pp. 319–329. arXiv: `1509.08734 [nucl-ex]`.

[7] Shreyasi Acharya et al. “Centrality and pseudorapidity dependence of the charged-particle multiplicity density in Xe–Xe collisions at $\sqrt{s_{\mathrm{NN}}}$ = 5.44 TeV”. *Phys. Lett. B* 790 (2019), pp. 35–48. arXiv: `1805.04432 [nucl-ex]`.

[8] Shreyasi Acharya et al. “Charged-particle production as a function of multiplicity and transverse spherocity in pp collisions at $\sqrt{s}$ = 5.02 and 13 TeV”. *Eur. Phys. J. C* 79.10 (2019), p. 857. arXiv: `1905.07208 [nucl-ex]`.

[9] Shreyasi Acharya et al. “Pseudorapidity distributions of charged particles as a function of mid- and forward rapidity multiplicities in pp collisions at $\sqrt{s}$ = 5.02, 7 and 13 TeV”. *Eur. Phys. J. C* 81.7 (2021), p. 630. arXiv: `2009.09434 [nucl-ex]`.

[10] B Abelev et al. “Technical Design Report for the Upgrade of the ALICE Inner Tracking System”. *J. Phys. G* 41 (2014), p. 087002.

[11] J. Alme et al. “The ALICE TPC, a large 3-dimensional tracking device with fast readout for ultra-high multiplicity events”. *Nucl. Instrum. Meth.* A622 (2010), pp. 316–367. arXiv: `1001.1950 [physics.ins-det]`.

[12] G. Dellacasa et al. “ALICE technical design report of the time-of-flight system (TOF)”. *CERN-LHCC-2000-012* ().

[13] Francesca Carnesecchi. “Performance of the ALICE Time-Of-Flight detector at the LHC”. *JINST* 14.06 (2019), p. C06023. arXiv: `1806.03825 [physics.ins-det]`.

[14] Shreyasi Acharya et al. “Measurement of $K^*(892)^{\pm}$ production in inelastic pp collisions at the LHC”. *Phys. Lett. B* 828 (2022), p. 137013. arXiv: `2105.05760 [nucl-ex]`.

[15] R. L. Workman et al. “Review of Particle Physics”. *PTEP* 2022 (2022), p. 083C01.

[16] Shreyasi Acharya et al. “Multiplicity dependence of $K^*(892)^0$ and $\phi(1020)$ production in pp collisions at $\sqrt{s}$ =13 TeV”. *Phys. Lett. B* 807 (2020), p. 135501. arXiv: `1910.14397 [nucl-ex]`.

[17] Shreyasi Acharya et al. “$K^*(892)^{\pm}$ resonance production in Pb−Pb collisions at $\sqrt{s_{\mathrm{NN}}}$ = 5.02 TeV” (Aug. 2023). arXiv: `2308.16119 [nucl-ex]`.

[18] Jaroslav Adam et al. “$K^*(892)^0$ and $\phi(1020)$ meson production at high transverse momentum in pp and Pb-Pb collisions at $\sqrt{s_{\mathrm{NN}}}$ = 2.76 TeV”. *Phys. Rev. C* 95.6 (2017), p. 064606. arXiv: `1702.00555 [nucl-ex]`.

[19] Shreyasi Acharya et al. “Evidence of rescattering effect in Pb–Pb collisions at the LHC through production of $K^*(892)^0$ and $\phi(1020)$ mesons”. *Phys. Lett. B* 802 (2020), p. 135225. arXiv: `1910.14419 [nucl-ex]`.

[20] Peter Skands, Stefano Carrazza, and Juan Rojo. “Tuning PYTHIA 8.1: the Monash 2013 Tune”. *Eur. Phys. J. C* 74.8 (2014), p. 3024. arXiv: `1404.5630 [hep-ph]`.

[21] Xin-Nian Wang and Miklos Gyulassy. “HIJING: A Monte Carlo model for multiple jet production in pp, pA and AA collisions”. *Phys. Rev. D* 44 (1991), pp. 3501–3516.

[22] R Brun et al. “GEANT Detector Description and Simulation Tool”. *CERN Program Library, CERN, Geneva* (1993).

[23] Shreyasi Acharya et al. “Production of $K^*(892)^0$ and $\phi(1020)$ in pp and Pb–Pb collisions at $\sqrt{s_{\mathrm{NN}}}$ = 5.02 TeV”. *Phys. Rev. C* 106.3 (2022), p. 034907. arXiv: `2106.13113 [nucl-ex]`.

[24] Constantino Tsallis. “Possible Generalization of Boltzmann-Gibbs Statistics”. *J. Statist. Phys.* 52 (1988), pp. 479–487.

[25] Shreyasi Acharya et al. “System-size dependence of the hadronic rescattering effect at energies available at the CERN Large Hadron Collider”. *Phys. Rev. C* 109.1 (2024), p. 014911. arXiv: `2308.16115 [nucl-ex]`.

[26] Shreyasi Acharya et al. “Production of light-flavor hadrons in pp collisions at $\sqrt{s}$ = 7 and $\sqrt{s}$ = 13 TeV”. *Eur. Phys. J. C* 81.3 (2021), p. 256. arXiv: `2005.11120 [nucl-ex]`.

[27] K. Aamodt et al. “Two-pion Bose-Einstein correlations in central Pb-Pb collisions at $\sqrt{s_{NN}}$ = 2.76 TeV”. *Phys. Lett. B* 696 (2011), pp. 328–337. arXiv: `1012.4035 [nucl-ex]`.

[28] Shreyasi Acharya et al. “Multiplicity dependence of π, K, and p production in pp collisions at $\sqrt{s}$ = 13 TeV”. *Eur. Phys. J. C* 80.8 (2020), p. 693. arXiv: `2003.02394 [nucl-ex]`.

[29] Ulrich W. Heinz and J. Scott Moreland. “Hydrodynamic flow in small systems or: “How the heck is it possible that a system emitting only a dozen particles can be described by fluid dynamics?”” *J. Phys. Conf. Ser.* 1271.1 (2019), p. 012018. arXiv: `1904.06592 [nucl-th]`.

[30] Jaroslav Adam et al. “Production of K* (892)^0 and ϕ (1020) in p–Pb collisions at $\sqrt{s_{\mathrm{NN}}}$= 5.02 TeV”. *Eur. Phys. J. C* 76.5 (2016), p. 245. arXiv: `1601.07868 [nucl-ex]`.

[31] Shreyasi Acharya et al. “Multiplicity dependence of light-flavor hadron production in pp collisions at $\sqrt{s}$ = 7 TeV”. *Phys. Rev. C* 99.2 (2019), p. 024906. arXiv: `1807.11321 [nucl-ex]`.

[32] Shreyasi Acharya et al. “Production of pions, kaons, (anti-)protons and ϕ mesons in Xe–Xe collisions at $\sqrt{s_{\mathrm{NN}}}$ = 5.44 TeV”. *Eur. Phys. J. C* 81.7 (2021), p. 584. arXiv: `2101.03100 [nucl-ex]`.

[33] A. G. Knospe et al. “Hadronic resonance production and interaction in partonic and hadronic matter in the EPOS3 model with and without the hadronic afterburner UrQMD”. *Phys. Rev. C* 93.1 (2016), p. 014911. arXiv: `1509.07895 [nucl-th]`.

[34] Volodymyr Vovchenko, Benjamin Dönigus, and Horst Stoecker. "Canonical statistical model analysis of pp , p–Pb, and Pb–Pb collisions at energies available at the CERN Large Hadron Collider". *Phys. Rev. C* 100.5 (2019), p. 054906. arXiv: 1906.03145 [hep-ph].

[35] H. J. Drescher et al. "Parton based Gribov-Regge theory". *Phys. Rept.* 350 (2001), pp. 93–289. arXiv: hep-ph/0007198.

[36] Klaus Werner. "Core-corona separation in ultra-relativistic heavy ion collisions". *Phys. Rev. Lett.* 98 (2007), p. 152301. arXiv: 0704.1270 [nucl-th].

[37] M. Bleicher et al. "Relativistic hadron hadron collisions in the ultrarelativistic quantum molecular dynamics model". *J. Phys. G* 25 (1999), pp. 1859–1896. arXiv: hep-ph/9909407.

[38] Fernando Antonio Flor, Gabrielle Olinger, and René Bellwied. "System size and flavour dependence of chemical freeze-out temperatures in ALICE data from pp, pPb and PbPb collisions at LHC energies". *Phys. Lett. B* 834 (2022), p. 137473. arXiv: 2109.09843 [nucl-ex].

[39] Anton Andronic et al. "Decoding the phase structure of QCD via particle production at high energy". *Nature* 561.7723 (2018), pp. 321–330. arXiv: 1710.09425 [nucl-th].

[40] Volodymyr Vovchenko, Benjamin Dönigus, and Horst Stoecker. "Multiplicity dependence of light nuclei production at LHC energies in the canonical statistical model". *Phys. Lett. B* 785 (2018), pp. 171–174. arXiv: 1808.05245 [hep-ph].

[41] Shreyasi Acharya et al. "Measurements of chemical potentials in Pb-Pb collisions at $\sqrt{s_{\mathrm{NN}}} = 5.02$ TeV" (Nov. 2023). arXiv: 2311.13332 [nucl-ex].

[42] Volodymyr Vovchenko and Horst Stoecker. "Thermal-FIST: A package for heavy-ion collisions and hadronic equation of state". *Comput. Phys. Commun.* 244 (2019), pp. 295–310. arXiv: 1901.05249 [nucl-th].

[43] Shreyasi Acharya et al. "Production of charged pions, kaons, and (anti-)protons in Pb–Pb and inelastic pp collisions at $\sqrt{s_{\mathrm{NN}}} = 5.02$ TeV". *Phys. Rev. C* 101.4 (2020), p. 044907. arXiv: 1910.07678 [nucl-ex].

[44] B. Abelev et al. "$\mathrm{K}^*(892)^0$ and $\phi(1020)$ production in Pb–Pb collisions at $\sqrt{s_{\mathrm{NN}}} = 2.76$ TeV". *Phys. Rev. C* 91 (2015), p. 024609. arXiv: 1404.0495 [nucl-ex].

[45] B. Abelev et al. “Production of charged pions, kaons and protons at large transverse momenta in pp and Pb–Pb collisions at $\sqrt{s_{\mathrm{NN}}} = 2.76$ TeV”. *Phys. Lett. B* 736 (2014), pp. 196–207. arXiv: `1401.1250 [nucl-ex]`.

[46] Magdalena Djordjevic. “Heavy flavor puzzle at LHC: a serendipitous interplay of jet suppression and fragmentation”. *Phys. Rev. Lett.* 112.4 (2014), p. 042302. arXiv: `1307.4702 [nucl-th]`.

CHAPTER 5

Measurement of production cross section of an exotic $f_1(1285)$ resonance in ALICE

Contents

5.1 Analysis details 130
5.2 Systematic uncertainties 138
5.3 Results 140
5.4 Summary 146

A Appendix **155**
A.1 CMW systematic uncertainties 155
A.2 BlastWave LCC model 202

This study introduces the first measurement of the exotic $f_1(1285)$ resonance using the ALICE detector in inelastic proton-proton collisions at a center-of-mass energy of 13 TeV.

The resonance is reconstructed at midrapidity ($|y| < 0.5$) via the hadronic decay channel $f_1 \rightarrow K^0_S K^\mp \pi^\pm$. Key observations include the determination of its mass, transverse momentum integrated yield, and average transverse momentum. Furthermore, the ratio of the transverse momentum integrated yield of $f_1(1285)$ to that of pions is compared with calculations from the canonical statistical thermal model. The thermal model calculation, assuming zero total strangeness content for $f_1(1285)$, demonstrates consistency with the data within a deviation of 1σ, providing insights into the quark composition of $f_1(1285)$. These measurements in proton-proton collisions establish a valuable foundation for exploring the partial restoration of chiral symmetry and conducting a systematic analysis of hadronic rescattering effects in heavy-ion collisions.

5.1 Analysis details

5.1.1 Data sample, event and track selections

The dataset, collected during the years 2016, 2017, and 2018 under a magnetic field strength (B) of 0.5 T, is obtained via a minimum bias (MB) trigger, which necessitates simultaneous signals in both the V0A and V0C detectors. Selected events are ensured to possess a primary collision vertex within ±10 cm along the beam axis from the ALICE detector's nominal center. Offline event selection processes outlined in Refs. [1, 2] are employed to remove beam-induced background and pileup events. After applying all event selection criteria, around 1.5 billion minimum-bias events are subjected to analysis.

Due to the short-lived nature of the $f_1(1285)$ meson, its reconstruction is executed via the hadronic decay channel, $f_1 \rightarrow K^0_S K^\mp \pi^\pm$, considering a branching ratio (BR) of $(2.25 \pm 0.001)\%$ [3]. This encompasses all potential combinations of kaons and pions, with a 0.5 probability for a K^0 to be reconstructed as K^0_S. The analysis covers a transverse momentum range from 1 GeV/c to 12 GeV/c. At low-p_{T} (< 1 GeV/c), the $f_1(1285)$ signal is not statistically significant due to the presence of substantial background. Primary charged tracks within a selected event are reconstructed utilizing the ITS [4] and TPC [5] detectors. A set of track selection criteria, in line with previous studies [6, 7], is applied to ensure high track quality. Charged tracks originating from the primary collision vertex are chosen with a minimum p_{T} of 0.15 GeV/c and $|\eta| < 0.8$. These selected tracks must register at least one hit in the two innermost layers of the ITS and traverse a minimum of 70 out of the total 159 rows along the transverse readout plane of the TPC. The maximum χ^2 per space point in the TPC and ITS, derived from the track fit, is stipulated to be 4 and 36, respectively. To mitigate the influence of secondary charged particles, the distance of the closest approach in the transverse plane of reconstructed tracks to the primary vertex ($\mathrm{DCA_{xy}}$) is kept to be smaller than 7σ, where σ signifies the $\mathrm{DCA_{xy}}$ resolution. The p_{T}-dependent $\mathrm{DCA_{xy}}$ resolution is modeled as $\sigma = 0.0105 + 0.0350/(p_{\mathrm{T}})^{1.1}$. The DCA in the longitudinal direction is ensured to be smaller than 2 cm. Identified charged particles are discerned utilizing information from the TPC and TOF [8] detectors based on their specific ionization energy loss ($\mathrm{d}E/\mathrm{d}x$) in the TPC and flight time measured in the TOF. Pions (π) and kaons (K) are identified by ensuring their specific energy loss falls within 2 standard deviations (σ_{TPC}) from the expected $\mathrm{d}E/\mathrm{d}x$ values, where σ_{TPC} denotes the TPC's $\mathrm{d}E/\mathrm{d}x$ resolution, typically around 5% of the measured $\mathrm{d}E/\mathrm{d}x$ value. Additionally, if the track registers a hit in the TOF, the measured time of flight must be within 3σ of its expected value for each particle species [9].

The reconstruction of the $\mathrm{K^0_S}$ proceeds through its weak decay topology ($\mathrm{V^0}$ topology) [10], where it decays into two oppositely charged pions ($\mathrm{K^0_S} \rightarrow \pi^-\pi^+$) with a branching ratio of $(69.2 \pm 0.05)\%$ [3]. Detailed selection criteria for $\mathrm{K^0_S}$ reconstruction are outlined in Table 5.1. Pions (the daughters of $\mathrm{K^0_S}$) are identified as two oppositely charged tracks within the acceptance window $|\eta| < 0.8$, employing a $4\sigma_{\mathrm{TPC}}$ selection criterion. The distance of closest approach (DCA) between negatively and positively charged tracks must be less than 1.0 cm. Additionally, the DCA of charged tracks and the V^0 to the primary vertex must be greater than 0.06 cm and less than 0.3 cm, respectively. The cosine of the pointing angle, representing the angle between the V^0 momentum and the line connecting the secondary to the primary vertex, must be greater than 0.97. Only K^0_S candidates with a radius of the reconstructed secondary vertex larger than 0.5 cm are considered. Moreover, candidates with a proper lifetime exceeding 15 cm, calculated as $LM_{\mathrm{K}^0_\mathrm{S}}/p$, where L denotes the linear distance between the primary and secondary vertex, $M_{\mathrm{K}^0_\mathrm{S}}$ is the mass of K^0_S and p indicates the total momentum of K^0_S, are excluded to reduce the presence of combinatorial background from interactions with the detector material. Competing V0 rejection is also implemented: the V0 mass is recalculated assuming that one of the pions is a (anti-)proton, and the V0 candidates are rejected if their mass is compatible with the Λ mass within $\pm$ 0.0043 GeV/c^2, which is approximately three times the typical mass resolution for the reconstructed Λ in ALICE [11]. Finally, the invariant mass of $\pi^+\pi^-$ must be compatible within 6σ of the K^0_S nominal mass, where σ represents the detector mass resolution, approximately equal to ~5 MeV/c^2. Following all these topological criteria, only K^0_S candidates with $|y| < 0.8$ are included in the analysis.

5.1.2 Signal extraction

Initially, the reconstruction of K^0_S involves utilizing the weak decay topology described in Section 5.1.1. Following this, the reconstructed K^0_S is paired with charged kaons to form a $\mathrm{K}^0_\mathrm{S}\mathrm{K}$ pair. Subsequently, this pair is combined with oppositely charged pions in the same event to reconstruct the $f_1(1285)$ resonance. An invariant mass selection, $\mathrm{M}_{\mathrm{K}^0_\mathrm{S}\mathrm{K}}$ < 1.04 GeV/c^2, is imposed on the $\mathrm{K}^0_\mathrm{S}\mathrm{K}$ pair to enhance the significance of the $\mathrm{f}_1(1285)$

TABLE 5.1: Selection criteria for K^0_S.

Selection criteria	Value	Variations
Crossed rows	>70	-
Acceptance window of pions ($\|\eta\|$)	< 0.8	-
Pion dE/dx (σ)	<4	5
DCA V^0 daughters	< 1.0 cm	0.8 cm
DCA of V^0 daughters to PV	> 0.06 cm	0.08 cm
DCA of V^0 to PV	< 0.3 cm	-
V^0 cosine pointing angle	> 0.97	0.98
V^0 radius	> 0.5 cm	0.8 cm
Proper lifetime	< 15 cm	12 cm
Competing V0 rejection	> 0.0043 GeV/c^2	-
K^0_S mass window (σ)	± 6	-

signal. The resulting invariant mass distribution of unlike-sign $K^0_S K\pi$ pairs comprises three resonances ($f_1(1285)$, $f_1(1420)$, and $\eta(1475)$) amidst a considerable combinatorial background. This combinatorial background is estimated using uncorrelated like-sign $K^0_S K\pi$ pairs, extracted from the same event [6, 12]. Like-sign pairs are preferred over mixed-event pairs for a more accurate representation of the combinatorial background. The left panel of Fig. 5.1 illustrates the invariant-mass distribution of unlike-sign $K^0_S K\pi$ pairs from the same event, along with the like-sign background, in the transverse momentum range $3 < p_T < 4$ GeV/c in inelastic pp collisions at $\sqrt{s}$= 13 TeV. The right panel of Fig. 5.1 presents the invariant mass distribution of unlike-sign $K^0_S K\pi$ pairs after subtracting the like-sign background. This combinatorial background-subtracted invariant mass distribution includes the three resonances ($f_1(1285)$, $f_1(1420)$, and $\eta(1475)$) along with a residual background of correlated pairs.

The correlated background pairs may originate from various sources, including jets, decays of resonances with misidentified daughters, and decays with multiple daughters [12]. The invariant mass distribution after subtracting the combinatorial background is then fitted

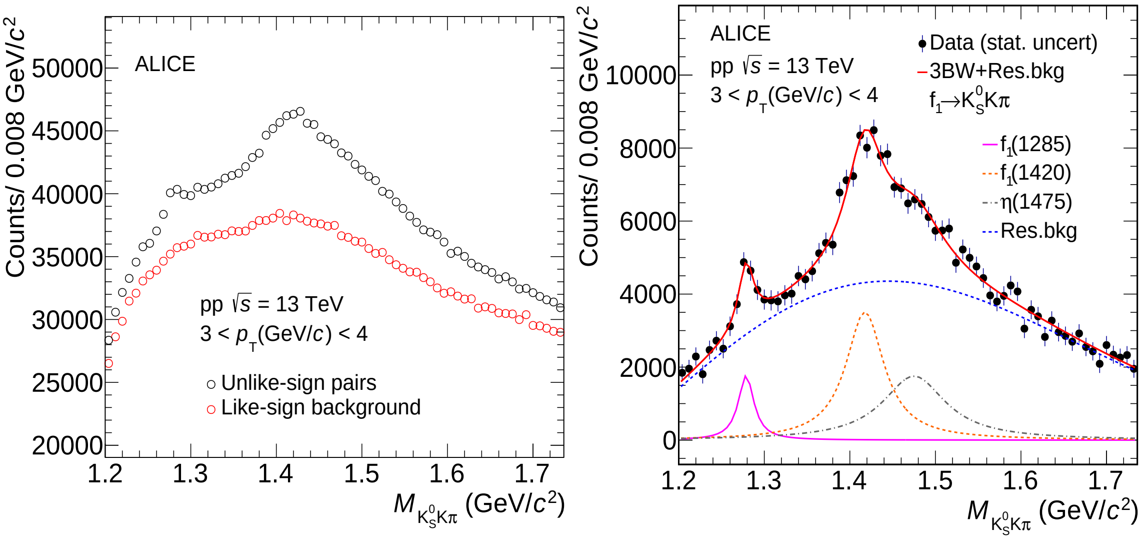

FIGURE 5.1: In the left panel, the invariant mass distribution is presented for both unlike (black markers) and like-sign (red markers) $\mathrm{K_S^0K}\pi$ pairs originating from the same events. Meanwhile, the right panel displays the invariant mass distribution of $\mathrm{K_S^0K}\pi$ pairs after subtracting the like-sign background. The solid red curve is the fit function defined by Eq. 5.1, with the dotted blue line describing the residual background distribution is given by Eq. 5.2.

using a sum of three non-relativistic Breit–Wigner distributions [12, 13] (described by Eq. 5.1) and a combination of an exponential function and a second-order polynomial [13] (described by Eq. 5.2). These three Breit–Wigner distributions correspond to the signals of the $f_1(1285)$, $f_1(1420)$, and $\eta(1475)$ mesons, respectively, while the residual background is modeled using a combined function of an exponential and a second-order polynomial. The resulting fit function can be expressed as:

$$\frac{\mathrm{d}N^c}{\mathrm{dM}} = \sum_{i=1}^{3} \frac{Y_i}{2\pi} \frac{\Gamma_i}{(M - M_i)^2 + \Gamma_i^2/4} + \mathrm{Res.bkg}, \tag{5.1}$$

where the index i traverses the three resonances ($f_1(1285)$, $f_1(1420)$, and $\eta(1475)$). M_i, Γ_i, and Y_i represent the masses, widths, and normalization constants of these three resonances, respectively. M denotes the invariant mass of the $\mathrm{K_S^0K}\pi$ pair ($M_{\mathrm{K_S^0K}\pi}$). Since the mass resolution of the detector for reconstructing $f_1(1285)$ is negligible compared to its vacuum width (0.022 ± 0.001) GeV/c^2 [3], it is not accounted for in the fit function. The final term in Eq. 5.1 represents a residual background function (Res.bkg) and is specified as [13].

$$\text{Res.bkg} = [M - (m_\pi + M_{\mathrm{K^0_S K}})]^{\mathrm{n}}\exp(-\mathrm{A}M - \mathrm{B}M^2), \tag{5.2}$$

where m_π and $M_{\mathrm{K^0_S K}}$ are the masses of pion, and $\mathrm{K^0_S K}$ pair, respectively. Here A, B, and n are the fit parameters. In the default fitting scenario, the width parameters of the three resonances, denoted as Γ_i, are held constant at their vacuum values [3], which are 0.022, 0.054, and 0.090 GeV/c^2, respectively. The masses, indicated by M_i, are left unconstrained. The significance of $f_1(1285)$ signal presented in Fig. 5.1 is 7.54. Finally, the raw yields of $f_1(1285)$ within each p_{T} interval are derived from the integral of the Breit–Wigner distribution, following the procedure outlined in Refs. [6, 14].

The initially extracted raw yields (N^{raw}) undergo further adjustments for detector acceptance and reconstruction efficiency ($A \times \epsilon_{\mathrm{rec}}$) as well as the branching ratio (BR) of the decay channel. The estimation of $A \times \epsilon_{\mathrm{rec}}$ involves employing an injected Monte Carlo (MC) event generator, PYTHIA8 [15], where particles are propagated through a simulation of the ALICE detector using GEANT3 [16]. The $A \times \epsilon_{\mathrm{rec}}$ as a function of p_{T} is shown in Fig. 5.2.

Furthermore the simulated resonance spectra used in the $A \times \epsilon_{\mathrm{rec}}$ calculation may have different shapes than the measured resonance spectra and $A \times \epsilon_{\mathrm{rec}}$ may vary significantly over the width of a p_{T} bin in the measured spectrum at low p_{T}. Therefore, a re-weighting procedure of simulated and measured p_{T} spectra is carried out to consider the shape of the simulated p_{T} distribution as well as the change in $A \times \epsilon_{\mathrm{rec}}$ over the width of a p_{T} bin at low p_{T}. Figure. 5.3 shows the generated and reconstructed $f_1(1285)$ spectrum plotted

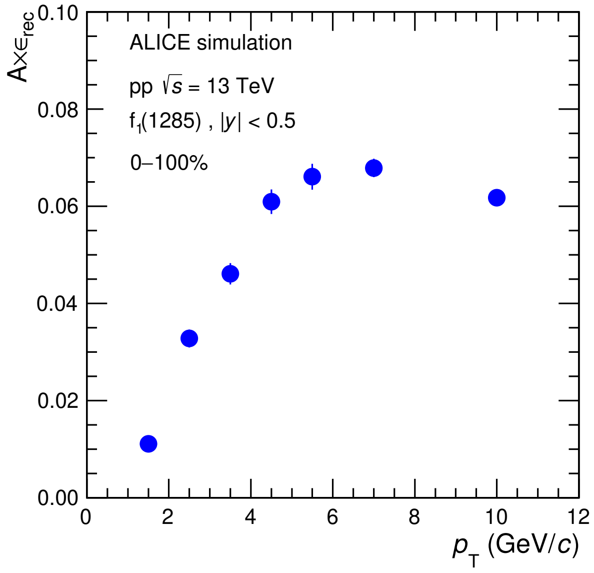

FIGURE 5.2: Efficiency times acceptance of $f_1(1285)$ as a function of transverse momentum in inelastic pp collisions at $\sqrt{s}$= 13 TeV.

along with the measured ($A \times \epsilon_{\text{rec}}$ corrected) $f_1(1285)$ spectrum. An iterative procedure is performed to determine the correct weighting and therefore the correct $A \times \epsilon_{\text{rec}}$.

- $A \times \epsilon_{\text{rec}}$ is calculated from MC generated and reconstructed p_{T} spectrum in similar p_{T} binning as used in data.
- $A \times \epsilon_{\text{rec}}$ is used to correct the measured p_{T} spectrum.
- $A \times \epsilon_{\text{rec}}$ corrected p_{T} spectrum is fitted with Levy-Tsallis function.
- MC simulated spectra are again extracted in smaller p_{T} bins. Levy-Tsallis fit of measured spectrum is used to weight the MC generated spectrum. A p_{T} dependent weight is applied to the generated spectrum so that it follows the fit. The same weight is also applied to the reconstructed spectrum.
- Now this weighted simulated spectra are used to calculate the $A \times \epsilon_{\text{rec}}$ in a similar p_{T} binning as used in data.

- Above mention procedure is repeated until the change between $A \times \epsilon_{\text{rec}}$ in two successive iteration becomes < 0.1 %. It is observed that two iterations are usually sufficient for this procedure to converge.

The ratio between original $A \times \epsilon_{\text{rec}}$ and weighted $A \times \epsilon_{\text{rec}}$ is the re-weighted factor and is shown in Fig. 5.4. Final corrected yield is obtained with the weighted $A \times \epsilon_{\text{rec}}$.

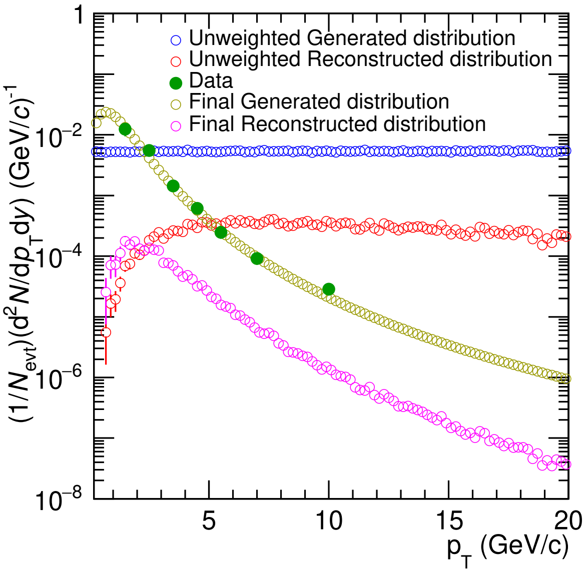

FIGURE 5.3: Generated, reconstructed and experimental data p_{T} spectras in both unweighted and reweighted case for the $f_1(1285)$ meson in inelastic pp collisions at $\sqrt{s}$ = 13 TeV.

Ultimately, the yields are normalized by the number of accepted events ($N^{\text{acc}}_{\text{event}}$) to obtain the corrected p_{T} spectrum. The measurements undergo additional corrections for both event loss (f_{ev}) and signal loss (f_{SL}), which are generally determined through MC simulation. Recognizing that a simulation incorporating injected $f_1(1285)$ signals may not provide a truly realistic assessment of correction factors, these factors are borrowed from Ref. [7]. In summary, the corrected p_{T} spectrum can be formally expressed as

$$\frac{1}{N_{\text{evt}}}\frac{\text{d}^2N}{\text{d}y\text{d}p_{\text{T}}} = \frac{1}{N^{\text{acc}}_{\text{event}}}\frac{\text{d}^2N^{\text{raw}}}{\text{d}y\text{d}p_{\text{T}}}\frac{\text{f}_{\text{ev}}\text{f}_{\text{SL}}}{(\text{A}\times\epsilon_{\text{rec}})\text{BR}}, \tag{5.3}$$

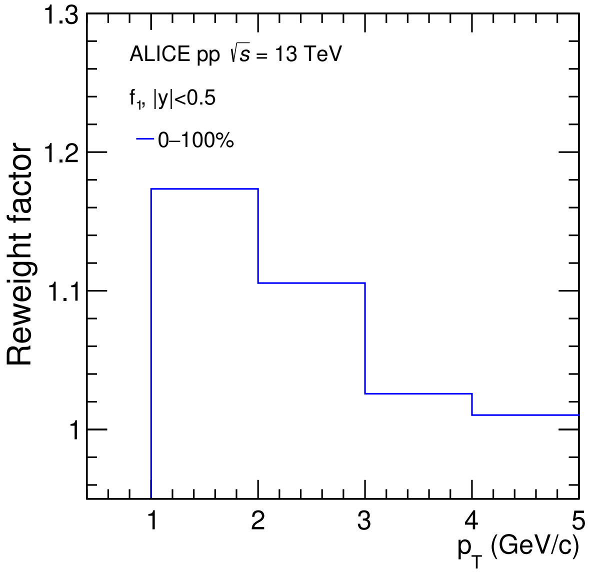

FIGURE 5.4: Ratio between original $A \times \epsilon_{\mathrm{rec}}$ and weighted $A \times \epsilon_{\mathrm{rec}}$ for the $f_1(1285)$ meson in inelastic pp collisions at $\sqrt{s}$ = 13 TeV.

where N is the number of $f_1(1285)$ produced per N_{evt} inelastic events in a given rapidity (dy) and transverse momentum (dp_{T}) interval.

5.2 Systematic uncertainties

The measured yields of $f_1(1285)$ are subject to various sources of systematic uncertainties, which include factors such as the signal extraction method, selection criteria for primary and secondary tracks, particle identification procedures, the strategy for matching track segments in the ITS with those in the TPC, as well as uncertainties associated with the material budget and interaction cross section. To assess these systematic uncertainties, variations and corrections are applied throughout the entire analysis chain, and the resulting changes in the $f_1(1285)$ yields for each p_{T} bin are observed. Table 5.2 provides a summary of the systematic uncertainties affecting the measured $f_1(1285)$ yields, reporting the uncertainties for both low- and high-p_{T} intervals.

TABLE 5.2: Systematic uncertainties on measured $f_1(1285)$ yield in pp collisions at $\sqrt{s}$ = 13 TeV. The systematic uncertainties are shown for different sources for a low- and a high-p_T interval.

Systematic variation	p_T (GeV/c)	
	1.0–2.0	8.0–12.0
Signal extraction (%)	12.74	14.46
Primary track selection (%)	3.90	4.97
Secondary track selection (%)	9.24	6.46
Particle identification (%)	3.58	0.07
Global tracking efficiency (%)	2	2
Material budget (%)	1.8	negl.
Hadronic interaction (%)	1.8	negl.
Total (%)	16.92	16.73

To comprehensively evaluate the uncertainty in signal extraction, several factors undergo variation, encompassing adjustments to fitting ranges, residual background fit functions, and variations in the mass and width parameters for the three resonances under consideration ($f_1(1285)$, $f_1(1420)$, and $\eta(1475)$). Specifically, in the evaluation of fitting ranges, boundaries are expanded by 20 MeV/c^2 on both sides compared to the default scenario, which involves fixed-width fits of resonances to the invariant mass distributions. In the systematic analysis, the widths of all resonances are left unconstrained, and the resulting differences in their yields are factored into the systematic uncertainty assessment. Additionally, the mass of $f_1(1420)$ is held fixed (rather than being allowed to vary freely in the default case) during the systematic uncertainty evaluation to gauge its impact on the $f_1(1285)$ yield estimation. The residual background is further characterized using both second and third-order polynomials to explore potential systematic effects. Regarding primary track selection, the selection criteria which undergoes variation are listed in Table 5.3. The uncertainty in K^0_S reconstruction is estimated through modifications to the topological selection criteria outlined in Table 5.1. The uncertainties associated with the identification of primary daughter tracks are assessed by varying the selection criteria in the TPC and

TOF from $|n\sigma_{\rm TPC}| < 2$, $|n\sigma_{\rm TOF}| < 3$ to $|n\sigma_{\rm TPC}| < 2$, $|n\sigma_{\rm TOF}| < 4$. Additionally, uncertainties linked to the material budget, hadronic cross section, and global tracking efficiency are derived from Ref. [7]. The total uncertainty is computed by summing the uncertainties from each source in quadrature, resulting in a range of approximately 17-18% across the measured $p_{\rm T}$ intervals and is shown in Fig. 5.5.

TABLE 5.3: Selection criteria for primary pions.

Selection criteria	Value	Variations
Crossed rows	>70	80
χ^2_{ITS}	<36	4
DCA	$p_{\rm T}$ dependent	2.4 cm

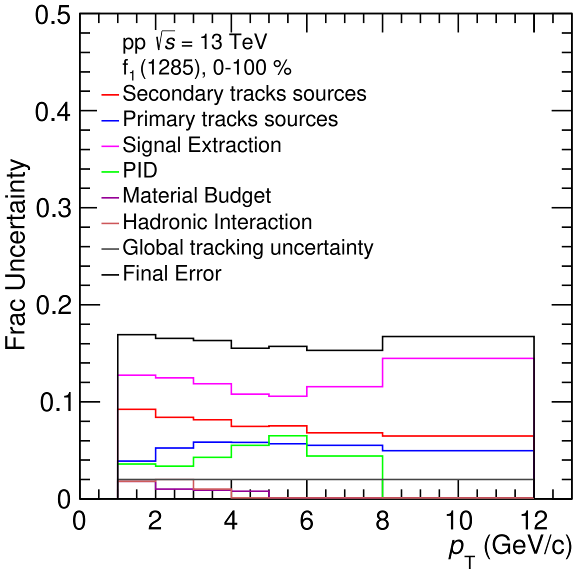

FIGURE 5.5: Systematic uncertainty for the $f_1(1285)$ meson in inelastic pp collisions at $\sqrt{s}$ = 13 TeV.

5.3 Results

The mass of the $f_1(1285)$ resonance, indicated by the fit parameter M_0 as derived from Eq. 5.1, is depicted in Fig. 5.6. The systematic uncertainties affecting the measured mass are assessed using procedures akin to those outlined in Sections 5.2. The measured mass demonstrates agreement with its theoretical vacuum value [3] within the range of uncertainties considered.

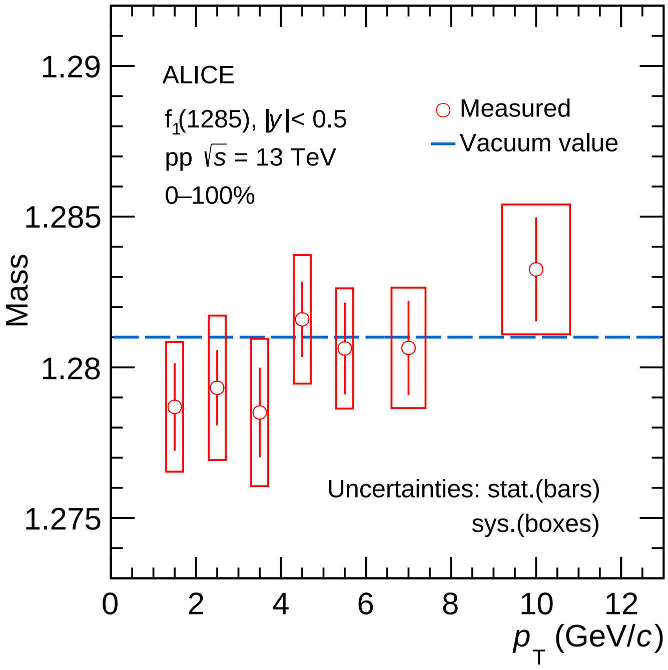

FIGURE 5.6: Measured $f_1(1285)$ mass at midrapidity ($|y| < 0.5$) in inelastic pp collisions at $\sqrt{s}$ = 13 TeV. The statistical and systematic uncertainties are shown as bars and boxes, respectively. The blue dotted line represents the vacuum mass of $f_1(1285)$.

Figure 5.7 presents the transverse momentum (p_T) spectra of the $f_1(1285)$ resonance in proton-proton (pp) collisions at a center-of-mass energy of 13 TeV, incorporating all the corrections outlined in Section 5.1.2. To extend the spectra to unmeasured p_T regions, including down to zero p_T, the p_T distribution is fitted with a Levy-Tsallis function, which is a combination of an exponential and a power-law function [17]. The low-p_T section of the spectrum is described by an exponential function, while the high-p_T region (> 6 GeV/c) is characterized by a power law. Since there are only two p_T bins above 6 GeV/c with a large bin width, the Levy-Tsallis fit is performed in the range of $0 < p_T < 6$ GeV/c.

This fitting approach facilitates the extraction of the p_{T}-integrated yields ($\mathrm{d}N/\mathrm{d}y$) and the average transverse momentum ($\langle p_{\mathrm{T}} \rangle$) of the $f_1(1285)$ resonance, utilizing both the measured and extrapolated distributions. Approximately 41% of the total $f_1(1285)$ yield is encompassed by the extrapolation to low-p_{T} (< 1 GeV/c), while the contribution from high-p_{T} extrapolation is found to be negligible.

The $\langle p_{\mathrm{T}} \rangle$ is determined by evaluating the mean value of the fit function within each p_{T} bin, weighted by the measured yield in that bin. The systematic uncertainties in the p_{T} spectra, stemming from various sources, also contribute to the systematic uncertainties in $\mathrm{d}N/\mathrm{d}y$ and $\langle p_{\mathrm{T}} \rangle$. Different parameterizations, such as the Boltzmann-Gibbs blast wave function [18], Bose-Einstein distribution, and $\mathrm{m_T}$ exponential [7], are employed in addition to the Levy-Tsallis function. The resulting variations in $\mathrm{d}N/\mathrm{d}y$ and $\langle p_{\mathrm{T}} \rangle$ are integrated into the systematic uncertainties. The uncertainty for the extrapolation is approximately 25% for $\mathrm{d}N/\mathrm{d}y$ and around 15% for $\langle p_{\mathrm{T}} \rangle$. The resulting per-event p_{T}-integrated yield ($\mathrm{d}N/\mathrm{d}y$) and $\langle p_{\mathrm{T}} \rangle$ values are provided in Table 5.4. The yield is compared with calculations from the Canonical ensemble-based Statistical Model (γ_{S}CSM) [19]. The γ_{S}CSM employs an ideal Hadron Resonance Gas (HRG) in thermal and chemical equilibrium at the chemical freeze-out stage. In this model, the values of three Abelian charges: baryon number (B), electric charge (Q), and strangeness (S) are fixed and conserved precisely across the designated correlation volume $\mathrm{V_C}$. The multiplicity dependence of hadron production in this model is influenced by the canonical suppression of these three Abelian charges. The model incorporates a correlation volume spanning three units of rapidity and includes the incomplete equilibrium of strangeness through the strangeness saturation parameter γ_{S} (denoted as γ_{S}CSM), successfully reproducing a broad range of multiplicity-dependent hadron-to-pion ratios, including the multiplicity dependence of the ϕ/π ratio [19]. Thermal fits to the yields of various particles, including π, K, p, K^{*0}, Λ, Ω, $\mathrm{K^0_S}$, Ξ, and ϕ mesons, as measured by the ALICE Collaboration in pp collisions at 13 TeV [7], have been conducted. The fit parameters include the freeze-out temperature, radius of the produced fireball, correlation volume (V_C), and γ_S. It is assumed that the baryon chemical potential is zero [20]. The thermal model calculations for the p_T-integrated yield of $f_1(1285)$ are carried out for two different scenarios: one with |S| = 0 (indicating the presence of no strange or anti-strange quarks within $f_1(1285)$) and another with |S| = 2 (representing a total strangeness content of 2 within $f_1(1285)$). The yield obtained with |S| = 0 calculation is consistent with ALICE data within 1σ.

TABLE 5.4: The p_T-integrated yield and mean transverse momentum of the f_1(1285) meson in proton-proton collisions at a center-of-mass energy of 13 TeV. The integrated yield obtained from experimental data is compared with the thermal model (γ_S-CSM) calculations.

Variable of interest	ALICE data	Thermal model predictions	
		|S|=0	|S|=2
dN/dy	0.034 ± 0.004 (stat) ± 0.009 (sys)	0.025	0.014
$\langle p_T \rangle$	1.52 ± 0.10 (stat) ± 0.23 (sys)	-	-

Furthermore, in Fig. 5.8, the mean transverse momentum of $f_1(1285)$ is compared with that of all other light-flavor hadrons [7] at midrapidity ($|y| < 0.5$) in proton-proton collisions at $\sqrt{s}$ = 13 TeV. Two distinct linear trends emerge, one for mesons and the other for baryons. Interestingly, $f_1(1285)$ follows the same linear trend as other mesons. For particles with comparable masses (K^{*0}, p, ϕ, Λ, f_1, Ξ^-), mesons exhibit a higher mean transverse momentum compared to baryons. This discrepancy in $\langle p_T \rangle$ defies the mass ordering typically observed and is commonly attributed to the disparity in p_T spectra between mesons and baryons [7].

To probe the valence quark composition of the $f_1(1285)$ meson, the p_T-integrated yield ratio of f_1/π in proton-proton collisions at $\sqrt{s}$ = 13 TeV is contrasted with predictions from the γ_SCSM, as depicted in Fig. 5.9. The γ_SCSM computes the f_1/π ratio under two

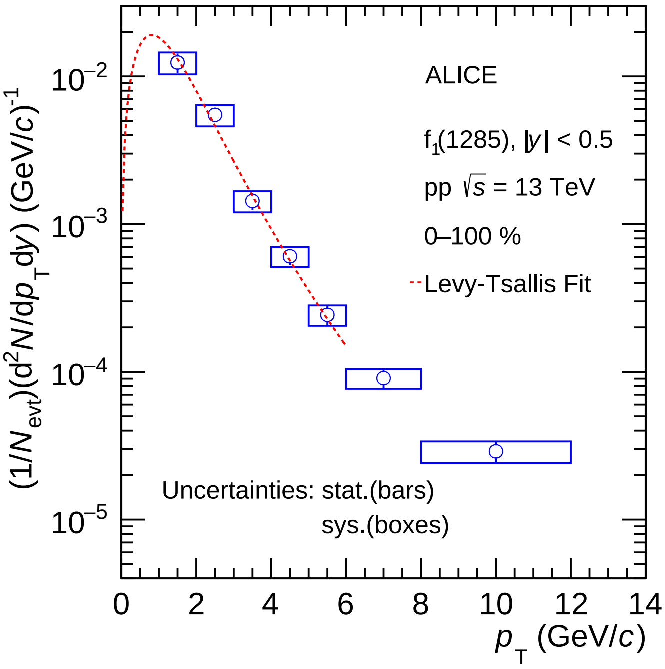

FIGURE 5.7: Transverse momentum spectra of $f_1(1285)$ measured at midrapidity ($|y| < 0.5$) in inelastic pp collisions at $\sqrt{s} = 13$ TeV. The statistical and systematic uncertainties are shown as bars and boxes, respectively. The data points are fitted using a Levy-Tsallis function shown by the red dotted line.

scenarios: firstly, assuming a total strangeness content of $f_1(1285)$ to be zero (|S| = 0, represented by the blue dotted line), and secondly, assuming a total strangeness content of $f_1(1285)$ to be two (|S| = 2, represented by the magenta dotted line). The measured f_1/π ratio deviates by 1.0σ from |S| = 0 and by 2.11σ from |S| = 2, indicating that the γ_SCSM calculations with |S| = 0 align better with the ALICE data than those with |S| = 2. Additionally, as a reference test for this approach, the ϕ/π ratio is examined. The ϕ meson, being a neutral particle composed of a strange quark-antiquark pair, has a net strangeness of zero and is unaffected by precise strangeness conservation in the canonical suppression scenario. However, in the context of strangeness nonequilibrium, the ϕ meson is considered as a double-strange particle [19]. Hence, the experimental data is compared with γ_SCSM

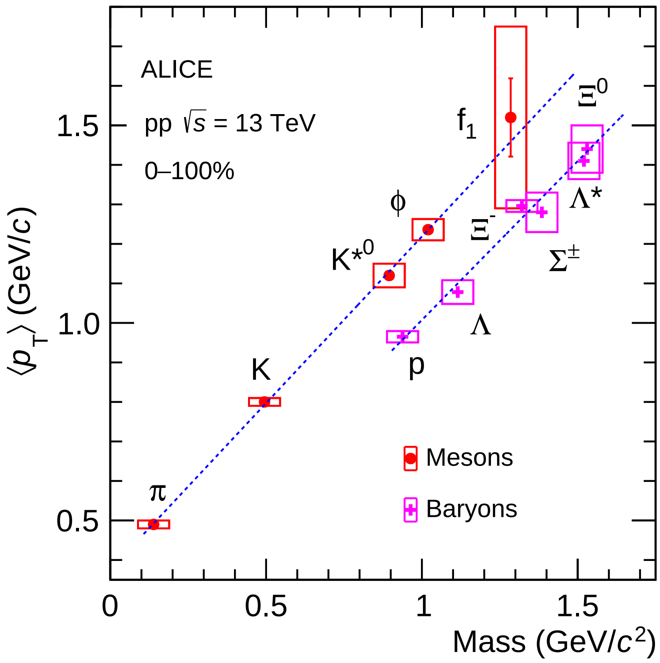

FIGURE 5.8: Average transverse momentum of light-flavor hadrons as a function of hadron mass at midrapidity ($|y| < 0.5$) in inelastic pp collisions at $\sqrt{s} = 13$ TeV. The statistical and systematic uncertainties are shown as bars and boxes, respectively.

calculations in Fig. 5.9 for |S| = 0 (indicating a total strangeness content of ϕ to be zero, depicted by the yellow dotted line) and |S| = 2 (indicating a total strangeness content of ϕ to be two, represented by the black dotted line). Notably, while adjusting |S| for the ϕ meson, |S| for the $f_1(1285)$ meson remains constant, and vice versa. Consistent with the strangeness nonequilibrium perspective, the γ_SCSM calculation for the ϕ/π ratio with the ϕ meson having |S| = 0 demonstrates a significant deviation of 9.15σ from the experimental measurements, while |S| = 2 is in close agreement with the experimental data within 0.5σ. Hence, this investigation indicates that $f_1(1285)$ is more likely to lack a strange quark content than to consist of a combination of a strange and an anti-strange quark.

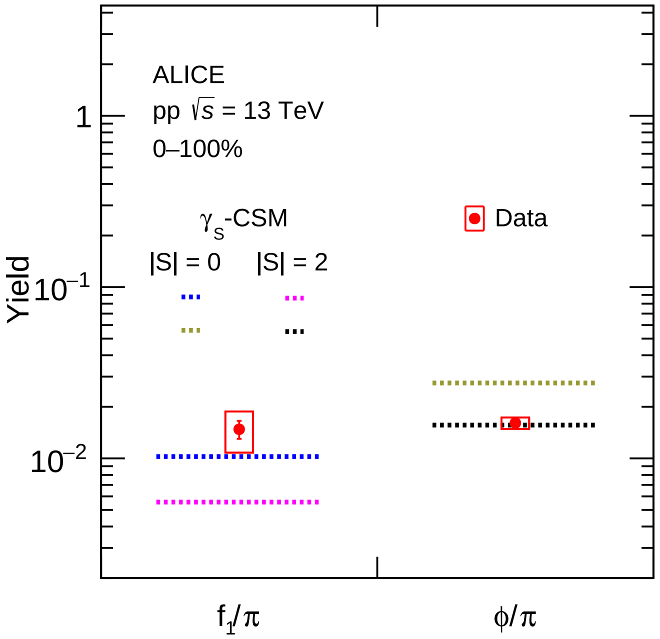

FIGURE 5.9: The transverse momentum integrated yield ratio f_1/π (left) and ϕ/π (right) measured in inelastic pp collisions at $\sqrt{s}$ = 13 TeV. The statistical and systematic uncertainties on the data points are shown as bars and boxes, respectively. The dotted line represents the γ_S-CSM model predictions with different strangeness content of $f_1$and ϕ mesons.

5.4 Summary

We report the inaugural measurement of the exotic $f_1(1285)$ meson in inelastic proton-proton collisions at a center-of-mass energy of 13 TeV. This measurement covers a broad transverse momentum range from 1 to 12 GeV/c at midrapidity ($|y| < 0.5$). The measured mass of $f_1(1285)$ aligns with its expected vacuum value within the associated uncertainties. Notably, the mean transverse momentum of $f_1(1285)$ follows a linear trend with other mesons but exhibits a higher value compared to baryons of similar masses. Additionally, the γ_SCSM calculation for the f_1/π p_T-integrated yield ratio, assuming the absence of strange quarks within $f_1(1285)$, closely agrees with the ALICE data, showing a deviation of only 1σ. This weakens the tetraquark hypothesis of $f_1(1285)$. This study establish a crucial foundation for future investigations into the partial restoration of chiral symmetry and the systematic exploration of hadronic rescattering effects in heavy-ion collisions.

Bibliography

[1] Betty Bezverkhny Abelev et al. “Performance of the ALICE Experiment at the CERN LHC”. *Int. J. Mod. Phys. A* 29 (2014), p. 1430044. arXiv: `1402.4476 [nucl-ex]`.

[2] Shreyasi Acharya et al. “Multiplicity dependence of (multi-)strange hadron production in proton-proton collisions at $\sqrt{s}$ = 13 TeV”. *Eur. Phys. J. C* 80.2 (2020), p. 167. arXiv: `1908.01861 [nucl-ex]`.

[3] R. L. Workman et al. “Review of Particle Physics”. *PTEP* 2022 (2022), p. 083C01.

[4] B Abelev et al. “Technical Design Report for the Upgrade of the ALICE Inner Tracking System”. *J. Phys. G* 41 (2014), p. 087002.

[5] J. Alme et al. “The ALICE TPC, a large 3-dimensional tracking device with fast readout for ultra-high multiplicity events”. *Nucl. Instrum. Meth.* A622 (2010), pp. 316–367. arXiv: `1001.1950 [physics.ins-det]`.

[6] Shreyasi Acharya et al. “Multiplicity dependence of $K^*(892)^0$ and $\phi(1020)$ production in pp collisions at $\sqrt{s}$ =13 TeV”. *Phys. Lett. B* 807 (2020), p. 135501. arXiv: `1910.14397 [nucl-ex]`.

[7] Shreyasi Acharya et al. “Production of light-flavor hadrons in pp collisions at $\sqrt{s}$ = 7 and $\sqrt{s}$ = 13 TeV”. *Eur. Phys. J. C* 81.3 (2021), p. 256. arXiv: `2005.11120 [nucl-ex]`.

[8] G. Dellacasa et al. “ALICE technical design report of the time-of-flight system (TOF)”. *CERN-LHCC-2000-012* ().

[9] Francesca Carnesecchi. “Performance of the ALICE Time-Of-Flight detector at the LHC”. *JINST* 14.06 (2019), p. C06023. arXiv: `1806.03825 [physics.ins-det]`.

[10] Shreyasi Acharya et al. “Measurement of $K^*(892)^{\pm}$ production in inelastic pp collisions at the LHC”. *Phys. Lett. B* 828 (2022), p. 137013. arXiv: `2105.05760 [nucl-ex]`.

[11] Betty Bezverkhny Abelev et al. “Multiplicity Dependence of Pion, Kaon, Proton and Lambda Production in p-Pb Collisions at $\sqrt{s_{NN}} = 5.02$ TeV”. *Phys. Lett. B* 728 (2014), pp. 25–38. arXiv: `1307.6796 [nucl-ex]`.

[12] J. Adams et al. “K*(892) resonance production in Au+Au and p+p collisions at $\sqrt{s_{\mathrm{NN}}} = 200$ GeV at STAR”. *Phys. Rev. C* 71 (2005), p. 064902. arXiv: `nucl-ex/0412019`.

[13] P. Gavillet. “Measurement of inclusive f(1)(1285) and f(1)(1420) production in Z decays with the DELPHI detector”. In: *31st International Symposium on Multiparticle Dynamics*. Nov. 2001, pp. 56–61. arXiv: `hep-ph/0111397`.

[14] Shreyasi Acharya et al. “Evidence of rescattering effect in Pb–Pb collisions at the LHC through production of $\mathrm{K}^*(892)^0$ and $\phi(1020)$ mesons”. *Phys. Lett. B* 802 (2020), p. 135225. arXiv: `1910.14419 [nucl-ex]`.

[15] Peter Skands, Stefano Carrazza, and Juan Rojo. “Tuning PYTHIA 8.1: the Monash 2013 Tune”. *Eur. Phys. J. C* 74.8 (2014), p. 3024. arXiv: `1404.5630 [hep-ph]`.

[16] R Brun et al. “GEANT Detector Description and Simulation Tool”. *CERN Program Library, CERN, Geneva* (1993).

[17] Constantino Tsallis. “Possible Generalization of Boltzmann-Gibbs Statistics”. *J. Statist. Phys.* 52 (1988), pp. 479–487.

[18] Ekkard Schnedermann, Josef Sollfrank, and Ulrich W. Heinz. “Thermal phenomenology of hadrons from 200-A/GeV S+S collisions”. *Phys. Rev. C* 48 (1993), pp. 2462–2475. arXiv: `nucl-th/9307020`.

[19] Volodymyr Vovchenko, Benjamin Dönigus, and Horst Stoecker. “Canonical statistical model analysis of pp , p–Pb, and Pb–Pb collisions at energies available at the CERN Large Hadron Collider”. *Phys. Rev. C* 100.5 (2019), p. 054906. arXiv: `1906.03145 [hep-ph]`.

[20] Shreyasi Acharya et al. “Measurements of chemical potentials in Pb-Pb collisions at $\sqrt{s_{\mathrm{NN}}} = 5.02$ TeV” (Nov. 2023). arXiv: `2311.13332 [nucl-ex]`.

Conclusions

In the heavy-ion collisions at the Large Hadron Collider (LHC) facility, a unique state of matter known as quark-gluon plasma (QGP) emerges, resembling conditions seen in the early Universe. Investigating this novel form of matter is the focus of a Large Ion Collider Experiment (ALICE). The space-time evolution of ultra-relativistic heavy-ion collisions mainly has three stages:i) initial stage ii) intermediate stage: QGP formation and hydrodynamics expansion of the medium, and iii) final stage: hadronization, late stage hadronic dynamics. The initial stage of the collision is influenced by two significant factors: (a) large transient magnetic fields, generated by rapidly moving spectator protons, and (b) substantial angular momentum. The persistence of the magnetic field depends on the medium's conductivity. These conditions lead to various chiral currents within the QGP, including the Chiral Magnetic Effect (CME), Chiral Separation Effect (CSE), Chiral Magnetic Wave (CMW), and Chiral Vortical Effect (CVE). These currents result in the formation of parity-odd domains in the QCD vacuum, potentially causing local parity violation in strong interactions. With this motivation, this thesis delves into studying the CMW phenomenon in Pb–Pb collisions at $\sqrt{s_{\mathrm{NN}}}$ = 5.02 TeV. CMW induces a measurable finite electric quadrupole moment through charge-dependent elliptic flow measurements, v_2. Specifically, the normalized difference of v_2 between positive and negative charges ($r_2^{\rm Norm}$) is expected to show a positive slope ($r_2^{\rm Norm} > 0$) with respect to the asymmetry ($A_{\rm ch}$) in particle charges per event. However, non-CMW mechanisms like Local Charge Conservation (LCC), coupled with collective flow, can also contribute to a similar slope. To discern this background, measurements of v_3 need to be performed, as v_3 is unaffected by CMW signal. Our measurements of the charge-dependent anisotropic flow coefficients (v_2 and v_3) in Pb–Pb collisions at $\sqrt{s_{\rm NN}}$ = 5.02 TeV reveal a positive slope ($r_2^{\rm Norm} > 0$) for $\Delta v_2/\langle v_2 \rangle$, indicating the influence of CMW. Additionally, a non-zero slope is observed for $\Delta v_3/\langle v_3 \rangle$ ($r_3^{\rm Norm} > 0$). Within large uncertainties, $r_3^{\rm Norm}$ is comparable in magnitude to $r_2^{\rm Norm}$ across most centrality ranges, with no noticeable particle dependence. The resemblance in magnitudes of $r_2^{\rm Norm}$ and $r_3^{\rm Norm}$ for all particles suggests their primary influence by the LCC background. These findings align with CMS measurements for the same collision system and energy. Furthermore, comparing $r_2^{\rm Norm}$ with blast wave LCC model calculations underscores a significant background contribution. As the signal observable for CMW closely resembles the background observable, we extract an upper limit of 26% for the fraction of CMW signal at a 95% confidence level.

In principle, various identified particles can behave distinctly in response to novel QCD processes due to differences in quark content and masses [1]. However, significant uncertainties in the measurements of $r_2^{\rm Norm}$ and $r_3^{\rm Norm}$ from the limited event statistics in Run 2 data prevented a clear indication of flavor dependence at LHC energy. Additionally, the upper limit extracted in Run 2 also suffered from significant statistical and systematic uncertainties, with the latter primarily driven by DCA variation. With the increase in statistics in Run 3 data and the improved resolution of ITS [2–4], it is now feasible to investigate the flavor dependence of the CMW phenomenon at LHC energies and provide more stringent constraints on the upper limit of CMW contribution.

In the second part of the thesis, we delved into the late-stage evolution of heavy-ion collisions by examining K^* (K^{*0} and $\mathrm{K}^{*\pm}$) resonances in pp and Pb–Pb collisions at $\sqrt{s_{\mathrm{NN}}}$ = 5.02 TeV, respectively. Our findings reveal that the results for $\mathrm{K}^{*\pm}$ are in good agreement with previously published results for K^{*0} in Pb–Pb collisions at the same energy. Given that K^* resonances have lifetimes comparable to that of the hadronic phase, they undergo rescattering and regeneration effects that alter their yields. We investigated the dependence of K^* production and these effects on decay products in the hadronic phase by comparing results across various collision systems (pp, p–Pb, Xe–Xe, and Pb–Pb) at similar charge particle multiplicities. Our analysis shows that the p_{T}-integrated K^* yield and K^*/K yield ratio exhibit a consistent trend with $\langle \mathrm{d}N_{\mathrm{ch}}/\mathrm{d}\eta \rangle^{1/3}_{|\eta|<0.5}$, regardless of the size of the colliding nuclei. However, we observed a more pronounced increase in $\langle p_{\mathrm{T}} \rangle$ in smaller collision systems compared to heavy-ion collisions, indicating a faster expansion of matter in these smaller systems. Furthermore, we found that the K^*/K yield ratio in central Pb–Pb collisions is suppressed relative to pp collisions and peripheral Pb–Pb collisions, indicating significant rescattering of K^* decay daughters in the hadronic phase. This observation is further supported by the p_{T}-differential yield ratio K^*/K, which suggests the predominance of rescattering effects at low p_{T}. Moreover, the extraction of the kinetic freeze-out temperature, using the HRG-PCE model fit to experimental data at a fixed chemical freeze-out temperature, suggests a longer-lived hadronic phase in central collisions compared to peripheral collisions. The comparison of R_{AA} between light flavor hadrons signifies the energy loss of hadrons independent of their quark content and masses.

In the last part of the thesis, we present the pioneering measurement of the production cross-section of the exotic $f_1(1285)$ resonance in pp collisions at a center-of-mass energy of 13 TeV. We provide insights into its mass, p_{T}-integrated yield, and average transverse momentum ($\langle p_{\rm T} \rangle$). Notably, the mass of the $f_1(1285)$ aligns with its expected vacuum value within the reported uncertainties. Furthermore, we compare the ratio of the $p_{\rm T}$-integrated yield of $f_1(1285)$ to that of pions with calculations derived from the $\gamma_{\rm S}$CSM. Remarkably, when considering the absence of strange quarks within the $f_1(1285)$ structure, the $\gamma_{\rm S}$CSM predictions closely match the experimental measurements obtained by ALICE, deviating by just 1σ. This study weakens the tetraquark hypothesis of $f_1(1285)$.

Future investigations into the elliptic flow of $f_1(1285)$ and femtoscopy measurements within the $\rm K^*\overline{K}$ coupled channel, utilizing the extensive statistical data from Run 3 and the upcoming Run 4, can help discern the diquark or molecular nature of $f_1(1285)$. Furthermore, theoretical models based on $\rm K^*\overline{K}$ dynamics [5, 6] offer intriguing insights into the nature of $f_1(1420)$ resonance, which could be explored in future studies.

Bibliography

[1] Yoshitaka Hatta, Akihiko Monnai, and Bo-Wen Xiao. “Elliptic flow difference of charged pions in heavy-ion collisions”. en. *Nuclear Physics A* 947 (Mar. 2016), pp. 155–160.

[2] Wladyslaw Henryk Trzaska. “New ALICE detectors for Run 3 and 4 at the CERN LHC”. *Nucl. Instrum. Meth. A* 958 (2020). Ed. by Manfred Krammer et al., p. 162116.

[3] B Abelev et al. “Upgrade of the ALICE Experiment: Letter Of Intent”. *J. Phys. G* 41 (2014), p. 087001.

[4] Felix Reidt. “Upgrade of the ALICE ITS detector”. *Nucl. Instrum. Meth. A* 1032 (2022), p. 166632. arXiv: `2111.08301 [physics.ins-det]`.

[5] F. Aceti, Ju-Jun Xie, and E. Oset. “The $K\bar{K}\pi$ decay of the $f_1(1285)$ and its nature as a $K^*\bar{K} - cc$ molecule”. *Phys. Lett. B* 750 (2015), pp. 609–614. arXiv: `1505.06134 [hep-ph]`.

[6] V. R. Debastiani et al. “Revising the $f_1(1420)$ resonance”. *Phys. Rev. D* 95.3 (2017), p. 034015. arXiv: `1611.05383 [hep-ph]`.

APPENDIX **A**

Appendix

A.1 CMW systematic uncertainties

A.1.1 Barlow check

The Barlow ratio is estimated for each bin of centrality and is defined as

$$B = \frac{Y}{\sigma_B} = \frac{|y_{def} - y_{var}|}{\sqrt{\sigma_{def}^2 \pm \sigma_{var}^2}} \tag{A.1}$$

where y$_{def}$ and y$_{var}$ are the results obtained with default and varied cuts with σ being their statistical errors(estimated using subsampling method) respectively, '+'sign in the denominator is used in case of two independent samples(eg. results from different runs) and '-' sign if one sample is a subset of other (eg. results obtained with tighter/looser cuts). If B>1 for more than 33% of the total bins, contribution from that particular systematic source has been considered for all the bins and **in this case we say the systematic source passes the Barlow test**, otherwise the contribution from that source is omitted for all the bins and **we say the systematic source does not pass the Barlow test**.

This analysis is done in 9 centrality bins hence if 3 out of 9 bins passes the Barlow

test then we consider that source contribution in final systematic error calculation. A smoothing procedure has been applied by fitting the maximum differences between default and systematic values with pol0/pol1/pol2 and the systematic uncertainty is estimated from the fit function. The statistical error from $|y_{def} - y_{var}|$ is considered in the fitting procedure to perform good fits.
The contribution from different sources is added in quadrature for the total systematic uncertainty.

For protons the analysis is carried out in 4 centrality bins and if 2 out of 4 bins passes the Barlow test then we consider that source contribution in final systematic error calculation and uncertainty is taken from the fit function. But in this case if barlow doesn't pass, we follow a conservative approach and uncertainty is estimated from pol0 fit function.

A.1.2 Systematic variation on r_n^{Norm}due to V$_z$ for hadrons

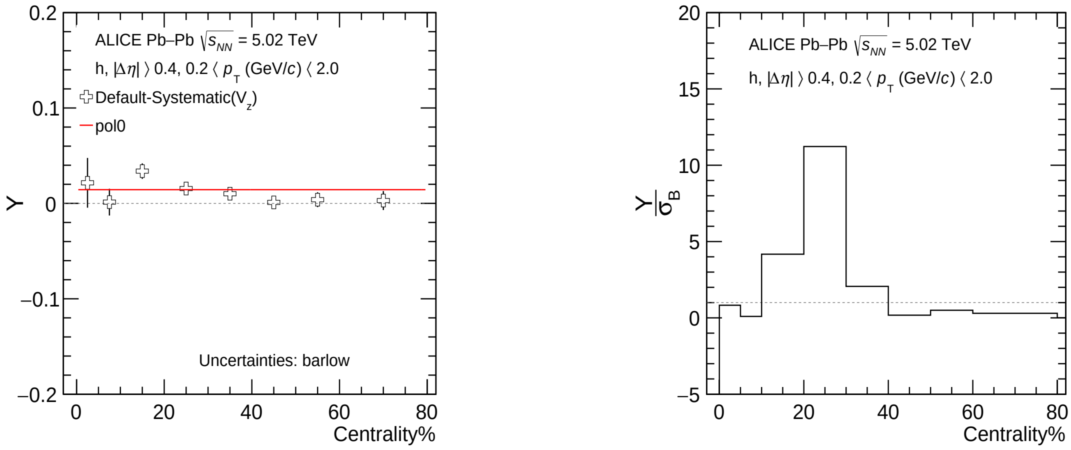

FIGURE A.1: Left panel shows absolute systematic uncertainty for normalised v$_2$ slope of hadrons and right panel shows its Barlow ratio (passed) both as function of centrality. The errors shown are Barlow only.

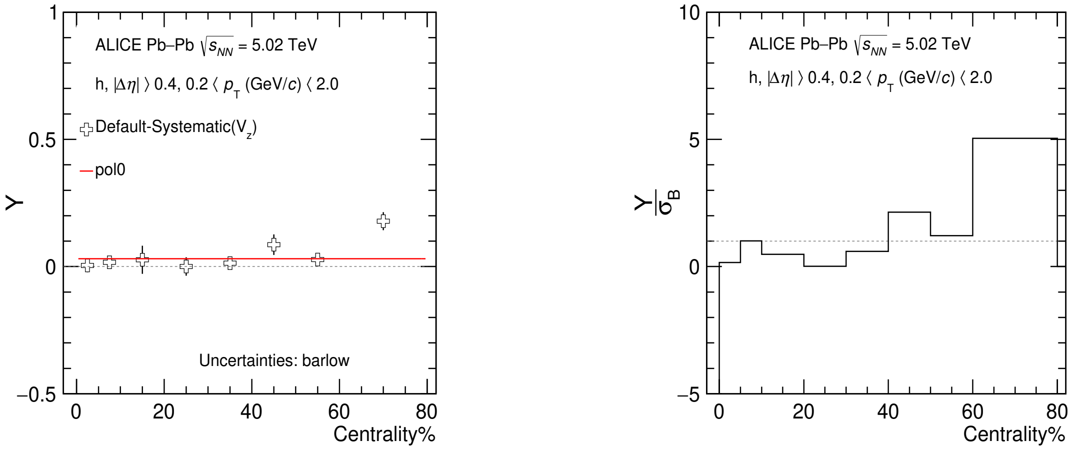

FIGURE A.2: Left panel shows absolute systematic uncertainty for normalised v$_3$ slope of hadrons and right panel shows its Barlow ratio (passed) both as function of centrality. The errors shown are Barlow only.

Observation: Fig A.1 and fig A.2 shows the absolute value of systematic uncertainty(left) and Barlow ratio(right) due to V$_z$ variation on r$_{\Delta v_2}^{norm}$ and r$_{\Delta v_3}^{norm}$ respectively for hadrons. A smoothing procedure is applied i.e fiting the data points of fig A.1 with pol0 and of fig A.2 with pol0.

Inference: We see **both $\mathbf{r}_{\Delta v_2}^{norm}$ and $\mathbf{r}_{\Delta v_3}^{norm}$ passes the Barlow test** hence considered as one of the source of systematic uncertainty.

A.1.3 Systematic variation on r_n^{Norm}due to $\mathrm{V_z}$ for pions

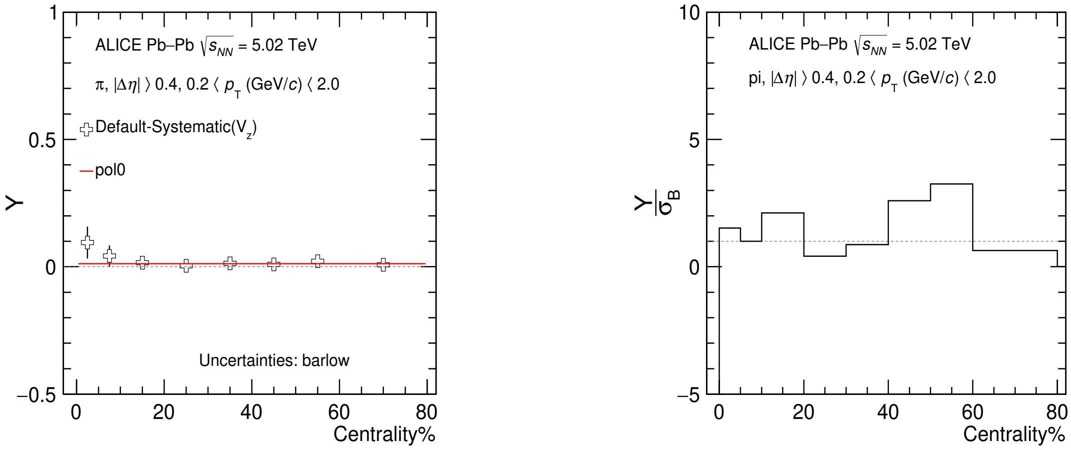

FIGURE A.3: Left panel shows absolute systematic uncertainty for normalised v_2 slope of pions and right panel shows its Barlow ratio (passed) both as function of centrality. The errors shown are Barlow only.

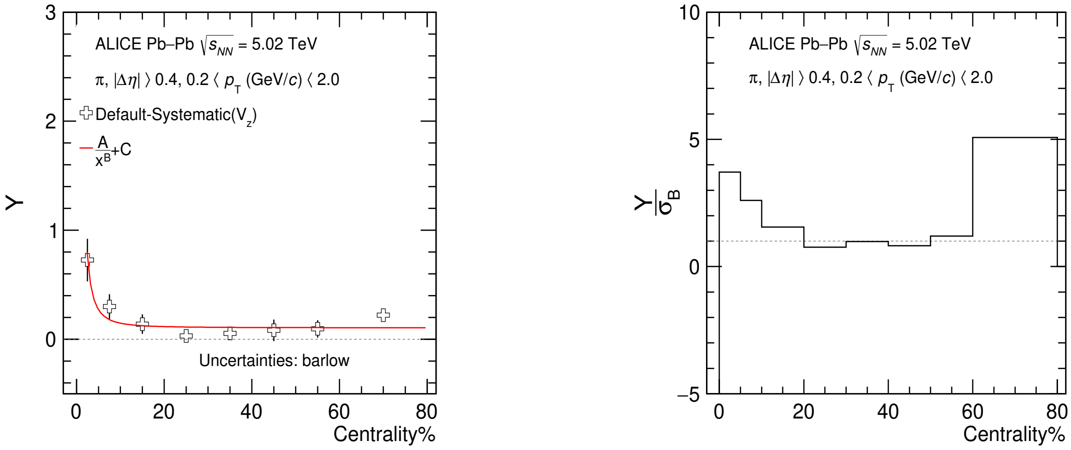

FIGURE A.4: Left panel shows absolute systematic uncertainty for normalised v_3 slope of pions and right panel shows its Barlow ratio (passed) both as function of centrality. The errors shown are Barlow only.

Observation: Fig A.3 and fig A.4 shows the absolute value of systematic uncertainty(left) and Barlow ratio(right) due to V_z variation on $\mathrm{r}_{\Delta v_2}^{norm}$ and $\mathrm{r}_{\Delta v_3}^{norm}$ respectively for pions. A smoothing procedure is applied i.e fiting the data points of fig A.3 with pol0 and of fig A.4 with function A/x^B + C.

Inference: We see **both** $\mathbf{r}^{norm}_{\Delta v_2}$ **and** $\mathbf{r}^{norm}_{\Delta v_3}$ **passes the Barlow test** hence considered as one of the source of systematic uncertainty.

A.1.4 Systematic variation on r_n^{Norm}due to V$_z$ for kaons

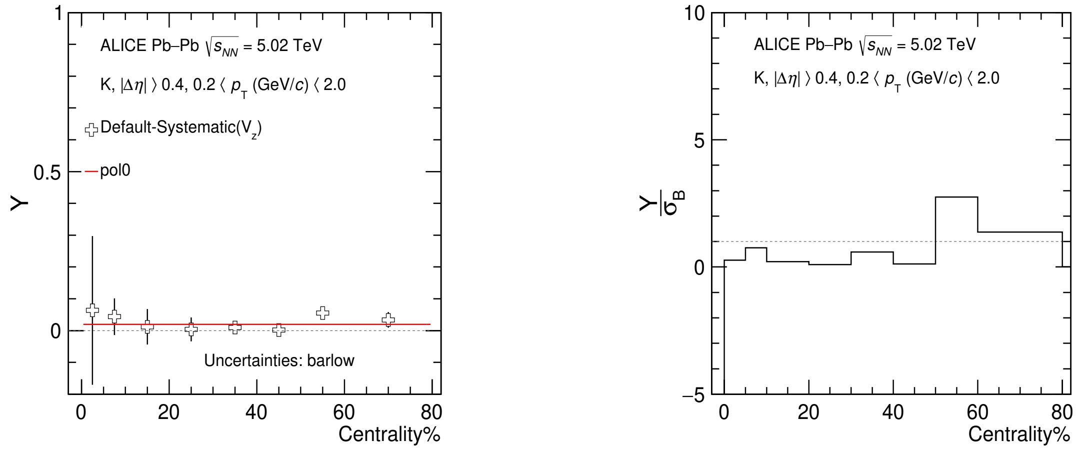

FIGURE A.5: Left panel shows absolute systematic uncertainty for normalised v$_2$ slope of kaons and right panel shows its Barlow ratio (not passed) both as function of centrality. The errors shown are Barlow only.

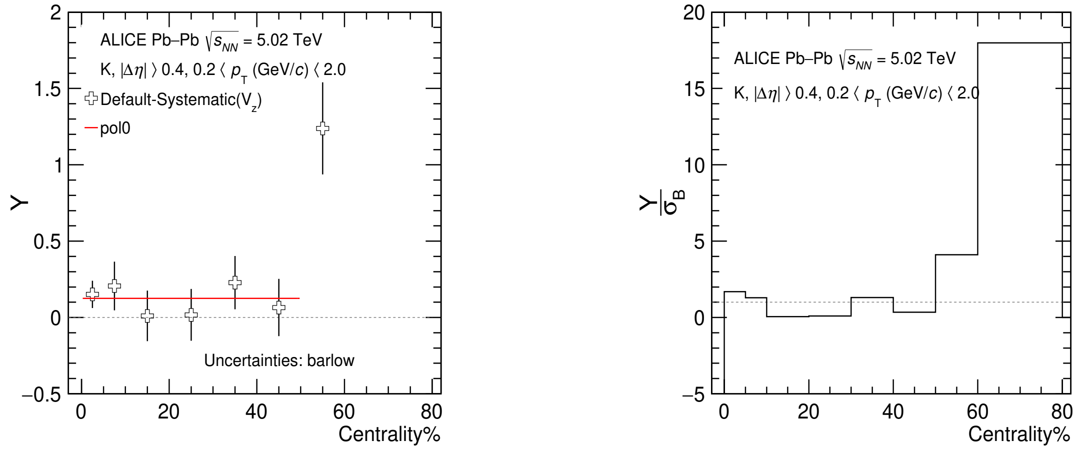

FIGURE A.6: Left panel shows absolute systematic uncertainty for normalised v$_3$ slope of kaons and right panel shows its Barlow ratio (passed) both as function of centrality. The errors shown are Barlow only.

Observation: Fig A.5 and fig A.6 shows the absolute value of systematic uncertainty(left) and Barlow ratio(right) due to V$_z$ variation on r$^{norm}_{\Delta v_2}$ and r$^{norm}_{\Delta v_3}$ respectively for kaons. A smoothing procedure is applied i.e fiting the data points of fig A.5 with pol0 and of fig A.6 with pol0.

Inference: We see **only $\mathbf{r}^{norm}_{\Delta\nu_3}$ passes the Barlow test** hence considered as one of the source of systematic uncertainty.

A.1.5 Systematic variation on r_n^{Norm}due to V_z for protons

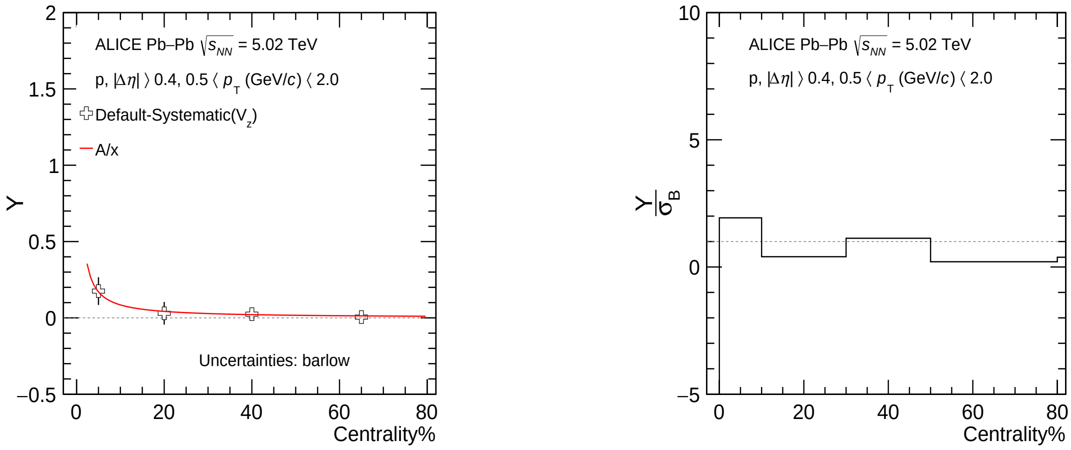

FIGURE A.7: Left panel shows absolute systematic uncertainty for normalised v_2 slope of protons and right panel shows its Barlow ratio (passed) both as function of centrality. The errors shown are Barlow only.

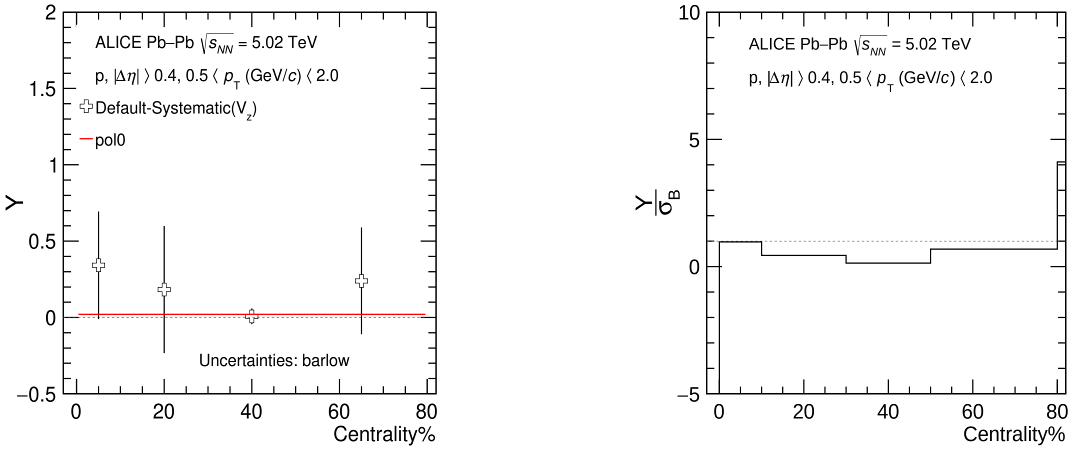

FIGURE A.8: Left panel shows absolute systematic uncertainty for normalised v_3 slope of protons and right panel shows its Barlow ratio (not passed) both as function of centrality. The errors shown are Barlow only.

Observation: Fig A.7 and fig A.8 shows the absolute value of systematic uncertainty(left) and Barlow ratio(right) due to V_z variation on $r_{\Delta v_2}^{norm}$ and $r_{\Delta v_3}^{norm}$ respectively for protons. A smoothing procedure is applied i.e fiting the data points of fig A.7 with function

A/x and of fig A.8 with pol0.

Inference: We see only $\mathbf{r}^{norm}_{\Delta v_2}$ **passes the Barlow test** hence considered as one of the source of systematic uncertainty. For $\mathbf{r}^{norm}_{\Delta v_3}$ systematic uncertainty is estimated from pol0 function.

A.1.6 Systematic variation on r_n^{Norm} due to χ^2_{TPC} for hadrons

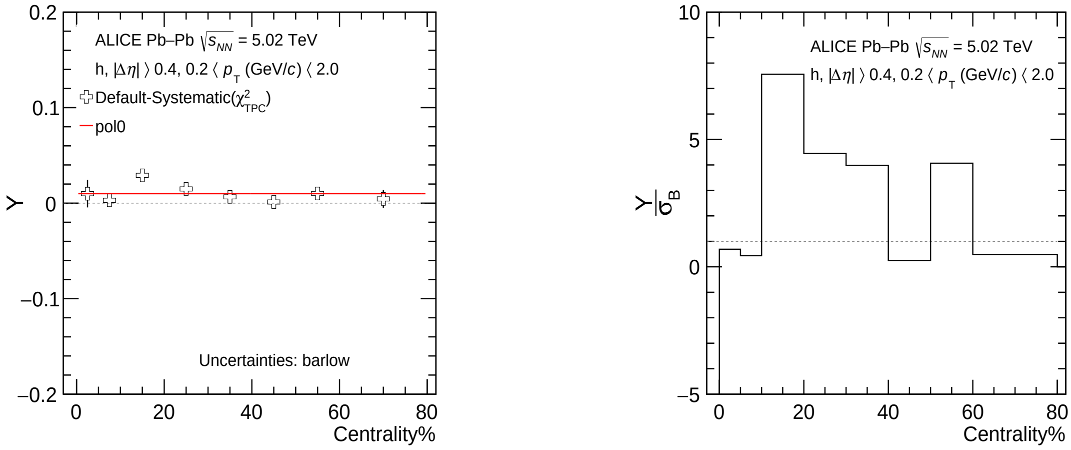

FIGURE A.9: Left panel shows absolute systematic uncertainty for normalised v_2 slope of hadrons and right panel shows its Barlow ratio (passed) both as function of centrality. The errors shown are Barlow only. The systematic uncertainty is taken from fitting function.

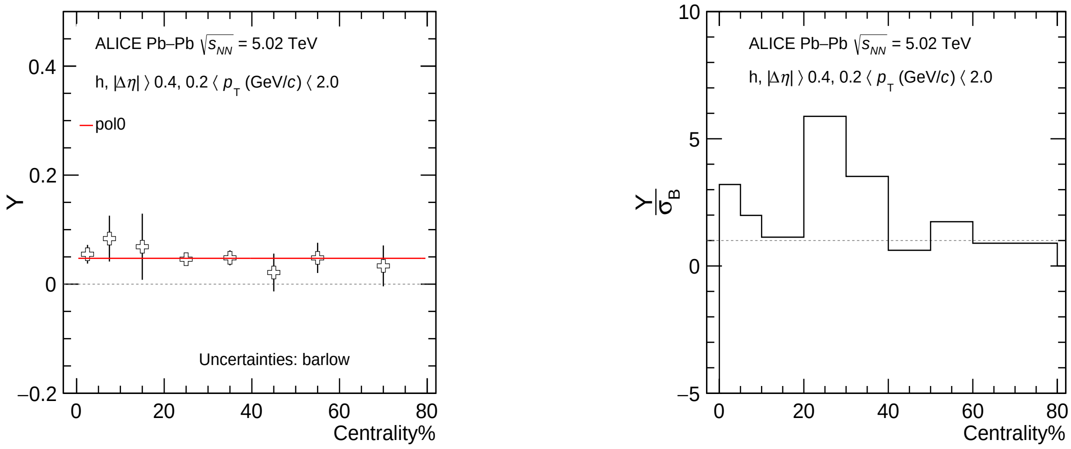

FIGURE A.10: Left panel shows absolute systematic uncertainty for normalised v_3 slope of hadrons and right panel shows its Barlow ratio (passed) both as function of centrality. The errors shown are Barlow only.

Observation: Fig A.9 and fig A.10 shows the absolute value of systematic uncertainty(left) and Barlow ratio(right) due to variation of χ^2_{TPC} cut on $r^{norm}_{\Delta v_2}$ and $r^{norm}_{\Delta v_3}$ respectively for hadrons. A smoothing procedure is applied i.e fiting the data points of fig A.9

with pol0 and of fig A.10 with pol0.

Inference: We see **both $\mathbf{r}^{norm}_{\Delta v_2}$ and $\mathbf{r}^{norm}_{\Delta v_3}$ passes the Barlow test** hence considered as one of the source of systematic uncertainty.

A.1.7 Systematic variation on r_n^{Norm}due to χ^2_{TPC} for pions

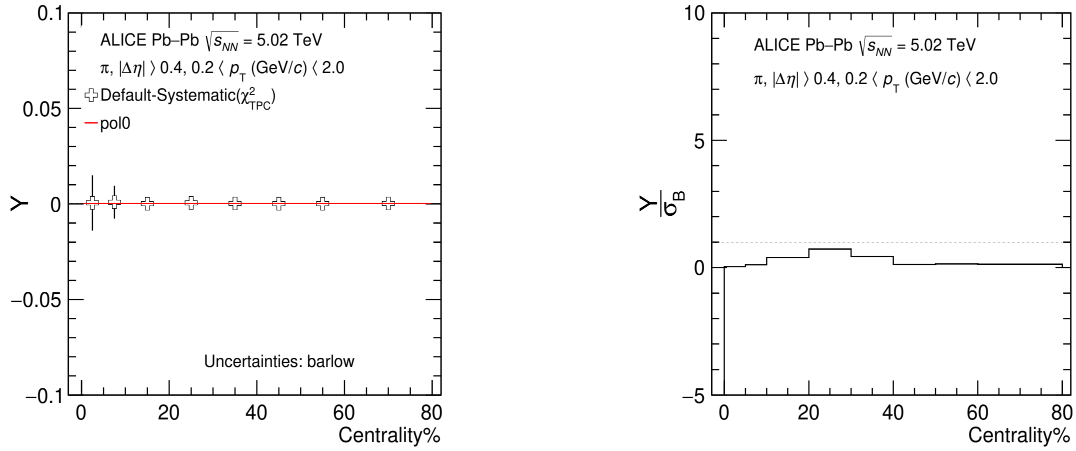

FIGURE A.11: Left panel shows absolute systematic uncertainty for normalised v_2 slope of pions and right panel shows its Barlow ratio (not passed) both as function of centrality. The errors shown are Barlow only. The systematic uncertainty is taken from fitting function.

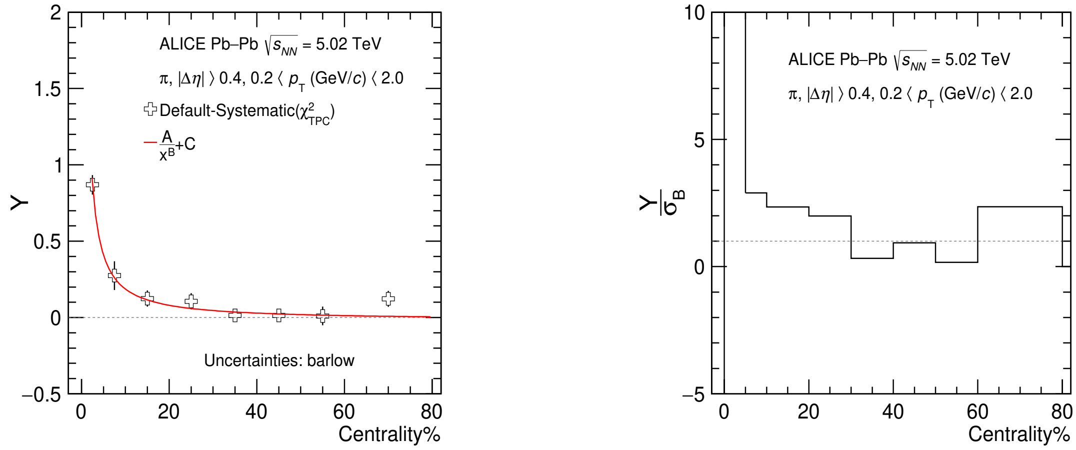

FIGURE A.12: Left panel shows absolute systematic uncertainty for normalised v_3 slope of pions and right panel shows its Barlow ratio (passed) both as function of centrality. The errors shown are Barlow only.

Observation: Fig A.11 and fig A.12 shows the absolute value of systematic uncertainty(left) and Barlow ratio(right) due to variation of χ^2_{TPC} cut on $r^{norm}_{\Delta v_2}$ and $r^{norm}_{\Delta v_3}$ respectively for pions. A smoothing procedure is applied i.e fiting the data points of fig A.11 with pol0 and of fig A.12 with function $A/x^B + \mathrm{C}$.

Inference: We see **only $\mathbf{r}_{\Delta v_3}^{norm}$ passes the Barlow test** hence considered as one of the source of systematic uncertainty.

A.1.8 Systematic variation on r_n^{Norm}due to χ^2_{TPC} for kaons

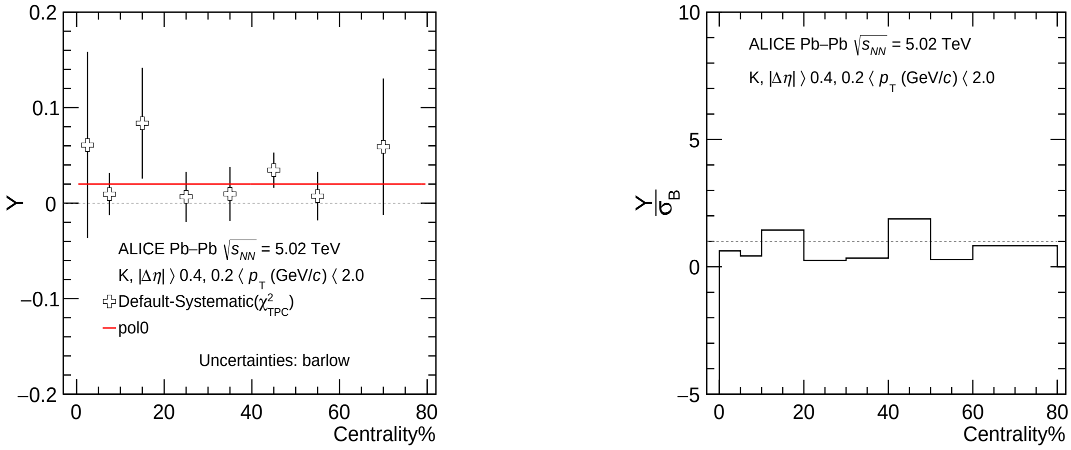

FIGURE A.13: Left panel shows absolute systematic uncertainty for normalised v_2 slope of kaons and right panel shows its Barlow ratio (passed) both as function of centrality. The errors shown are Barlow only. The systematic uncertainty is taken from fitting function.

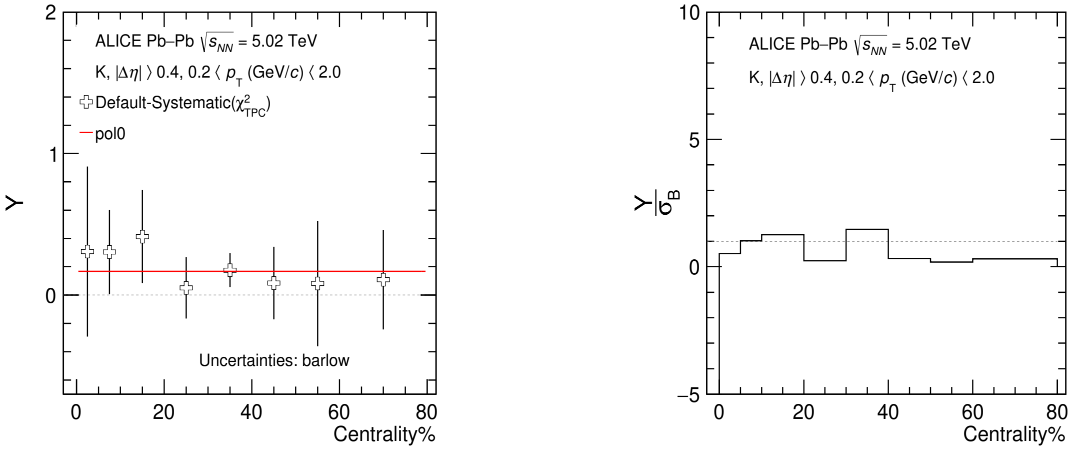

FIGURE A.14: Left panel shows absolute systematic uncertainty for normalised v_3 slope of kaons and right panel shows its Barlow ratio (passed) both as function of centrality. The errors shown are Barlow only. The systematic uncertainty is taken from fitting function.

Observation: Fig A.13 and fig A.14 shows the absolute value of systematic uncertainty(left) and Barlow ratio(right) due to variation of χ^2_{TPC} cut on $\mathrm{r}^{norm}_{\Delta v_2}$ and $\mathrm{r}^{norm}_{\Delta v_3}$ respectively for kaons. A smoothing procedure is applied i.e fiting the data points of fig A.13

with pol0 and of fig A.14 with pol0.

Inference: We see **both** $\mathbf{r}_{\Delta v_2}^{norm}$ **and** $\mathbf{r}_{\Delta v_3}^{norm}$ **passes the Barlow test** hence considered as one of the source of systematic uncertainty.

A.1.9 Systematic variation on r_n^{Norm}due to χ^2_{TPC} for protons

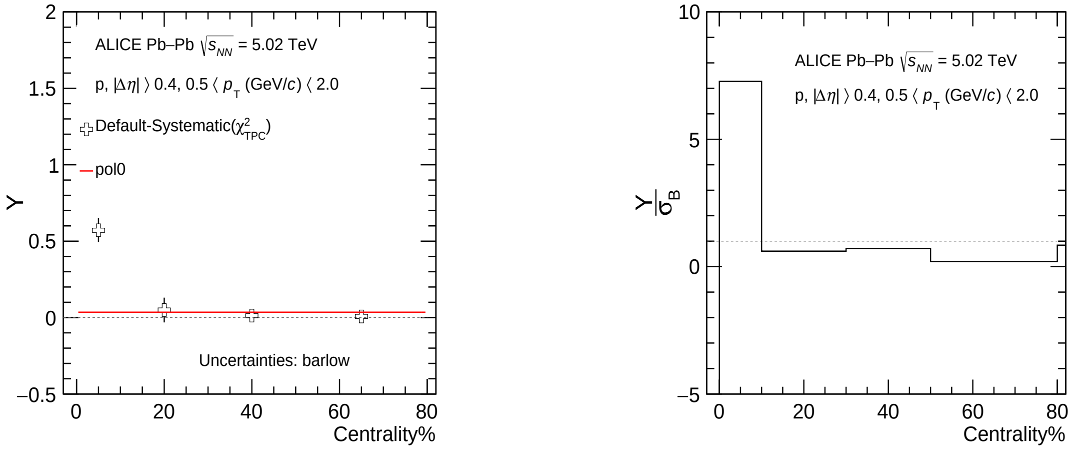

FIGURE A.15: Left panel shows absolute systematic uncertainty for normalised v_2 slope of protons and right panel shows its Barlow ratio (not passed) both as function of centrality. The errors shown are Barlow only.

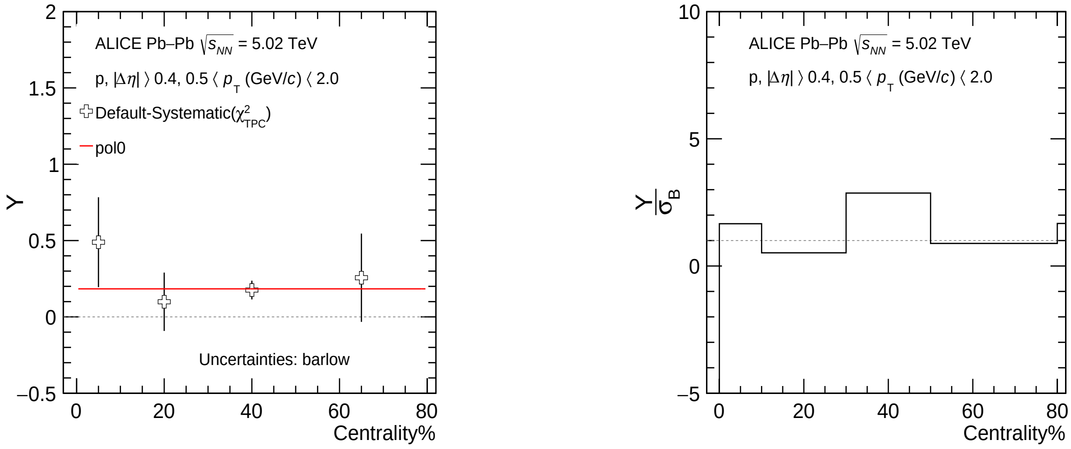

FIGURE A.16: Left panel shows absolute systematic uncertainty for normalised v_3 slope of protons and right panel shows its Barlow ratio (not passed) both as function of centrality. The errors shown are Barlow only. The systematic uncertainty is taken from fitting function.

Observation: Fig A.15 and fig A.16 shows the absolute value of systematic uncertainty(left) and Barlow ratio(right) due to variation of χ^2_{TPC} cut on $r^{norm}_{\Delta v_2}$ and $r^{norm}_{\Delta v_3}$ respectively for protons. A smoothing procedure is applied i.e fiting the data points of fig A.15

with pol0 and of fig A.16 with pol0.

Inference: We see **both $\mathbf{r}^{norm}_{\Delta v_2}$ and $\mathbf{r}^{norm}_{\Delta v_3}$ do not passes the Barlow test** hence systematic uncertainty is estimated from pol0 fit function.

A.1.10 Systematic variation on r_n^{Norm}due to TPC Cluster for hadrons

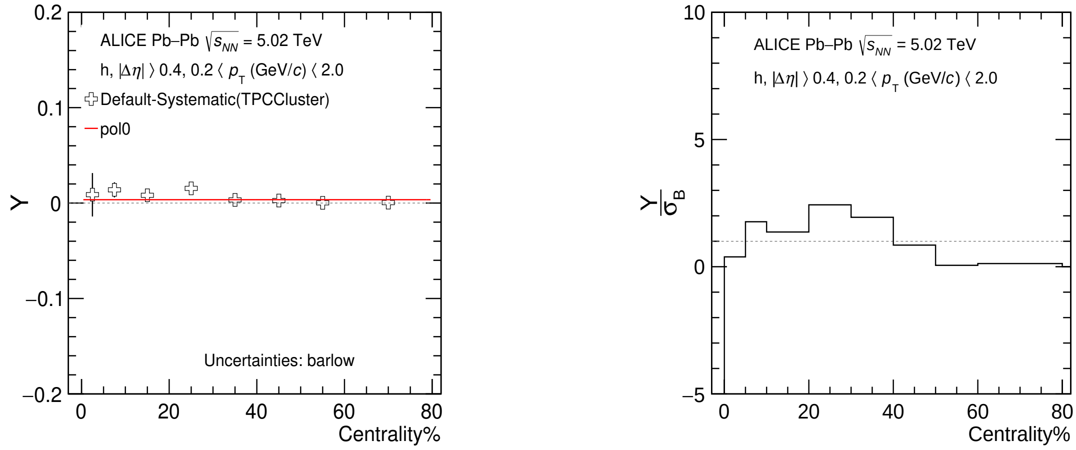

FIGURE A.17: Left panel shows absolute systematic uncertainty for normalised v_2 slope of hadrons and right panel shows its Barlow ratio (passed) both as function of centrality. The errors shown are Barlow only. The systematic uncertainty is taken from fitting function.

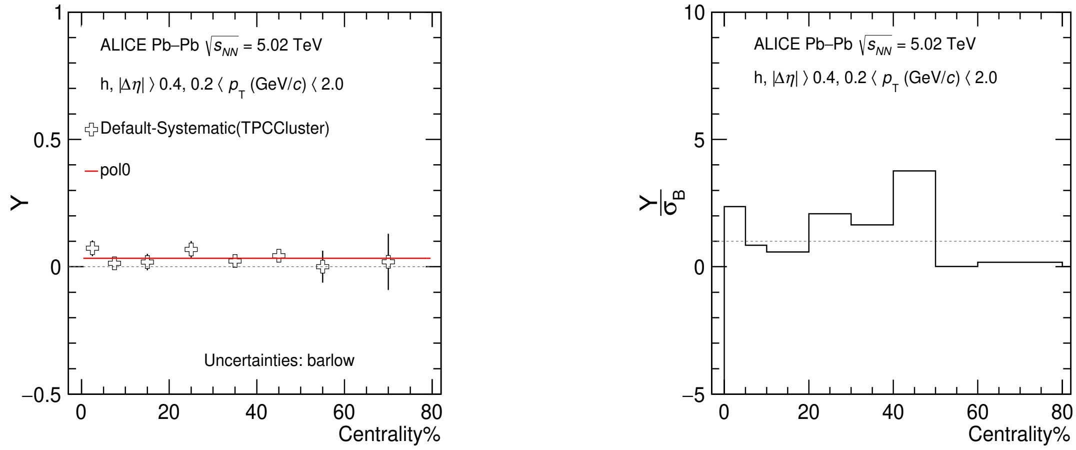

FIGURE A.18: Left panel shows absolute systematic uncertainty for normalised v_3 slope of hadrons and right panel shows its Barlow ratio (passed) both as function of centrality. The errors shown are Barlow only. The systematic uncertainty is taken from fitting function.

Observation: Fig A.17 and fig A.18 shows the absolute value of systematic uncertainty(left) and Barlow ratio(right) due to variation of TPC cluster cut on $r^{norm}_{\Delta v_2}$ and $r^{norm}_{\Delta v_3}$

respectively for hadrons. A smoothing procedure is applied i.e fiting the data points of fig A.17 with pol0 and of fig A.18 with pol0.

Inference: We see **both** $\mathbf{r}^{norm}_{\Delta v_2}$ **and** $\mathbf{r}^{norm}_{\Delta v_3}$ **passes the Barlow test** hence considered as one of the source of systematic uncertainty.

A.1.11 Systematic variation on r_n^{Norm}due to TPC Cluster for pions

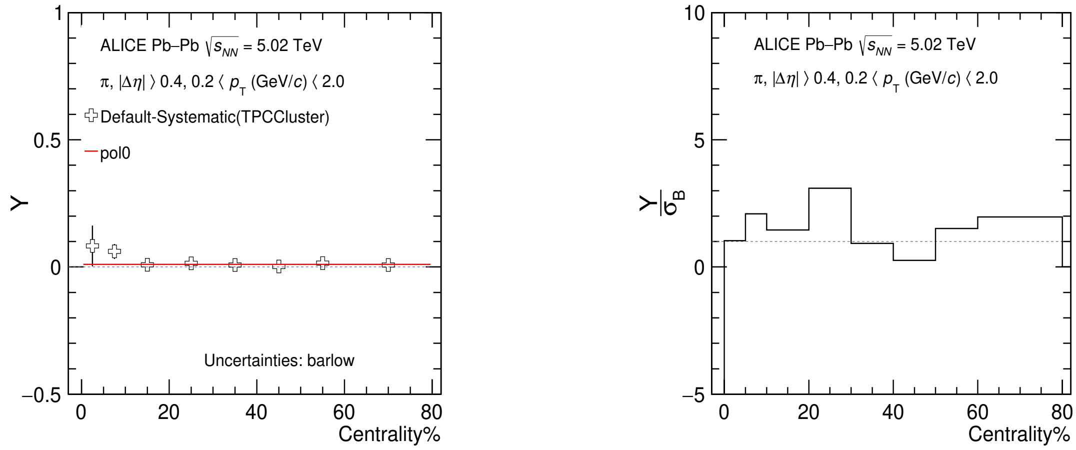

FIGURE A.19: Left panel shows absolute systematic uncertainty for normalised v_2 slope of pions and right panel shows its Barlow ratio (passed) both as function of centrality. The errors shown are Barlow only. The systematic uncertainty is taken from fitting function.

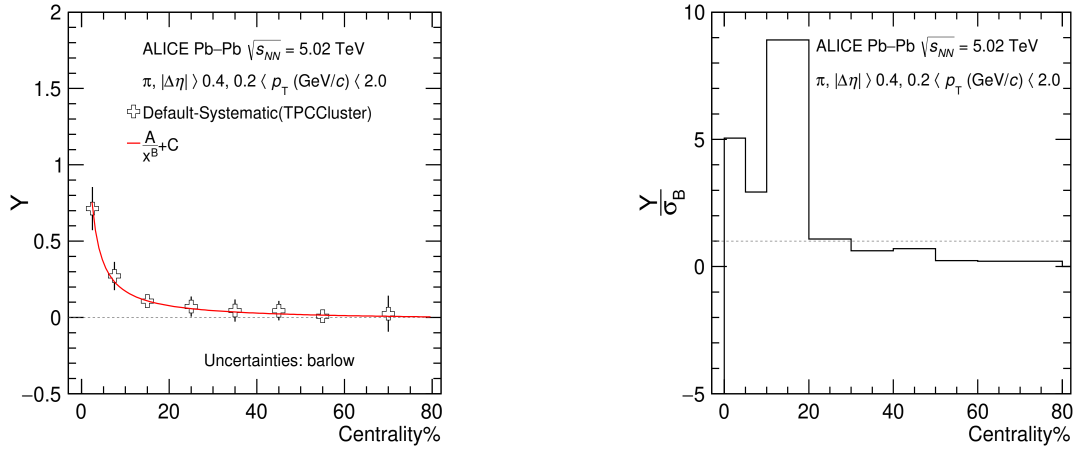

FIGURE A.20: Left panel shows absolute systematic uncertainty for normalised v_3 slope of pions and right panel shows its Barlow ratio (passed) both as function of centrality. The errors shown are Barlow only. The systematic uncertainty is taken from fitting function.

Observation: Fig A.19 and fig A.20 shows the absolute value of systematic uncertainty(left) and Barlow ratio(right) due to variation of TPC cluster cut on $r_{\Delta v_2}^{norm}$ and $r_{\Delta v_3}^{norm}$ respectively for pions. A smoothing procedure is applied i.e fiting the data points of fig

A.11 with pol0 and of fig A.12 with function A/x^B + C.

Inference: We see **both $\mathbf{r}^{norm}_{\Delta v_2}$ and $\mathbf{r}^{norm}_{\Delta v_3}$ passes the Barlow test** hence considered as one of the source of systematic uncertainty.

A.1.12 Systematic variation on r_n^{Norm}due to TPC Cluster for kaons

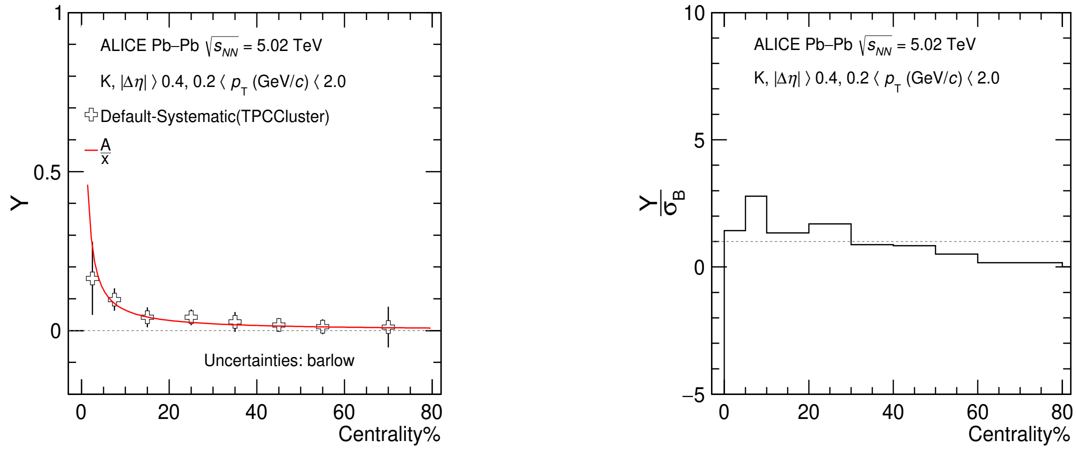

FIGURE A.21: Left panel shows absolute systematic uncertainty for normalised v_2 slope of kaons and right panel shows its Barlow ratio (passed) both as function of centrality. The errors shown are Barlow only. The systematic uncertainty is taken from fitting function.

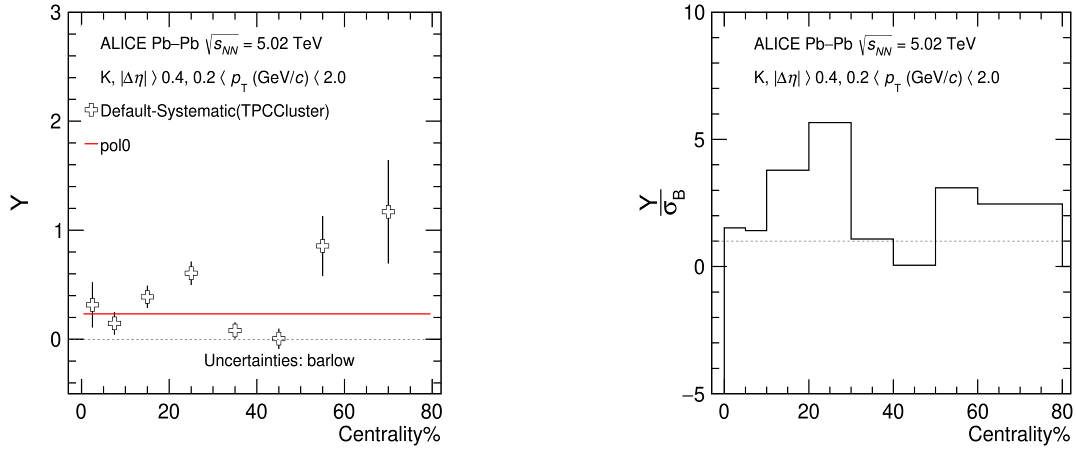

FIGURE A.22: Left panel shows absolute systematic uncertainty for normalised v_3 slope of kaons and right panel shows its Barlow ratio (passed) both as function of centrality. The errors shown are Barlow only. The systematic uncertainty is taken from fitting function.

Observation: Fig A.21 and fig A.22 shows the absolute value of systematic uncertainty(left) and Barlow ratio(right) due to variation of χ^2_{TPC} cut on $r^{norm}_{\Delta v_2}$ and $r^{norm}_{\Delta v_3}$ respectively for kaons. A smoothing procedure is applied i.e fiting the data points of fig A.21

with pol0 and of fig A.22 with pol0.

Inference: We see **both** $\mathbf{r}^{norm}_{\Delta v_2}$ **and** $\mathbf{r}^{norm}_{\Delta v_3}$ **passes the Barlow test** hence considered as one of the source of systematic uncertainty.

A.1.13 Systematic variation on r_n^{Norm}due to TPC Cluster for protons

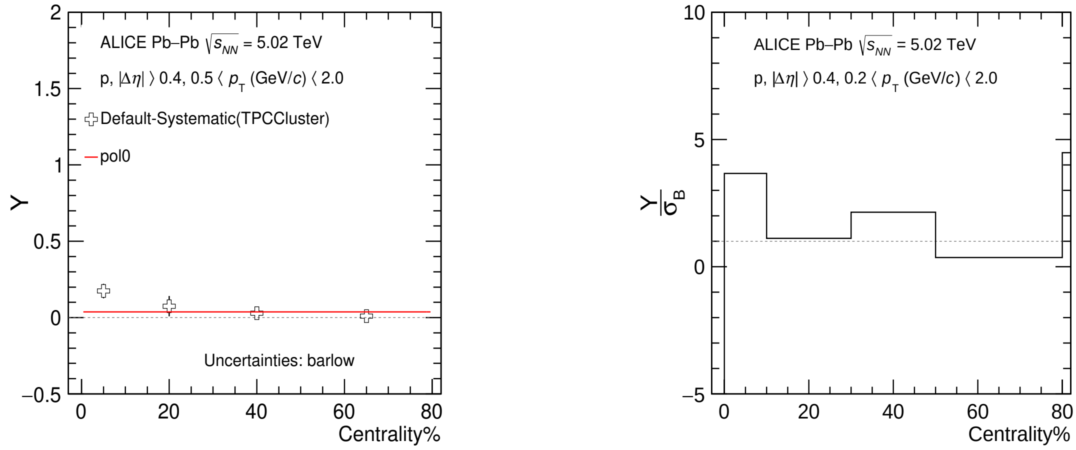

FIGURE A.23: Left panel shows absolute systematic uncertainty for normalised v_2 slope of protons and right panel shows its Barlow ratio (passed) both as function of centrality. The errors shown are Barlow only. The systematic uncertainty is taken from fitting function.

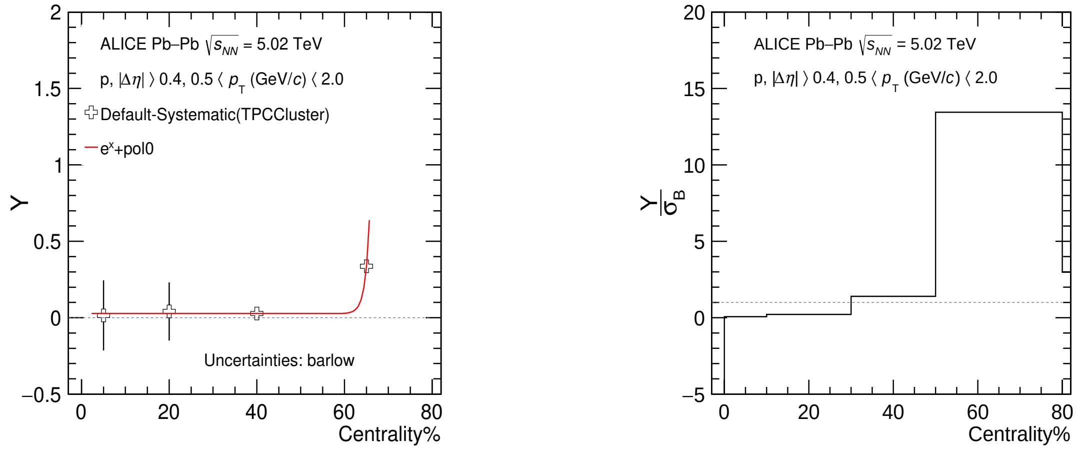

FIGURE A.24: Left panel shows absolute systematic uncertainty for normalised v_3 slope of protons and right panel shows its Barlow ratio (passed) both as function of centrality. The errors shown are Barlow only. The systematic uncertainty is taken from fitting function.

Observation: Fig A.23 and fig A.24 shows the absolute value of systematic uncertainty(left) and Barlow ratio(right) due to variation of χ^2_{TPC} cut on $r_{\Delta v_2}^{norm}$ and $r_{\Delta v_3}^{norm}$ respectively for protons. A smoothing procedure is applied i.e fiting the data points of fig A.23 with pol0 and of fig A.24 with exponential+pol0.

Inference: We see **both $\mathbf{r}^{norm}_{\Delta v_2}$ and $\mathbf{r}^{norm}_{\Delta v_3}$ passes the Barlow test** hence considered as one of the source of systematic uncertainty.

A.1.14 Systematic variation on r_n^{Norm}due to $|\eta| > 0.6$ for hadrons

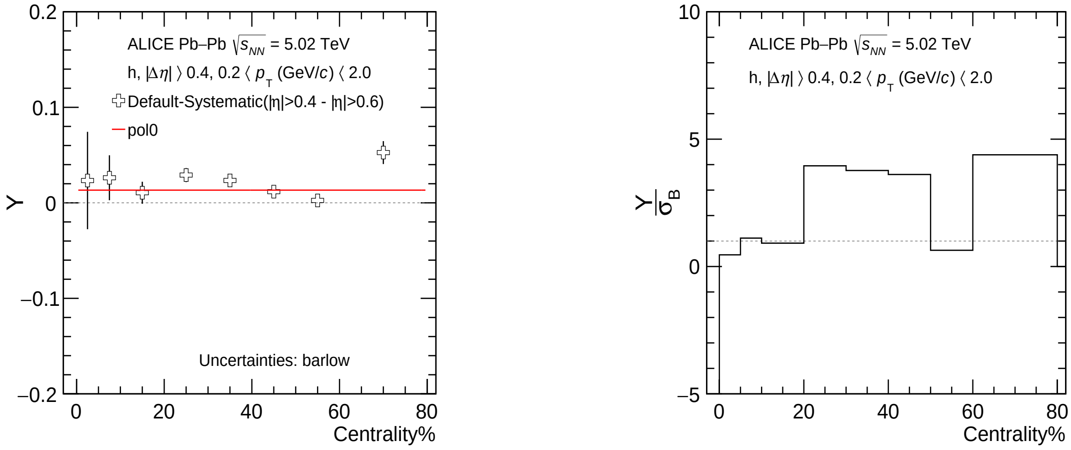

FIGURE A.25: Left panel shows absolute systematic uncertainty for normalised v_2 slope of hadrons and right panel shows its Barlow ratio (passed) both as function of centrality. The errors shown are Barlow only. The systematic uncertainty is taken from fitting function.

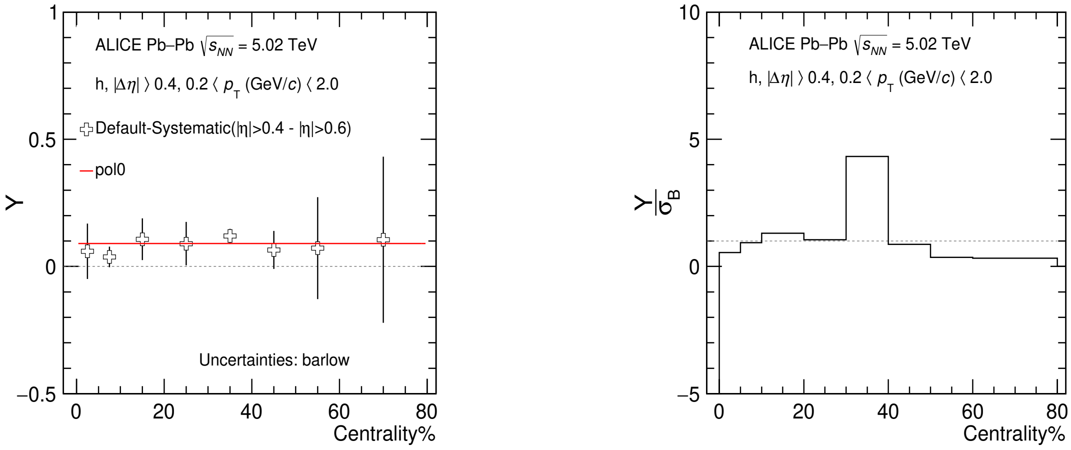

FIGURE A.26: Left panel shows absolute systematic uncertainty for normalised v_3 slope of hadrons and right panel shows its Barlow ratio (passed) both as function of centrality. The errors shown are Barlow only. The systematic uncertainty is taken from fitting function.

Observation: Fig A.25 and fig A.26 shows the absolute value of systematic uncertainty(left) and Barlow ratio(right) due to variation of pseudorapidity gap on $r^{norm}_{\Delta v_2}$ and

$r^{norm}_{\Delta v_3}$ respectively for hadrons. A smoothing procedure is applied i.e fiting the data points of fig A.25 with pol0 and of fig A.26 with pol0.

Inference: We see **both $r^{norm}_{\Delta v_2}$ and $r^{norm}_{\Delta v_3}$ passes the Barlow test** hence considered as one of the source of systematic uncertainty.

A.1.15 Systematic variation on r_n^{Norm}due to $|\eta| > 0.6$ for pions

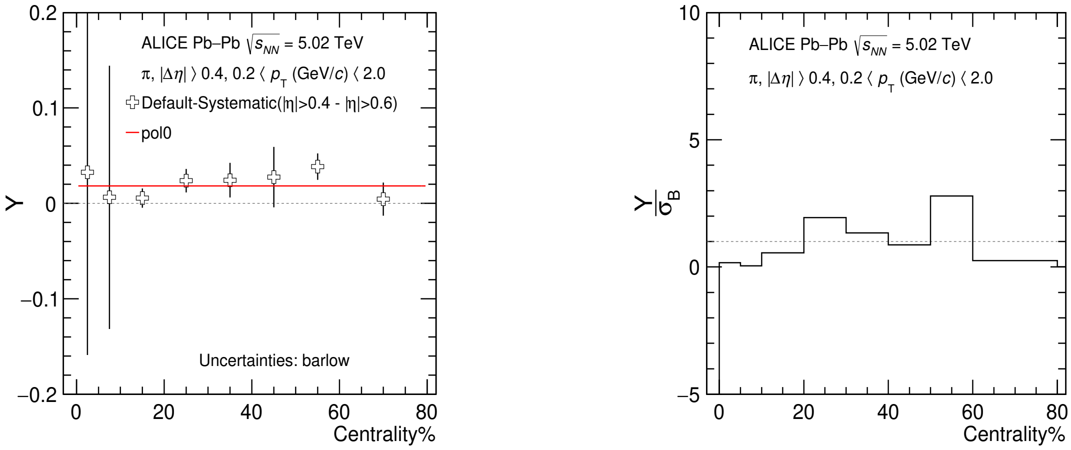

FIGURE A.27: Left panel shows absolute systematic uncertainty for normalised v_2 slope of pions and right panel shows its Barlow ratio (passed) both as function of centrality. The errors shown are Barlow only. The systematic uncertainty is taken from fitting function.

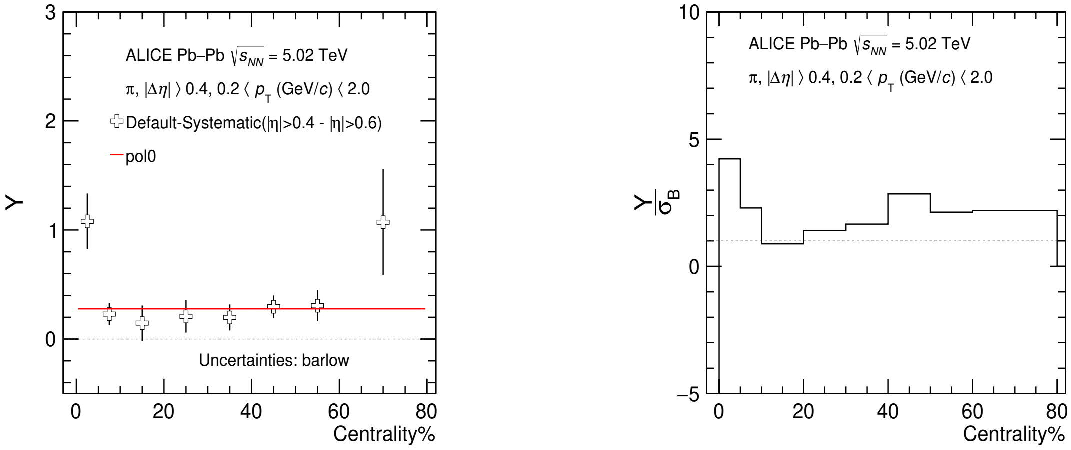

FIGURE A.28: Left panel shows absolute systematic uncertainty for normalised v_3 slope of pions and right panel shows its Barlow ratio (passed) both as function of centrality. The errors shown are Barlow only. The systematic uncertainty is taken from fitting function.

Observation: Fig A.27 and fig A.28 shows the absolute value of systematic uncertainty(left) and Barlow ratio(right) due to variation of pseudorapidity gap on $\mathrm{r}_{\Delta v_2}^{norm}$ and $\mathrm{r}_{\Delta v_3}^{norm}$ respectively for pions. A smoothing procedure is applied i.e fiting the data points of fig A.27 with pol0 and of fig A.28 with pol0.

Inference: We see **both $\mathbf{r}_{\Delta v_2}^{norm}$ and $\mathbf{r}_{\Delta v_3}^{norm}$ passes the Barlow test** hence considered as one of the source of systematic uncertainty.

A.1.16 Systematic variation on r_n^{Norm}due to $|\eta| > 0.5$ for kaons

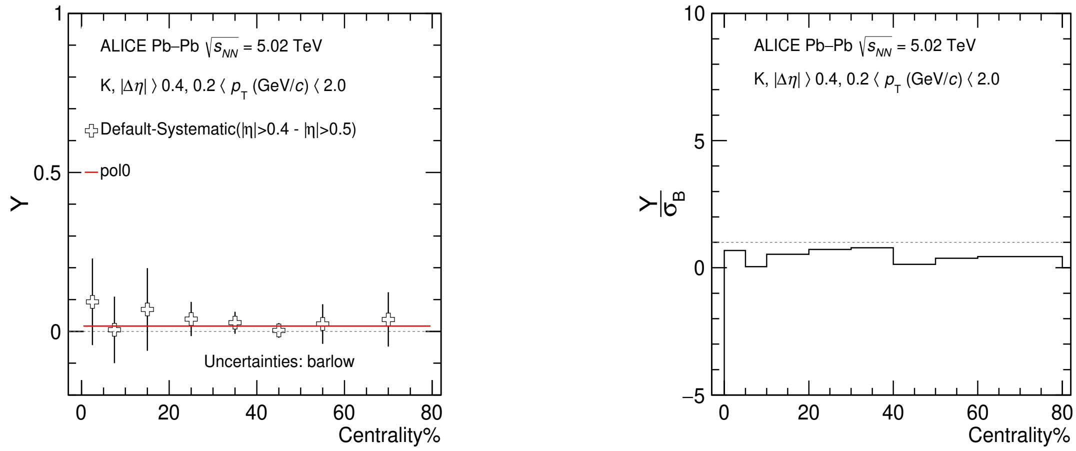

FIGURE A.29: Left panel shows absolute systematic uncertainty for normalised v_2 slope of kaons and right panel shows its Barlow ratio (not passed) both as function of centrality. The errors shown are Barlow only. The systematic uncertainty is taken from fitting function.

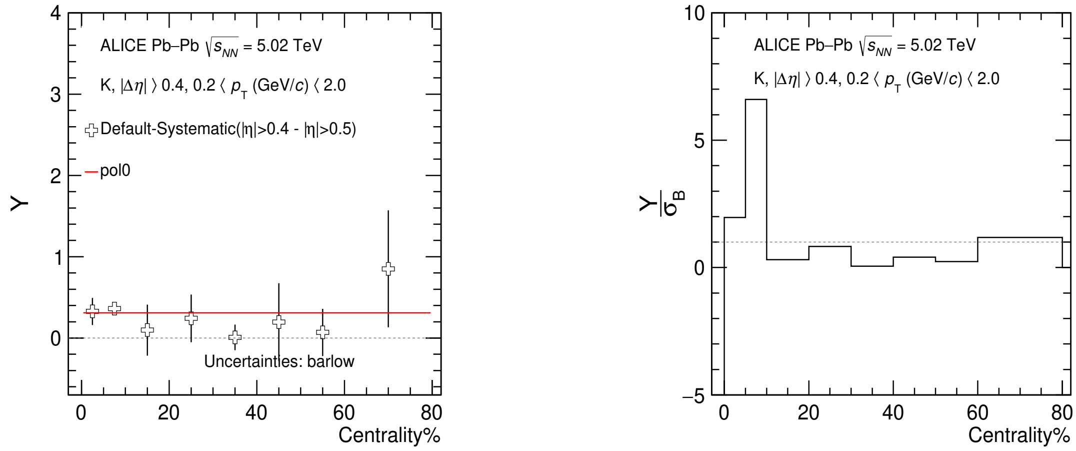

FIGURE A.30: Left panel shows absolute systematic uncertainty for normalised v_3 slope of kaons and right panel shows its Barlow ratio (passed) both as function of centrality. The errors shown are Barlow only. The systematic uncertainty is taken from fitting function.

Observation: Fig A.29 and fig A.30 shows the absolute value of systematic uncertainty(left) and Barlow ratio(right) due to variation of pseudopaidity gap on $\text{r}_{\Delta v_2}^{norm}$ and $\text{r}_{\Delta v_3}^{norm}$ respectively for kaons. A smoothing procedure is applied i.e fiting the data points of fig

A.29 with pol0 and of fig A.30 with pol0.

Inference: We see **only $\mathbf{r}^{norm}_{\Delta v_3}$ passes the Barlow test** hence considered as one of the source of systematic uncertainty.

A.1.17 Systematic variation on r_n^{Norm}due to $|\eta| > 0.5$ for protons

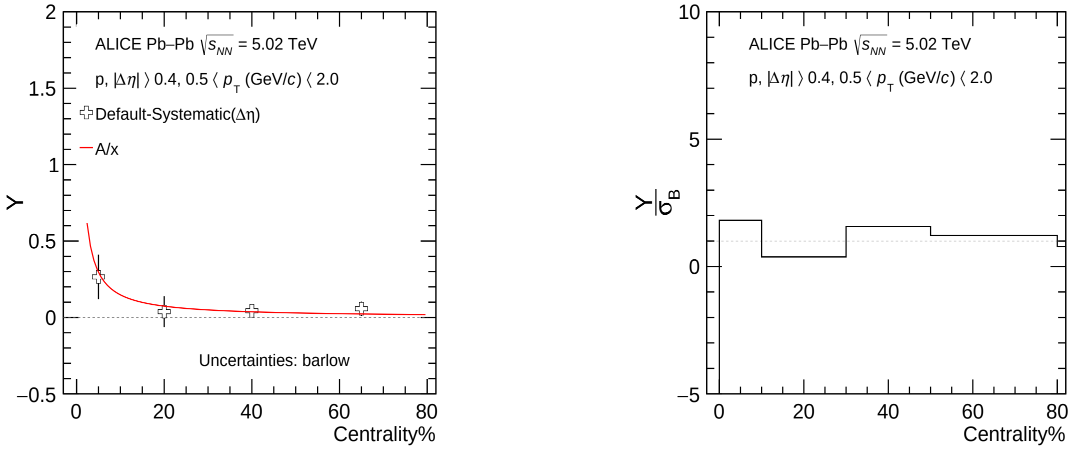

FIGURE A.31: Left panel shows absolute systematic uncertainty for normalised v_2 slope of protons and right panel shows its Barlow ratio (passed) both as function of centrality. The errors shown are Barlow only. The systematic uncertainty is taken from fitting function.

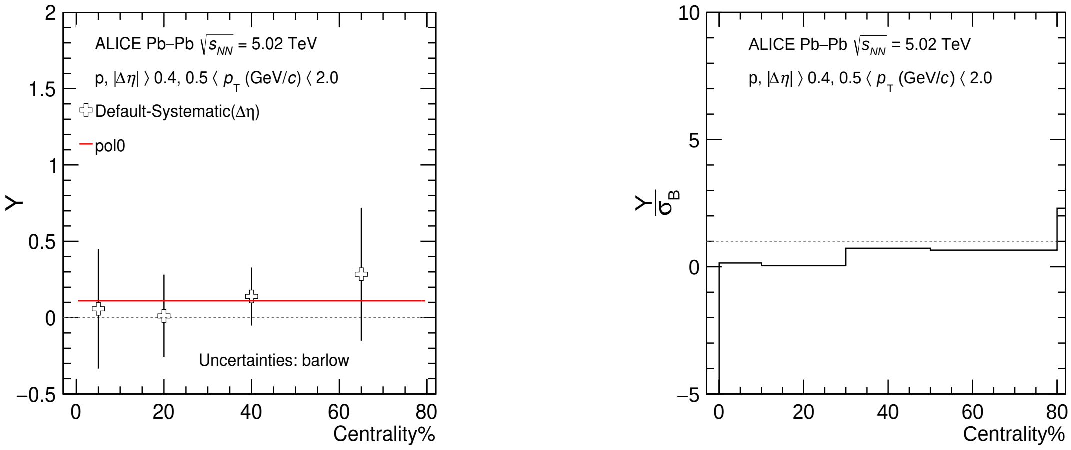

FIGURE A.32: Left panel shows absolute systematic uncertainty for normalised v_3 slope of protons and right panel shows its Barlow ratio (not passed) both as function of centrality. The errors shown are Barlow only. The systematic uncertainty is taken from fitting function.

Observation: Fig A.31 and fig A.32 shows the absolute value of systematic uncertainty(left) and Barlow ratio(right) due to variation of pseudopaidity gap on $r_{\Delta v_2}^{norm}$ and $r_{\Delta v_3}^{norm}$

respectively for protons. A smoothing procedure is applied i.e fiting the data points of fig A.31 with function A/x and of fig A.32 with pol0.

Inference: We see **only r$_{\Delta v_2}^{norm}$ passes the Barlow test** hence considered as one of the source of systematic uncertainty. Systematic uncertainty is estimated for r$_{\Delta v_3}^{norm}$ is estimated from pol0 function.

A.1.18 Systematic variation on r_n^{Norm}due to PID for pions

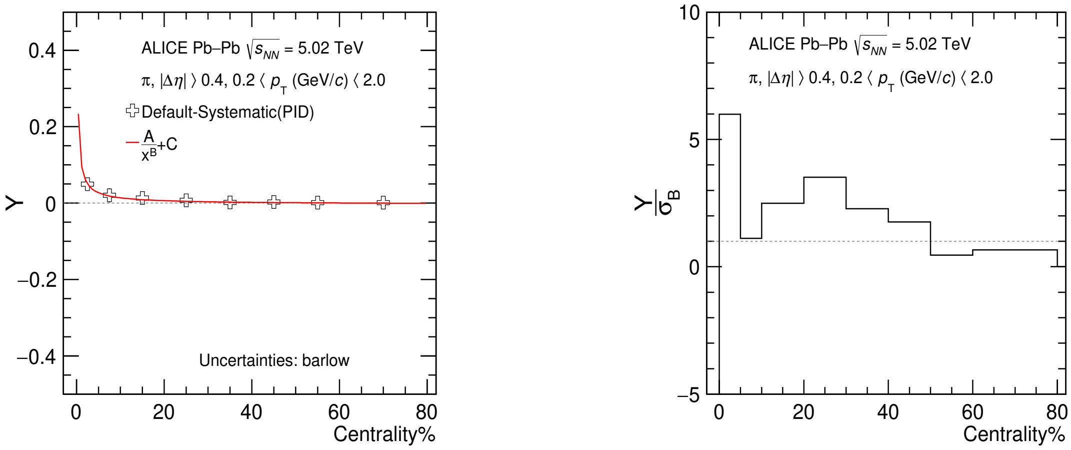

FIGURE A.33: Left panel shows absolute systematic uncertainty for normalised v_2 slope of pions and right panel shows its Barlow ratio (passed) both as function of centrality. The errors shown are Barlow only. The systematic uncertainty is taken from fitting function.

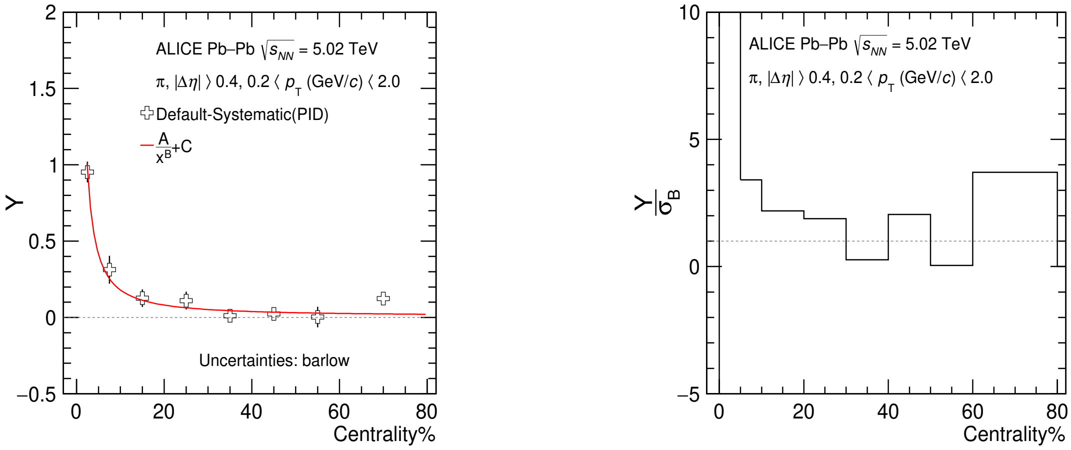

FIGURE A.34: Left panel shows absolute systematic uncertainty for normalised v_3 slope of pions and right panel shows its Barlow ratio (passed) both as function of centrality. The errors shown are Barlow only. The systematic uncertainty is taken from fitting function.

Observation: Fig A.33 and fig A.34 shows the absolute value of systematic uncertainty(left) and Barlow ratio(right) due to variation of PID cut on $r_{\Delta v_2}^{norm}$ and $r_{\Delta v_3}^{norm}$ respectively for pions. A smoothing procedure is applied i.e fiting the data points of fig A.33 with function $A/x^B + C$ and of fig A.34 with function $A/x^B + C$.

Inference: We see **both** $\mathbf{r}^{norm}_{\Delta v_2}$ **and** $\mathbf{r}^{norm}_{\Delta v_3}$ **passes the Barlow test** hence considered as one of the source of systematic uncertainty.

A.1.19 Systematic variation on $r_n^{\rm Norm}$due to PID for kaons

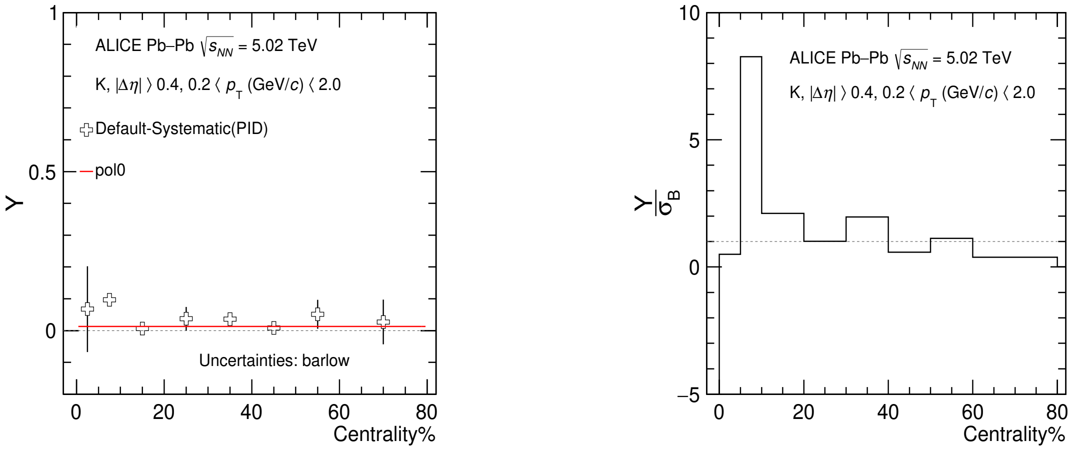

FIGURE A.35: Left panel shows absolute systematic uncertainty for normalised v_2 slope of kaons and right panel shows its Barlow ratio (passed) both as function of centrality. The errors shown are Barlow only. The systematic uncertainty is taken from fitting function.

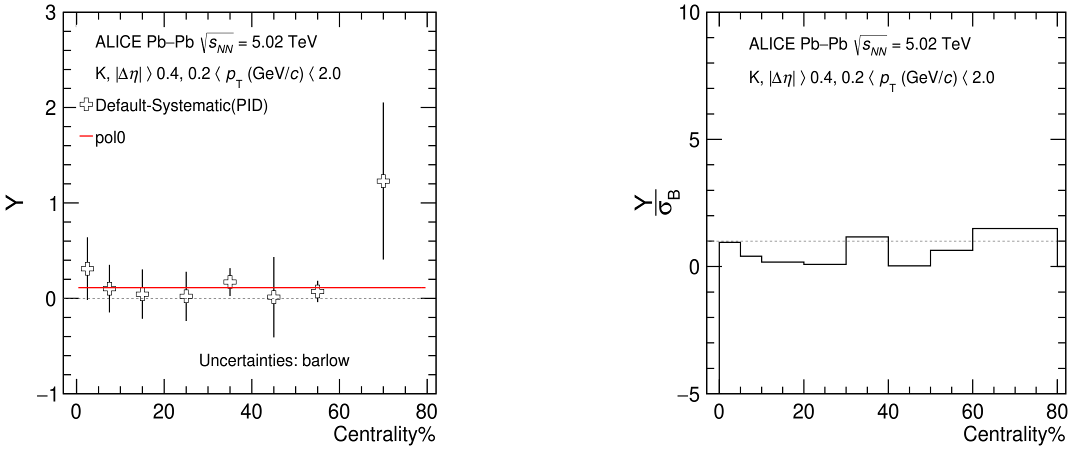

FIGURE A.36: Left panel shows absolute systematic uncertainty for normalised v_3 slope of kaons and right panel shows its Barlow ratio (not passed) both as function of centrality. The errors shown are Barlow only.

Observation: Fig A.35 and fig A.36 shows the absolute value of systematic uncertainty(left) and Barlow ratio(right) due to variation of PID cut on $r_{\Delta v_2}^{norm}$ and $r_{\Delta v_3}^{norm}$ respectively for kaons. A smoothing procedure is applied i.e fiting the data points of fig A.35

with pol0 and of fig A.36 with pol0.

Inference: We see **only $\mathbf{r}_{\Delta\nu_2}^{norm}$ passes the Barlow test** hence considered as one of the source of systematic uncertainty.

A.1.20 Systematic variation on r_n^{Norm}due to PID for protons

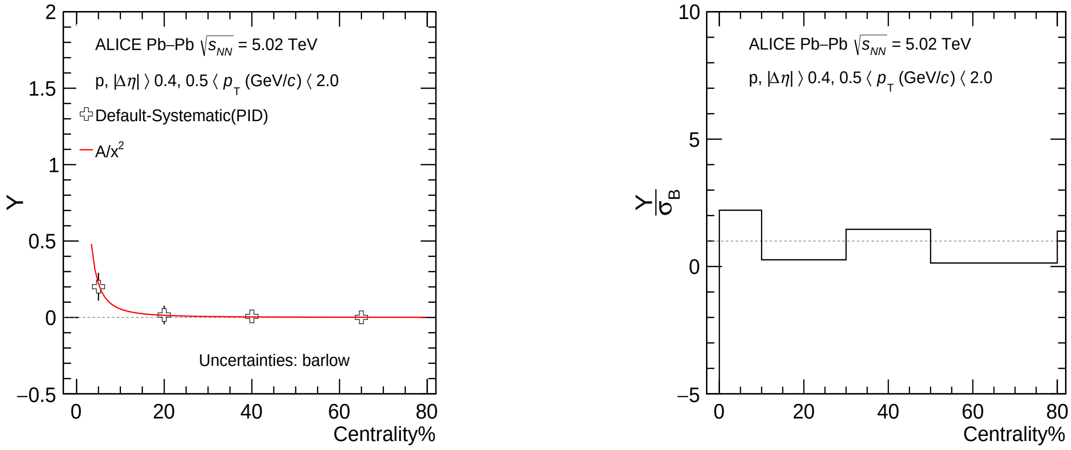

FIGURE A.37: Left panel shows absolute systematic uncertainty for normalised v_2 slope of protons and right panel shows its Barlow ratio (passed) both as function of centrality. The errors shown are Barlow only. The systematic uncertainty is taken from fitting function.

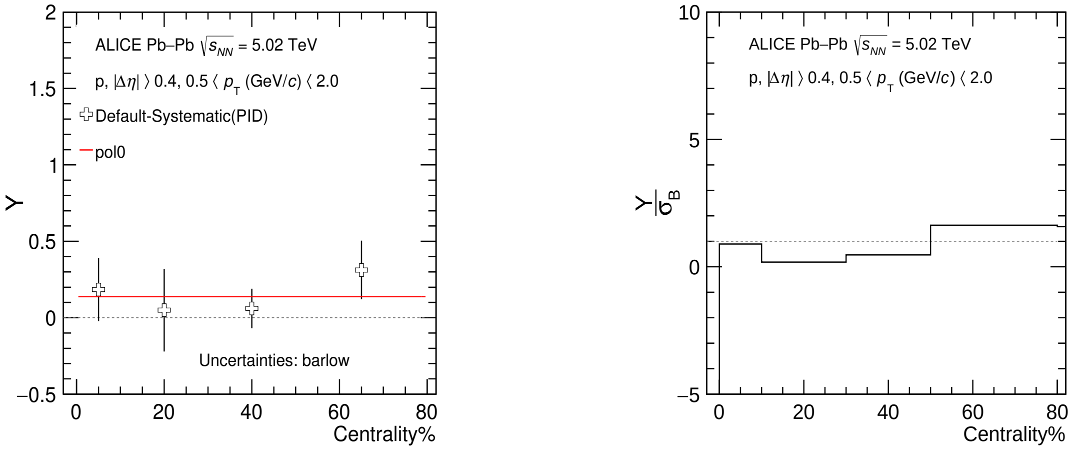

FIGURE A.38: Left panel shows absolute systematic uncertainty for normalised v_3 slope of protons and right panel shows its Barlow ratio (not passed) both as function of centrality. The errors shown are Barlow only. The systematic uncertainty is taken from fitting function.

Observation: Fig A.37 and fig A.38 shows the absolute value of systematic uncertainty(left) and Barlow ratio(right) due to variation of PID cut on $r^{norm}_{\Delta v_2}$ and $r^{norm}_{\Delta v_3}$ respectively for protons. A smoothing procedure is applied i.e fiting the data points of fig A.37 with function A/x and of fig A.38 with pol0.

Inference: We see **only r$^{norm}_{\Delta v_2}$ passes the Barlow test** hence considered as one of the source of systematic uncertainty. For r$^{norm}_{\Delta v_3}$ systematic uncertainty is estimated from pol0 function.

A.1.21 Systematic variation on r_n^{Norm}due to DCA for hadrons

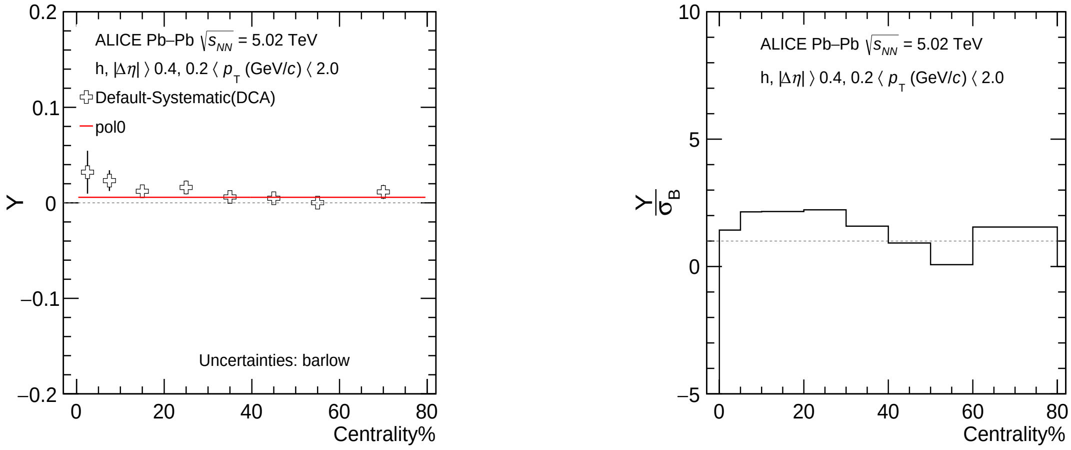

FIGURE A.39: Left panel shows absolute systematic uncertainty for normalised v_2 slope of hadrons and right panel shows its Barlow ratio (passed) both as function of centrality. The errors shown are Barlow only. The systematic uncertainty is taken from fitting function.

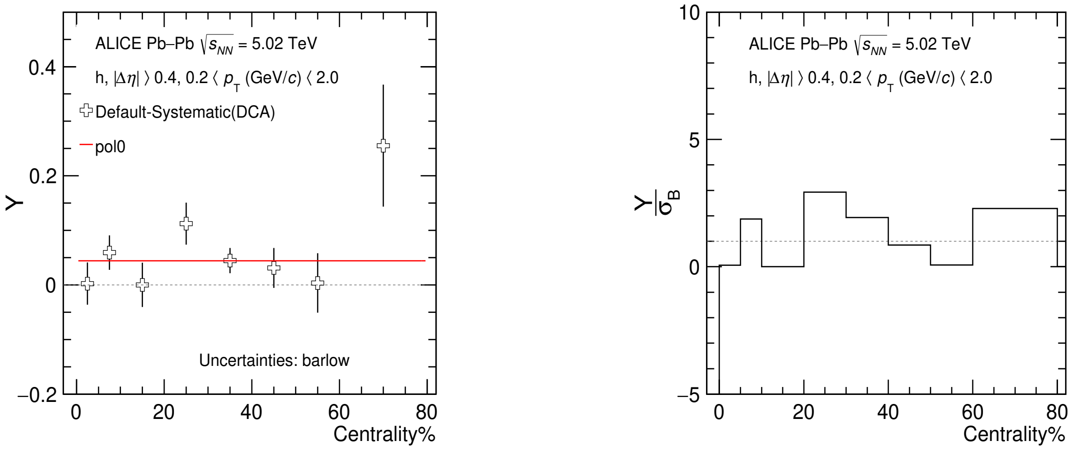

FIGURE A.40: Left panel shows absolute systematic uncertainty for normalised v_3 slope of hadrons and right panel shows its Barlow ratio (passed) both as function of centrality. The errors shown are Barlow only. The systematic uncertainty is taken from fitting function.

Observation: Fig A.39 and fig A.40 shows the absolute value of systematic uncertainty(left) and Barlow ratio(right) due to variation of DCA cut on $r_{\Delta v_2}^{norm}$ and $r_{\Delta v_3}^{norm}$ respectively for hadrons. A smoothing procedure is applied i.e fiting the data points of fig A.39 with pol0 and of fig A.40 with pol0.

Inference: We see **both $\mathbf{r}^{norm}_{\Delta v_2}$ and $\mathbf{r}^{norm}_{\Delta v_3}$ passes the Barlow test** hence considered as one of the source of systematic uncertainty.

A.1.22 Systematic variation on r_n^{Norm}due to DCA for pions

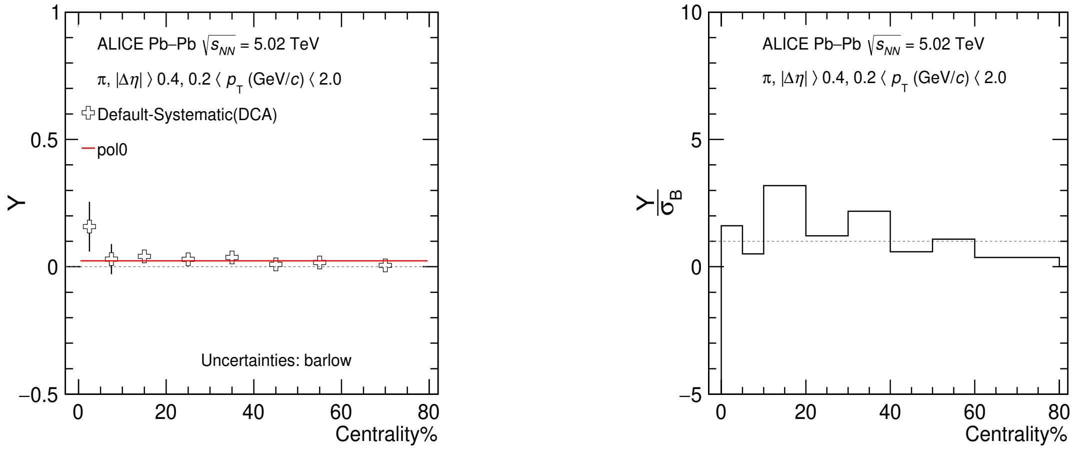

FIGURE A.41: Left panel shows absolute systematic uncertainty for normalised v_2 slope of pions and right panel shows its Barlow ratio (passed) both as function of centrality. The errors shown are Barlow only. The systematic uncertainty is taken from fitting function.

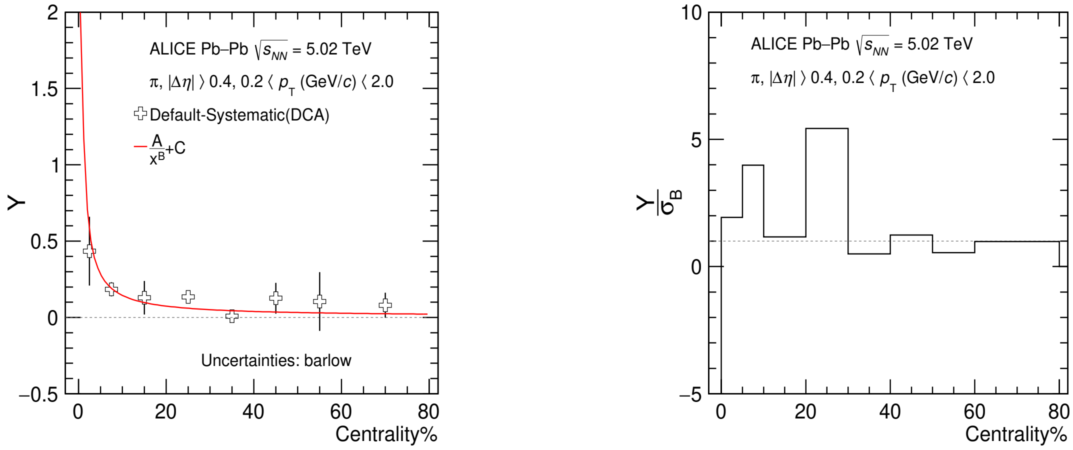

FIGURE A.42: Left panel shows absolute systematic uncertainty for normalised v_3 slope of pions and right panel shows its Barlow ratio (passed) both as function of centrality. The errors shown are Barlow only. The systematic uncertainty is taken from fitting function.

Observation: Fig A.41 and fig A.42 shows the absolute value of systematic uncertainty(left) and Barlow ratio(right) due to variation of DCA cut on $r_{\Delta v_2}^{norm}$ and $r_{\Delta v_3}^{norm}$ respectively for pions. A smoothing procedure is applied i.e fiting the data points of fig A.41 with pol0 and of fig A.42 with function $A/x^B + C$.

Inference: We see **both** $\mathbf{r}_{\Delta v_2}^{norm}$ **and** $\mathbf{r}_{\Delta v_3}^{norm}$ **passes the Barlow test** hence considered as one of the source of systematic uncertainty.

A.1.23 Systematic variation on r_n^{Norm} due to DCA for kaons

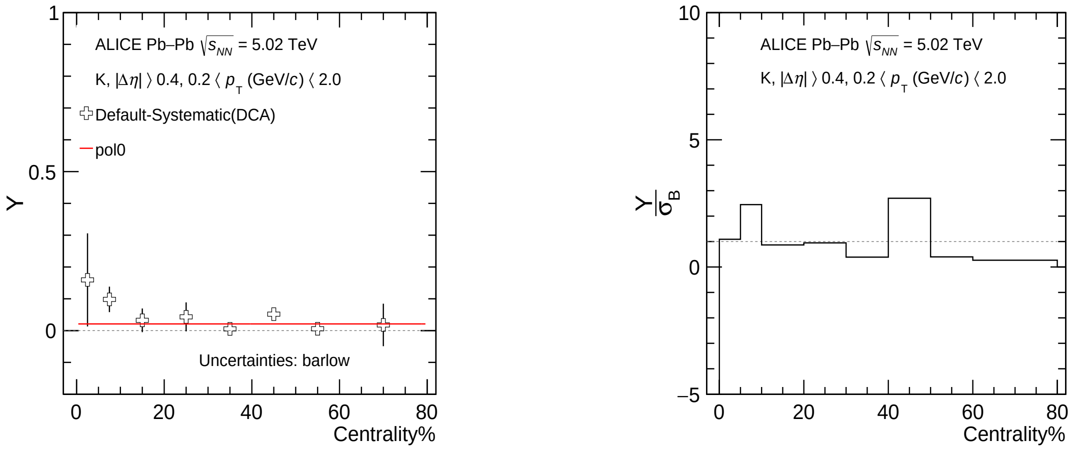

FIGURE A.43: Left panel shows absolute systematic uncertainty for normalised v_2 slope of kaons and right panel shows its Barlow ratio (passed) both as function of centrality. The errors shown are Barlow only. The systematic uncertainty is taken from fitting function.

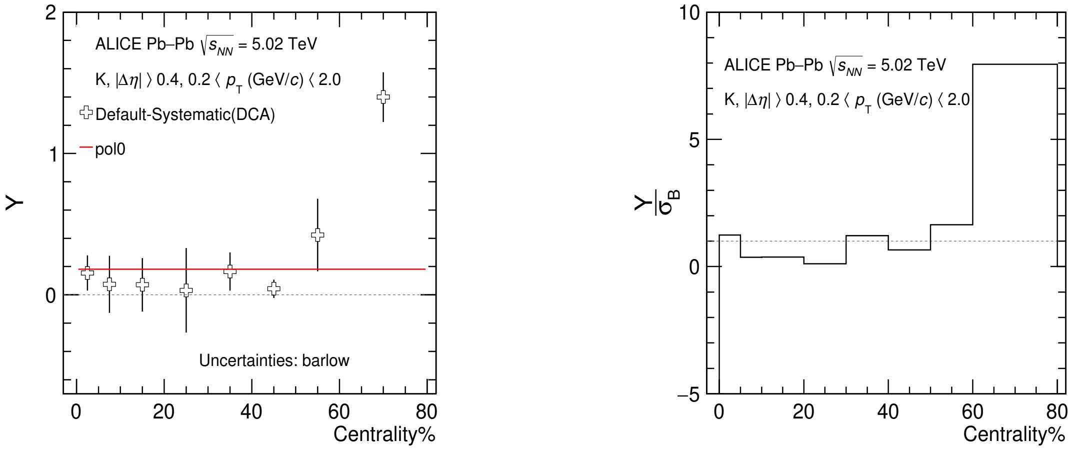

FIGURE A.44: Left panel shows absolute systematic uncertainty for normalised v_3 slope of kaons and right panel shows its Barlow ratio (passed) both as function of centrality. The errors shown are Barlow only. The systematic uncertainty is taken from fitting function.

Observation: Fig A.43 and fig A.44 shows the absolute value of systematic uncertainty(left) and Barlow ratio(right) due to variation of DCA cut on $\mathrm{r}_{\Delta v_2}^{norm}$ and $\mathrm{r}_{\Delta v_3}^{norm}$ respectively for kaons. A smoothing procedure is applied i.e fiting the data points of fig A.43

with pol0 and of fig A.44 with pol0.

Inference: We see **both $\mathbf{r}^{norm}_{\Delta v_2}$ and $\mathbf{r}^{norm}_{\Delta v_3}$ passes the Barlow test** hence considered as one of the source of systematic uncertainty.

A.1.24 Systematic variation on r_n^{Norm}due to DCA for protons

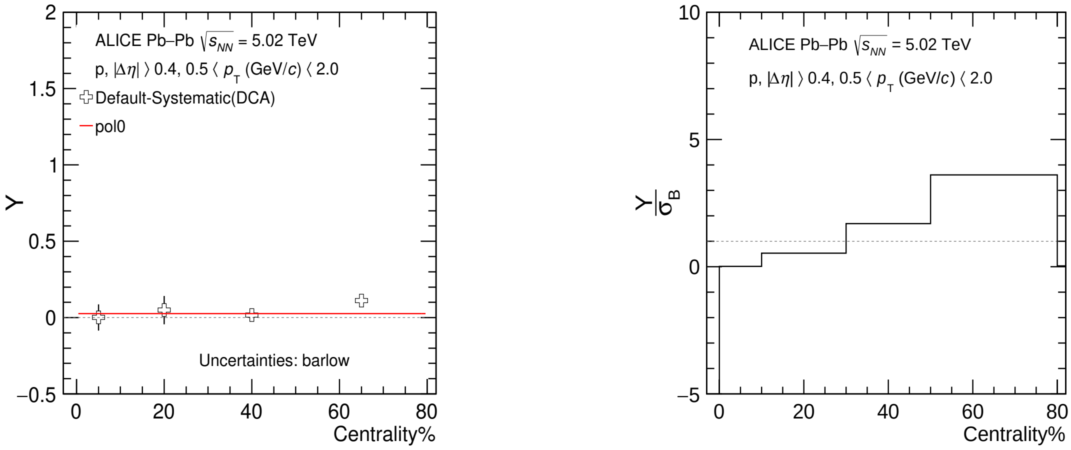

FIGURE A.45: Left panel shows absolute systematic uncertainty for normalised v_2 slope of protons and right panel shows its Barlow ratio (passed) both as function of centrality. The errors shown are Barlow only. The systematic uncertainty is taken from fitting function.

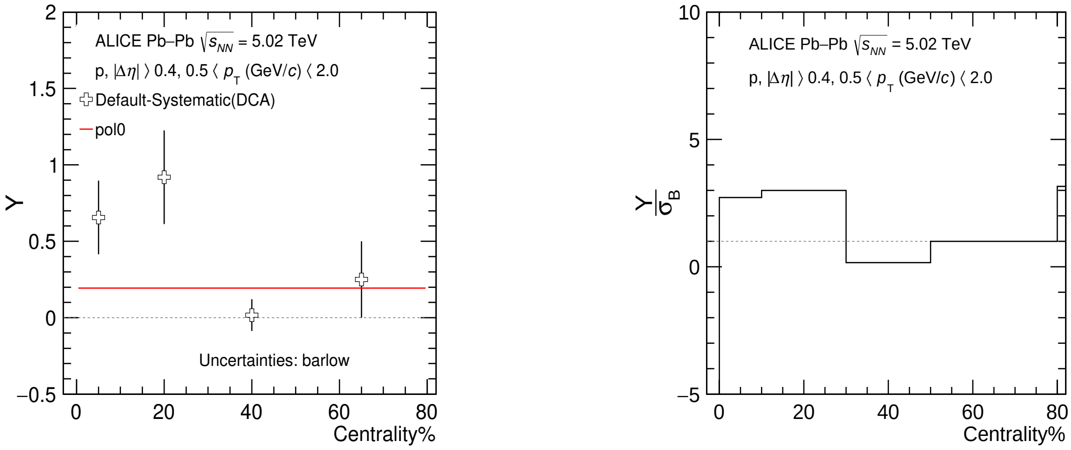

FIGURE A.46: Left panel shows absolute systematic uncertainty for normalised v_3 slope of protons and right panel shows its Barlow ratio (passed) both as function of centrality. The errors shown are Barlow only. The systematic uncertainty is taken from fitting function.

Observation: Fig A.45 and fig A.46 shows the absolute value of systematic uncertainty(left) and Barlow ratio(right) due to variation of DCA cut on $r_{\Delta v_2}^{norm}$ and $r_{\Delta v_3}^{norm}$ respectively for protons. A smoothing procedure is applied i.e fiting the data points of fig A.45 with pol0 and of fig A.46 with pol1.

Inference: We see **both $\mathbf{r}^{norm}_{\Delta v_2}$ and $\mathbf{r}^{norm}_{\Delta v_3}$ passes the Barlow test** hence considered as one of the source of systematic uncertainty.

A.2 BlastWave LCC model

The Blast Wave (BW) model is widely utilized in the study of heavy-ion collisions, offering a convenient framework for understanding particle production and collective motion. It simulates the evolution of an expanding, locally thermalized fireball, which eventually decays into fragments and emits hadrons. The geometry of the QGP system at freeze-out is represented by an ellipse in the transverse direction, with its major axis aligned with the reaction plane, while boost-invariance is assumed along the beam direction. Thermal equilibrium of the hadrons is described by the Boltzmann distribution with a kinetic freeze-out temperature T_{kin}. The initial shape of the fireball is determined by a geometry parameter $R_{\text{x}}/R_{\text{y}}$, representing its spatial asymmetry, where R_{x} and R_{y} denote the lengths of its major and minor axes, respectively. The collective behavior is characterized by the radial flow parameter ρ_0 and the elliptic flow parameter ρ_2 in the form of $\rho \cos 2\phi$, with ϕ denoting the boost angle. In the analysis conducted on Pb–Pb collisions at $\sqrt{s_{\text{NN}}}$ = 5.02 TeV, the BW model's parameters are specified in the first four rows of Table A.1, which effectively describe the ALICE measurements of transverse momentum (p_{T}) spectra and the p_{T}-differential v_2 values for charged pions, kaons, and protons within a relative deviation of 3%.

In the study of Chiral Magnetic Wave (CMW), it is crucial to accurately match the observable A_{ch} distribution (charge asymmetry) to experimental data. By definition, A_{ch}

follows a negative binomial distribution (NBD), where higher multiplicities result in narrower A_{ch} distributions. In each centrality bin, the multiplicity is sampled event by event, following an NBD with mean and variance extracted from ALICE results [1]. The multiplicity for each centrality interval is detailed in the fifth row of Table A.1. Following this sampling, it is evident that the A_{ch} distribution obtained in the BW model closely matches the ALICE data, as depicted in Fig. A.47.

TABLE A.1: BW parameters for Pb–Pb collisions at $\sqrt{s_{NN}}$ = 5.02 TeV.

Centrality	0-5%	5-10%	10-20%	20-30%	30-40%	40-50%	50-60%	60-70%
T_{kin}	111.34	106.96	104.78	103.37	111.63	115.14	118.14	128.20
R_x/R_y	0.956	0.934	0.905	0.872	0.845	0.823	0.807	0.786
ρ_0	1.262	1.267	1.254	1.226	1.196	1.148	1.087	0.994
ρ_2	0.054	0.063	0.11	0.135	0.15	0.145	0.121	0.115
N_{ch}	2290	1858	1334	904	608	369	222	117
f_{LCC}	0.71	0.62	0.58	0.56	0.54	0.48	0.47	0.46

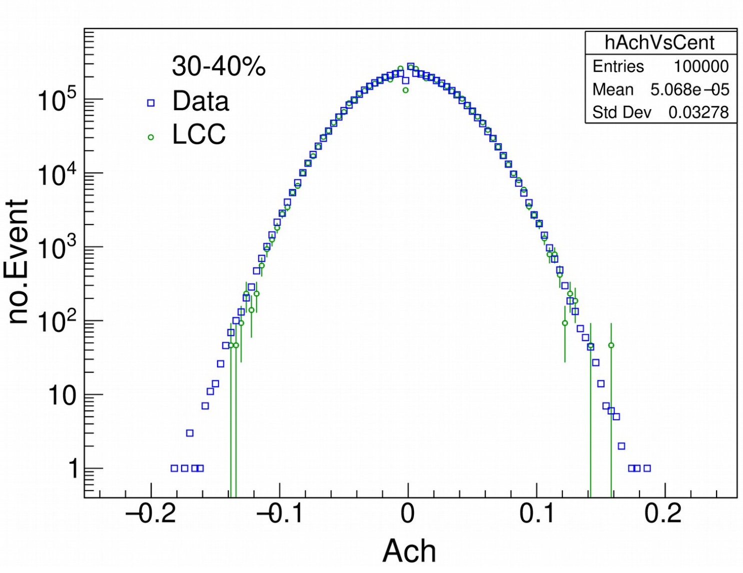

FIGURE A.47: Comparison of A_{ch} distribution obtained in BW-LCC model with ALICE data in Pb–Pb collisions at $\sqrt{s_{NN}}$ = 5.02 TeV for 30-40% centrality.

Furthermore, on the basis of charge conservation, for every particle produced within a specific phase space window, there should be a corresponding antiparticle with an opposite charge. This phenomenon is commonly studied using the balance function [2]. Therefore, in addition to matching the $A_{\rm ch}$ distribution, it is essential to align the balance charge obtained in the model with that observed in the ALICE data. To incorporate a local charge-dependent conservation into the Blast Wave (BW) model (referred to as BW+LCC), particles are emitted in pairs with conserved charge (one positively charged and one negatively charged) at spatial points uniformly distributed within an ellipse. The momenta of particles within a pair are independently sampled from a Maxwell-Boltzmann distribution, determined by the system freeze-out temperature ($\rm T_{kin}$), and then boosted together so that particles follow a common collective velocity. For the remaining spatial points, only one particle is generated with a random charge. The percentage of points emitting pairs, denoted as $\rm f_{LCC}$, is used to characterize the strength of the local charge conservation. We adjust the value of $\rm f_{LCC}$ in each centrality bin to match the experimental results of the charge balance function observed in Pb–Pb collisions at $\sqrt{s_{\rm NN}}$ = 5.02 TeV. The width of the balance function is found to be consistent with ALICE measurements within relative deviations of 5%. The values of $\rm f_{LCC}$ for each centrality interval are provided in the sixth row of Table A.1. Finally, with both the $A_{\rm ch}$ distribution and the balance charge well reproduced in this model compared to ALICE data, we calculated the normalized $r_2^{\rm Norm}$ slope, which is found to be in good agreement with ALICE measurements, as depicted in Fig. 3.8.

Bibliography

[1] Shreyasi Acharya et al. “Production of charged pions, kaons and (anti-)protons in Pb–Pb and inelastic pp collisions at $\sqrt{s_{\mathrm{NN}}} = 5.02$ TeV” (2019). arXiv: `1910.07678 [nucl-ex]`.

[2] Steffen A. Bass, Pawel Danielewicz, and Scott Pratt. “Clocking hadronization in relativistic heavy ion collisions with balance functions”. *Phys. Rev. Lett.* 85 (2000), pp. 2689–2692. arXiv: `nucl-th/0005044`.